Track Fitting in the ATLAS Experiment

CERN-THESIS-2006-072
12/12/2006

Cover: The figure of Atlas, bearing the world on his shoulders, at the rear of the Royal Palace on Dam Square in Amsterdam.

Track Fitting in the ATLAS Experiment

ACADEMISCH PROEFSCHRIFT

ter verkrijging van de graad van doctor
aan de Universiteit van Amsterdam
op gezag van de Rector Magnificus
prof. mr. P.F. van der Heijden
ten overstaan van een door het college voor promoties
ingestelde commissie, in het openbaar te verdedigen
in de Aula der Universiteit
op dinsdag 12 december 2006, te 11:00 uur

door

Thijs Gerrit Cornelissen

geboren te Amsterdam

Promotor:	Prof. dr. F.L. Linde
Co-promotores:	Prof. dr. S.C.M. Bentvelsen
	Dr. P.M. Kluit

Faculteit der Natuurwetenschappen, Wiskunde en Informatica

ISBN: 90-6464-051-3

Printed by Ponsen & Looijen b.v., Wageningen.

The work described in this thesis is part of the research program of 'het Nationaal Instituut voor Kernfysica en Hoge-Energiefysica' (NIKHEF) in Amsterdam, the Netherlands. The author was financially supported by the 'Stichting Fundamenteel Onderzoek der Materie' (FOM).

Aan mijn ouders

Contents

Introduction

In the 20th century, particle physics experiments have proven crucial for our understanding of nature. Particle accelerators like the Large Hadron Collider (LHC) boost subatomic particles to nearly the speed of light, before letting them collide. The extreme energy densities in these collisions are similar to those that existed just after the Big Bang, when the universe was created. Hence, by studying the collisions, the origins of the universe can be studied.

The particles that are created in the collisions are detected by a particle detector. These detectors are extraordinarily complex, requiring years of research and development. The subject of this thesis is the ATLAS experiment, a particle detector that is currently under construction at CERN near Geneva.

The outline of this thesis is as follows.

Chapter 1 starts with a brief overview of the Standard Model, the theory that describes elementary particles and their interactions. Though this theory has proven to be very successful, many questions still remain. Physicists have developed a number of theories that try to answer these questions. Among the most promising of these are models with extra dimensions, which are discussed in the second part of chapter 1.

In chapter 2, an overview of the ATLAS experiment is given. Also the Large Hadron Collider is briefly described, the particle accelerator that will provide the proton beams for ATLAS.

Chapter 3 gives an overview of the simulation and reconstruction software in the ATLAS experiment. One part of the simulation software, the digitization package for the silicon strip detector in ATLAS, is described in detail.

In chapter 4 the software is discussed that reconstructs the tracks in ATLAS. The performance of the software is studied by reconstructing both real and simulated data.

An important test for ATLAS was the 'combined testbeam', which is described in chapter 5. The performance of the actual detector is studied, and the results are compared to the results obtained from the simulation.

The final chapter, chapter 6, studies the potential of ATLAS to discover the existence of extra dimensions. Models with extra dimensions predict the existence of heavy graviton resonances, which can decay into particles that can be detected with ATLAS.

Chapter 1

Theoretical background

This chapter gives a brief overview of the Standard Model, the theory that describes elementary particles and their interactions. This model has proven to be extremely successful, giving theoretical predictions that are in superb agreement with experimental observations. The theory is not complete however, because it does not describe gravity. We will discuss a possible theory beyond the Standard Model that may shed some light on this problem, namely models with large extra dimensions.

1.1 The Standard Model

1.1.1 Introduction

The world around us is built of atoms. In the past century, physicists have discovered that atoms consist of smaller particles, namely protons, neutrons and electrons. It was then found that protons and neutrons consist of even smaller particles, quarks and gluons. So far no evidence has been found that these consist of yet smaller particles, therefore they are called 'elementary'. Particles that consist of quarks and gluons are called *hadrons*. A hadron can be either a *baryon* (three quarks) or a *meson* (two quarks). Quarks are never observed freely, they are always *confined* in bound states (i.e. hadrons).

Though quarks, gluons and electrons are by far the most common type of particle in ordinary matter, they are certainly not the only ones that exist. For example, the electron has two partners that have similar properties: the *muon* (μ) and the *tau* (τ). Each of these has a corresponding *neutrino* particle: the electron neutrino (ν_e), the muon neutrino (ν_μ) and the tau neutrino (ν_τ). Neutrinos are produced abundantly in the Sun, together with photons that are responsible for the light that we see.

Concerning the quarks, there are six types or *flavors*. Only the up (u) and down (d) quarks are found in ordinary matter. The heaviest quark, the top quark (t), is 175 times heavier than a proton! It took until 1995 before particle accelerators had enough energy to produce and discover it [1]. Nevertheless its existence was already expected, since the Standard Model would be in serious trouble without it[1]. Table 1.1 summarizes

[1]More precisely, leaving out the top quark would introduce an *anomaly* in the theory.

the types of quarks and leptons that exist. Note that both the quarks and leptons are divided in three *generations*.

Fermion	Family			Q
	1	2	3	
Leptons	e^- (electron)	μ^- (muon)	τ^- (tau)	-1
	ν_e (electron neutrino)	ν_μ (muon neutrino)	ν_τ (tau neutrino)	0
Quarks	u (up)	c (charm)	t (top)	+2/3
	d (down)	s (strange)	b (bottom)	-1/3

Table 1.1: *The quarks and leptons in the Standard Model. The charge is given in units of absolute electron charge. For each particle there is a corresponding anti-particle (with opposite charge).*

The particles interact with each other through four fundamental interactions:

- **Electromagnetic**. This interaction occurs between particles that have an electrical charge. The particle that is responsible for this interaction is the photon (γ). Since the photon is massless, it (and therefore also the interaction) has infinite range.
- **Weak**. This interaction is responsible for radioactive decays, and for nuclear fusion in the sun. It is mediated by the $W^{\pm}$ and Z particles. These particles have very large masses (nearly 100 GeV) which severely limits the strength and range of the interaction (hence the name 'weak').
- **Strong**. This is the interaction that holds quarks together in protons and neutrons, and it holds protons and neutrons together in atomic nuclei. The strong interaction affects particles that have color charge, namely quarks and gluons. The gluons may be thought of as exchangers of this color charge between the quarks.
- **Gravity**. Supposedly mediated by the graviton, this interaction affects all particles and has infinite range.

The first three of these interactions (electromagnetic, weak and strong) are described by the Standard Model. It is a theory that is based on three separate theories: the theory of quantum electrodynamics (QED), the theory of weak interactions (sometimes called quantum flavordynamics, QFD), and the theory of quantum chromodynamics (QCD). The theory of QED is the oldest of the three, and also the most successful. It was formed by quantizing the theory of classical electrodynamics. The theory of weak interactions was developed in the fifties and sixties. It introduced the idea that weak interactions are mediated by massive intermediate bosons.

In the sixties the electromagnetic and weak interactions were unified in a single electroweak theory by Glashow, Weinberg and Salam, employing the Higgs mechanism of spontaneous symmetry breaking. Veltman and 't Hooft proved in the early seventies

that this electroweak theory is renormalizable. The theory predicts the existence of neutral current interactions, which were observed by the Gargamelle experiment at CERN in 1973. It also predicts the existence of massive gauge bosons, which were found in 1983 by the UA1 and UA2 experiments (also at CERN). However, the Higgs mechanism has not been verified experimentally so far (see section 1.1.3).

The theory of QCD describes the interactions between quarks and gluons. Two characteristic properties of this theory are *asymptotic freedom* and *confinement*. Confinement implies that quarks and gluons cannot be observed in isolation, it would require an infinite amount of energy to pull them apart. That QCD is a confining theory can be demonstrated using lattice QCD computations. Asymptotic freedom means that the strength of the interaction decreases with increasing energy.

The three interactions in the Standard Model are the result of certain symmetries, called *gauge symmetries*. The theory is described by a *Lagrangian* that is invariant under transformations that correspond to these symmetries. The Lagrangian has terms for each individual particle type that describe its kinematics and interactions, but no mass terms. The symmetry associated with the electroweak part of the theory is broken by the Higgs mechanism, which gives masses to the particles. The Higgs mechanism will be described in section 1.1.3, after discussing the Standard Model Lagrangian and its symmetries in section 1.1.2. It is assumed that the reader is already familiar with these concepts. Otherwise, Refs. [2] and [3] provide good overviews.

1.1.2 The Standard Model Lagrangian

In classical physics, a Lagrangian is constructed such that it reproduces the equations of motion, via the Euler-Lagrange equations. For example, the Lagrangian $L = T - U$, where T is the classical kinetic energy and U the potential energy, results in Newton's equation $\vec{F} = m\vec{a}$. In Feynman's formulation of quantum mechanics, the Lagrangian appears in the *path integral*. The path integral gives the amplitude for a particle to move from point A to point B by integrating over all the possible paths, each of which is weighted by the action S ($S \equiv \int L d^4x$) that belongs to that path.

The total number of possible paths is infinite, which makes the path integral ill defined. Thus, the integral needs to be regularized to obtain finite answers for quantities like cross sections. Many of these regularization procedures are done in the context of perturbation theory, where a saddle point approximation is performed on the path integral. Quantities like cross sections can then be expressed as a series expansion, where only the first few terms in the series need to be taken into account if the expansion parameter is small. Each term in the series can be represented by a *Feynman diagram*. The rules that relate the diagrams to the mathematical expressions, the *Feynman rules*, are derived from the Lagrangian.

The theories in the Standard Model are based on invariance principles, i.e. there exist sets of transformations (*symmetry groups*) that leave the Lagrangian L invariant. For example, the symmetry group that is associated with QED is $U(1)$, the group of

complex numbers with modulus 1. The QED Lagrangian is[2]:

$$L = \overline{\psi}(i\gamma^{\mu}D_{\mu} - m)\psi - \frac{1}{4}F_{\mu\nu}F^{\mu\nu}, \tag{1.1}$$

where:

$$F_{\mu\nu} = \partial_{\mu}A_{\nu} - \partial_{\nu}A_{\mu}, \tag{1.2}$$

$$D_{\mu} = \partial_{\mu} + ieA_{\mu}. \tag{1.3}$$

The field ψ is a fermion field[3], while A_{μ} is the photon field. The Lagrangian (1.1) is invariant under the transformation

$$\psi \rightarrow e^{-ie\lambda(x)}\psi, \tag{1.4}$$

$$A_{\mu} \rightarrow A_{\mu} + \partial_{\mu}\lambda. \tag{1.5}$$

Note that λ is supposed to depend on x, therefore the symmetry is called a 'local' symmetry. Local gauge invariance is a stronger requirement than global gauge invariance. If λ does not depend on x then the covariant derivative D_{μ} would not be needed in Eq. (1.1), the derivative ∂_{μ} would be sufficient. In other words, requiring local gauge invariance makes it necessary to replace ordinary derivatives with covariant derivatives. This introduces a term proportional to $\overline{\psi}A_{\mu}\psi$, which represents the coupling between the fermions and the photon. The fermions now interact by exchanging gauge bosons (the photon).

The complete symmetry group of the Standard Model is $SU(3) \otimes SU(2)_L \otimes U(1)_Y$. $SU(3)$ is the symmetry group associated with the strong interactions, while the $SU(2)_L \otimes U(1)_Y$ group is associated with the electroweak part of the theory. The gauge bosons in the theory of strong interactions are the gluons, which act on color charge. The electroweak counterparts of the gluon fields are the fields W_{μ} and B_{μ}, which correspond to weak isospin and weak hypercharge (Y) respectively. These last two are the *generators* of the symmetry groups $SU(2)_L$ and $U(1)_Y$. The subscript L in $SU(2)_L$ denotes that the weak isospin symmetry only affects left-handed fermions. Table 1.2 lists the most important properties of the gauge bosons in the Standard Model.

interaction	name	symbol	spin	mass (GeV)	Q (q_e)
electromagnetic	photon	γ	1	0	0
weak		Z	1	91.187±0.007	0
		$W^{\pm}$	1	80.417±0.10	±1
strong	gluon	g	1	0	0

Table 1.2: *The gauge bosons in the Standard Model. The masses are from Ref. [4].*

The left- and right-handed fermions are grouped as follows:

[2]In this thesis, the convention $\hbar = c = 1$ is used.

[3]Fermions are particles with half-integer spin ($s = \frac{1}{2}$). Quarks and leptons are fermions.

$$\ell_{A_L} = \begin{pmatrix} \nu_A \\ l_A \end{pmatrix}_L, \qquad l_{A_R}, \qquad q_{A_L} = \begin{pmatrix} p_A \\ n_A \end{pmatrix}_L, \qquad p_{A_R}, \qquad n_{A_R}, \tag{1.6}$$

$$\nu_A = (\nu_e, \nu_\mu, \nu_\tau), \tag{1.7}$$

$$l_A = (l_e, l_\mu, l_\tau), \tag{1.8}$$

$$p_A = (u, c, t), \tag{1.9}$$

$$n_A = (d, s, b), \tag{1.10}$$

where A is the generation index ($A = 1, 2, 3$). The kinematics of the fermions, and their interactions with the weak gauge fields, are given by the Lagrangian:

$$L_F = i \sum_A \left(\overline{\ell_{A_L}} \not{D}_L \ell_{A_L} + \overline{l_{A_R}} \not{D}_R l_{A_R} + \overline{q_{A_L}} \not{D}_L q_{A_L} + \overline{p_{A_R}} \not{D}_R p_{A_R} + \overline{n_{A_R}} \not{D}_R n_{A_R} \right), \tag{1.11}$$

where $\not{D}_{L,R} = \gamma^\mu D_{L,R_\mu}$, and D_{L_μ} and D_{R_μ} are the covariant derivatives for left- and right-handed fermions:

$$D_{L_\mu} = \partial_\mu - i g_1 \mathbf{I} \cdot \mathbf{W}_\mu - i g_2 \frac{Y}{2} B_\mu, \tag{1.12}$$

$$D_{R_\mu} = \partial_\mu - i g_2 \frac{Y}{2} B_\mu, \tag{1.13}$$

where g_1 is the weak isospin coupling, and g_2 is the weak hypercharge coupling. Note that the right-handed fermions do not couple to the fields $\mathbf{W}$. Furthermore, the value of Y (the weak hypercharge) is different for left-handed and right-handed fermions.

The Lagrangian that describes the gauge fields and their self interactions is given by:

$$L_G = -\frac{1}{4} F^a_{\mu\nu} F^{\mu\nu}_a - \frac{1}{4} F_{\mu\nu} F^{\mu\nu}, \tag{1.14}$$

where:

$$F^a_{\mu\nu} = \partial_\mu W^a_\nu - \partial_\nu W^a_\mu + g_1 \epsilon^{abc} W^b_\mu W^c_\nu, \tag{1.15}$$

$$F_{\mu\nu} = \partial_\mu B_\nu - \partial_\nu B_\mu. \tag{1.16}$$

Here ϵ^{abc} is the Levi-Civita tensor, the structure constants of the group $SU(2)$.

Two more contributions are needed to obtain the full electroweak Lagrangian: a part that describes the Higgs field and its interactions with the gauge fields, and a part that describes the Higgs-fermion interactions. These are discussed in the next section.

1.1.3 The Higgs mechanism

The gauge fields W_μ and B_μ are massless. Adding mass terms for these fields 'by hand' in the Lagrangian would break the gauge invariance of the theory, which would make the theory non-renormalizable. Such a theory cannot be used to compute observable quantities like cross sections, because of infinities that appear in the calculations. On the other hand, the W and Z bosons are clearly not massless, so mass terms in the Lagrangian are definitely needed.

A solution for this problem is provided by the Higgs mechanism [5], in which the gauge symmetry is spontaneously broken. Spontaneous symmetry breaking implies that the theory is still gauge invariant, but the ground state no longer exhibits this symmetry. To accomplish this, a complex scalar field ϕ is introduced, which (as it turns out) generates the masses of the gauge bosons and the fermions. The Lagrangian that corresponds with this field is:

$$L = \frac{1}{2}\partial_\mu\phi^\dagger\partial^\mu\phi + \frac{1}{2}\mu^2|\phi|^2 - \frac{1}{4}\lambda^2|\phi|^4. \tag{1.17}$$

The potential in this Lagrangian has the shape of a Mexican hat if $\mu^2 > 0$ (see Fig. 1.1), and it reaches a minimum at $|\phi| = \frac{\mu}{\lambda}$. Since one should expand around the ground state to perform perturbation theory, the fields $\rho = \phi_1 - \frac{\mu}{\lambda}$ and $\xi = \phi_2$ are introduced, where ϕ_1 and ϕ_2 are the real and imaginary components of the field ϕ. In terms of these fields, the Lagrangian reads:

$$L = \frac{1}{2}(\partial_\mu\rho)(\partial^\mu\rho) - \mu^2\rho^2 + \frac{1}{2}(\partial_\mu\xi)(\partial^\mu\xi) + \lambda\mu(\rho^3 + \rho\xi^2) - \frac{\lambda^2}{4}(\rho^4 + \xi^4 + 2\rho^2\xi^2) + \frac{\mu^4}{4\lambda^2}. \tag{1.18}$$

This Lagrangian is no longer invariant under $U(1)$ transformations, but the symmetry is still there, it is merely hidden by the choice of ground state. The field ρ is called the Higgs field. Its mass is $\sqrt{2}\mu$, while the field ξ is massless (there is no term proportional to ξ^2 in Eq. (1.18)). The field ξ corresponds to motion along the valley of the Higgs potential (Fig. 1.1), where the potential is constant. That the field ξ is massless is no coincidence: according to Goldstone's theorem, a massless scalar state appears for every degree of freedom of a spontaneously broken continuous symmetry. The field ξ is called a Nambu-Goldstone boson. It can be transformed away by choosing a suitable gauge (the 'unitary gauge').

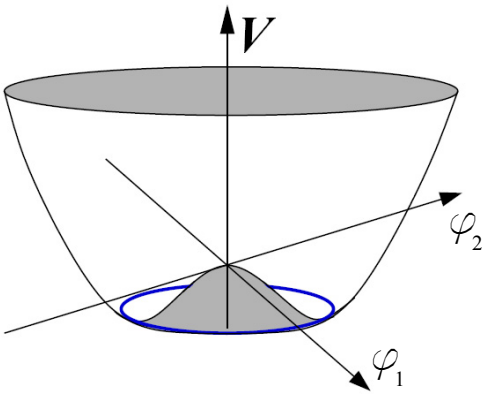

Figure 1.1: *A vacuum potential shaped like a Mexican hat.*

The Lagrangian is now extended with the electroweak Lagrangian. The derivatives in Eq. (1.17) are replaced by covariant derivatives, which yields coupling terms between

the Higgs field and the gauge fields W_μ and B_μ. After transforming the Higgs field to the minimum of its potential, these coupling terms generate masses for the following fields:

$$W_\mu^\pm = \frac{1}{\sqrt{2}}(W_{\mu,1} \mp iW_{\mu,2}), \tag{1.19}$$

$$Z_\mu = -\sin\theta_W B_\mu + \cos\theta_W W_{\mu,3}, \tag{1.20}$$

where θ_W is the weak mixing angle. These fields are the familiar W and Z bosons. Their masses are:

$$m_{W^\pm}^2 = \frac{g_2^2 v^2}{4}, \qquad m_Z = (g_1^2 + g_2^2)\frac{v^2}{4} = \frac{m_W^2}{\cos^2\theta_W}, \tag{1.21}$$

where $v = \frac{\mu}{\lambda}$ is called the vacuum expectation value of the Higgs field. One combination remains massless:

$$A_\mu = \cos\theta_W B_\mu + \sin\theta_W W_{\mu,3}, \tag{1.22}$$

which is the photon field. Since it is massless, the Lagrangian is still invariant under $U(1)_{EM}$ transformations, while the $SU(2)_L \otimes U(1)_Y$ symmetry has been broken.

The masses of the fermions are generated by introducing Yukawa couplings between the Higgs and fermion fields, which yield masses of the form $m_f = g_f v/\sqrt{2}$. The coupling g_f is different for each fermion species, which 'explains' why their masses are different (although this does not explain why the couplings are different).

The Higgs field itself has a mass $m_H = \sqrt{2}\mu$, the value of which is unknown. Direct searches at LEP have placed a lower bound of 114 GeV on the mass (at 95% confidence level). Theoretical arguments require the Higgs mass to be below 1 TeV. The LHC experiments will be able to detect the Higgs particle in this mass range, if it exists. Note that the complete absence of a Higgs particle would not contradict any observations that are currently available. In that case, there must be other new physics that explains the origin of the electroweak symmetry breaking (and hence the particle masses). Also, this new physics must explain why e.g. the W-W scattering amplitude does not violate unitarity at $\sqrt{s} \approx 1.5$ TeV (in the Standard Model, the Higgs particle makes this (and other amplitudes) finite [6]).

1.2 Models with extra dimensions

A fundamental problem in physics is the hierarchy problem: while electroweak interactions take place at an energy scale $M_{EW} \sim 10^2$ GeV, the gravitational interaction only becomes important at the Planck scale ($M_{Pl} \sim 10^{19}$ GeV). There is thus a hierarchy of 17 orders of magnitude between the two interactions. In recent years, several theories have emerged that explain this hierarchy by postulating the existence of extra space dimensions. In these theories, the Standard Model fields are confined to a 4-dimensional manifold, while gravity can propagate through all the dimensions (the 'bulk'). The observed weakness of the gravitational interaction is then not fundamental, it is merely a consequence of the existence of the extra dimensions. The extra dimensions are assumed to be curled up, such that their small size explains why they have escaped detection so far.

If one of these theories is right, this would imply that quantum gravity can be probed by current and future experiments. For example, Newton's gravity force law could already break down at distances $r \sim 0.1$ mm, instead of at the Planck length (about 10^{-33} m). In a collider experiment like ATLAS, real gravitons could be produced that escape into the extra dimensions, which would lead to events with large amounts of missing energy. Virtual graviton exchange could enhance the cross sections of certain processes, e.g. the Drell-Yan process, and modify the angular distributions of the decay products.

Two models with extra dimensions are currently the most popular. The first model was proposed by Arkani-Hamed, Dimopoulos and Dvali, it is called the ADD model. The second model was proposed by Randall and Sundrum. We will briefly discuss both of these models in this section. More complete overviews can be found in Refs. [7] and [8].

1.2.1 Large extra dimensions (ADD model)

In the ADD model [9], a $4+d$-dimensional factorizable geometry is used, i.e. space-time is assumed to be a simple product of a four-dimensional space-time with an independent d-dimensional space. The extra dimensions are curled up (compactified), such that they have no effect on macroscopic distance scales. Gravity is allowed to propagate in the full $4+d$ dimensions, while the Standard Model fields can only live on a 4-dimensional submanifold, called 3-brane. In what follows, we will denote coordinates in the $4+d$-dimensional space as $\{\hat{x}^M\} = \{x^\mu, y^m\}$, where $M = 0, 1, \ldots, 3+d$, $\mu = 0, 1, 2, 3$ and $m = 1, 2, \ldots, d$.

The effect of the extra dimensions on Newton's force law can be derived using Gauss' law [10]. Consider the easiest example, one extra dimension that is compactified to the circle S_1 with length L, and a point mass m placed at the origin. This situation can be reproduced by replacing the circle S_1 with the line $\mathbb{R}$, and placing mirror masses at $y = nL, n \in \mathbb{Z}, n \neq 0$. At distances $r \ll L$, the gravitational field of the mirror masses is negligible compared to the field of the mass at $y = 0$. Thus, one obtains the force law in $4+d$ dimensions:

$$F(r) = \frac{m_1 m_2}{(M_{4+d})^{d+2}} \frac{1}{r^{d+2}}. \tag{1.23}$$

At long distances ($r \gg L$), the effect of the mirror masses is that the gravitational field decreases slower than $1/r^{d+2}$. By applying Gauss' law, the force law is now found to be:

$$F(r) = \frac{m_1 m_2}{M_{Pl}^2} \frac{1}{r^2}, \tag{1.24}$$

which is the usual $1/r^2$ law. The relation between M_{Pl} and M_{4+d}, the Planck scales in 4 and in $4+d$ dimensions respectively, is also obtained using Gauss' law. In the general case, where the extra dimensions can be any manifold, they are related as follows:

$$M_{Pl}^2 \sim R^n (M_{4+d})^{2+d}, \tag{1.25}$$

where R is the size of the (compactified) extra dimensions, and the constant of proportionality depends on the topology of the extra dimensions (a torus is the easiest example). Thus, the hierarchy between M_{4+d} and M_{Pl} is explained by the extra dimensions, although this introduces a new hierarchy between R and M_{4+d} whose origin is not explained.

Assuming that $M_{4+d} = M_{EW} \approx 1$ TeV (so there is only one fundamental scale in Nature), the size R depends on the number of extra dimensions as follows [11]:

$$R \approx \frac{1}{\pi} 10^{-17+\frac{32}{n}} \quad \text{cm}. \tag{1.26}$$

For $d = 1$ one obtains $R \approx 10^{14}$ cm, which would lead to deviations from Newton's gravity law at the scale of the Solar System. Such behavior is clearly excluded experimentally. The case $d = 2$ ($R \approx 0.3$ mm) also seems to be excluded by recent experiments [12]. The cases $d \geq 3$ do not contradict the current observations. These cases cannot be tested by Cavendish-type experiments (which are based on a torsion balance) because they can only probe gravity down to a distance of about 0.1 mm, whereas $d \geq 3$ implies that gravity remains unchanged at distances larger than a few nanometer. Thus, a collider experiment like the LHC seems to be the only option to probe these dimensions.

The fields that describe the fluctuations of the gravitational field around the Minkowski metric η_{MN} are denoted as $h_{MN}(x, y)$. If the extra dimensions are compactified to the torus T_d, then the fields $h_{MN}(x, y)$ are periodic in y and can be expanded as follows:

$$h_{MN}(x, y) = \sum_n h^{(n)}_{MN}(x) Y_n(y), \tag{1.27}$$

$$Y_{\{n_1, n_2, \ldots n_d\}} = \frac{1}{\sqrt{V_d}} exp\left(\frac{i n_m y^m}{R}\right), \tag{1.28}$$

where $V_d = (2\pi R)^d$ is the volume of the torus, and the multi-index $n = \{n_1, n_2, \ldots, n_d\}$ with n_m being integer numbers, $-\infty \leq n_m \leq \infty$. The coefficients $h^{(n)}_{MN}(x)$ are the Kaluza-Klein modes. From the 4-dimensional point of view, a massless graviton in $4+d$ dimensions looks like a tower of Kaluza-Klein excitations. Their masses are given by q_T, the component of the momentum transverse to the 3-brane. To see this, consider the dispersion relations in $4 + d$ and 4 dimensions respectively (with $d = 1$):

$$E^2 = \sum_{i=0}^{3} P_i^2 + P_4^2, \tag{1.29}$$

$$E^2 = \sum_{i=0}^{3} P_i^2 + M^2. \tag{1.30}$$

Thus, we identify $M = P_4$, where M is the mass in our 4-dimensional manifold.

The interactions of the graviton with the Standard Model fields are given by

$$L = -\frac{1}{(\overline{M})_{4+d})^{d/2+1}} h^{MN}(x, y) T_{MN}(x, y), \tag{1.31}$$

where $T_{MN}(x,y)$ is the energy-stress tensor that describes the Standard Model fields. The Standard Model fields are confined to the 4-dimensional brane by setting $T_{MN}(x,y) = \eta^{\mu}_{M}\eta^{\nu}_{N}T_{\mu\nu}(x)\delta(y)$. The interaction Lagrangian (1.31) can then be integrated over y, which gives a 4-dimensional Lagrangian that describes the interactions between the Kaluza-Klein (KK) gravitons and the Standard Model fields. The corresponding Feynman rules can be found in Ref. [13]. The KK fields couple to the Standard Model fields in a universal way, with a coupling that is suppressed by a factor M_{Pl}. Since the mass splitting between the KK modes is small ($\Delta m \sim \frac{1}{R}$), a large number of modes may be available to a collider like the LHC. We will discuss the experimental consequences of this in section 1.2.3.

1.2.2 Warped extra dimensions (RS model)

An alternative scenario with extra dimensions was proposed by Randall and Sundrum [14]. Their model describes Einstein gravity in a five-dimensional space-time, with the fifth dimension being compactified to the orbifold S_1/Z_2. Two 3-branes are placed at the points $y = 0$ and $y = \pi R$ on the orbifold, where R is the radius of the circle S_1. The metric that describes this geometry is:

$$ds^2 = e^{-2\sigma(y)}\eta_{\mu\nu}dx^{\mu}dx^{\nu} + dy^2. \tag{1.32}$$

This metric is a solution to the five-dimensional Einstein equations if $\sigma(y) = ky$ (with k a constant), and if there is a negative cosmological constant $\Lambda = -24M_5^3k^2$. M_5 is the five-dimensional 'Planck mass'.

The reduced fundamental Planck scale $\overline{M}_5$ and the reduced four-dimensional Planck scale $\overline{M}_{Pl}$ are related as follows:

$$\overline{M}_{Pl}^2 = \frac{\overline{M}_5^3}{k}(1 - e^{-2kR\pi}). \tag{1.33}$$

Note that the exponential $e^{-2kR\pi}$ can almost be ignored in this equation if kR is not too small. However, we will see in a moment that the exponential is crucial for creating TeV scales (i.e. of the order of the electroweak scale) from the observed Planck scale.

The fields $h_{\mu\nu}(x,y)$ that describe the fluctuations around the Minkowski metric $\eta_{\mu\nu}$ are expanded as follows:

$$h_{\mu\nu}(x,y) = \sum_{n=0}^{\infty} h_{\mu\nu}^{(n)}(x)\frac{\chi_n(y)}{R}. \tag{1.34}$$

The solutions for χ_n are given by [7]:

$$\chi_n(y) = N_n\left[C_1Y_2\left(\frac{m_n}{k}e^{k|y|}\right) + C_2J_2\left(\frac{m_n}{k}e^{k|y|}\right)\right] \quad (n \neq 0), \tag{1.35}$$

where J_2 and Y_2 are Bessel functions of order 2, N_n is the wavefunction normalization, and C_1 and C_2 are constant coefficients. The interactions with the Standard Model fields are given by the Lagrangian:

$$L = \frac{-1}{\overline{M}_{Pl}}T^{\mu\nu}(x)h_{\mu\nu}^{(0)}(x) - \frac{1}{\Lambda_{\pi}}T^{\mu\nu}(x)\sum_{n=1}^{\infty}h_{\mu\nu}^{(n)}(x), \tag{1.36}$$

where $\Lambda_\pi \equiv \overline{M}_{Pl} e^{-kR\pi}$.

The fields $h^{(n)}_{\mu\nu}(x)$ with $n \geq 1$ describe massive KK modes. Their masses are given by $m_n = \beta_n k e^{-\pi kR}$, where β_n are the roots of the Bessel function of order 1 (β_n=3.8317, 7.0156, 10.1735 for n=1,2,3). The KK modes are well separated in mass, which makes them quite different from ADD gravitons. Note that the massive modes are only suppressed by a factor Λ_π, which is of the order of 1 TeV if $kR \approx 12$. This makes it possible to produce these modes in a particle accelerator. The existence of massive resonances, with a mass spacing given by the Bessel function, is a prediction that can be verified experimentally.

1.2.3 Experimental searches

So far, no experimental evidence has been found that suggests the existence of extra dimensions. Lower and upper bounds can be obtained using data from astrophysics, particle accelerators, and experiments that directly probe Newton's $1/r^2$ law. We will only discuss the particle physics probes in this section. More complete overviews may be found in Refs. [15] and [16].

Exploring large extra dimensions (ADD model)

For the ADD model, the main collider signal is the production of real KK modes, which escape from the world brane into the bulk. The KK graviton then shows up as missing energy in the detector. The corresponding cross section scales as follows:

$$\sigma_{KK} \propto \frac{1}{M_{Pl}^2}(\sqrt{s}R)^d \sim \frac{1}{(M_{4+d})^2}\left(\frac{\sqrt{s}}{M_{4+d}}\right)^d. \tag{1.37}$$

The cross section per KK mode is suppressed by a factor $\frac{1}{M_{Pl}^2}$, but the number of available modes is of the order of $(\sqrt{s}R)^d$, which cancels the factor $\frac{1}{M_{Pl}^2}$. In Ref. [17], the final states of jets plus missing energy and photons plus missing energy were studied, using the fast (parametrized) simulation of ATLAS. The Standard Model background processes were also simulated. The resulting missing energy distribution is shown in Fig. 1.2. Depending on the number of extra dimensions, the fundamental Planck scale M_{4+d} could be probed from 4 up to 7.5 TeV. The number of extra dimensions could then be determined by measuring the cross section at two different center-of-mass energies, e.g. $\sqrt{s}$ = 10 TeV and $\sqrt{s}$ = 14 TeV. The ratio of the two cross sections is almost independent of M_{4+d} and varies with d.

Apart from real graviton emission, the ADD model also predicts processes with virtual graviton exchange. In Ref. [19], the graviton contribution to di-photon and di-lepton production ($G \to \gamma\gamma$ and $G \to \ell^+\ell^-$) was studied, again using the parametrized ATLAS simulation. It was found that ATLAS could probe gravity with extra dimensions up to a scale $M_{4+d} \sim 6.3 - 7.9$ TeV in the di-photon channel, and up to $M_{4+d} \sim 6.6 - 7.9$ TeV in the di-lepton channel.

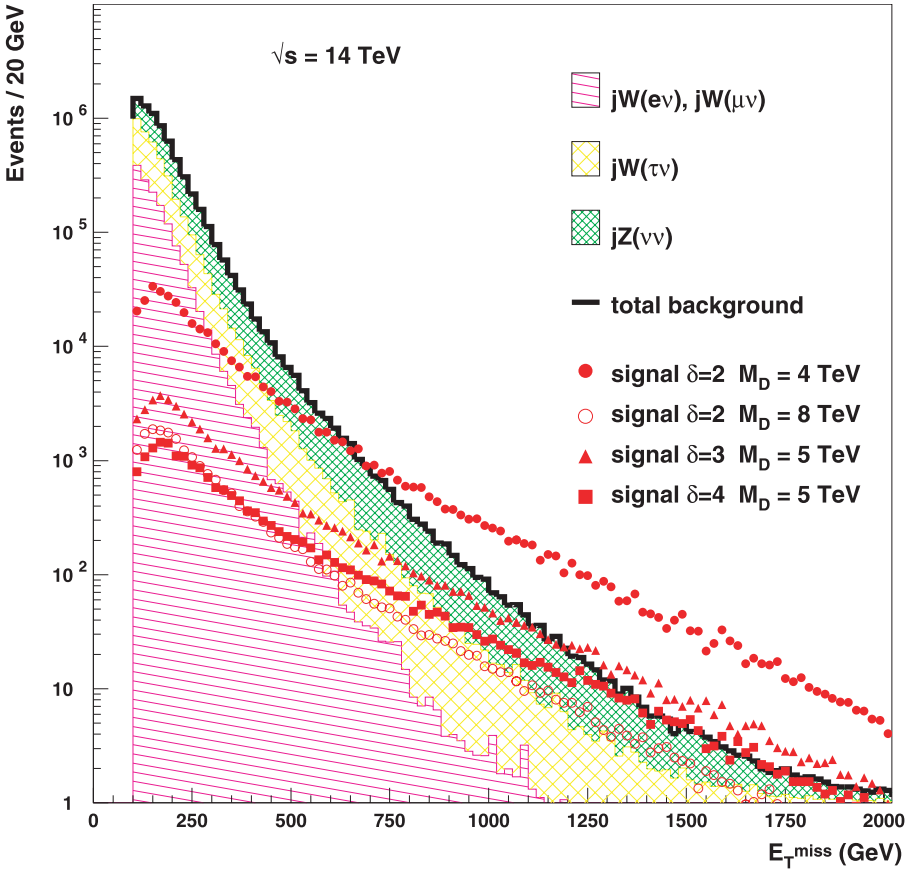

Figure 1.2: *Distribution of the missing transverse energy in a simulation of ATLAS, using the ADD model and 100 fb^{-1} of data. The distributions of the Standard Model background are shown as well as the signal. From [18].*

Exploring warped extra dimensions (RS model)

As in the ADD model, the production of RS gravitons at the LHC could affect e.g. the di-lepton rates. Fig. 1.3 shows the Drell-Yan cross sections at the LHC when the mass of the lightest graviton is 1.5 TeV. Note that both the widths of the resonances and the total cross section depend strongly on $k/\overline{M}_{Pl}$, they are proportional to $(k/\overline{M}_{Pl})^2$. Also, interference between the different resonances starts to play a role when $k/\overline{M}_{Pl}$ increases. For large values of $k/\overline{M}_{Pl}$ it would be impossible to reconstruct the individual resonances, instead one would observe a shoulder over the Standard Model Drell-Yan cross section.

Searches for the first graviton KK resonance have already been performed at the Tevatron, using Drell-Yan and di-jet data from Run I. The graviton contributes to these processes through the $q\bar{q}, gg \rightarrow G \rightarrow \ell^+\ell^-$ and $q\bar{q}, gg \rightarrow G \rightarrow q\bar{q}, gg$ channels, respectively. A graviton signal will show up as an excess of events in the Drell-Yan

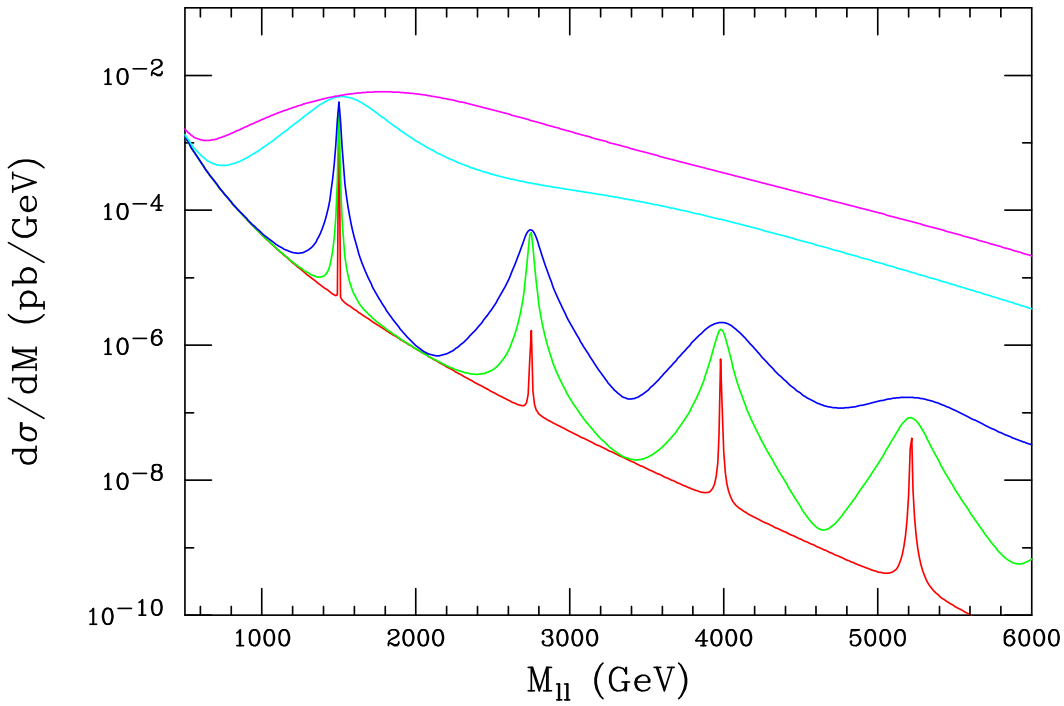

Figure 1.3: *Drell-Yan production of the KK graviton at the LHC, with* $m_1 = 1.5$ *TeV. The subsequent tower states are also visible. From top to bottom,* $k/\overline{M}_{Pl} = 1, 0.5, 0.1, 0.05, 0.01$ *respectively. From [15].*

and di-jet processes. Note that gluon-gluon initiated processes now contribute to the Drell-Yan process.

The Tevatron experiments would be able to detect the resonance, provided that two requirements are fulfilled:

- The mass of the resonance is within the kinematic limit of the accelerator;
- The production cross section (and hence $k/\overline{M}_{Pl}$) is sufficiently high.

The negative results of the Tevatron searches make it possible to exclude a region in $(m_1, k/\overline{M}_{Pl})$ space, namely a region with small masses and large $k/\overline{M}_{Pl}$ values. The region $k/\overline{M}_{Pl} > 0.1$ is disfavored theoretically, because the curvature of the bulk becomes too large in this region. Furthermore, it is not unreasonable to expect that $\Lambda_\pi < 10$ TeV, as otherwise a large hierarchy would be generated between the electroweak and the fundamental Planck scales, which we were trying to avoid in the first place. Yet another constraint comes from the oblique parameters T and S, which were measured by performing a global fit to the electroweak data. This measurement excludes those parameters in the RS model where the graviton contribution to T and S becomes too large [15].

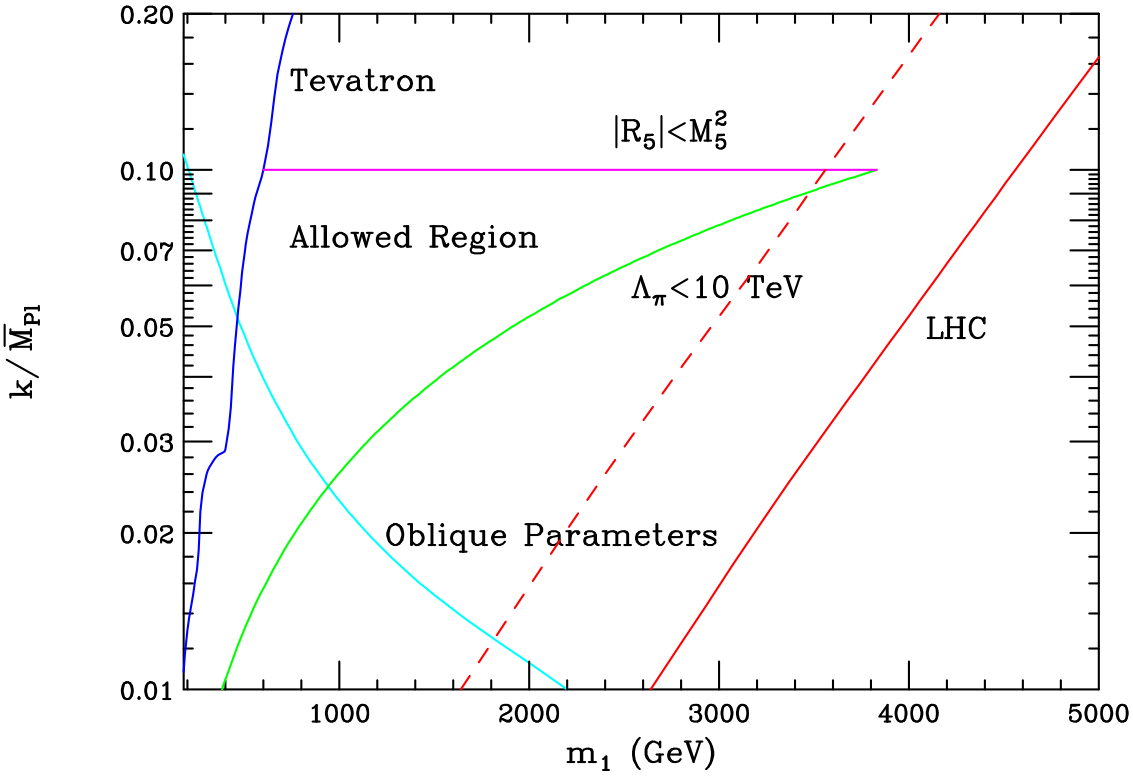

Figure 1.4: *Experimental and theoretical constraints on the Randall-Sundrum model. The diagonal dashed and solid lines represent the LHC sensitivity, using 10 and 100 fb^{-1} of integrated luminosity respectively. From [16].*

The result of all these constraints is a region in parameter space that is open to experimental searches, see Fig. 1.4. The discovery reach of the LHC experiments, after one year of running at design luminosity, is also shown. The LHC experiments will probably not be able to detect the graviton in the di-jet process, because of the large QCD background. Therefore the LHC curve in Fig. 1.4 is only based on the Drell-Yan discovery channel. The figure shows that the LHC is able to cover the entire allowed region in the parameter space, given the theoretical assumptions above. Thus, the LHC will be able to either discover or exclude the RS model.

Exploring black holes

Another spectacular consequence of the extra dimensions could be the production of mini black holes at the LHC. The extra dimensions cause the Schwarzschild radius of the black hole to be much larger than expected from 4-dimensional gravity. The black hole could then be formed if the relative impact parameter of two colliding partons is smaller than the Schwarzschild radius. The black hole then decays, via Hawking

radiation, into Standard Model particles. Fig. 1.5 shows an example of a simulated black hole decay in ATLAS.

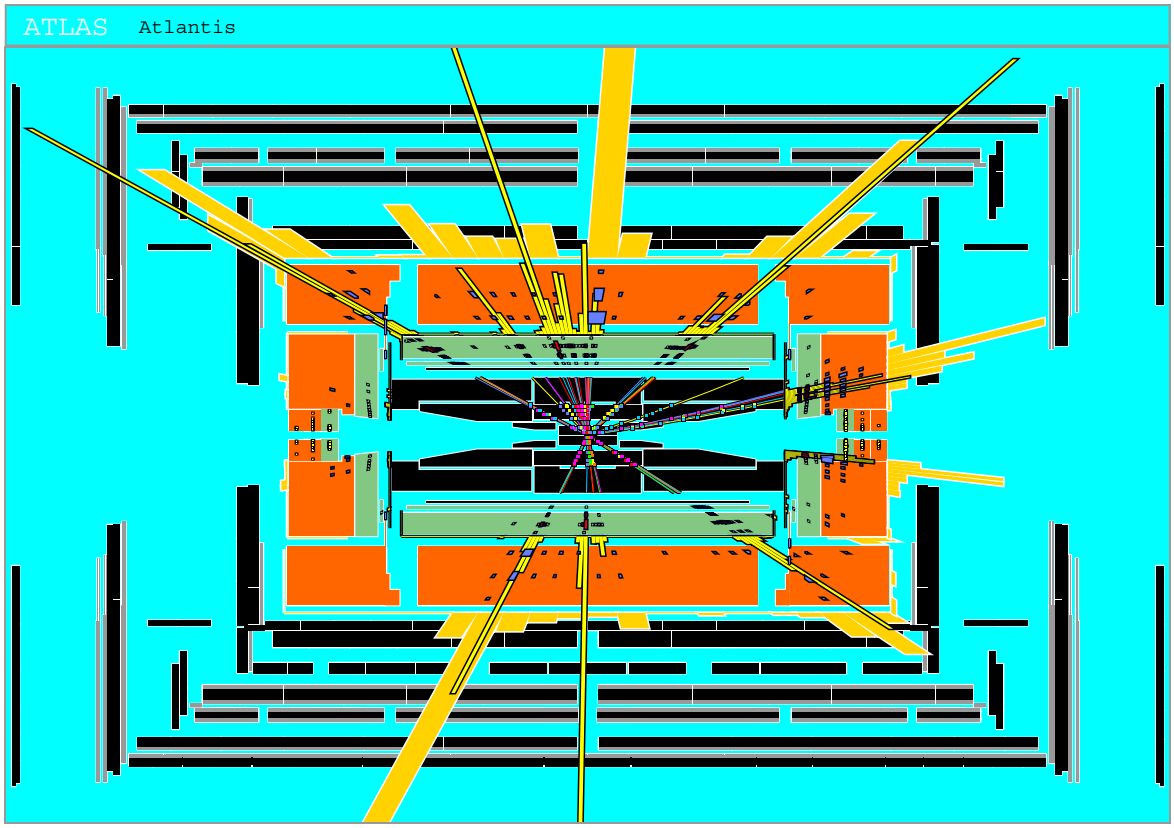

Figure 1.5: *Event display of a simulated black hole event in ATLAS.*

Chapter 2

ATLAS & LHC

2.1 The Large Hadron Collider

The Large Hadron Collider (LHC) [20] will become CERN's main accelerator complex. It is currently under construction in the same tunnel that was used for the LEP accelerator, which was decommissioned in 2000 [21]. The LHC will accelerate two counter-rotating proton beams to an energy of 7 TeV, which will collide head-on at four points along the ring. The resulting interactions have an unprecedented center of mass energy of 14 TeV, which will allow physicists to study new fields of physics. The startup is scheduled for 2007.

The acceleration of the protons starts at a dedicated linear accelerator (linac), which accelerates bunches of 10^{11} protons to an energy of 50 MeV. These bunches are then transferred to the PS Booster (PSB), where the energy is increased to 1.4 GeV. The energy is further increased to 26 GeV by the Proton Synchrotron (PS). The protons are then injected into the Super Proton Synchrotron (SPS) where they are accelerated to 450 GeV. Finally, the SPS injects the protons clockwise and counter-clockwise into the LHC ring, where they are accelerated to their final energy of 7 TeV. More than 1200 dipole magnets are installed along the LHC ring to keep the protons on track in the ring. The dipoles provide a magnetic field of up to 9 Tesla. The main parameters of the LHC accelerator are given in Table 2.1.

Like its center of mass energy, the luminosity of the LHC is also unprecedented for a proton collider. The luminosity is defined as the number of protons that pass by, per unit area, per unit time. The higher the luminosity, the more proton-proton interactions per second will occur. At the LHC design luminosity of 10^{34} $\mathrm{cm}^{-2}\mathrm{s}^{-1}$, on average about 27 interactions will occur per bunch crossing, with a bunch spacing of 25 ns. Thus, the number of proton-proton interactions per second will be around 10^9. Such a high luminosity is needed because many interesting physics processes at the LHC energy have very small cross sections, 1 pb or less (1 pb=10^{-36} cm^2).

Four detectors are under construction at the points where the beams collide (see Fig. 2.1): ALICE, ATLAS, CMS and LHCb. ATLAS [22] and CMS [23] are general purpose detectors, i.e. they are designed to cover a wide range of physics. Their primary task will be to discover the Higgs particle (if it exists), but they will also explore the physics

Parameter	Value	Unit
Circumference	26659	m
Beam energy	7	TeV
Injection energy	0.45	TeV
Dipole field at 450 GeV	0.535	T
Dipole field at 7 TeV	8.33	T
Helium temperature	1.9	K
Coil aperture	56	mm
Distance between apertures	194	mm
Luminosity	10^{34}	$\mathrm{cm}^{-2}\mathrm{s}^{-1}$
Luminosity lifetime	10	h
Bunch spacing	25	ns
Particles per bunch	10^{11}	
Bunches per beam	2808	

Table 2.1: *Main LHC parameters.*

beyond the Standard Model, like supersymmetry, extra dimensions, and even mini black holes. The ATLAS experiment is described in more detail in the next section.

The LHCb experiment [24] is dedicated to the study of CP-violation in the B-system, it is therefore optimized for the detection of B-mesons. LHCb uses a lower luminosity of about 10^{32} $\mathrm{cm}^{-2}\mathrm{s}^{-1}$, by defocusing the proton beams near the interaction point. This is needed because the production and decay vertices of the B-mesons are difficult to reconstruct if there is more than one interaction per bunch crossing.

The ALICE experiment [25] focuses on the study of the quark-gluon plasma, by measuring the particles that are produced in heavy ion collisions. The quark-gluon plasma is a hadronic state where quarks and gluons are not in bound states like protons anymore, but move freely in the plasma. It is expected that the extreme energy densities in the heavy ion collisions is sufficient to create this state of matter for a fraction of a second.

2.2 The ATLAS experiment

The ATLAS[1] detector is currently under construction at 'point 1', the interaction point near the CERN Meyrin site. Like most colliding beam experiments it has approximate cylindrical symmetry. The detector is organized in a central *barrel* where the detection elements form cylindrical layers around the beam pipe, and two *endcaps* where it is organized in wheels. Fig. 2.2 gives an overall picture of the detector.

The cylindrical symmetry makes a cylindrical coordinate system useful. The z-axis points along the cylinder (i.e. along the beam pipe). The polar angle θ is the angle with the z-axis, and the azimuthal angle ϕ is the angle in the x-y plane. The distance to the

[1] ATLAS is an acronym for A Toroidal Lhc ApparatuS.

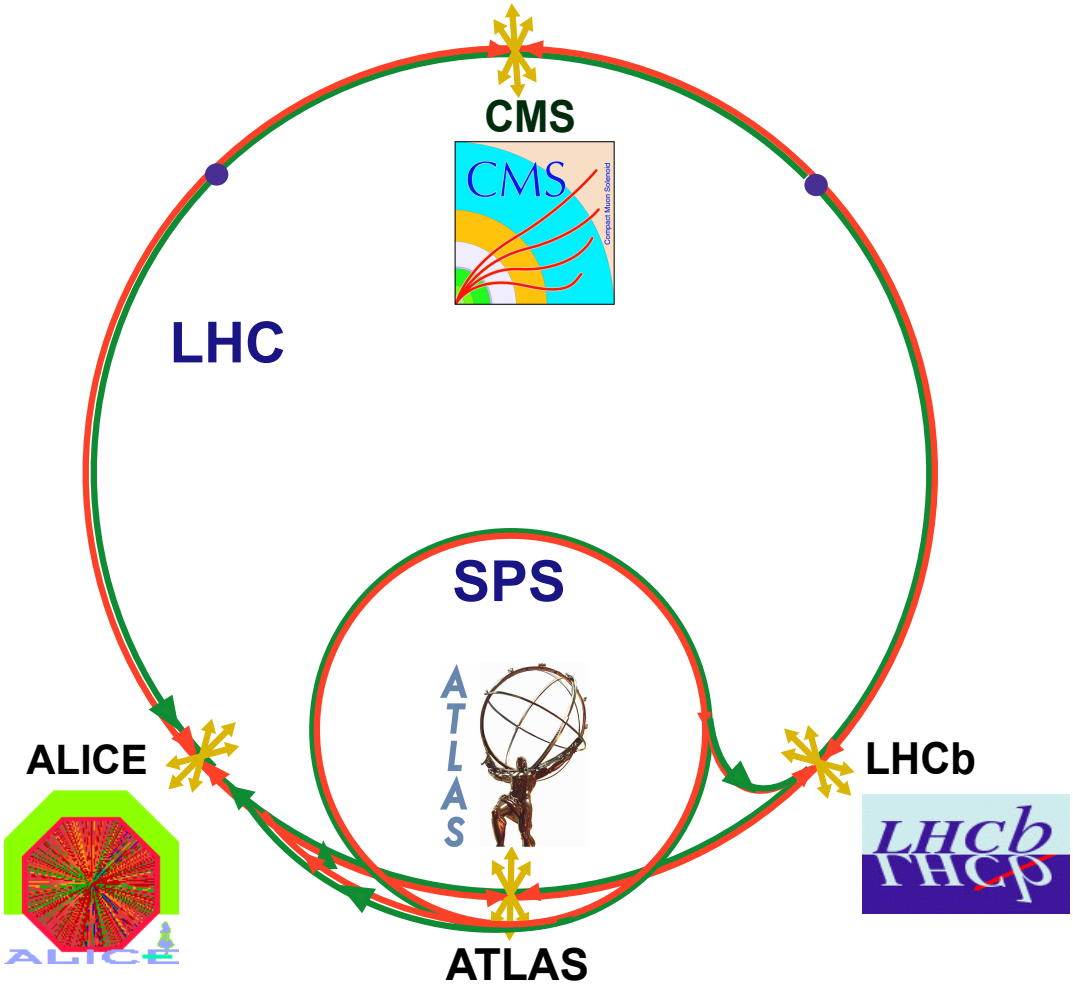

Figure 2.1: *The LHC complex with its four experiments.*

z-axis is R. Instead of the polar angle θ, the pseudorapidity η is often used:

$$\eta = -\log(\tan(\theta/2)). \tag{2.1}$$

The pseudorapidity is a convenient quantity because the particle multiplicity is approximately constant as a function of η. In the massless limit it is equal to the rapidity $y = \frac{1}{2}\log\frac{E+p_z}{E-p_z}$.

ATLAS consists of three subsystems. The inner-most system is the inner detector, which detects the tracks of charged particles. The energies of the particles and jets are measured by the calorimeters, which are built around the inner detector. The only (known) charged particles that can penetrate the calorimeters are muons, which are measured by the outer-most detector, the muon spectrometer. The various subsystems in ATLAS will be described in the next sections.

ATLAS is 45 meters long and 22 meters high, which makes it an order of magnitude larger than previous collider experiments. This is a direct consequence of the 14 TeV

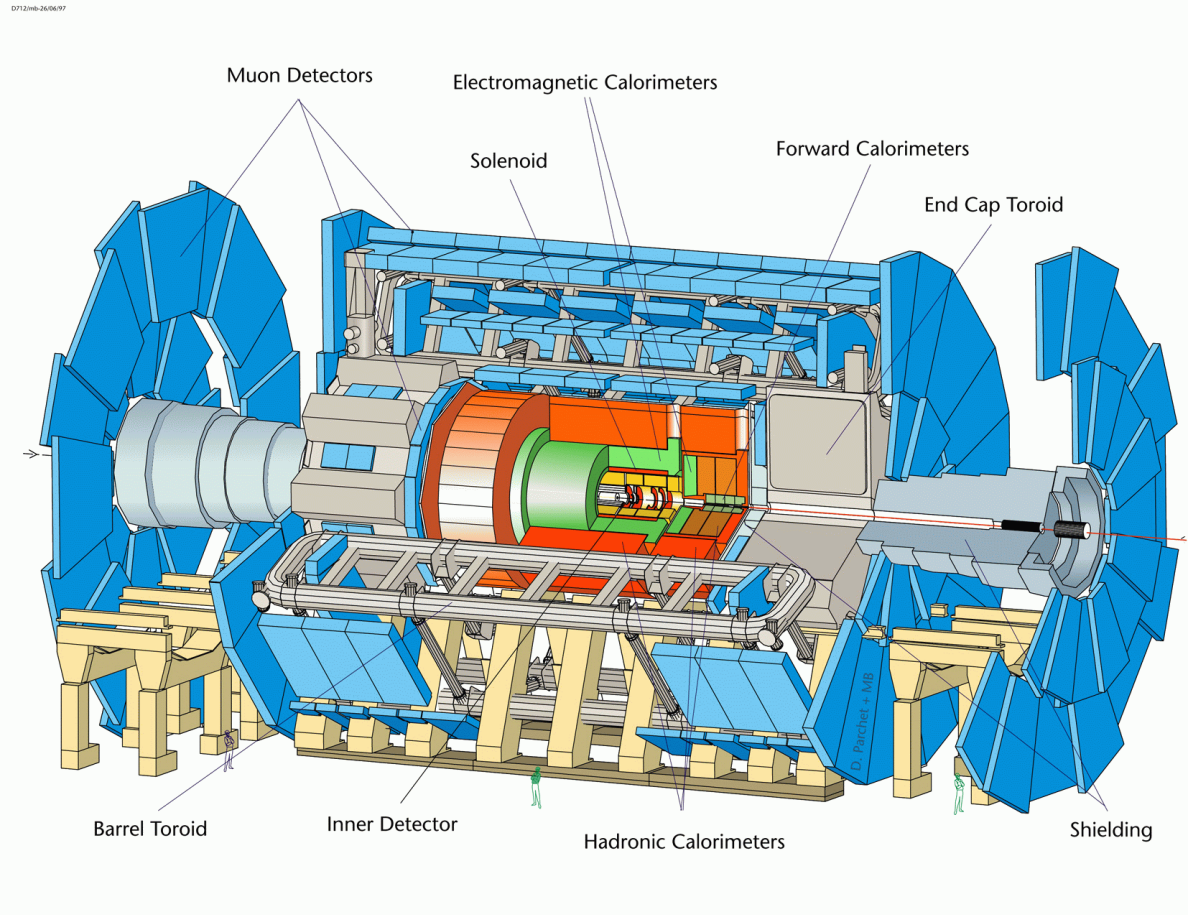

Figure 2.2: *Overview of the ATLAS detector. Some parts have been removed to show the inner part of the detector. The various subsystems have been indicated.*

center of mass energy of the LHC beams. The large volume gives the trackers a long lever arm, which improves the momentum resolution, particularly at high momenta. Thick calorimeters are required to fully contain the showers in the calorimeter, and reduce the amount of punch-through into the muon chambers to a minimum. Fast electronics are required to 'keep up' with the bunch crossing rate, which is also higher than in previous experiments.

A large number of particles is expected to be produced in the proton collisions. Many of these particles are grouped into sprays of particles, called *jets*. Since jets often have a large boost, the particles in a jet are often nearly collinear. A detector with fine granularity is required to be able to distinguish between the particles within a jet. Since the particle flux decreases as $1/R^2$, the requirement of granularity becomes less important for the detector elements that are further away from the interaction point.

The basic design criteria of the ATLAS detector are [26]:

- Very good electromagnetic calorimetry for electron and photon identification and

measurement, complemented by full-coverage hadronic calorimetry for accurate jet and missing transverse-energy measurements;

- High-precision muon momentum measurements, with the capability to guarantee accurate measurements at the highest luminosity using the external muon spectrometer alone;
- Efficient tracking at high-luminosity for momentum measurement of high p_T leptons, electron and photon identification, τ-lepton and heavy-flavor identification, and full event-reconstruction capability at lower luminosity;
- Large acceptance in pseudorapidity with almost full azimuthal angle coverage everywhere;
- Triggering and measurements of particles at low-p_T thresholds, providing high efficiencies for most physics processes at the LHC.

2.2.1 The inner detector

The inner detector [27] is the detector closest to the interaction point in ATLAS. Its task is to reconstruct the trajectories (tracks) of charged particles that are produced in the proton collisions. The charge, momentum, direction of the track and its distance of closest approach to the beamline (impact parameter) are measured. It also reconstructs the primary and possible secondary vertices, the latter being needed to identify e.g. B-mesons and converted photons. The inner detector is installed in a solenoid magnet, which provides a magnetic field of 2 T. The magnetic field makes it possible to measure the momentum of the particles, by measuring the curvature of the tracks in the inner detector.

For the ATLAS inner detector a layout was chosen with three different subdetectors:

- A pixel detector with very high granularity, providing three 3-dimensional points per track;
- A silicon strip detector (SCT, 'SemiConducting Tracker') surrounding the pixel detector, that provides at least four 3-dimensional spacepoints;
- A straw tracker (TRT, 'Transition Radiation Tracker') that surrounds the other two subsystems, providing a large number (about 36) of measurements in the bending plane.

The pixel and SCT detectors are based on silicon as a detection medium. They provide a very good granularity and very precise position measurements. On the other hand they are quite expensive, and require a lot of material in the form of support structures and cooling pipes. This material has a negative effect on the performance of the tracker (see page 29). Therefore the outermost layer, the TRT, is based on straws filled with a gas mixture, which makes it more 'transparent' to incoming particles.

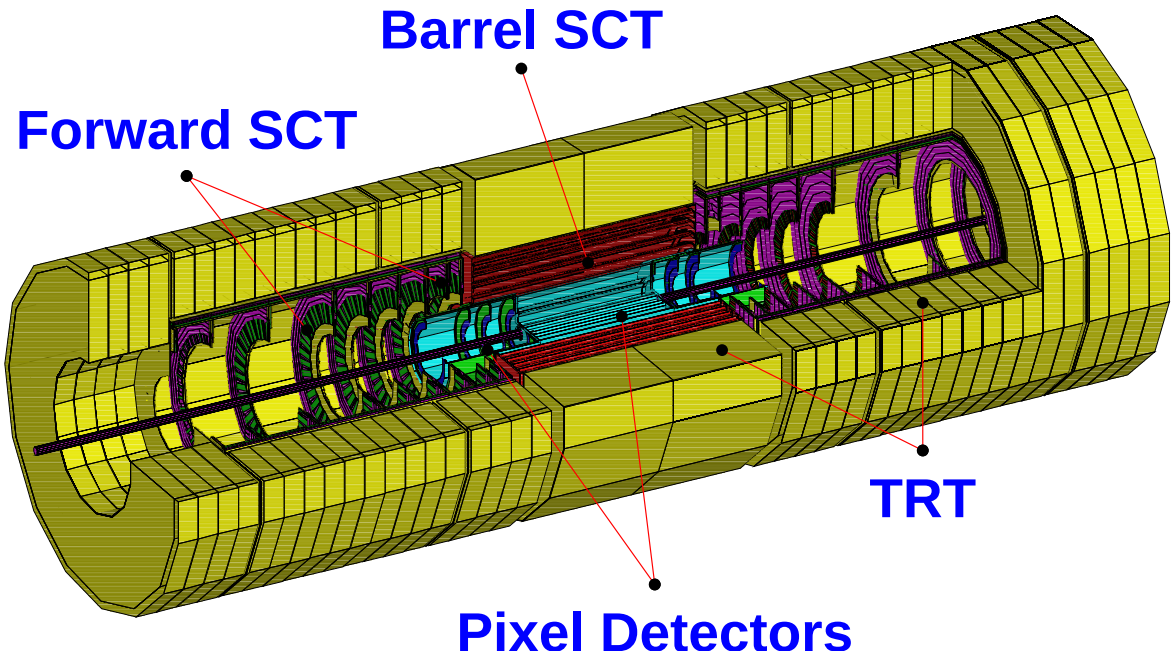

Figure 2.3: *The ATLAS inner detector.*

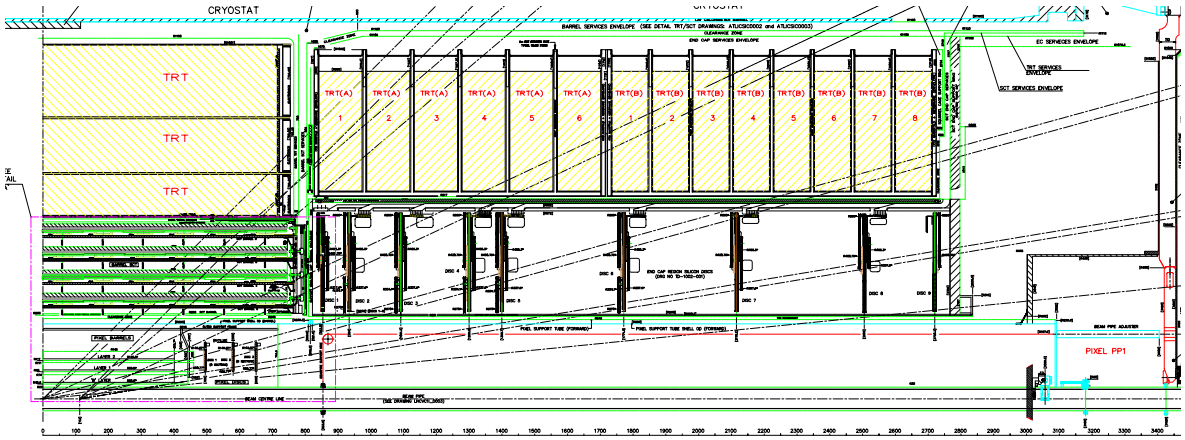

Figure 2.4: *r-z view of the ATLAS inner detector.*

The acceptance of the inner detector is made as large as possible, to prevent particles from escaping undetected. The acceptance is usually given in terms of the pseudorapidity η. The ATLAS inner detector covers the region $|\eta| < 2.5$[2].

The resolution of the inner detector can be parametrized as a function of the transverse momentum p_T and the polar angle θ. This was done in the ATLAS Physics TDR (Ref. [26]), using the layout as it was foreseen in 1999. The momentum resolution can

[2]The construction of the outermost TRT wheels ('C-wheels') is deferred. The TRT only covers the region $|\eta| < 2.0$ if the C-wheels are omitted.

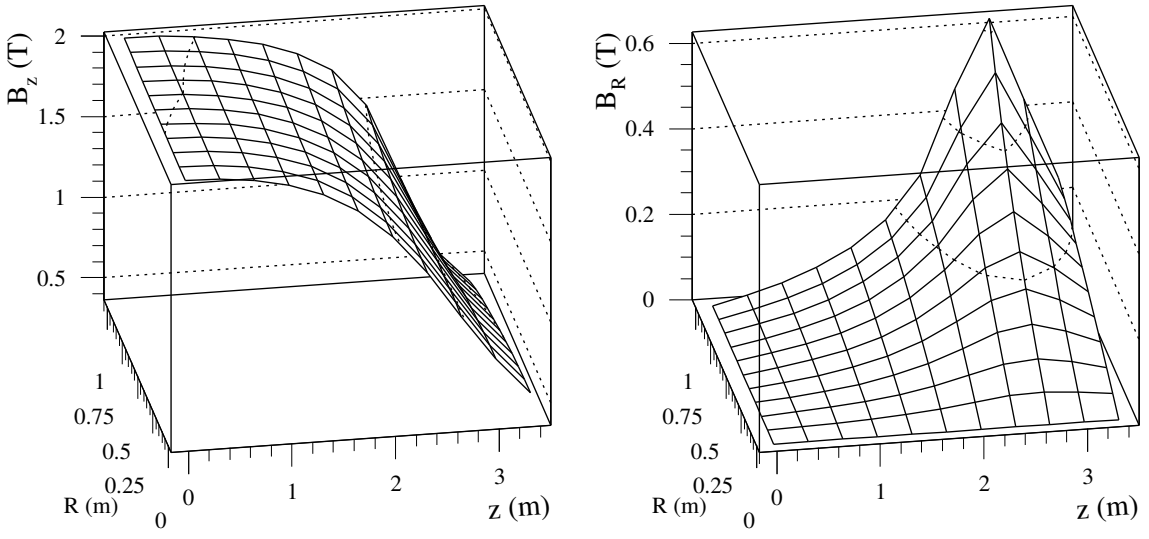

Figure 2.5: *z- and R-components of the magnetic field in the solenoid, as a function of z and R.*

be approximated as follows:

$$\frac{\sigma_{p_T}}{p_T} = 0.036\% \cdot p_T \oplus \frac{1.30\%}{\sqrt{\sin\theta}} \qquad (p_T \text{ in GeV}), \tag{2.2}$$

while the resolution on the impact parameter is approximately:

$$\sigma_{d_0} = 11\ \mu\text{m} \oplus \frac{73\ \mu\text{m}}{p_T\sqrt{\sin\theta}} \qquad (p_T \text{ in GeV}). \tag{2.3}$$

In Eqs. (2.2) and (2.3), the first term on the right hand side represents the intrinsic resolution of the tracker, which depends on the resolution of the position measurements and the strength of the magnetic field. The second term represents the resolution degradation due to multiple scattering. The factor $1/\sqrt{\sin\theta}$ arises because particles have to traverse more material as the angle with the beam direction gets smaller, due to the angle of incidence with the material layers. The material in the endcaps is dominated by the support cylinders and services, therefore the same relation holds there as well.

The solenoid magnet

The inner detector is housed in a superconducting NbTi/Cu solenoid magnet that generates a field of around 2 Tesla, with a peak value of 2.6 Tesla near the superconducting material. The magnet has a diameter of 2.5 meters and is 5.3 meters long. It is shorter than the inner detector itself, which makes the field quite inhomogeneous in the forward region. Figure 2.5 shows the z- and R-components of the magnetic field (B_z and B_R) as a function of z and R.

One sees that the z-component of the field drops from 2 T to 1 T at the end of the tracker, while the R-component reaches up to 0.6 T in the forward region. The inhomogeneity of the magnetic field in the endcaps enforces the use of a field map in simulation and reconstruction.

The resolution on the momentum is directly related to the bending power of the magnet, which is given by the field integral $\int Bdl$. In the ATLAS solenoid magnet, the integral drops from about 2 Tm at $|\eta| = 0$ to about 0.5 Tm at $|\eta| = 2.5$, for two reasons:

- The field strength in the endcaps is lower than in the barrel;
- Tracks in the very forward region ($|\eta| > 1.85$) exit the tracker longitudinally (along z) before reaching the solenoid.

The second effect reduces the length of the measured trajectory in the $R - \phi$ plane ('lever arm'), increasing the relative extrapolation distance to the beamline. Thus, the resolution on the impact parameter is also worse in the forward region. The resolutions in the forward region are further worsened because there is more material than in the barrel (see page 29).

The pixel detector

The pixel detector is positioned closest to the beamline in ATLAS. The detector is made up of three cylindrical layers in the barrel, and three disks in each of the forward regions. The distances of the three barrel layers to the beamline are 5.05, 8.85 and 12.25 cm respectively. The layers and disks are outfitted with silicon sensors that are segmented into small rectangles, the *pixels*. The area of the silicon sensor is approximately $2{\times}6$ cm^2, the thickness is 250 μm. A charged particle traversing the silicon sensor will produce free electron/hole pairs in the silicon[3]. By applying a bias voltage, these free charges drift to the readout side of the sensor. A discriminator in the readout electronics determines if the deposited charge is above threshold, the nominal threshold is 0.5 fC (i.e. around 3000 e$^-$). If the signal is above threshold, the pixel address and the time over threshold (ToT) are written out. The ToT makes it possible to reconstruct the amount of charge that was deposited.

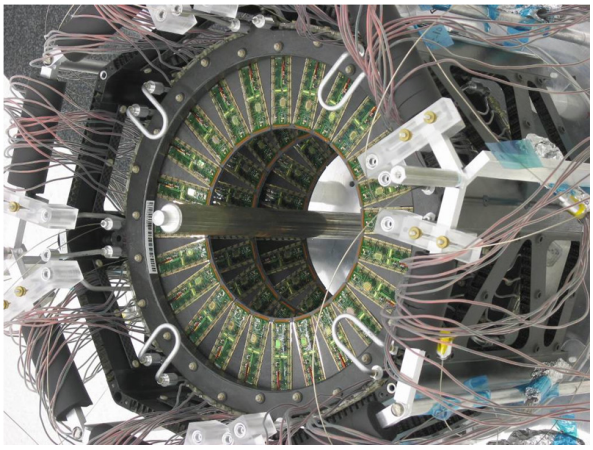

Figure 2.6: *Photograph of a pixel endcap. The pixel modules can be seen mounted on the disks.*

[3]The silicon junction is described in more detail in section 3.2.1.

The size of most of the pixels is 50×400 μm^2, about 10% has size 50×600 μm^2 ('long' pixels). Each pixel is bump bonded to a readout chip, of which there are 16 per sensor. The readout chips do not cover the entire silicon surface, therefore the pixels that lie between two chips have to share a readout channel with another pixel. These pixels are called *ganged pixels*. If a particle hits such a pixel then it is a task for the reconstruction to decide which pixel was actually hit.

There are 47,268 pixels per module, and 1744 modules in total. The total number of pixels is thus more than 80 million.

Testbeam results show that the pixel modules have a resolution of approximately 12 μm in the $R - \phi$ coordinate, and 110 μm in the z coordinate. The number of defective channels is less than 10^{-3}, the non-defective channels have a tracking efficiency of practically 100%. The efficiency drops to 98% for highly irradiated modules, which is still above the end-of-life requirement of 95%.

Due to its close proximity to the interaction point, the pixel detector dominates the resolution on the impact parameter. Its very high granularity gives it an excellent two-track resolution, thus making it very important for the pattern recognition.

The SCT detector

The SCT surrounds the pixel detector. It uses silicon sensors (like the pixel detector) which are segmented in *strips*, thus giving a one-dimensional position measurement. There are 768 strips per sensor, with an average width (strip pitch) of around 80 μm. Unlike the pixel modules, the readout of the SCT modules is binary, i.e. one only knows if a strip was hit or not. This limits the spatial resolution per sensor to about 23 μm. An SCT module has two sensors that are glued back-to-back with a small relative angle (around 40 mrad), which makes it possible to measure the second coordinate, by finding the intersection of two strips in the sensor (forming a *spacepoint*). The resolution on this second coordinate is about 800 μm.

In the barrel the SCT modules are arranged in four cylindrical layers. The sensors in the barrel modules have a rectangular shape, their size is 6×12 cm^2. The strips are oriented along the long side of the rectangle. The circuit board with the readout chips (called 'hybrid') is installed near the middle of the sensor. In the endcaps the sensors are wedge shaped. The strips in the endcap modules have a fan geometry (i.e. they are not parallel), to match the wedge shape of the sensor. The endcap modules are mounted such that their strips point roughly towards the beamline. The length of the strips in the endcap modules is either 6 or 12 cm, depending on the module type. The modules are mounted on 18 disks in total (nine per endcap). In both the barrel and the endcap, the modules are mounted such that each track will on average encounter eight sensors (four modules). There are 2112 modules in the barrel and 988 in each of the two endcaps. The total number of channels (i.e. strips) is more than 6 million. More information about the design of the SCT can be found in Refs. [28] and [29].

The expected threshold setting during data taking is 1 fC. The threshold is calibrated for each channel by injecting charge using a calibration capacitor. By measuring the number of hits, the physical value (in fC) of the threshold and the noise level can be

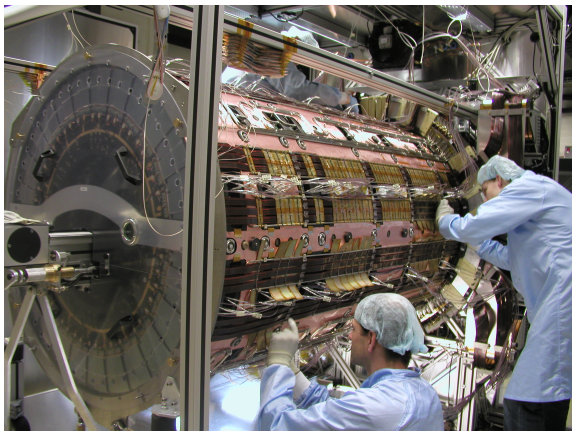

Figure 2.7: *Photograph of SCT endcap 'A', which was assembled at NIKHEF.*

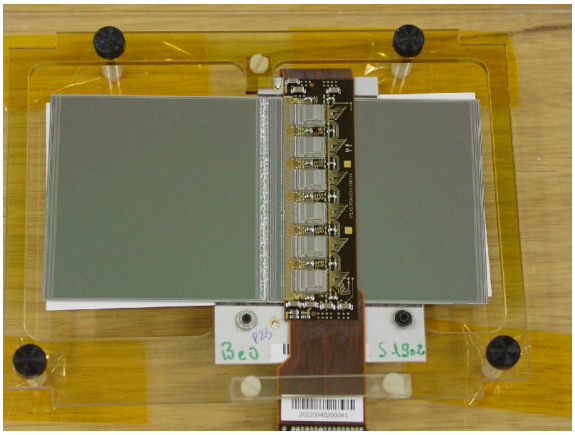

Figure 2.8: *Photograph of an SCT barrel module.*

deduced. The noise level is required to be less than $5 \cdot 10^{-4}$, for a tracking efficiency of at least 99%. Beam tests have shown that these requirements will be met, also after irradiation [29].

The SCT contributes to the resolution of the impact parameter, the momentum, and the z-position of the vertex. Its high granularity also makes it important for the pattern recognition.

The TRT detector

The TRT is the outermost subdetector in the inner tracker. It consists of straws that are arranged axially along z in the barrel, and radially in the endcaps. The straws have a diameter of 4 mm, with a gold-plated tungsten wire in the middle. The straws are filled with a 70:27:3 Xe:CO_2:O_2 gas mixture, that is ionized when a particle traverses it. The ionization clusters are collected by applying a large potential difference between the wall of the straw and the wire. By measuring the time it takes the clusters to reach the wire, the distance of the track to the wire can be determined. The resolution on this measured drift radius is about 170 micron. In addition, the xenon gas in the straws is sensitive to transition radiation photons that are produced in the radiator material (polyethylene-polypropylene) that fills up the space between the straws. The number of transition radiation photons depends on the relativistic factor $\gamma = E/m$ of the particle that traverses the material. Therefore electrons produce many more photons than other particles, this difference is used to identify a particle as an electron. For energies larger than 1 GeV, an electron identification efficiency of 90% with a pion rejection factor of 100 can be achieved.

Due to the large size of a straw compared to a pixel or microstrip, the occupancy in the TRT is much higher than in the pixels and SCT. Some straws are expected to have an occupancy of 50% when LHC is running at its design luminosity. To reduce the occupancies, the wires in the barrel straws are electrically separated in the middle by

a glass wire-joint, which results in two independent halves that are read out on either side of the straw. The wires in the first nine layers have two wire-joints, resulting in two active lengths of 36 cm on either side and a dead region in the middle.

The total number of straws in the barrel is 52,544, arranged in 73 cylindrical layers. A particle hits a straw in every other layer on average, resulting in about 36 crossed straws per track. The endcap consists of wheels where the straws point towards the beamline. There are 18 wheels in each endcap, with 319,488 straws in total. The four outermost wheels in each endcap, called C-wheels, will not be installed initially. It is uncertain when they will be installed.

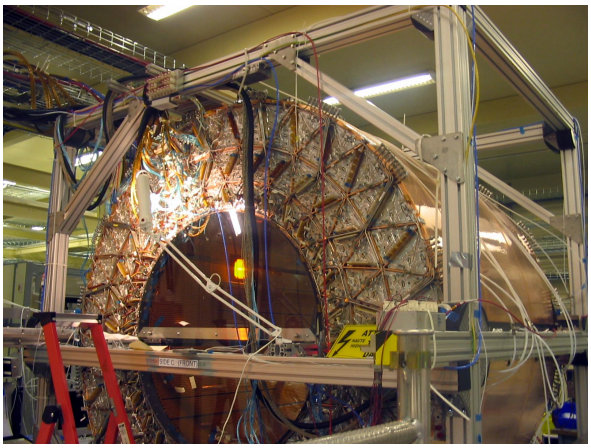

Figure 2.9: *Photograph of the TRT barrel.*

From the track reconstruction point of view, the TRT plays a significant role in the momentum resolution because of its long lever arm. The momentum resolution for a 500 GeV muon improves by roughly a factor two when the TRT is included. The identification of electrons allows an electron track model to be applied in the track fit. The high occupancy makes pattern recognition difficult, but not impossible thanks to the large number of straw hits per track.

Material budget

Particles that traverse the inner detector will interact with the material (sensors, cables, support structures etc.). The most important effects are:

- Charged particles undergo multiple Coulomb scattering, causing them to deviate from their ideal trajectory;
- Hadronic interactions between hadrons and the detector material can cause the hadron to produce a stream of secondary particles;
- Electrons suffer from highly fluctuating energy losses due to Bremsstrahlung;
- Photons can convert into an electron-positron pair ($\gamma \rightarrow e^+e^-$).

The reconstruction can correct for these effects up to a certain extent, but the interactions always reduce the performance of the reconstruction. Therefore the amount of material should be kept at an absolute minimum. Light-weight, low-Z materials like carbon fiber are used for the support structures. Fig. 2.10 shows the amount of material that a particle traverses as a function of pseudorapidity. The material is expressed

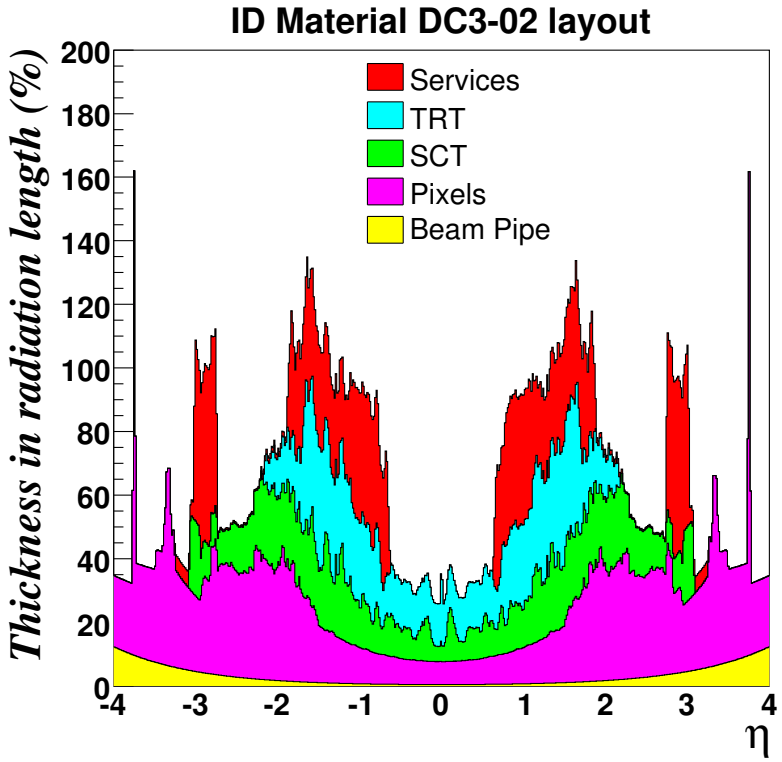

Figure 2.10: *Thickness of the inner detector in terms of radiation length, as a function of pseudorapidity η. The layout 'DC3-02' is the one that was used for the performance studies in chapter 4.*

in terms of radiation lengths (X_0). The radiation length is the length over which the energy of an electron is, on average, reduced by a factor $e(= 2.71\ldots)$.

2.2.2 The calorimeters

The calorimetry system in the ATLAS detector identifies and measures the energy of particles (both charged and neutral) and jets. It also detects missing transverse energy by summing all the measured energy deposits: $E_T^{miss} = \sqrt{(\sum E_T \cos\phi)^2 + (\sum E_T \sin\phi)^2}$. Missing energy can be a sign of interesting new physics, such as the production of gravitons (see chapter 1).

The calorimeters contain dense materials (absorbers), which cause an incoming particle to initiate a shower. Particles that are created in this shower are detected in the *active* material, which is interleaved with the absorbers. The total signal in the active material is a measure of the energy of the incoming particle. ATLAS uses two types of active material: liquid argon (LAr) and scintillating plastic. Particles that traverse the liquid argon create charge by ionization, which is collected on readout electrodes. The scintillating plastic is doped with fluorescent dye molecules, which emit light when the atoms in the plastic are excited by a passing particle. This light is detected and

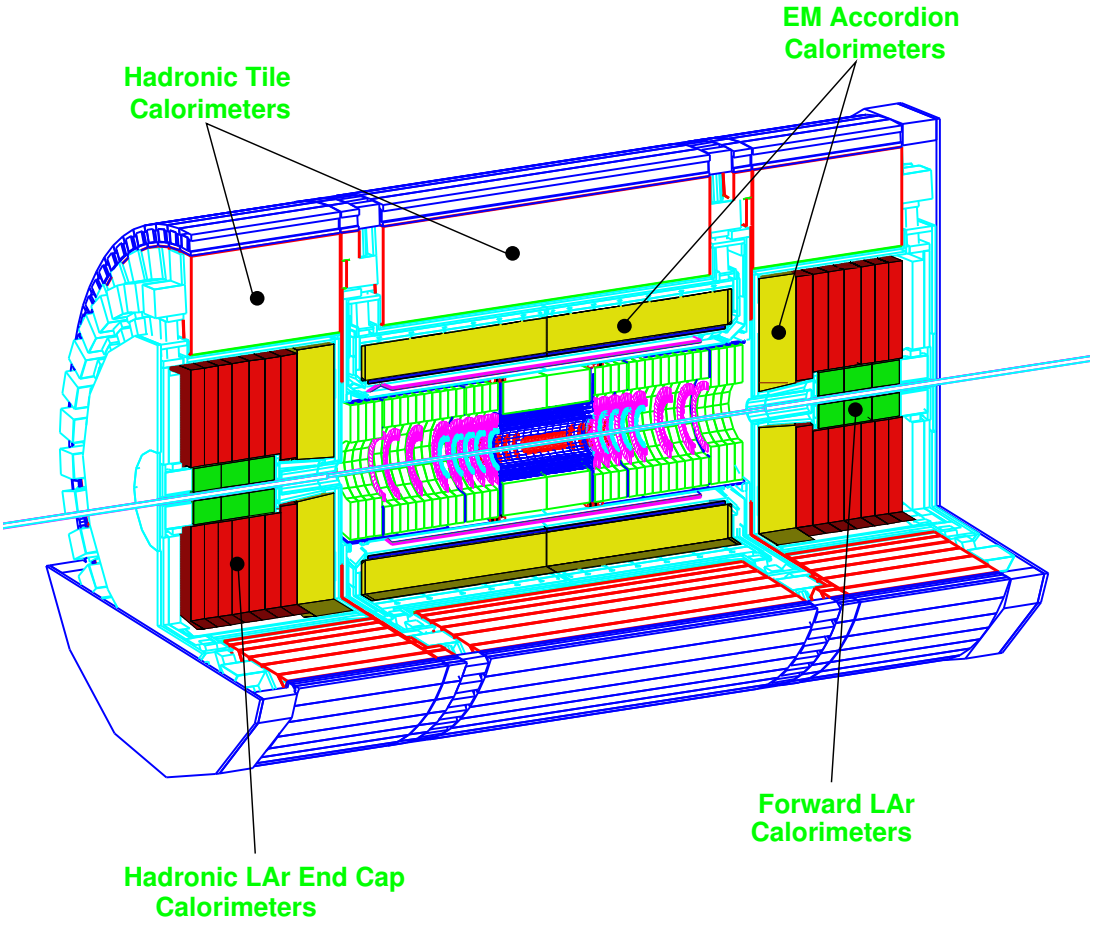

Figure 2.11: *An overview of the calorimeter systems in ATLAS.*

amplified by photomultiplier tubes. For the absorbers several different types of material are used, depending on factors like space constraints and ease of manufacturing: lead, iron, copper and tungsten.

Like many high energy experiments, ATLAS has separate electromagnetic and hadronic calorimeters up to $|\eta| = 3.2$. A special combined electromagnetic and hadronic calorimeter covers the range $3.1 < |\eta| < 4.9$. The location of the calorimeters is shown in Fig. 2.11.

The electromagnetic calorimeter

The electromagnetic calorimeter [30] identifies electrons and photons and measures their energy. It consists of a barrel ($0 < |\eta| < 1.475$) and two endcaps ($1.375 < |\eta| < 3.2$). It uses liquid argon as the active medium and lead absorber plates as the passive medium. The lead plates are folded into an accordion shape, see Fig. 2.12. This configuration prevents cracks along ϕ, which would degrade the energy resolution. The readout electrodes, made of copper and kapton, are installed between the lead plates.

The electrodes are separated from the lead by plastic meshes. The remaining space is filled with liquid argon. The argon is cooled by a cryostat, which is shared with the inner detector solenoid to save material.

The barrel modules are divided into three longitudinal compartments (samplings). The inner-most compartment is finely segmented in η, which makes a good γ/π_0 and e/π separation possible. The middle compartment is where electrons and photons lose most of their energy. The last compartment is used to complete the energy measurement of showers which extend past the middle compartment, and to distinguish between electromagnetic and hadronic showers.

Testbeam results show that the electromagnetic calorimeter will achieve an excellent energy resolution:

$$\frac{\sigma_E}{E} = \frac{11.5\%}{\sqrt{E}} \oplus 0.5\% \qquad (E \text{ in GeV}). \tag{2.4}$$

The first term is called the sampling term. It represents the statistical fluctuations in the development of the shower, such as fluctuations of the total number of particles in the shower, and of the fraction of particles that are lost in the absorbers. The second (constant) term is the systematic error and has various contributions, such as inhomogeneities in the response of the calorimeter.

The hadronic calorimeter

The hadronic calorimeter [31] is built around the electromagnetic calorimeter. It will measure the energy and direction of jets of particles, formed by the hadronization of quarks and gluons, and by hadronically decaying τ-leptons.

The barrel part, called the *tile calorimeter*, consists of a central barrel ($0 < |\eta| < 1.0$) and two extended barrels ($0.8 < |\eta| < 1.7$). The tile calorimeter uses iron plates as the absorber, which also serve as the return yoke for the solenoid magnet. The active medium is formed by scintillator plastic tiles, which are read out on both sides by optical fibres. The tiles are placed radially and are staggered in depth, see Fig. 2.13. Cells are formed by grouping tiles together. The readout cells are approximately projective to the interaction point, and have a granularity of $\delta\eta \times \delta\phi = 0.1 \times 0.1$ (0.2×0.1 in the third sampling). The total number of channels is about 10,000. Jets are reconstructed with an energy resolution:

$$\frac{\sigma_E}{E} = \frac{50\%}{\sqrt{E}} \oplus 3\% \qquad (E \text{ in GeV}). \tag{2.5}$$

The endcap hadronic calorimeter uses liquid argon technology, because of its higher radiation tolerance. It uses 25 and 50 mm copper plates as the absorber material, arranged in a parallel-plate geometry. The 8.5 mm gaps between the copper plates have three parallel electrodes, thus dividing the gap into four 1.8 mm drift spaces. Smaller drift spaces require a lower voltage (typically 2 kV instead of 4 kV) which reduces the risk of ion build-up and discharge currents.

Hadronic showers are much longer than electromagnetic showers, and also much wider. Therefore the hadronic calorimeter needs to be much thicker than the electro-

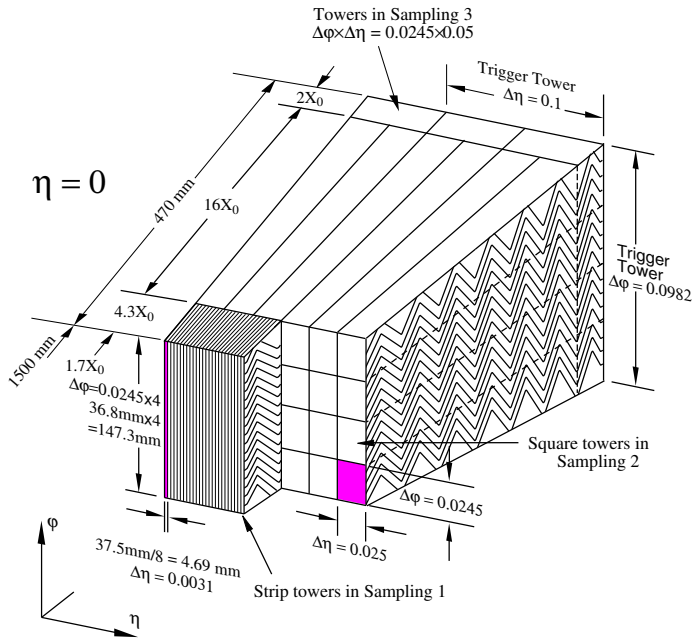

Figure 2.12: *The layout of an electromagnetic calorimeter module.*

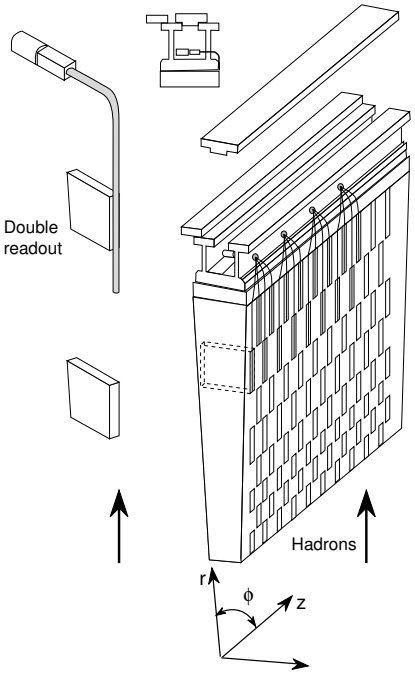

Figure 2.13: *The layout of a tile calorimeter module.*

magnetic calorimeter. The total thickness of the calorimeters is more than 10λ, where λ is the interaction length (the mean free path of a hadron between two interactions). This is sufficient to stop almost all the particles that are created in the shower, except muons and neutrinos. However, the calorimeters produce a large background (*cavern background*) for the muon detector, that consists mainly of thermalized slow neutrons and low-energy photons.

The forward calorimeter

The forward calorimeter (FCAL) is a copper-tungsten calorimeter. It covers the region $3.1 < |\eta| < 4.9$. It is split longitudinally into an electromagnetic compartment, and two hadronic compartments. The copper and tungsten have a regular grid of holes that hold the tube- and rod-shaped electrodes. The space between the tubes and rods is filled with liquid argon. The FCAL is integrated in the same cryostat as the electromagnetic and hadronic endcap calorimeters.

2.2.3 The muon spectrometer

The muon system [32] is by far the largest subdetector in ATLAS. High-p_T muons are a signature of interesting physics, therefore the muon trigger and reconstruction is very important. The muon system is designed to achieve a momentum resolution of 10% for 1 TeV muons. The sagitta of a 1 TeV muon is only about 0.5 mm, thus the sagitta has

to be measured with a precision of 50 μm or better. Fig. 2.14 gives an overview of the detector layout.

The magnet system in the muon detector is completely independent from the inner detector. It consists of eight superconducting coils in the barrel, and two toroids with eight coils each in the endcaps. The magnet is an air-core magnet system, i.e. the space between the coils is left open. Filling this space with iron would enhance the field strength and would also make the field more uniform, but it would also induce multiple scattering that would degrade the momentum resolution. The air-core system has an average field strength of 0.5 T, and a bending power that varies from 3 Tm in the barrel to more than 6 Tm in the endcaps.

Four types of detection chambers are used in the muon system: Monitored Drift Tube (MDT) chambers, Resistive Plate Chambers (RPCs), Thin Gap Chambers (TGCs) and Cathode Strip Chambers (CSCs). The MDT chambers provide precise muon tracking and momentum measurement. The chambers consist of aluminium tubes with a 30 mm diameter and a central wire. The tubes are filled with a 97:3 Ar:CO_2 mixture at 3

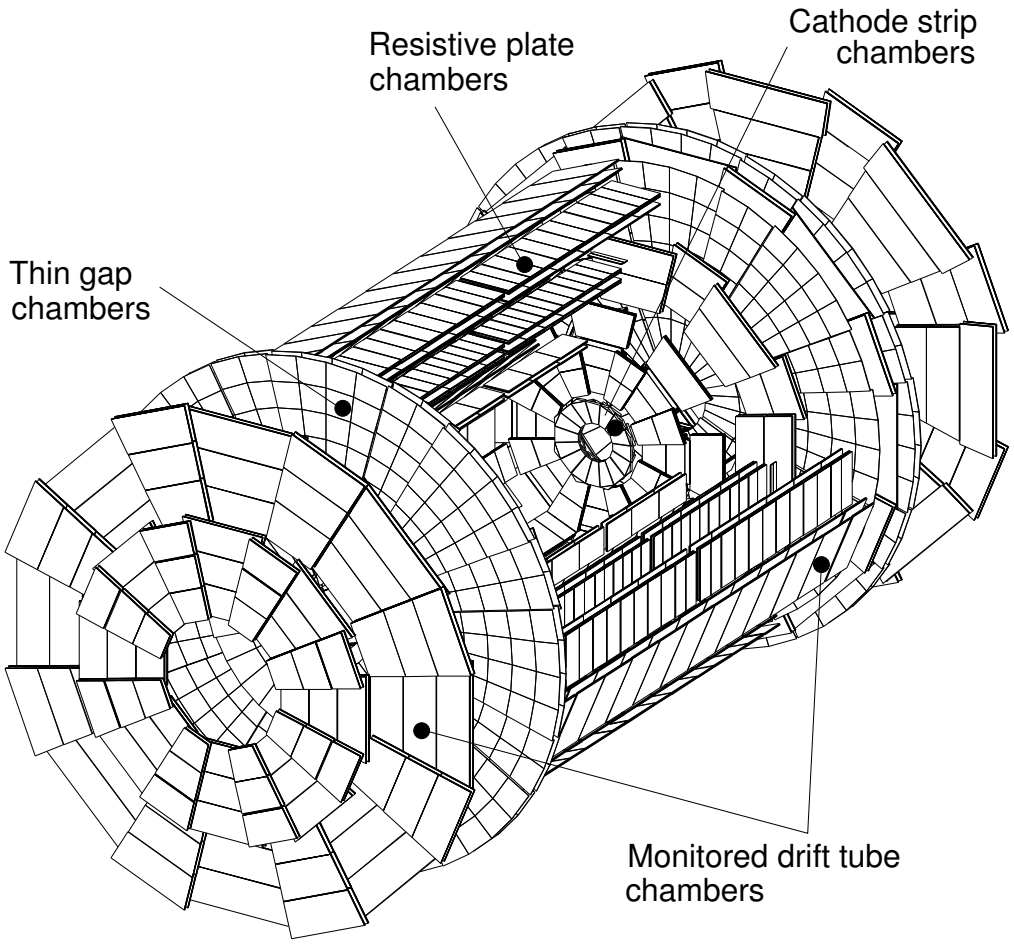

Figure 2.14: *Three-dimensional view of the ATLAS muon spectrometer.*

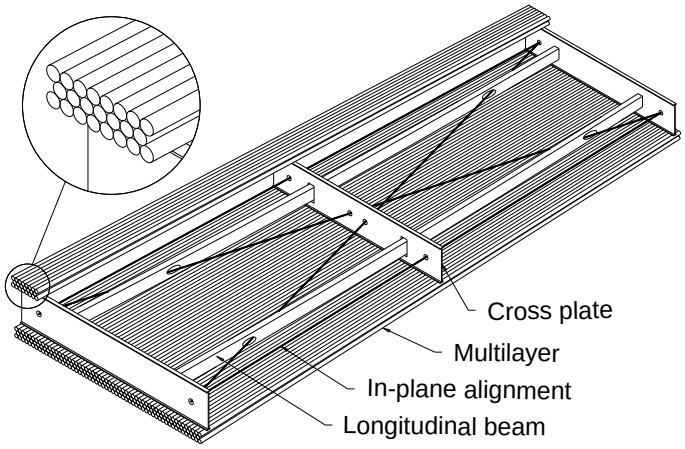

Figure 2.15: *The layout of a barrel MDT chamber.*

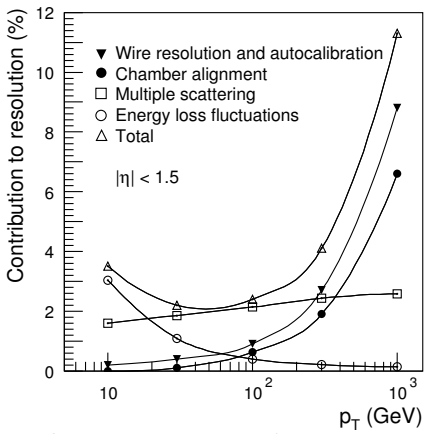

Figure 2.16: *The momentum resolution of the barrel precision chambers.*

bar absolute pressure. A muon that crosses a tube will produce ionization clusters in the gas, which will drift to the wire. The distance between the muon and the wire is determined by measuring the drift time of the first cluster that reaches the wire and passes over threshold. The resolution on the drift distance is around 80 μm. The layout of an MDT chamber is shown in Fig. 2.15. The various contributions to the momentum resolution are shown in Fig. 2.16.

In the inner-most ring of the inner-most endcap layer, CSCs are used instead of MDT chambers because of their finer granularity and faster operation. They are multiwire proportional chambers. The precision coordinate is read out with cathode strips, the second coordinate is read out using strips which are parallel to the anode wires (orthogonal to the cathode strips). The spatial resolution on the precision coordinate is around 60 μm.

The RPCs and TGCs are the muon trigger chambers in ATLAS. Their task is also to identify the bunch crossing to which a trigger belongs. Their adequate position resolution (about 1 cm) and excellent time resolution (about 2 ns) make them well suited for this task. The RPC has narrow gas gaps filled with $C_2H_2F_4$, between Bakelite plates that are covered with readout strips. The strips in the two plates in a gas gap are orthogonal, such that the chamber can measure both the η and ϕ coordinates. The ϕ coordinate measurement (i.e. along the direction of the tubes in the MDT chambers) is used to correct the drift time measurement in the MDT chamber for propagation delays. The TGCs are multiwire proportional chambers. The position measurement in these chambers is obtained from the strips and the wires, which are ganged in groups of 4 to 20 wires.

2.2.4 The trigger system

The bunch crossing rate in LHC is 40 MHz, and the size of an event, i.e. the data recorded in the detector during a bunch crossing, is about 1 MB. Clearly it would be impossible to store all this data on tape, therefore a trigger system is developed that selects the interesting events. The ATLAS trigger [33, 34] consists of three levels, which reduce the data rate to about 100 MB/s (see Fig. 2.17).

The level-1 trigger (LVL1) is a hardware based trigger that uses data from the calorimeters (with reduced granularity), and from the muon trigger chambers. In the case of the muon trigger a coarse estimate of the momentum is obtained from the RPC and TGC hits, the trigger fires if the muon has a sufficiently high p_T. The LVL1 trigger reduces the event rate to around 75 kHz. The calorimeter trigger is based on the total measured energy and the missing transverse energy in the event. The decision time of the LVL1 trigger (latency) is 2 μs. If an event is accepted, the information of all sub-detector systems is pre-processed and stored in the Read-Out Buffers (ROBs).

The level-2 trigger (LVL2) is based on software. It uses data from all subsystems, also the inner detector. It has access to the whole event, but only retrieves the data from the ROBs that correspond to 'regions of interest' (RoIs). The RoIs are produced

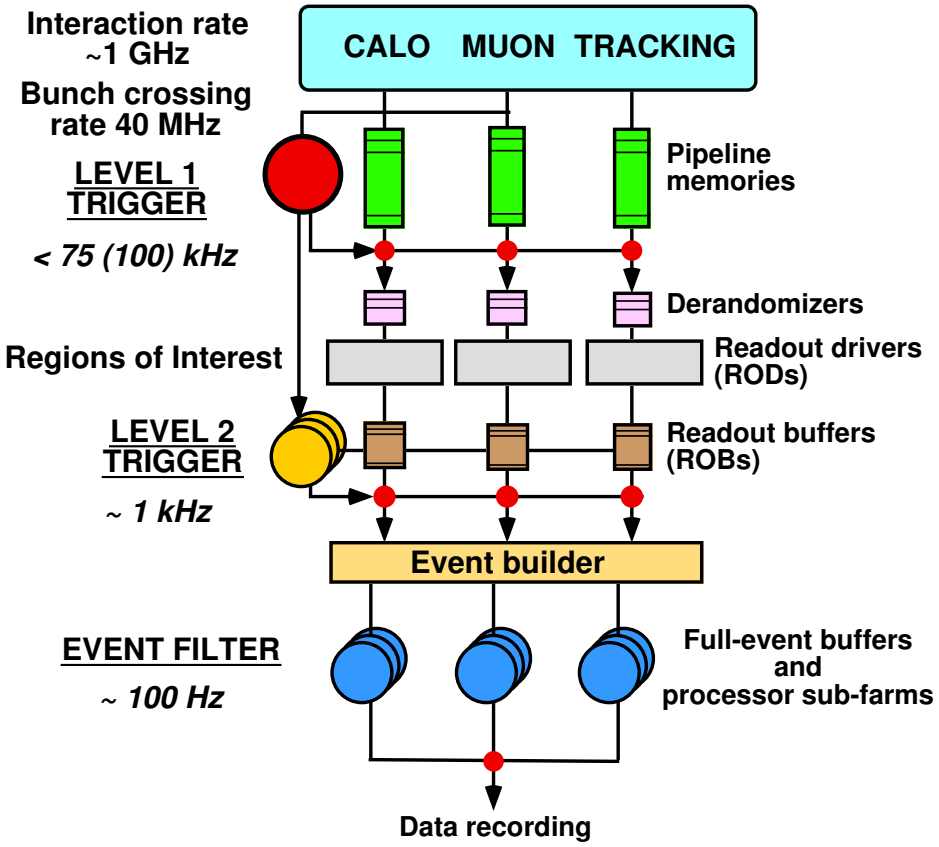

Figure 2.17: *Schematic overview of the trigger system.*

by the LVL1 and given to the LVL2. Using the data of the whole detector would make the LVL2 trigger too slow, since too much data would have to be processed. The event rate after the LVL2 trigger is around 1 kHz. The latency varies from 1 ms to 10 ms, depending on the complexity of the event. For the events that are accepted by the LVL2, the Event Builder collects the event fragments from the ROBs and builds a single event with these fragments. This event is then passed on to the Event Filter.

The Event Filter (EF) makes the final trigger selection and reduces the event rate to about 100 Hz. The EF has access to the whole event, with full granularity. The processing time available is of the order of seconds, which makes it possible to use detailed reconstruction algorithms. Examples of algorithms that can be run are vertex reconstruction, and track fitting with corrections for Bremsstrahlung by electrons. The EF runs on a dedicated computer farm near the ATLAS pit. The events that pass the EF are written to mass storage and are available for further analysis with the ATLAS offline software.

The operation of the trigger is configured using a *trigger menu*, which defines a set of trigger conditions. A condition consists of a physical object (e.g. an electron or a muon), together with certain thresholds and cuts (e.g. $p_T > 20$ GeV). If one or more of these conditions are fulfilled, the event is accepted. The trigger menu is designed such that events with interesting physics are likely to be accepted, while keeping the overall data volume at a manageable level. There are also calibration and monitoring triggers in the menu; these trigger items are used to monitor the detector performance and verify the correct functioning of its components. The trigger menu needs to be as unbiased as possible, such that new physics (which may have signatures that are difficult to predict) is not rejected at the trigger level.

Table 2.2 lists the most important items in the ATLAS trigger menu for the high level trigger (i.e. the LVL2 trigger and EF combined), and their expected rates at low luminosity ($L = 10^{33}$ cm^{-2}s^{-1}). The performance of the trigger will be evaluated during the initial low luminosity phase, which is likely to lead to changes in the settings (e.g. the thresholds). Also, new items may be added if required by the physics program.

Selection signature	Expected rate (Hz)
e25i	40
2e15i	<1
γ60i	25
2γ20i	2
μ20i	40
2μ10	10
j400	10
3j165	10
4j110	10
j70+xE70	20
τ35i+xE45	5
2μ6+secondary vertex	10
Other	20
Total	∼200

Table 2.2: *Trigger items and their expected rates at low luminosity. The first letter indicates the type of object:* e *for electrons,* γ *for photons,* μ *for muons,* j *for jets,* xE *for missing transverse energy,* τ *for taus. If the first letter is preceded by a number, this number is the number of objects required. The number after the object is the* p_T *threshold. The letter* i *indicates an isolated object, i.e. an object with no nearby objects in* $\eta - \phi$ *space.*

Chapter 3

Simulation and reconstruction software

This chapter gives an overview of the offline software programs that are used to simulate and reconstruct the events in ATLAS. An event can be a proton-proton collision, or a single particle traversing the detector, e.g. a cosmic muon or a testbeam event. Furthermore it can be a real, actually recorded event, or an event that is simulated in software by an event generator. The simulated events are used to study the performance of the detector, and to validate the reconstruction algorithms. The software framework is flexible enough to handle all these different cases.

We will focus on the inner detector part of the software in this chapter. Section 3.1 gives an overview of the simulation and reconstruction chain in the ATLAS software. One part of the simulation chain, the simulation of the SCT detector, will be discussed in detail in section 3.2. Section 3.3 gives an overview of the data preparation algorithms in the inner detector, which convert the raw data into calibrated measurements. Finally, section 3.4 describes the track propagation tools in the ATLAS reconstruction software.

3.1 Athena framework and applications

A common software framework is needed for the software applications, to allow them to communicate with each other. The ATLAS software is implemented in the ATHENA framework [35], which is derived from the GAUDI framework [36] developed for the LHCb experiment. It ensures that the requested algorithms are run in the correct order, and it offers common services like message logging, access to data on disk, and filling of histograms and ntuples. The output of an algorithm is written to a common place in memory, called the 'transient event store', from where the next algorithm can retrieve the output and process it further. The output can also be written to disk, using the POOL persistency scheme. The framework ensures that the data is read from disk (if it is not already present in the event store) if an algorithm requests it. In this way it is possible to run a chain of algorithms in one job, or to split it up into several jobs that read their input from disk. Fig. 3.1 summarizes how the framework is organized.

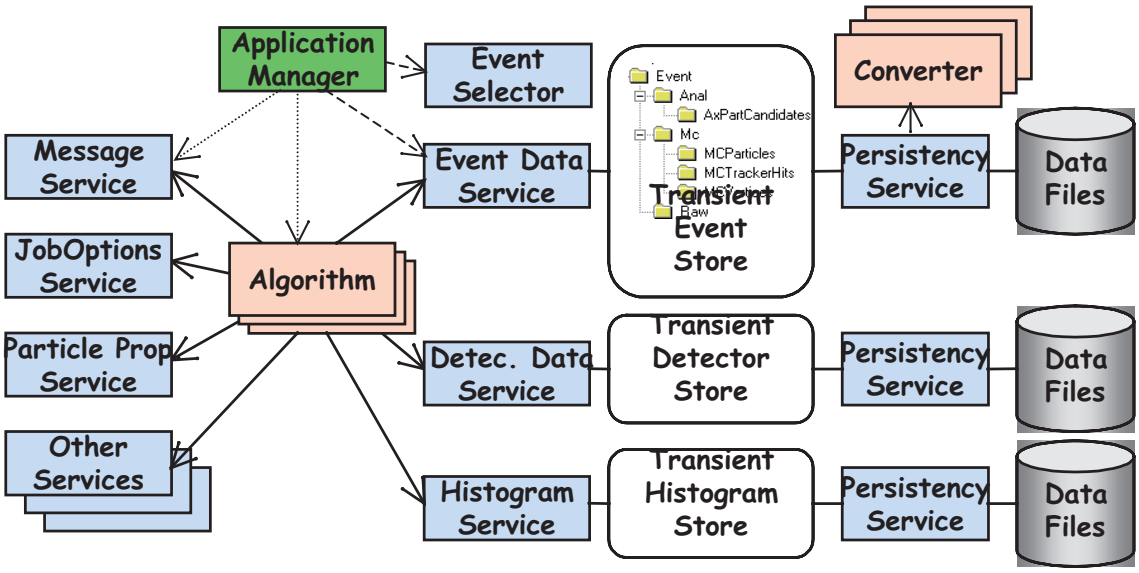

Figure 3.1: *Overview of the GAUDI framework. Each algorithm has access to a number of 'services', e.g. for the booking and filling of histograms. Event data (hits, tracks etc.) are stored in the 'transient event store', which is cleared after each event. Detector information is stored in the 'detector store'. The link between transient data (i.e. in memory) and persistified data (i.e. on disk) is formed by the 'converters'.*

The framework is used to generate simulated events, and to reconstruct both simulated and real events. The steps to simulate and reconstruct events are schematically:

- **Event generation**. The first step in the simulation chain is the simulation of the proton-proton collision itself. Several programs are available to perform this task, the most popular among them are PYTHIA [37] and HERWIG [38]. These programs calculate the particles that are produced in the collision, with their momentum four-vectors. The hard interaction between the partons in the protons is simulated using a leading-order calculation. The next-to-leading order contributions are approximated using the parton-shower model, which adds initial and final state radiation (ISR and FSR) to the interaction. The resulting partons are hadronized to form hadrons.

- **Detector simulation**. Here, the passage of the particles through the detector is simulated. This task is performed by the GEANT4 toolkit [39], which is controlled by the G4ATLAS application. GEANT4 transports the particles through the magnetic field and simulates the interactions with the detector material. Examples of such interactions are: multiple scattering, energy loss, and photon conversions. Also the decay of unstable particles is simulated.

- **Detector response**. At this stage, the response of the detector including electronics is simulated (also called digitization). In the simulation a volume can be

declared to be 'sensitive', e.g. a silicon sensor. If a particle hits such a volume, a 'hit' is written out. The digitization consists of simulating the response of the detector to the energy deposits in these hits. Both the response of the detector and of the electronics are simulated. For example, in the SCT the free charge that is produced by the energy deposits, drifts to the strips in the sensor, and the response of the electronics that read out these strips is simulated. The SCT digitization package is described in more detail in section 3.2.

- **Reconstruction**. Starting from the data produced by the detector, various algorithms are run to reconstruct the event. This includes algorithms that perform pattern recognition, track fitting, vertex determination, energy measurement etc. The reconstructed objects are matched to the simulated input ('truth'), such that the quality of the reconstruction can be studied. The output is written to ESD ('event summary data') and AOD ('analysis object data'). The ESD file has detailed versions of the reconstructed objects, e.g. tracks with the measurements on each track. The AOD file is more compact and contains only the information that is relevant for physics analysis (particles with their four-momenta).

- **Physics analysis**. The reconstructed particles can be used to study a particular physics process. For example, the invariant mass of electron-positron pairs can be plotted to detect a resonance, such as a graviton. In chapter 6 we will present a study of graviton production in ATLAS, using the full simulation and reconstruction chain.

- **Event display**. Two programs are available for the visualization of events: V-ATLAS [40] and Atlantis [41]. Both these programs produce a graphical representation of the event data and the detector geometry. V-ATLAS uses a 3-dimensional viewer, while Atlantis is based on 2-dimensional projections. The event display is an important tool for checking the quality of the reconstruction software, and for spotting problems in the detector description (e.g. clashes between volumes).

If real data are analyzed, the raw data are read in and converted (by bytestream converters) to digits. These digits are then in principle equivalent to the output of the detector response simulation.

An important ingredient for the event processing is the detector description. This part of the software has the information about the geometry and material of the detector, such as material properties, and the position and orientation of detector elements. All the simulation and reconstruction steps in ATLAS get their detector information from a common source, called GeoModel. This commonality ensures that each step uses exactly the same information, thus preventing inconsistencies. GeoModel consists of C++ classes that represent volumes and materials, these are used to build a representation of the actual detector. The numbers that define the size and position of each volume ('primary numbers') are stored in an Oracle database. Figure 3.2 shows a representation of the ATLAS detector in GeoModel.

Another important database for the reconstruction is the conditions database. This database holds the alignment constants, which are used by the detector description to

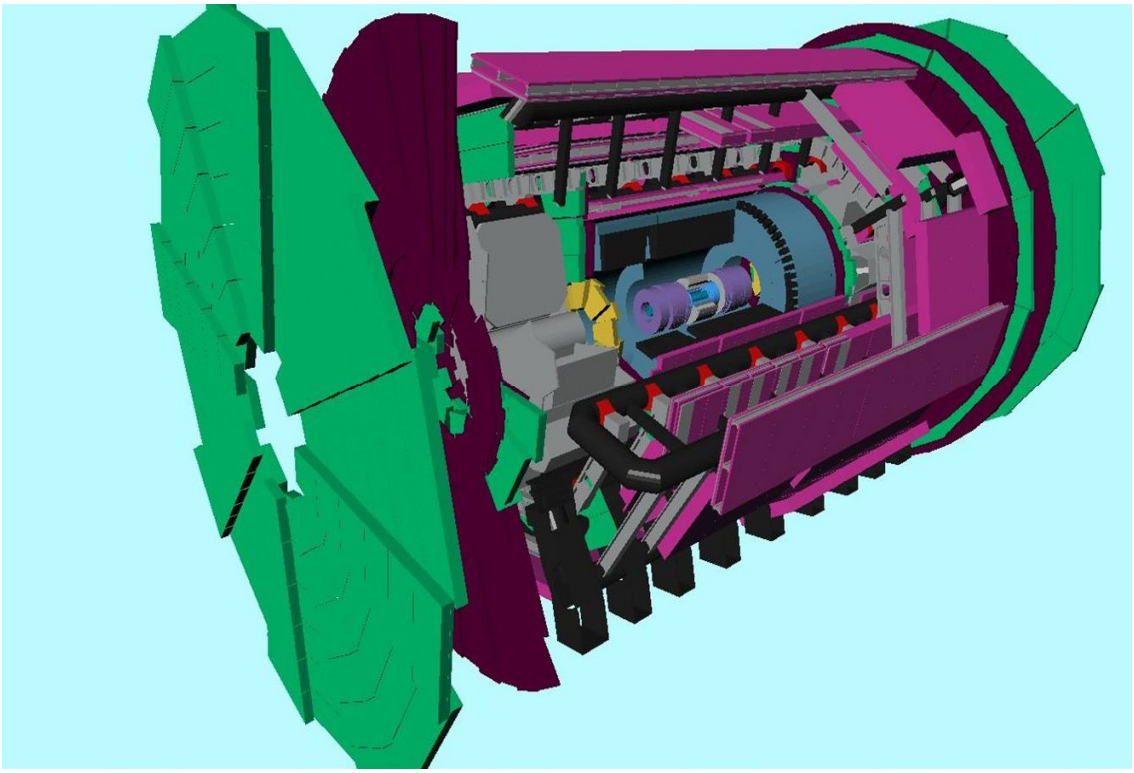

Figure 3.2: *View of the ATLAS detector in GeoModel.*

correct the positions of the sensors. It also holds the calibration constants, which are needed to convert the drift times in the TRT straws and the MDT tubes into drift radii. The calibration constants also comprise the list of channels that are dead or noisy. Since the performance of the detector may change over time (for example, readout boards may be added or removed), the constants in the conditions database are grouped in blocks, called 'intervals of validity' (IOVs). The reconstruction checks which IOV corresponds to the dataset that is reconstructed, and retrieves the constants that belong to this IOV.

3.2 Simulation of the SCT detector

The response of the SCT modules to the incoming particles is simulated by a software package, called 'SCT_Digitization'. We will first first discuss the basic operation principles of the SCT sensors in section 3.2.1. Section 3.2.2 deals with the SCT_Digitization package itself.

3.2.1 Silicon detection principle

Detectors based on silicon sensors offer a good position resolution and a high granularity. They are based on a reverse biased semi-conductor junction. The SCT has opted for

a design with p-type implants in an n-type bulk, which we will discuss here. Fig. 3.3 gives a schematic overview of the pn junction.

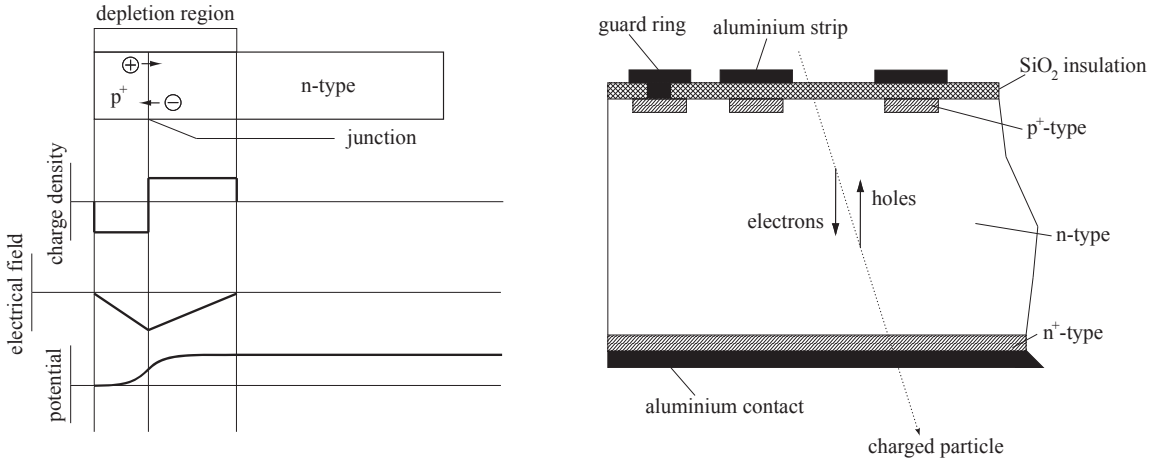

Figure 3.3: *Left: electrical properties of the pn junction. Right: schematic cross-section of a silicon strip sensor.*

The junction consists of an n-type bulk, with p-type implants. The bulk is doped with elements from group V (donors), while the implants are doped with elements from group III (acceptors). In the contact region between the bulk and the implant, electrons start to diffuse from the bulk to the implants. The implant and the bulk get a net charge, therefore a small potential difference is built up. The corresponding electrical field is nonzero in a small region near the contact area, this is called the *depletion region*. The diffusion of electrons towards the implant continues until the electrical field prevents any additional electrons from reaching the implant.

The dopant concentration in the implants is much higher (about a factor 100) than in the bulk, therefore the junction is called a 'p^+n' junction. This allows the implant to receive many electrons from the bulk even though it is much smaller in size. The depletion region extends deeper into the bulk as a result. The size of the depletion region can be further increased by applying an external voltage, the *bias voltage*. The voltage that is needed to fully deplete the bulk material is called the *depletion voltage*. The depletion voltage of the SCT sensors is around 70 Volts, although this increases when the silicon module is irradiated (as will happen in ATLAS).

When a particle traverses the sensor, it will ionize silicon atoms resulting in free electron-hole pairs. Because of the electrical field in the depletion region, the holes will drift to the strips while the electrons drift to the back of the sensor. The strips are read out by a front-end chip, which detects the induction signal from the moving holes and electrons. The position of the original particle is then found by determining which strip gave a signal. Because of the binary readout of the SCT (i.e. one only knows if a strip produced a hit or not), the probability distribution of the particle position within the

strip is uniform. The R.M.S. of a uniform distribution from $-\frac{1}{2}p$ to $\frac{1}{2}p$, where p is the width of a strip (strip pitch), is given by:

$$\sigma = \sqrt{\overline{x^2} - \overline{x}^2} = \sqrt{\frac{1}{p}\int_{-\frac{1}{2}p}^{\frac{1}{2}p} x^2 dx} = \frac{p}{\sqrt{12}}. \tag{3.1}$$

The SCT barrel modules have a strip pitch of 80 μm, giving a resolution of about 23 μm. In practice the resolution is slightly better, because a particle can deposit charge in two strips at the same time if it passes close to the boundary between two strips.

In the presence of a magnetic field, the free charges in the silicon will not drift perpendicular to the surface. Instead they will drift at an angle, called the *Lorentz angle*:

$$\tan\Theta_L = \mu^H B = r_H \mu B, \tag{3.2}$$

where μ^H is the Hall mobility, the conduction mobility μ multiplied by the Hall scattering factor r_H. The Lorentz angle causes a systematic shift in the position of the charges when they reach the strip or pixel at the surface, and hence a systematic shift in the determined position of the original particle. This shift is corrected for in the reconstruction. The right side of Fig. 3.4 shows the effect of the magnetic field on the drift charges, for the case where the primary particle travels perpendicularly to the surface. Due to the magnetic field the drift charges do not travel along the path of the primary particle. This means that the area where the charges reach the surface becomes larger. In absence of a magnetic field, the same effect is obtained by rotating the module by an angle $\alpha = \Theta_L$, as shown by the left side of Fig. 3.4.

3.2.2 The SCT digitization package

The SCT detector response is simulated in the SCT digitization package [42]. The input consists of 'hits' i.e. small steps in the silicon, each of which has a starting point, an end point, and the amount of energy that was deposited by the particle. The task of the digitization is to produce an output that is similar to what the actual detector produces. In the case of the SCT this output consists of (groups of) strips.

The algorithm starts by dividing each step (given by GEANT4) into smaller substeps, such that each substep is not longer than a certain value (currently set to 90 μm). The energy deposited in the GEANT4 step is divided evenly among the substeps. The free charge at each substep is calculated, assuming that each electron-hole pair requires 3.6 eV of energy deposited. The average total amount of deposited energy in the sensor is around 80 keV, resulting in about 20,000 electron-hole pairs. The charge at each substep is divided into ten subcharges, which are drifted to the surface. The drift time of a hole depends on the distance z to the surface [43]:

$$t_d(z) = \frac{d^2}{2\mu V_D} \ln\left(\frac{V_B + V_D}{V_B + V_D - 2V_D z/d}\right), \tag{3.3}$$

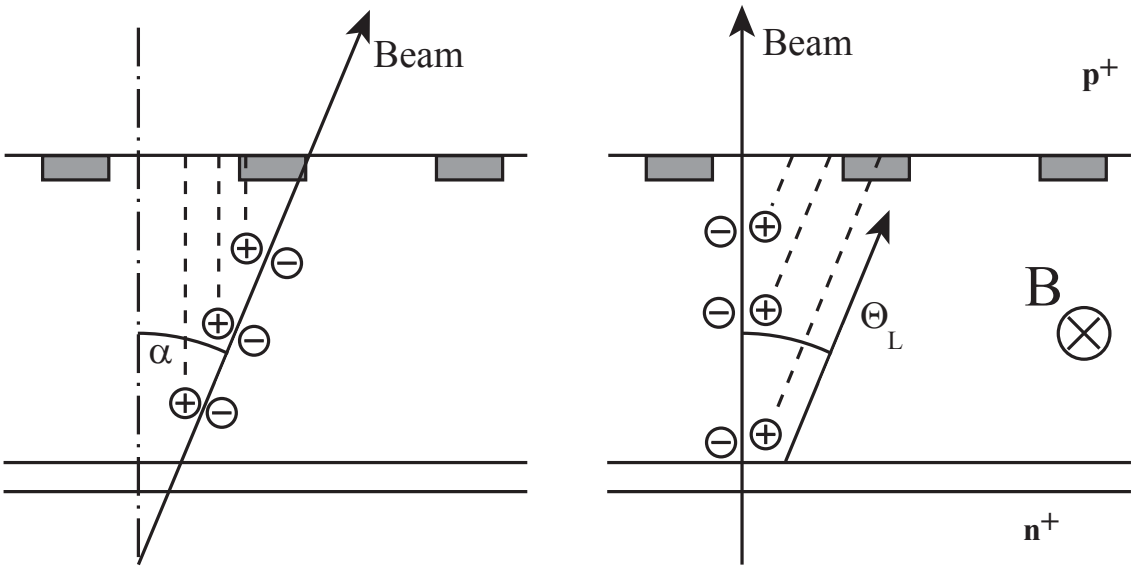

Figure 3.4: *The effect of a Lorentz angle Θ_L is equivalent to an incidence angle α of the incoming particle (in absence of a magnetic field).*

where d is the thickness of the sensor, μ is the hole mobility, V_D is the depletion voltage (taken to be 70 V) and V_B is the applied bias voltage. If $V_B < V_D$, the detector is only partially depleted, and the charges in the undepleted region are considered lost.

Holes in the SCT undergo lateral diffusion while being collected at the surface. In the digitization this is simulated by smearing the surface position of each charge by a Gaussian distribution, with σ given by [29][1]:

$$\sigma = \sqrt{2Dt}, \tag{3.4}$$

where $D = \frac{kT\mu}{q}$, and k is Boltzmann's constant. The position is also corrected for the shift caused by the Lorentz force. Using this position a surface drift time t_s is calculated, i.e. the time it takes for a hole to reach the center of the strip, starting from the surface position. The surface drift time is given by a combination of quadratic functions such that t_s(strip center) = 0, t_s(mid-strip) = 10 ns and t_s(half way to mid-strip) = 5 ns[2]. The total drift time is the surface drift time added to Eq. (3.3). Fig. 3.5 shows the behavior of the algorithm described so far.

Given a set of charges with different drift times, the next step is to simulate the response of the front-end electronics to these charges. The shaping circuit in the SCT front-end chip can be described by a $CR-(RC)^3$ filter. The response function (i.e. the

[1] This corrects a small typographical error in Ref. [42].

[2] A more accurate expression for t_s would be $t_s = -C \ln\left(1 - \frac{2x}{p}\right)$, where C is a constant, x is the distance to the middle of the strip, and p is the strip pitch [44]

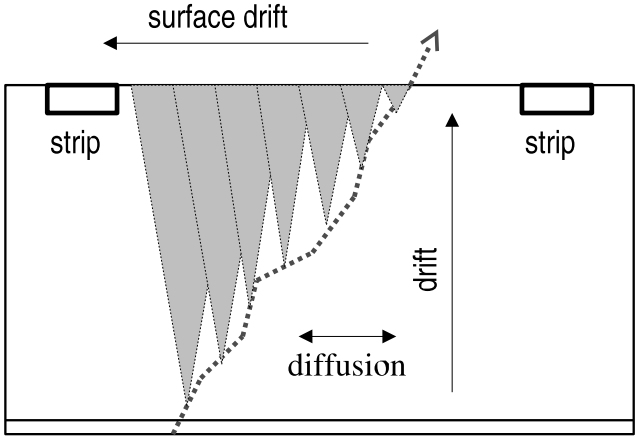

Figure 3.5: *Simulation of charge creation and collection in a SCT sensor. At several points along the path of the primary particle, free charges are created that drift to the surface. The cones represent the paths of the charges. The width of the cones represents the lateral diffusion. The cones are tilted if there is a Lorentz angle.*

response of the circuit to a delta pulse) is [28]:

$$V(\Delta t) = Ge^3 \left(\frac{\Delta t}{t_p}\right)^3 e^{-\frac{3\Delta t}{t_p}} \qquad (\Delta t > 0), \tag{3.5}$$

where t_p is the peaking time, the time at which the response function reaches its maximum. The peaking time is taken to be 21 ns. G is the gain factor, which varies from strip to strip. The algorithm generates gain factors for each strip by producing random numbers around 1, using a Gaussian distribution with an R.M.S. of 0.031. Fig. 3.6 shows the shape of the response function.

The response of the electronics is simulated by treating each surface charge as a delta pulse, calculating the corresponding response using Eq. (3.5), and adding the results. Note that the time Δt in Eq. (3.5) is the time since the bunch crossing, because the SCT electronics are timed relative to the beam clock. Therefore the time of flight (tof), i.e. the time that the particle needed to reach the sensor, is added to the drift time to get the total time[3] Δt. Thus, the expression for Δt is:

$$\Delta t = t_{tof} + t_{BC} + t_d + t_s, \tag{3.6}$$

where t_{BC} is a multiple of 25 ns (the bunch spacing).

There are two additional contributions to the response: noise, and capacitive coupling to nearby strips. The noise is simulated with a Gaussian distribution, with σ equal to

[3]The digitization could also just ignore the time of flight, i.e. it could assume that every particle arrives perfectly in time. This is not correct: in ATLAS there are many 'loopers' with low energy that arrive too late or too early at the sensor to create a signal.

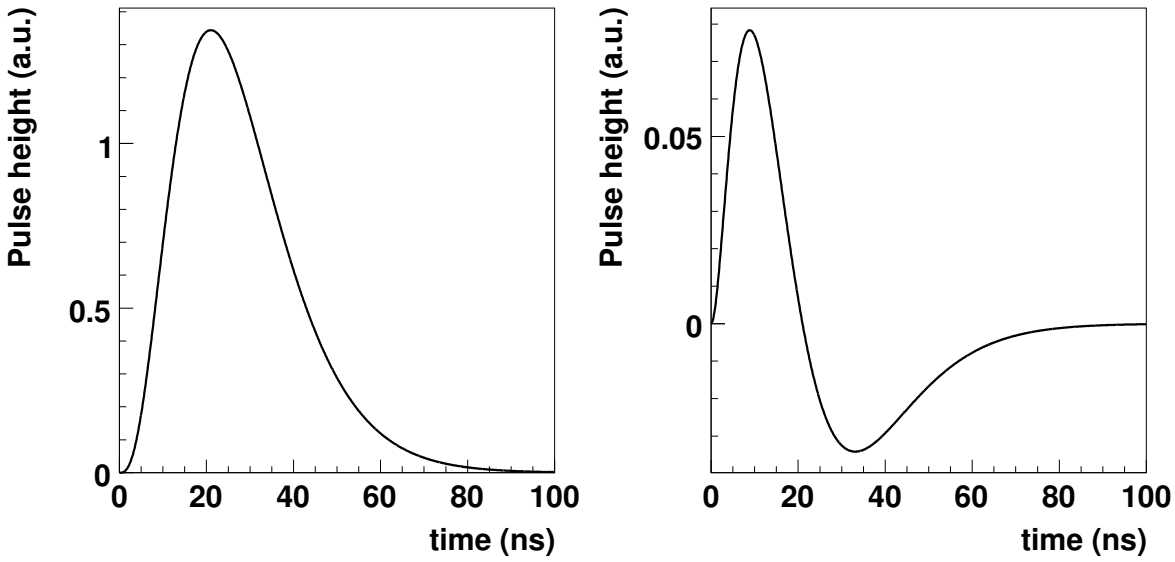

Figure 3.6: *Response to a delta pulse on the central strip (left) and on a neighboring strip (right).*

1400 ENC[4] ('equivalent noise charge', i.e. the charge in units of electrons that would be needed to produce the same signal as the noise). The capacitive coupling causes a signal on the two neighboring strips. The contribution to the signal on a neighboring strip from a delta pulse is given by:

$$V(\Delta t) = C\left(3 - 3\frac{\Delta t}{t_p}\right) e^{-\frac{3\Delta t}{t_p}} \left(\frac{\Delta t}{t_p}\right)^2 \qquad (\Delta t > 0). \tag{3.7}$$

Up to first order, the signal on the neighboring strips is subtracted from the signal on the primary strip.

The next step in the algorithm is the discriminator step: for each strip the total signal is computed at $\Delta t = t_{thresh}$ (set to 30 ns), and the algorithm checks for each strip if the signal is above threshold (by default 1 fC). Nearby strips are grouped into clusters. For each strip above threshold in the simulation a truth object is created, that holds the contributions to the signal from the various processes (particles, noise).

The digitization algorithm has been validated using testbeam data. Fig. 3.7 shows the efficiency as a function of threshold for data and simulation, using two different bias voltages. The cluster size in data and simulation is compared in Fig. 3.8.

[4]This should depend somewhat on the module type. For example, the short endcap modules have a noise that is closer to 1000 ENC.

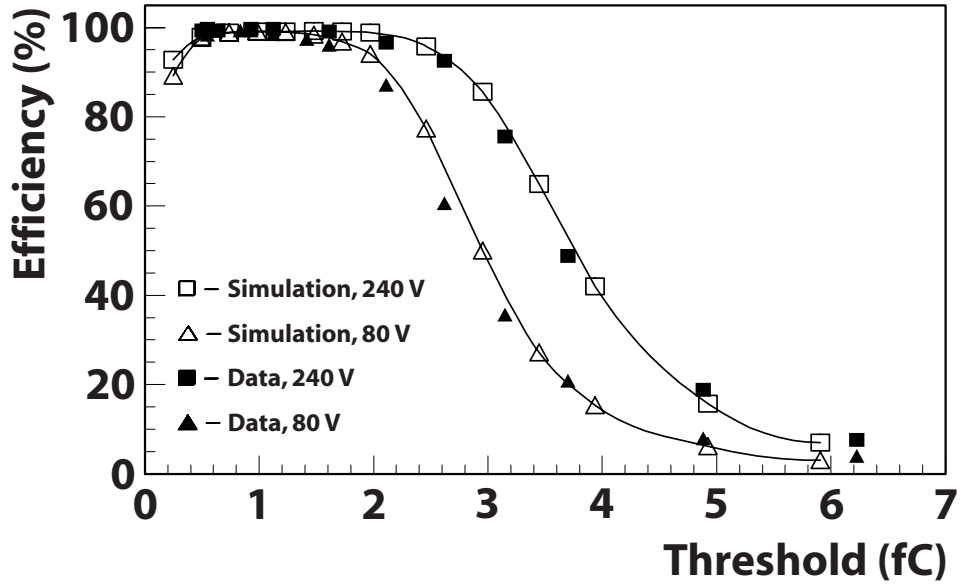

Figure 3.7: *Efficiency as a function of threshold, for data and simulation.*

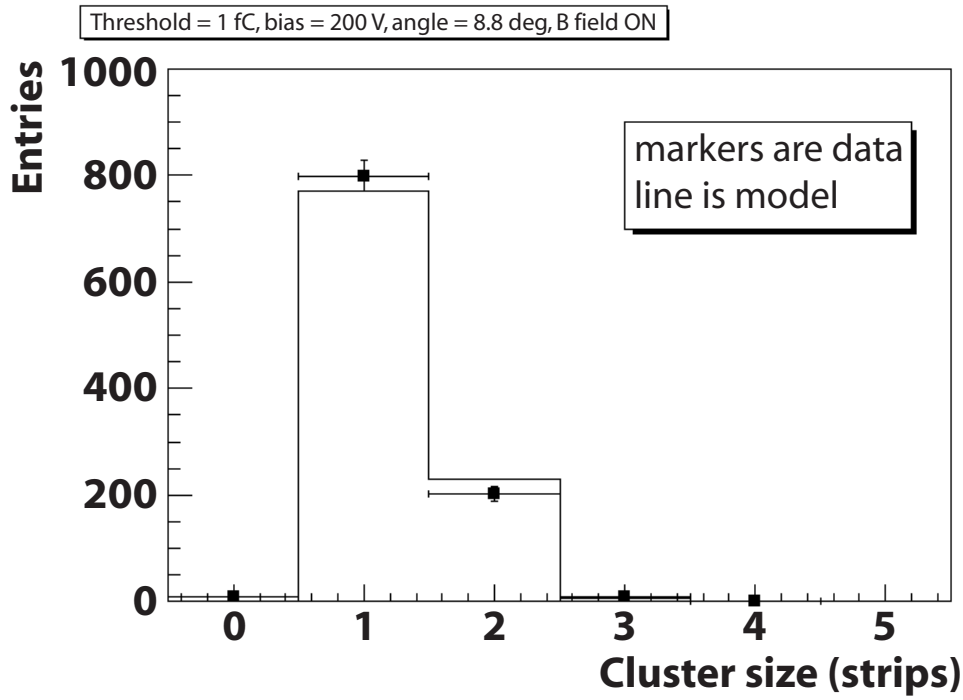

Figure 3.8: *Comparison of cluster size in simulation and data.*

3.3 Data preparation

The RDO (Raw Data Object) is an object representation of the raw data. An RDO corresponds to a pixel, or an SCT cluster (nearby strips are already clustered at the hardware level in the SCT), or a TRT straw. Each RDO has an identifier and a 32 bit word. For the pixels this word contains the ToT (time over threshold) information. For the SCT it contains the first strip and the number of strips in the cluster. For the TRT it contains the drift time, the ToT, and the HT (high threshold) information.

The RDOs are processed by data preparation algorithms that form PrepRawData objects, or 'RIOs' ('reconstruction input object'). In the case of the pixels, the pixels that share at least one edge (i.e. the pixels that are neighbors) are grouped into clusters. A local position of the cluster is calculated by taking a simple center of gravity of all the pixels in the cluster. If the ToT information is available then a charge interpolation algorithm can also be used. The ToT is a measure of the amount of charge that has been deposited in the pixel. This information can be used to get a more accurate estimate of the position of the cluster. The code checks if there are ganged pixels (see section 2.2.1) in the cluster and stores this information. Finally the position of the cluster is corrected for the Lorentz shift, and a two dimensional error matrix is assigned.

The SCT RDOs just need to be copied into the new objects (RIOs) for the most part, since they have already been clustered in the hardware. The clusterization algorithm loops over these clusters and checks them for channels that are marked as bad, using a map from the conditions database. If a strip is marked as bad then it is removed from the cluster. If the bad strip divides the cluster in two parts then two separate clusters are formed. A local position is calculated (corrected for the Lorentz shift) and a measurement error is assigned. The error is assumed to be pitch/$\sqrt{12}$. For the SCT endcap modules, the pitch and hence the error depends on the position along the strip, but this information is not available at this stage of the data processing. Therefore an average pitch is used to calculate the error.

For the TRT hits, the recorded drift time needs to be converted into a drift radius. First, the drift time is corrected by subtracting the t_0, i.e. the time offset of the straw in the readout electronics. After this correction, a time of 0 ns corresponds to a particle that passes at zero radius (i.e. right through the wire). The value of t_0 is in principle determined for each individual straw by the calibration procedure, e.g. by performing a fit to the leading edge of the drift time spectrum. In the reconstruction this fitted value is read from the conditions database. Using the corrected drift time, the radius is calculated as follows:

$$r = a_0 + a_1 t + a_2 t^2 + a_3 t^3. \tag{3.8}$$

The coefficients a_i are also read from the conditions database, they have also been determined by the calibration procedure. An example of a $r(t)$ plot is given in chapter 5 (Fig. 5.9).

For the measurement error on a TRT hit a constant value of 170 microns is used.

	Pixels	SCT	TRT
Simulation	Time over threshold	First strip in the group Group size	High level threshold Time over threshold Drift time
Testbeam	Time over threshold BCID	First strip in the group Group size Time bin Errors	High level threshold Time over threshold Drift time Time phase

Table 3.1: *Information encoded in the 32-bit word of the RDO. The BCID is the 'bunch crossing identifier', i.e. the bunch crossing to which the hit belongs.*

Silicon SpacePoints

Using the strips on the front and back sides of an SCT module a spacepoint can be formed, by calculating where the two strips overlap. Note that the two sensors in an SCT module are about 1 mm apart, therefore the constructed spacepoint depends on the incidence angle of the track with respect to the module. For ATLAS the spacepoint formation assumes that the track points from the origin to the module. For cosmic events it assumes that the tracks originate from a point high in the sky.

The spacepoint is a very convenient quantity for the offline pattern recognition algorithms in ATLAS, but its dependence on the incident angle makes it less precise than the individual clusters that form the spacepoint. Therefore the track fitters use the SCT clusters instead of the spacepoints in the final fit.

Measurements on track

The RIO_OnTrack is a fully calibrated measurement. It is a PrepRawData measurement that has been corrected using information that is only available after tracking. For example, a TRT hit can be corrected for sagging of the straw and propagation delays if the second coordinate (i.e. along the wire) is known. The measurement error of the SCT endcap hits is corrected using the position along the strip. The RIO_OnTracks are made in the pattern recognition stage, such that the final fit can use the full information.

Monte Carlo truth objects

If the RDOs are produced by the digitization algorithms they have a truth object associated with them, called 'SDO' (simulated data object). The SDO has information about which processes contributed to the hit (e.g. a particle, or noise), and how much energy is deposited. Truth objects are formed for each PrepRawData object by looking up the corresponding SDO, and checking which process deposited the largest amount of

energy[5]. The truth for the spacepoints is formed in the same way, while the truth for a track is formed by checking which particle is the originator of the majority of the hits on the track.

3.4 Track propagation

A tool that is heavily used by the track fitters is the propagator. The task of the propagator is to calculate the track parameters and errors at a destination surface, given a set of track parameters at a starting point. The implementation of the propagator depends on the track model. In absence of a magnetic field the track is a straight line, in that case the propagation can be calculated analytically. If there is an inhomogeneous magnetic field (as in ATLAS) then no analytical solution is available, and the solution has to be approximated numerically. These numerical methods have an intrinsic precision that should be tuned carefully, so that the propagated results are more accurate than the detector resolution. For tracking in ATLAS this means that the propagator should be accurate to within a few microns over distances of 10 meters or more.

A number of propagators are available in the ATLAS software: the straight line, the helix, the Runge-Kutta, and the STEP ('simultaneous track and error propagation') [45] propagators. We will describe the straight line and Runge-Kutta propagators in this section as these are the ones that are mostly used at the moment. We will only describe the propagation of track parameters, as the propagation of measurement errors is not needed for the track fitter that will be discussed in chapter 4.

3.4.1 The straight line propagator

The straight line propagator was designed as a faster alternative to the Runge-Kutta propagator for the cases where there is no magnetic field, and for regions where the field can be neglected. It can propagate a track to several types of surfaces, including plane surfaces, straight lines, cylinders and discs. The tracker hits in ATLAS are either associated with a plane surface (strip clusters), or with a straight line surface (drift circles). Cylinders and discs are used to represent material layers in the Inner Detector.

Propagation to a plane

A straight track can be described by a position and a direction vector:

$$\vec{r} = \vec{a} + \lambda \vec{b}. \tag{3.9}$$

A plane is described by a point $\vec{c}$ and a vector $\vec{d}$ that is normal to the plane. At the point where the track intersects the plane, the vector from the track to $\vec{c}$ is perpendicular to $\vec{d}$:

$$(\vec{a} + \lambda \vec{b} - \vec{c}) \cdot \vec{d} = 0. \tag{3.10}$$

[5]For the TRT hits, it would be more natural to select the particle that passed closest to the wire.

This equation can be solved for λ:

$$\lambda = \frac{\vec{c} \cdot \vec{d} - \vec{a} \cdot \vec{d}}{\vec{b} \cdot \vec{d}}, \tag{3.11}$$

which, together with Eq. (3.9), gives the propagated position of the track. The direction of the track does not change.

Propagation to a straight line

A straight line can be described by a position $\vec{c}$ and a direction $\vec{d}$, just like the track. At the point of closest approach, the vector from the straight line to the track should be perpendicular to the directions $\vec{b}$ and $\vec{d}$:

$$(\vec{a} + \lambda\vec{b} - \vec{c} - \mu\vec{d}) \cdot \vec{d} = 0; \tag{3.12}$$

$$(\vec{a} + \lambda\vec{b} - \vec{c} - \mu\vec{d}) \cdot \vec{b} = 0. \tag{3.13}$$

These are two equations in the unknowns λ and μ. One can solve for λ while eliminating μ, giving:

$$\lambda = \frac{\vec{a} \cdot \vec{b} - \vec{b} \cdot \vec{c} - (\vec{a} \cdot \vec{d})(\vec{b} \cdot \vec{d}) + (\vec{c} \cdot \vec{d})(\vec{b} \cdot \vec{d})}{1 - (\vec{b} \cdot \vec{d})^2}. \tag{3.14}$$

It has been assumed here that $\vec{b}$ and $\vec{d}$ have unit length.

Propagation to a cylinder

In the track reconstruction, cylinder surfaces are used in the material description of the Inner Detector and in the calorimeter. A straight line will in general have two intersections with a cylinder, except when it is exactly parallel to it, or when it touches the edge of the cylinder. It is convenient to calculate the intersections in the cylinder frame, i.e. the frame where the z-axis runs along the center of the cylinder. If $\vec{a'}$ and $\vec{b'}$ are the position and direction of the track in the cylinder frame (i.e. transformed from the global frame), then the equation to be solved is:

$$(a'_x + \lambda b'_x)^2 + (a'_y + \lambda b'_y)^2 = R^2, \tag{3.15}$$

where R is the radius of the cylinder. Solving for λ gives:

$$\lambda = -a'_x b'_x - a'_y b'_y \pm \sqrt{-\left(b'_x a'_y - b'_y a'_x\right)^2 + R^2}. \tag{3.16}$$

Again we assumed that $\vec{b'}$ has unit length. Using Eq. (3.16), the intersections can be computed in the cylinder frame, which can then be transformed to the global reference frame.

3.4.2 The Runge-Kutta propagator

The Runge-Kutta propagator is taken from the xKalman package [46]. It follows the path of a particle through an inhomogeneous magnetic field by taking one step at a time. At each step it uses the Runge-Kutta-Nystrøm integration technique [47, 48] to solve the equation of motion numerically. It can also perform straight line propagation and propagation in a constant field (helix) if required.

Neglecting material interactions and radiative corrections, the equation of motion for a particle with charge q in a magnetic $\vec{B}$ field is:

$$\frac{d\vec{p}}{dt} = q\vec{v} \times \vec{B}. \tag{3.17}$$

It can be shown [48] that this equation can be written as the following set of differential equations:

$$\frac{d^2x}{dz^2} = \frac{q}{p}R\left[\frac{dx}{dz}\frac{dy}{dz}B_x - \left(1 + \left(\frac{dx}{dz}\right)^2\right)B_y + \frac{dy}{dz}B_z\right], \tag{3.18}$$

$$\frac{d^2y}{dz^2} = \frac{q}{p}R\left[\left(1 + \left(\frac{dy}{dz}\right)^2\right)B_x - \frac{dx}{dz}\frac{dy}{dz}B_y - \frac{dx}{dz}B_z\right], \tag{3.19}$$

where the function R is:

$$R = \frac{ds}{dz} = \sqrt{1 + \left(\frac{dx}{dz}\right)^2 + \left(\frac{dy}{dz}\right)^2}. \tag{3.20}$$

The Runge-Kutta method solves these equations for a step of size h by evaluating the right side of Eq. (3.18) and Eq. (3.19) at a number of points along the step, and taking a weighted average of the results. The Runge-Kutta propagator in ATLAS uses a fourth order method that uses three points in each step. The error on the propagation is proportional to the step size to the fifth power. Higher order methods use more points per step and are therefore more accurate, but at the cost of requiring more computations.

The error on the propagation is monitored by also performing a third order propagation at each step, and comparing the results. If the positions of the two propagations differ too much then the propagation is attempted again with half the step size. This is called 'adaptive step size control'. The propagator also monitors the remaining distance to the target surface at each step. If this distance is below a certain value (typically a few microns), a Taylor expansion is performed on the position and direction of the track to reach the surface.

Chapter 4

Track finding & fitting

The combined testbeam in 2004 was the first opportunity to reconstruct real data with the ATLAS offline tracking software. Originally it was foreseen that only the standard ATLAS tracking algorithms would be used, but it soon became clear that these algorithms had difficulties in adapting to the testbeam setup. These difficulties became especially apparent during the beginning of the testbeam, when the inner detector setup was still incomplete and being worked upon.

To overcome these difficulties, a package was developed that is now called CTBTracking ('Cosmics + TestBeam'). This package serves a number of purposes:

- Being relatively small, it was easy to adapt to all the different setups that were used in the testbeam. It was the first to find tracks in real data, thus speeding up the understanding of the data.
- The package makes use of the new tracking tools that are currently being developed in the ATLAS offline software group [49]. Using CTBTracking as a platform, these tools have been (and are still being) tested on the millions of events that were taken.
- The package provides a pattern recognition that works without a vertex constraint. This is an ideal approach for the testbeam, and is also needed for other situations, e.g. reconstructing cosmic or beam halo events.

The package is being used in the combined testbeam, where it has already reconstructed millions of events, and for reconstructing cosmics in the setup at the SR1 assembly building. In addition, the track fit has been tested on full ATLAS physics events, since it can work with any detector setup and with or without the presence of a magnetic field (either a constant field or a 3-dimensional field map). We will describe the testbeam setup in detail in chapter 5. To summarize, the inner detector part of the testbeam setup consists of:

- Three layers with two pixel modules each;
- Four layers with two SCT endcap modules each;

- Six TRT barrel modules with 3284 straws in total.

The pixel and SCT setup is installed in a magnet that generates a field of up to 1.4 Tesla. The TRT is outside of the magnet, but it contributes significantly to the momentum resolution because it measures the deflection of the particle. The inner detector in the testbeam is shown in Fig. 4.1.

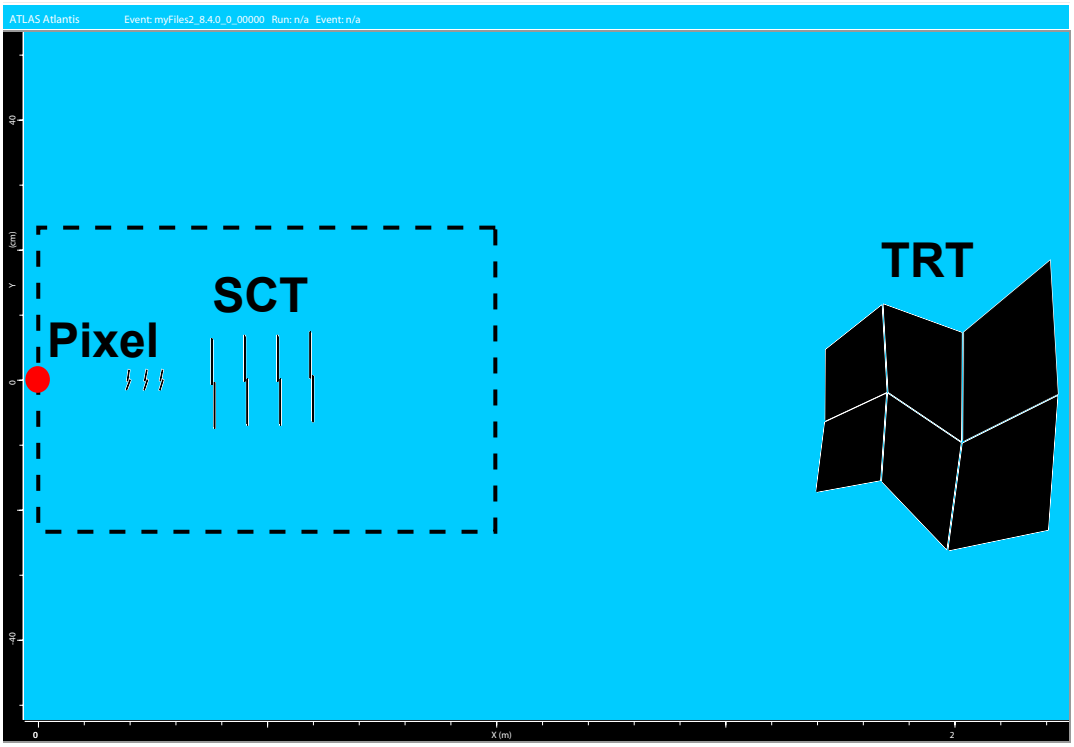

Figure 4.1: *Schematic overview of the inner detector in the combined testbeam. From left to right, the beam encounters six pixel modules, eight SCT modules, and six TRT modules. The solid dot shows the origin of the coordinate system, it is placed at the entrance of the magnet (about 200 mm before the first pixel layer). The dashed box represents the coverage of the magnet.*

The cosmics setup in the SR1 building was based on a part of the TRT barrel, and also (at a later stage) part of the SCT barrel. At first only modules near the top of the barrel were read out, this was later extended with modules near the bottom. More information about the setup can be found in section 4.3, and in Ref. [50].

Section 4.1 of this chapter deals with the pattern recognition algorithms, and their performance on the testbeam data and the cosmic ray data (the latter will be discussed only very briefly). Section 4.2 describes the track fit in full detail, with some technical details left to the appendix. First results with actually recorded cosmic ray data are presented in section 4.3. The performance of the track fit in ATLAS is discussed in section 4.4. We present the conclusions in section 4.5.

4.1 Pattern recognition

When a particle traverses a tracking detector, it will generate a point in that detector. The task of the pattern recognition is to determine which points belong to which tracks, and to give, for each track, an estimate of the track parameters. This information is then given to the track fitting algorithm, which tries to produce a track trajectory that is as close to the true trajectory as possible.

In the testbeam, most of the events have only one track. Still the pattern recognition is a nontrivial task, because it has to deal with misalignments and miscalibrations which can be far worse than what is expected for ATLAS. Furthermore, the noise level in the TRT is higher than in the current simulation, and the magnetic field is very inhomogeneous, which complicates things. As a result, loose cuts are needed to find tracks.

The pattern recognition of CTBTracking has two modes of operation. In the first mode, the track finding starts in the pixel and SCT detectors, and the tracks that are found are extrapolated to the TRT to collect the matching TRT hits. The second mode starts from the TRT, this mode is used when the silicon detectors are disabled or (optionally) when no track is found in the silicon detectors.

4.1.1 Pixel+SCT pattern recognition

The track finding in the pixel and SCT detectors works by looping over combinations of *spacepoints*. In the pixel detector, a spacepoint is the center of a cluster of pixels. In the SCT, a spacepoint is constructed by finding the intersection of the strips on the front and back sides of a module. Note that this intersection depends on the angle between the track and the module, because the front and back sides are about 1 mm apart. There is thus an inherent uncertainty in the reconstructed spacepoint (apart from the measurement resolution of the individual strip planes). Therefore the spacepoints are only used in the pattern recognition, while the fitting programs use the individual pixel and strip clusters. Both the clusters and the spacepoints are produced by the standard ATLAS reconstruction software (InDetPrepRawDataFormation and SiSpacePointFormation respectively).

The algorithm begins by checking how many modules have spacepoints in them. This number is the highest number of points that can be associated to a track, because only one point is allowed per track per module. The search begins for tracks with exactly this number of points. Sets of points are selected where every point lies in a different module, and fast fits are performed to decide if a set of points belongs to a track or not. For runs without magnetic field, two 2-dimensional straight line fits are performed and a χ^2 cut is performed to select 'good' tracks. If the magnet is switched on then the straight line fit in the bending plane is replaced by a circle search. This search takes the first, middle and last points of the point set, calculates the circle, and checks if the other points are within 0.7 mm of this circle. The cut of 0.7 mm was tuned such that 1 GeV tracks, which suffer from multiple scattering, are still reconstructed efficiently.

In order to keep the combinatorics down (without losing efficiency), the algorithm

performs intermediate fits with subsets of points. First it tries to fit the first three points of a given set. If the fit succeeds then it adds the fourth point, if the fit succeeds again then it adds the fifth point, etc. However, if the fit fails then all the combinations with the points that were fitted so far are skipped. In practice, the execution time remains acceptable up to a total of about 100 spacepoints. This is more than sufficient: events with so many points are very rare in the testbeam.

Sometimes it happens that only one side of an SCT module gives a strip hit. No spacepoint is reconstructed in that case, and a different approach is needed to find the strip. After a track has been found using the spacepoints, it is extrapolated to the SCT modules that have a 'hole' (i.e. no spacepoint) on the track. If a strip is closer than 0.7 mm to the track then it is added to the list of points on the track. If more than one strip satisfies this selection then the one closest to the track is chosen.

In practice it often happens that two or more track candidates share hits between them, especially when there are 'ganged' pixels in the event. Ganged pixels are pixels that share a readout channel with another pixel (this is done because the readout chips do not cover the entire sensor surface). Often a track passes the standard cuts with either hit, hence the extra track candidates. The next step in the pattern recognition solves these ambiguities, and disentangles these tracks. Given a set of tracks, it selects the track with the lowest χ^2, and removes all the tracks that share one or more points with that track. The procedure is repeated on the remaining tracks, until there are no more tracks left. Thus, the result is a set of tracks that don't share points anymore. Fig. 4.2 shows a simulated event where there were 12 track candidates that passed the standard cuts and selections, one can see that the ambiguity solver selects the correct one.

As already mentioned, the pattern recognition starts by searching for tracks with the highest number of points possible. The points that are assigned to a track are then flagged as 'in use' (if a point is a ganged pixel, then its ganged partner is also flagged), and the whole procedure is repeated on the remaining points, but this time the search looks for tracks with one point less. Thus, tracks with more points always get priority over tracks with fewer points. The track search stops when the minimum number of points on a track is reached, this minimum is currently set to be four spacepoints, or three spacepoints plus one SCT strip.

4.1.2 TRT pattern recognition

The pattern recognition in the TRT is done by a separate package called 'InDetCTB-Tracking'. It can use the extrapolated silicon tracks as seeds, but it can also perform a full scan of the whole TRT. We will first describe the former method.

Given a track from the pixel and SCT detectors, the track is first extrapolated to the TRT. The error on the extrapolated track is often large due to misalignments in the silicon detectors, and the large distance (about one meter) over which is extrapolated. At low energies (< 10 GeV) multiple scattering starts to play a role. Furthermore, the description of the magnetic field (field map) comes into play for runs where the magnet was switched on. As a result, the mismatch between the TRT hits and the extrapolated

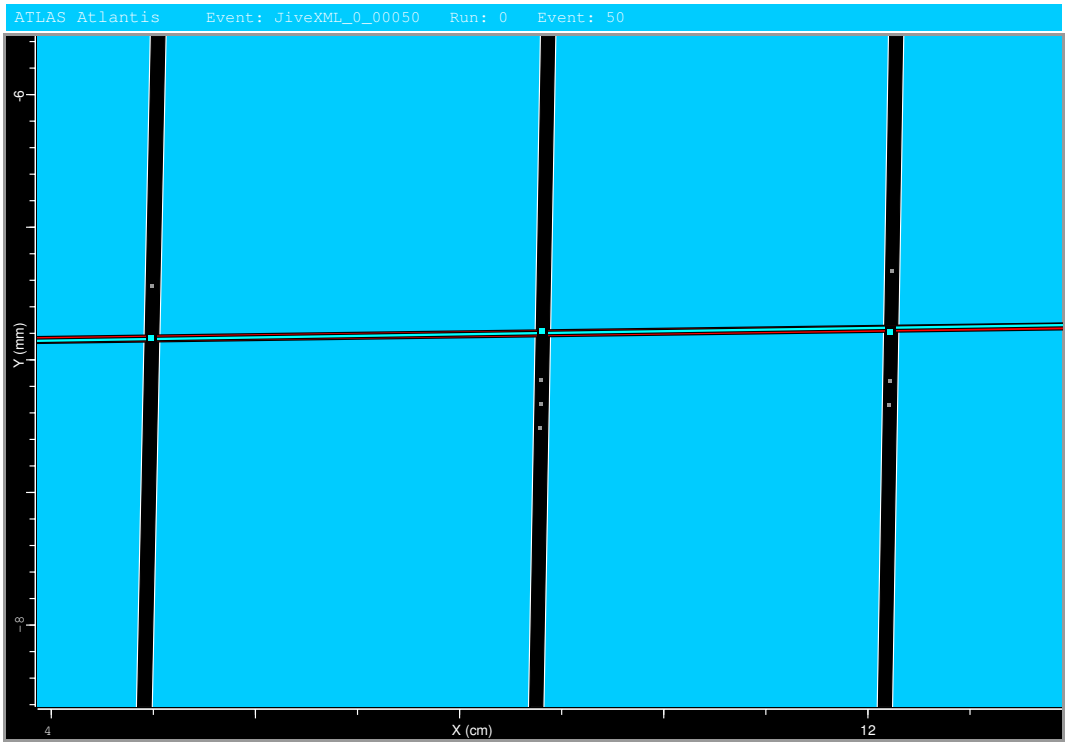

Figure 4.2: *A simulated event with ganged pixel ambiguities in all three pixel layers. Both the simulated and the reconstructed track are shown, one can see that they are right on top of each other.*

track is as large as a few millimeter, and sometimes up to a centimeter. Therefore the search window is taken to be quite large: TRT points that fall within 10 mm of the extrapolated track are collected for further processing.

The TRT points that are found near the track are first sorted along the beam direction. Then, the first and the last point are selected to form seeds. Given two drift circles, one can draw four straight lines that touch both circles (see Fig. 4.3). Four track candidates are built by determining the distance of the other points to each of these straight lines, if this distance is less than 1.5 mm then the point is added to the candidate track. The side (left or right) where the seed passes the point is also stored. For each candidate track a quality Q is computed, according to:

$$Q = N - w \sum \chi_i^2; \tag{4.1}$$

$$\chi_i^2 = \frac{r_i^2}{\sigma_i^2}. \tag{4.2}$$

Where N is the number of points on the candidate track, r_i is the distance between the point and the seed, σ_i is the measurement error of the point (taken to be 200 μm), and w is a weight factor that is set to 0.05. The track quality is thus a weighted sum of the number of hits and the χ^2: more hits means a better (higher) quality Q, but only

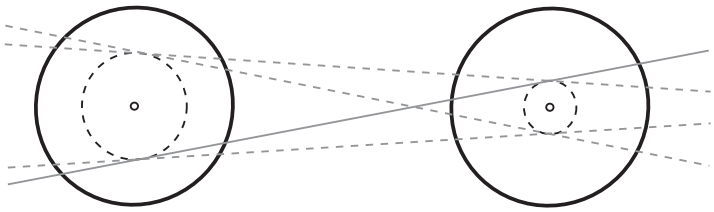

Figure 4.3: *Given two drift circles, there are four possible paths that traverse both drift circles. The reconstruction has to decide for each hit on which side of the wire (left or right) the particle went.*

if the χ^2 does not become unreasonably large. In practice this works better than solely cutting on the number of hits or on the χ^2, particularly in events with showers.

The two largest contributions to the χ^2 in Eq. (4.2) are removed, this is done to make sure that Q is not dominated by one or two points. The candidate with the best quality has to pass the following cuts:

- At least 25 points in the testbeam, 20 in the cosmics;
- $\frac{\chi^2_{tot}}{N-4} < 15$.

Where $\chi^2_{tot} = \sum \chi^2_i$. If none of the candidates passes these cuts, the next pair of points is selected. If a track is found then the algorithm continues the search with 25 more point pairs, to see if perhaps a better track can be found. The points that belong to the best track are then removed and the track finding algorithm is repeated on the remaining points, until no more tracks are found. Finally, the track that is closest to the extrapolated silicon track is selected.

Sometimes it happens that there are two or more tracks in the TRT, due to interactions of the particle with the detector material. The best that the pattern recognition can do is to select the one that is closest to the extrapolated track. But this can actually be the wrong choice if the detector is misaligned. Therefore, CTBTracking requires an isolated track in the TRT: if there are more than 70 hits within 10 mm of the extrapolated track then the search is aborted.

If the pattern recognition in the TRT starts without a seed from the silicon detectors, the scan is performed in two steps. First, the algorithm tries to find a track using all the points in the TRT. If it has found a track, the algorithm is run again on the points that fall within 10 mm of this initial candidate. As before, the points that belong to the best track are removed from the search, and the search continues with the remaining points until no more tracks are found. The tracks can optionally be extrapolated into the SCT, and SCT points can be added to the track. In the testbeam this association may fail if a magnetic field is present, as the TRT track has no momentum information.

Fig. 4.4 shows a real testbeam event where the track search started in the TRT. In the figure, the hits that belong to a track according to the tracking are drawn thicker

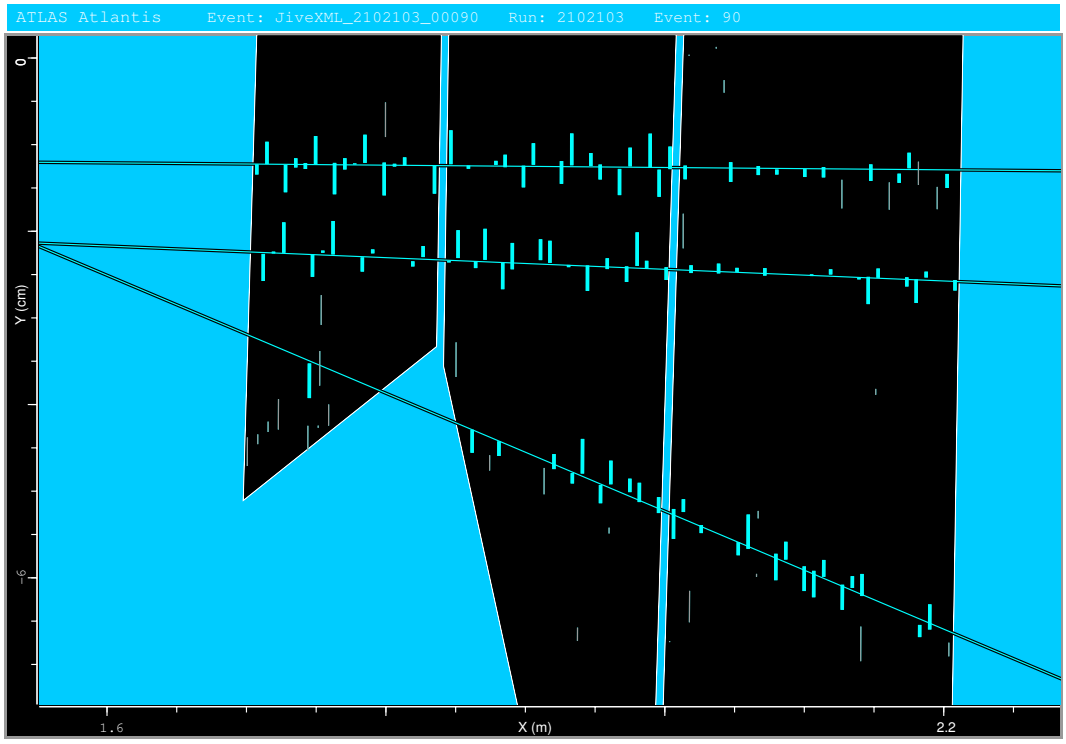

Figure 4.4: *A testbeam event (real data) with only TRT points, showing three reconstructed tracks.*

and brighter than the other hits. The two-track resolution and the noise rejection are seen to be quite good. Figs. 4.5 and 4.6 show two testbeam events (real data) where the tracking started from the pixel and SCT detectors. Finally, Fig. 4.7 shows an actually recorded cosmic event in the SR1 assembly building (see also section 4.3).

4.1.3 Pattern recognition performance

In this section we show results from the pattern recognition algorithms, using both simulated and real data. The simulated events were produced using the CTB_G4Sim package, which uses GEANT4 to perform the actual simulation of tracks. In the simulation the detector was assumed to be perfectly aligned and calibrated, and the magnetic field was assumed to be 1.4 Tesla (i.e. constant) in the volume that holds the pixel and SCT detectors, and zero outside. The origin of the coordinate system was moved from the beginning of the magnet to the beginning of the pixel box, to make the setup more similar to ATLAS.

Fig. 4.8 shows the number of tracks and the number of hits per track in real and in simulated testbeam data, using run 2102355 (100 GeV pions, no magnetic field). Only the events with at least one pixel spacepoint are used. About half of the tracks have seven SCT clusters instead of eight, this is because the back side of one module was not working. About 10% of the tracks don't have TRT points, this is mostly because of

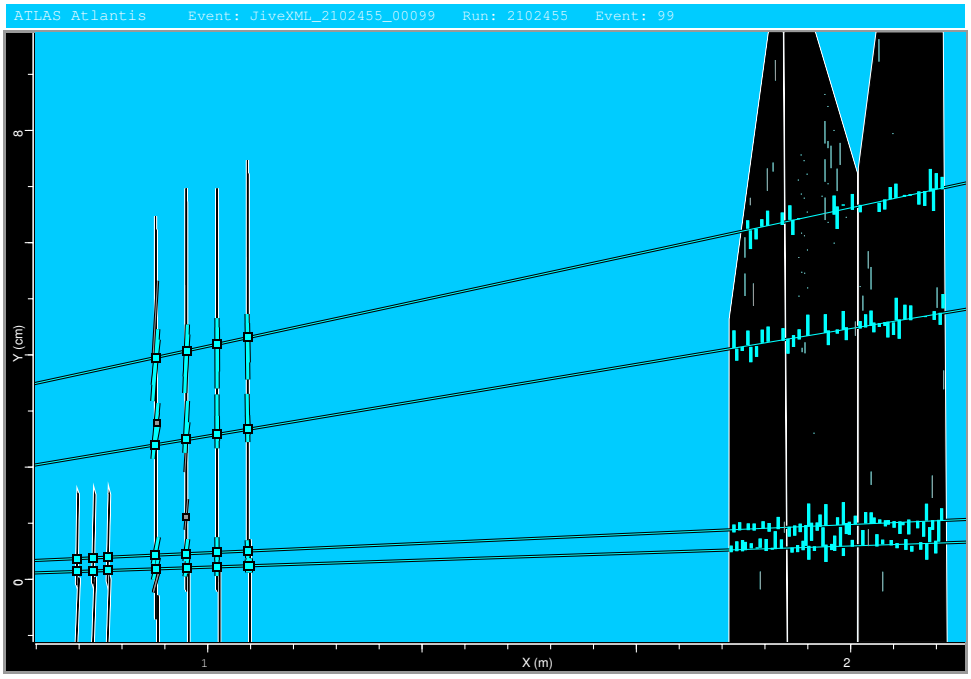

Figure 4.5: *A testbeam event (real data), showing four reconstructed tracks.*

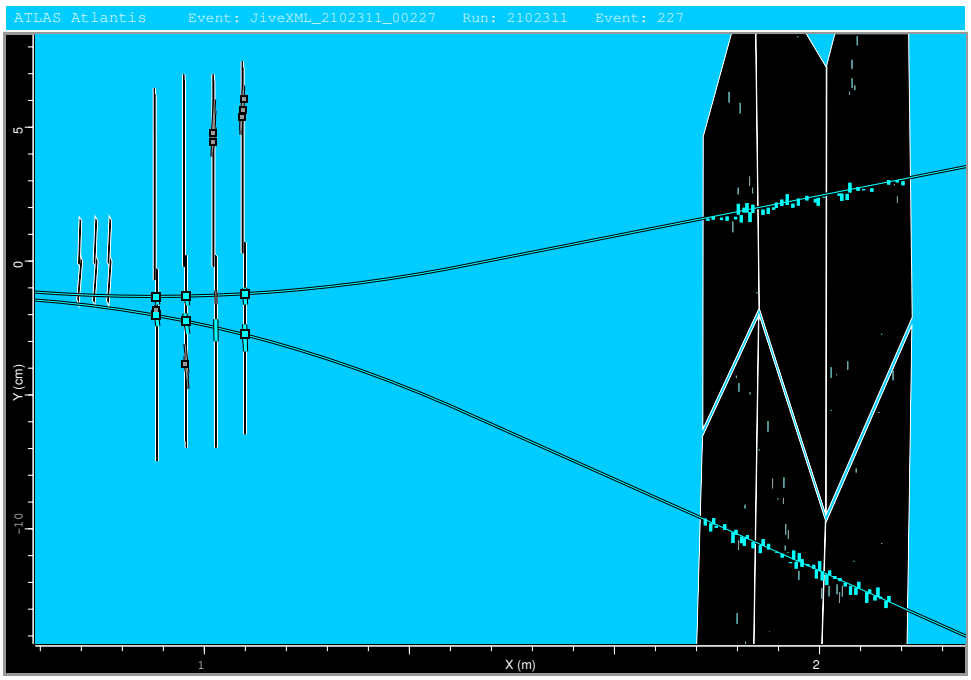

Figure 4.6: *A testbeam event from real data, showing two reconstructed tracks with opposite charge.*

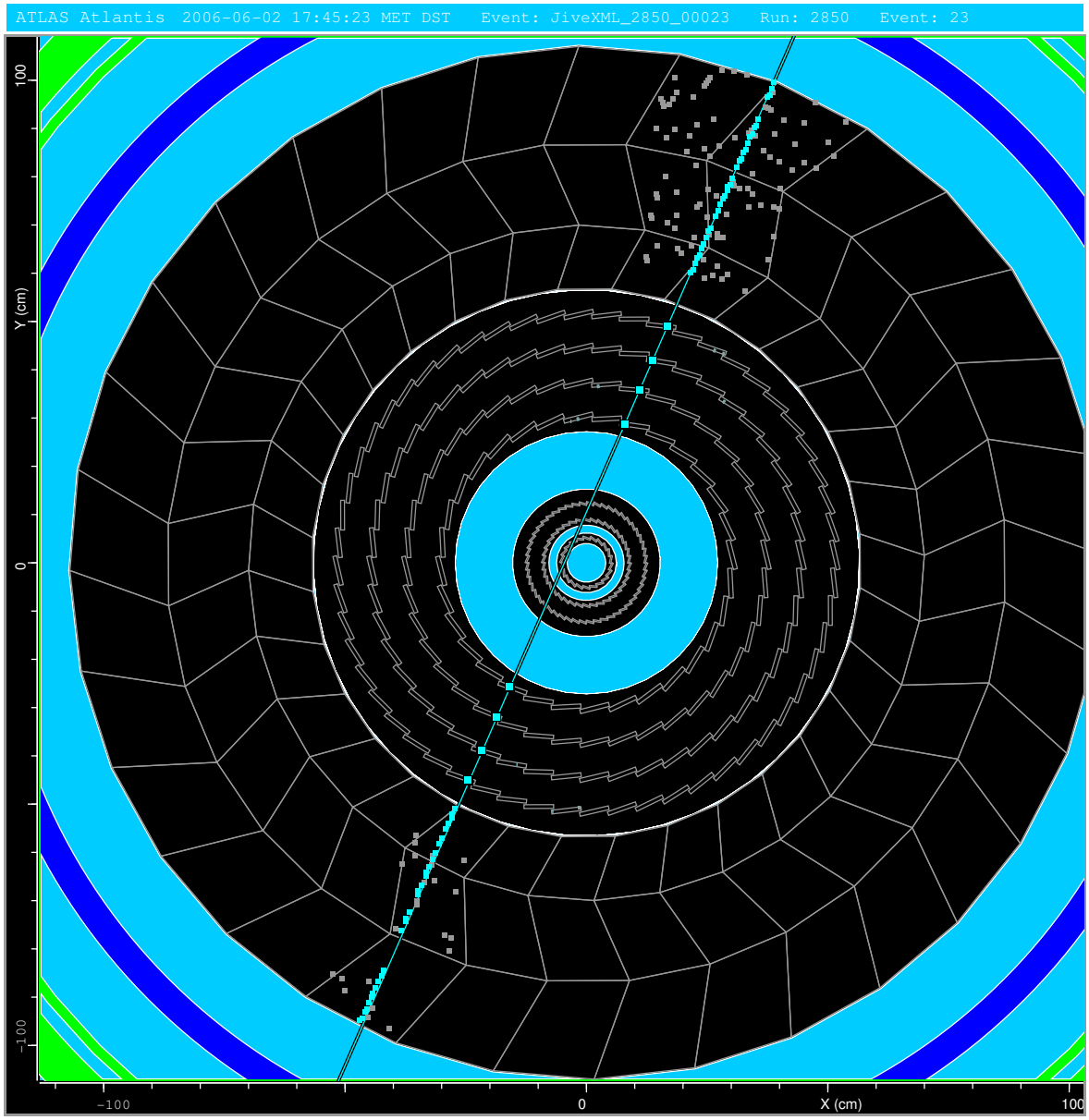

Figure 4.7: *A real cosmic event with TRT and SCT points, showing one reconstructed track.*

showers that are not reconstructed. Also, sometimes there are secondary particles that miss the TRT altogether. The agreement between data and simulation is fairly good, except that the number of TRT points per track is slightly lower in the data than in the simulation. This is probably because the channels that are found to be dead in the data are not masked in the simulation.

Fig. 4.9 shows the track finding efficiency for simulated muons and pions, both for CTBTracking and for the xKalman reconstruction program. Here, efficiency is defined as having a track where both the momentum and the impact parameter are within 5σ

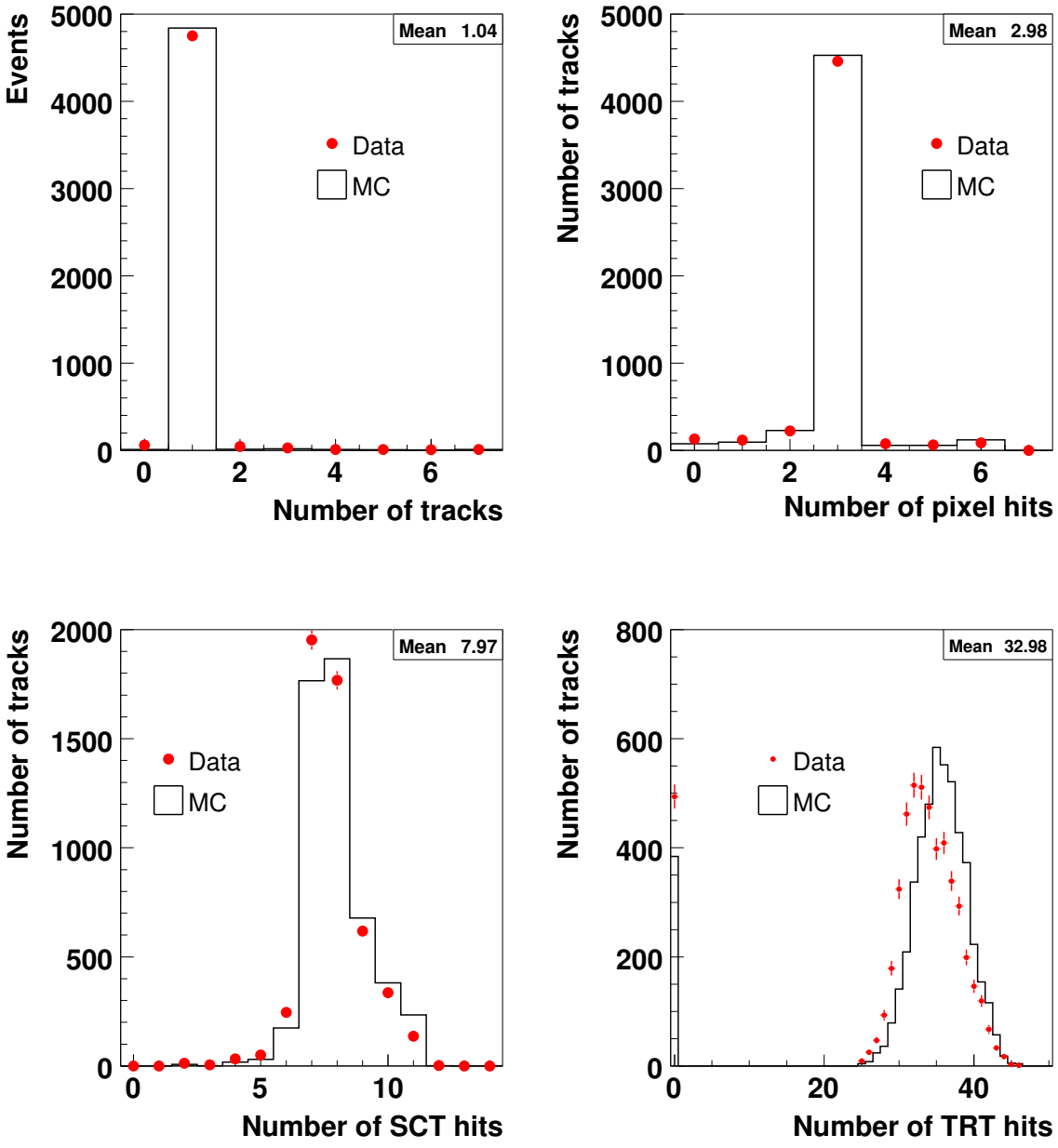

Figure 4.8: *Number of tracks and number of pixel, SCT and TRT hits per track in run 2102355 of the testbeam, for real and simulated data. The quoted mean values correspond to the simulated data.*

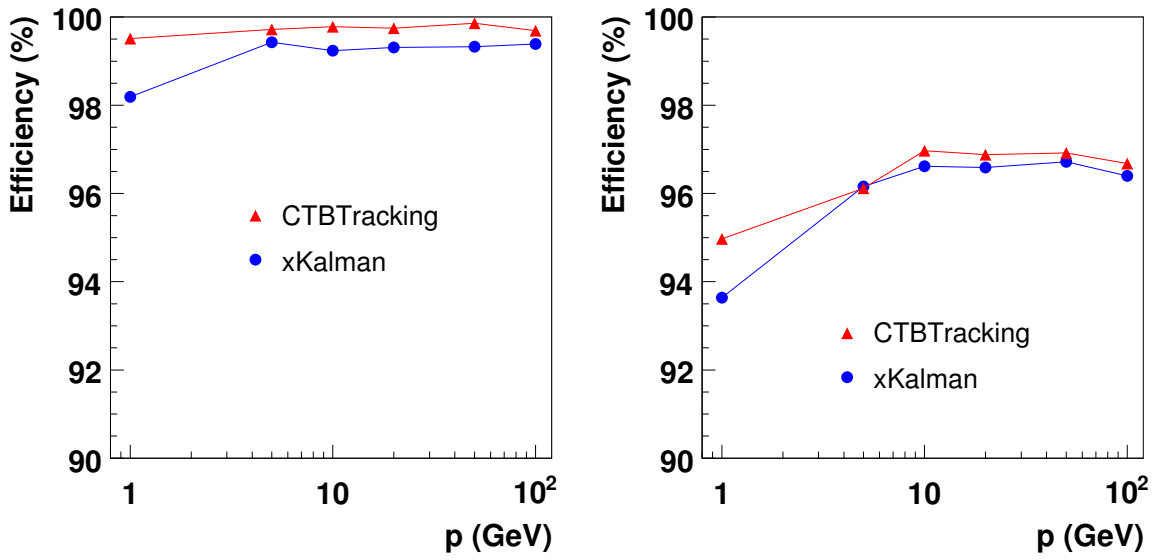

Figure 4.9: *Track finding efficiencies for CTBTracking and xKalman, using muons (left) and pions (right).*

of the true value[1]. The efficiency for finding muons is more than 99.5% in the case of CTBTracking. The remaining 0.5% of the events have a track where an ambiguity in the pixel detector was resolved incorrectly. If these events are also counted, the efficiency is practically 100%. The fake rate is negligible. xKalman achieves a lower efficiency with muons, most likely it needs more tuning for the testbeam setup.

When running with pions, the efficiency of both xKalman and CTBTracking drops to around 95%. This drop of efficiency is inevitable, mostly due to nuclear interactions of the pion with the detector material. The number of tracks reconstructed by CTBTracking that cannot be associated to the primary particle is around 5%. Inspection of the events with the event display shows that most of these tracks are secondaries resulting from the nuclear interactions.

4.2 Track fitting

The pattern recognition produces a list of hits on a track, and an estimate of the track parameters of the particle. From there, the track fit has to compute the best possible estimate of the track parameters. For CTBTracking a global χ^2 minimization algorithm was chosen for the track fit. This algorithm has a number of advantages:

- It only needs an initial estimate of the track parameters, not of their errors. The initialization of the covariance matrix is a delicate point in the Kalman fit.

[1]This requires that the track *fit* also works correctly. Still, the efficiency is mainly determined by the pattern recognition.

- It solves the left/right ambiguities in drift circle hits. For example, if the pattern recognition accidentally chooses the wrong solution then the track fit can correct it.

- The global χ^2 fit yields the scattering angles on the track, which can e.g. be used in alignment procedures.

The track fit in CTBTracking can correct for multiple scattering and energy loss (both Bethe-Bloch and Bethe-Heitler energy loss corrections), provided that a material description is available. Furthermore it is independent of detector technology, i.e. it can use hits from any tracking detector in ATLAS, in any setup. The fit is currently operational for the testbeam data, the cosmic ray data, and full physics events in ATLAS. We will show the performance of the fit in each of these setups in this chapter. We will first discuss the implementation of the global χ^2 fit algorithm. Section 4.2.3 deals with the performance of the fit using simulated data.

4.2.1 The global χ^2 fit algorithm

General least squares fitting theory in track fitting is discussed in several books (e.g. [51]). The χ^2 function to be minimized is:

$$\chi^2 = \sum_{i=1}^{N} \frac{r_i^2}{\sigma_i^2}. \tag{4.3}$$

Where r_i are the *residuals* (i.e. the difference between the measurement position and the position as predicted by the track), and σ_i their errors. The Gauss-Markov theorem states that minimizing Eq. (4.3) is the optimal algorithm, i.e. no algorithm can do better, if the residuals r_i are distributed according to Gaussians. In practice this is not always the case, in that case it is just the optimal linear algorithm.

We will first discuss the definitions of the track parameters and the residuals in the fit. Then we will briefly discuss the update formula that minimizes Eq. (4.3).

Track parameters

The CTB track fit uses the same track parameter definitions as the other tools in the Tracking realm [52]. Fig. 4.10 shows the definition of the track parameters at the reference point, called 'perigee'. It is the point of closest approach to the z-axis. ϕ_0 is the angle in the x-y plane at this point, and θ_0 is the angle with the z-axis. d_0 is the signed distance to the z-axis, it is defined to be positive when the direction of the track is clockwise with respect to the origin. z_0 is the z-coordinate of the perigee. The fifth parameter is q/p, the charge of the particle divided by the momentum. Obviously, this last parameter only plays a role for curved tracks.

If material corrections are enabled then the list of track parameters is extended with two scattering angles and (optionally) an energy loss parameter, for each scattering plane. This is discussed in section 4.2.2.

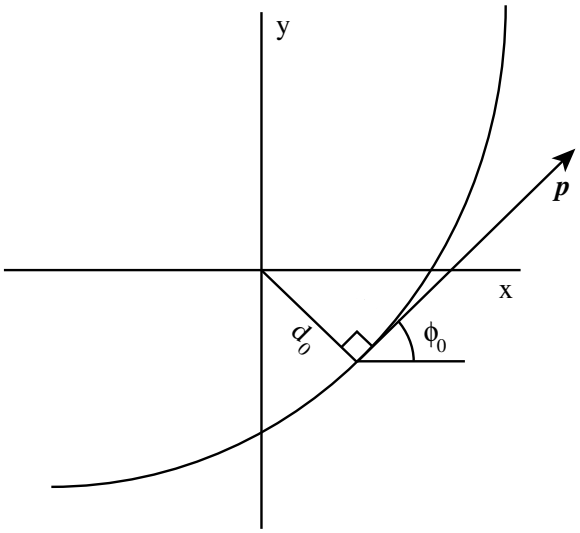

Figure 4.10: *Track parameter definitions near the origin.*

Detector	Type	Resolution
Pixel	Strip cluster	10 μm
SCT	Strip cluster	20 μm
RPC	Strip cluster	1 cm
TGC	Strip cluster	1 cm
CSC	Strip cluster	50 μm
TRT	Drift circle	170 μm
MDT	Drift circle	80 μm

Table 4.1: *Tracking technologies in ATLAS, and their treatment in the track fit. The resolutions given are averages, the actual resolution varies from hit to hit (e.g. depending on the local strip pitch).*

Residuals

The residual is the difference between the track prediction and the hit. From the point of view of the track fit, a hit is either a strip cluster or a drift circle. Table 4.1 shows how all the different tracking technologies in ATLAS are treated in the fit. All the hits are treated as 1-dimensional measurements, except for the pixel hits, which are split into two 1-dimensional measurements in the fit.

The cluster hits have a plane surface associated with them that describes the sensor surface. The residual is the distance between the intersection of the track with the plane and the middle of the cluster. If $\vec{m}_i$ is the position of the center of the strip, $\vec{t}$ is the intersection of the track with the surface, and $\hat{\phi}$ is a unit vector parallel to the surface and perpendicular to the strip, then the residual is:

$$r = (\vec{t} - \vec{m}_i) \cdot \hat{\phi}. \tag{4.4}$$

The drift circle hits have a straight line surface that describes the wire. If R_{track} is the distance from the track to the wire, and R_{drift} is the drift radius of the hit, then the residual is:

$$r = R_{track} - R_{drift}. \tag{4.5}$$

Both R_{drift} and R_{track} are signed quantities, the sign decides the side (left/right) where the track passes the wire. Alternatively, the residual can be defined as:

$$r = |R_{track}| - |R_{drift}|. \tag{4.6}$$

Both definitions can be used in the CTB track fit, the default being the latter. The advantage of the second definition is that the pattern recognition does not need to resolve the left/right ambiguities of the hits, only the absolute value of the radius counts. If the pattern recognition does resolve these ambiguities then the track fit can correct possible mistakes that the pattern recognition makes. A possible danger is that the residual reaches a minimum on either side of the hit. The possible local minima in the χ^2 that this can cause should be avoided by starting the fit reasonably close to the global minimum. No failed fits have been observed in CTBTracking that were caused by this sign ambiguity.

In order to calculate the residuals, the track fit uses a propagator tool (section 3.4). This tool transports the track parameters at the vertex to a measurement, or from one measurement to another. The residual is then the difference between the measurement and the propagated track. The CTB track fit can use several different propagators, such as the StraightLinePropagator and the RungeKuttaPropagator. The StraightLinePropagator performs the propagation analytically, assuming that the particle is not deflected by a magnetic field. The track fit selects the RungeKuttaPropagator if a magnetic field is present, this tool approximates the trajectory numerically. Contrary to the Kalman fit, the global χ^2 fit only needs to propagate the track parameters themselves, not their errors.

Residual derivatives

The track fit needs to evaluate the derivatives of the residuals with respect to the track parameters. The derivatives can be calculated either analytically or numerically. The numerical derivatives are mainly used to cross-check the analytical expressions. They are calculated as follows:

$$\frac{\partial r(\vec{\alpha})}{\partial \alpha_i} \approx \frac{r(\alpha_i + \epsilon) - r(\alpha_i - \epsilon)}{2\epsilon}. \tag{4.7}$$

Where $\vec{\alpha}$ are the track parameters. The error on this expression is in principle of order ϵ^2, but in practice the accuracy of the propagator can also introduce errors. Careful tuning of ϵ and of the propagator is required to obtain a stable track fit.

Momentum derivatives are always calculated numerically. For the other derivatives it is also possible to derive analytical expressions, under the assumption that the track does not deform too much for small changes in offset and direction. These expressions do not require additional propagations, unlike Eq. (4.7), and are therefore much faster. The derivations of the expressions are presented in appendix A.

Track errors

Given the residual derivatives and the covariance matrix V_α of the track parameters, it is possible to estimate the error of the track at each hit, in local hit coordinates. It is given by:

$$\begin{aligned}\sigma^2_{track} &= \left(\frac{\partial r}{\partial \vec{\alpha}}\right)^T V_\alpha \frac{\partial r}{\partial \vec{\alpha}} \\ &= \left(\frac{\partial r}{\partial \alpha_1} \quad \frac{\partial r}{\partial \alpha_2} \quad \dots\right) \begin{pmatrix} \delta\alpha_1\delta\alpha_1 & \delta\alpha_1\delta\alpha_2 & \dots \\ \delta\alpha_2\delta\alpha_1 & \delta\alpha_2\delta\alpha_2 & \dots \\ \vdots & \vdots & \ddots \end{pmatrix} \begin{pmatrix} \frac{\partial r}{\partial \alpha_1} \\ \frac{\partial r}{\partial \alpha_2} \\ \vdots \end{pmatrix}. \end{aligned} \tag{4.8}$$

The tracking error can be used to calculate an unbiased residual, i.e. a residual where the hit does not participate in the track fit. This is useful e.g. for validating the fit (section 4.2.3).

Update formula

Given the residuals and their derivatives, it is possible to calculate the track parameters that minimize the χ^2 function, using the update formula. This formula is derived by linearizing the χ^2 function, i.e. the residuals are assumed to depend linearly on the track parameters. This assumption is correct for small changes in the track parameters. The update formula for the track parameters is then:

$$\sum_{l=1}^{M} a_{kl}\, \Delta\alpha_l = b_k; \tag{4.9}$$

$$a_{kl} = \sum_{i=1}^{N} \frac{1}{\sigma_i^2} \cdot \frac{\partial r_i(\vec{\alpha})}{\partial \alpha_k} \cdot \frac{\partial r_i(\vec{\alpha})}{\partial \alpha_l}; \tag{4.10}$$

$$b_k = \sum_{i=1}^{N} \frac{1}{\sigma_i^2} \cdot r_i(\vec{\alpha}) \cdot \frac{\partial r_i(\vec{\alpha})}{\partial \alpha_k}. \tag{4.11}$$

Where $\Delta\alpha_l$ is the difference between the old and the new track parameter α_l. It can be shown that the matrix a is the inverse of V_α, the covariance matrix of the track parameters.

The CTB track fit has the option to use a slightly modified update formula, called the Levenberg-Marquardt method (see e.g. [53]). This minimization method is better behaved if the fit starts far away from the minimum. Here the matrix elements a_{kl} are replaced by the matrix elements a'_{kl}:

$$a'_{kl} = a_{kl}(1 + \delta_{kl}\lambda). \tag{4.12}$$

Where δ_{kl} is the Kronecker delta, and λ is a fudge parameter that regulates the step size.

4.2.2 Correcting for material effects

The CTB track fit is able to correct for material interactions like multiple scattering and energy loss, provided that a material description is available. The track fit has a hand-coded description of the material in the testbeam setup. The material is described with thin scattering planes. The thickness of the layer represents the amount of material in the layer, it is described in terms of radiation lengths. The material description in the track fit has the following layers:

- One scattering plane per pixel layer, each with 2.3% X_0;
- One scattering plane per SCT layer (four in total), each with 1.25% X_0;
- Three scattering planes in the TRT, each with 4.3% X_0;
- One scattering plane between the pixels and the SCT and between the SCT and TRT, with 11% and 22% of a radiation length, respectively.

The planes between the pixels and SCT and between the SCT and TRT are meant to describe the extra material that was inserted in part of the testbeam runs. These extra planes are omitted if a run was chosen that does not have this extra material.

Multiple scattering

Given the material description with scattering planes, it is possible to estimate and fit the multiple scattering and energy loss at each of these planes.

In a material layer with thickness x and radiation length X_0, the distribution of scattering angles for a particle with momentum p, charge number Z' and velocity βc can be approximated with a Gaussian with an R.M.S. given by [54]:

$$\sigma_{scat} = \frac{13.6 \text{ MeV}}{\beta c p} Z' \sqrt{\frac{x}{X_0}} \left(1 + 0.038 \ln \frac{x}{X_0}\right). \tag{4.13}$$

This equation is known as the Highland form, it is accurate within 11% for the range $0.001 < \frac{x}{X_0} < 100$. More accurate formulas exist, but Eq. (4.13) is accurate enough for practical purposes.

The scattering angle formulation of the track fit was first proposed by Poppleton [27, 55]. The fit treats multiple scattering by allowing the track to change its direction at each scattering plane. At each plane there are two angles, θ_{scat} and ϕ_{scat}, that become extra fit parameters in the fit. In addition, they contribute to the χ^2 just like ordinary measurements:

$$\chi^2 = \sum_{meas} \frac{r^2_{meas}}{\sigma^2_{meas}} + \sum_{scat} \left(\frac{\theta^2_{scat}}{\sigma^2_{scat}} + \frac{(\sin \theta_{loc})^2 \phi^2_{scat}}{\sigma^2_{scat}} \right). \tag{4.14}$$

The first sum runs over all the 'real' measurements, while the second sum runs over all the scattering planes in the fit. θ_{loc} is the angle between the track and the z-axis at the scattering plane, the factor $\sin\theta_{loc}$ is needed because ϕ_{scat} is defined in the x-y plane (i.e. it is a projection of the actual scattering angle).

In addition to the change in the direction, the track is displaced with an R.M.S. given by:

$$\sigma_{disp} = \frac{x}{\sqrt{3}}\sigma_{scat}. \tag{4.15}$$

The scattering angle and the displacement are correlated (the correlation coefficient ρ is $\sqrt{3}/2$). The material layers in the inner detector are so thin that the displacement can be ignored. In other places (e.g. the calorimeter) one has to allow both the angle and the displacement of the track to change, or place two scattering planes where only the angle is allowed to change. One can show that the two approaches are equivalent.

Energy loss

Charged particles lose energy through ionization when they traverse material. The average energy loss per unit length due to ionization is described by the Bethe-Bloch formula. In the CTB track fit, the energy loss in a material layer with thickness dx and radiation length X_0 is approximated by:

$$-\frac{dE}{dx} = \frac{C_{ion}}{X_0}. \tag{4.16}$$

C_{ion} is a constant of about 50 MeV [56]. The fluctuations in the energy loss are small in the inner detector and can be ignored. If the fluctuations are large, e.g. in the calorimeter, then the energy loss has to become an additional free fit parameter.

4.2.3 Validating the fit

This section shows the results of testing the track fit on simulated testbeam data. It should be noted that the results in this section actually show the combined performance of the pattern recognition and track fit algorithms. Problems in either of these affect the final result of the fit.

Hit errors

The track fit needs an accurate error estimate for each measurement to obtain an optimal result. Currently the pixel and SCT errors in the fit are equal to $\frac{p}{\sqrt{12}}$, where p is the length or width of a pixel (400 microns[2] or 50 microns respectively), or the width of an SCT strip (around 80 microns). The error used for the TRT is 170 microns.

The hit errors can be checked by calculating a *pull* for each hit:

$$pull = \frac{r}{\sqrt{\sigma^2_{meas} + \sigma^2_{track}}}. \tag{4.17}$$

[2]Some pixels have a length of 600 microns ('long' pixels).

Where r is the residual, σ_{meas} is the estimated measurement error, and σ_{track} is the track error at the hit (Eq. (4.8)). The residual needs to be an *unbiased* residual, i.e. the hit should not participate in the track fit. This is achieved by removing the hit from the track using the Kalman updator formalism [57], and then calculating the distance between the resulting track and the hit.

If the errors are estimated correctly then the distribution of pull values should have mean 0 and R.M.S. equal to 1. Fig. 4.11 shows the pulls of the pixel, SCT and TRT hits, using simulated muons of 5 GeV. The pixel modules measure two coordinates at the same time, therefore two separate pull distributions are presented. All the plots have an R.M.S. close to 1, although the pixel ϕ errors appear to be somewhat overestimated. The pixel η pulls show strong discretization effects, due to the binary readout and because the SCT and TRT don't measure η. The CTB track fit has an outlier cut for drift circles that is set to 3σ for simulated data, this removes most of the tails in the TRT pull distribution. Tails are common in the TRT, they are caused by large fluctuations on the drift radius close to the wire, and by delta electrons[3] that mask the primary hit. The pattern recognition in CTBTracking has a loose cut of 1.5 mm in the TRT, therefore these hits have to be removed in the track fitting stage.

Track parameter pulls and resolutions

A measure of the reliability of the track fit are the pull distributions of the track parameters. The pull is defined as the difference between the reconstructed and the true track parameter, divided by the estimated error on the reconstructed parameter. Fig. 4.12 shows the pull distributions of the five track parameters at the origin, for simulated muons of 5 GeV. All the distributions are Gaussian with a width close to 1, which indicates that the errors are correctly estimated. Thus, the material in the setup appears to be understood to within a few percent in the track fit. The pulls of ϕ_0 and q/p are slightly offset from zero. These shifts become larger at higher momentum: at 100 GeV, the momenta are systematically underestimated by about 1%. Possible causes for this are: differences in the transport of track parameters in simulation and reconstruction, and/or systematic shifts of the positions of the hits in the reconstruction.

The resolutions of the track parameters (impact parameter and momentum) are shown in Fig. 4.13. The data points are the result of a single Gaussian fit to the distributions at each energy. xKalman and CTBTracking agree very well on the impact parameter, but CTBTracking obtains a somewhat better momentum resolution at 1 GeV and at 100 GeV. This shows that CTBTracking has apparently received more tuning for the testbeam setup than xKalman. Note that the 1 GeV muons don't go through the acceptance of the TRT due to the magnetic field, this explains the worse momentum resolution compared to e.g. 5 GeV muons.

Fig. 4.14 shows the track parameter resolutions when extra material is included between the pixels and SCT, and between the SCT and TRT. CTBTracking clearly outperforms xKalman at low momentum, because it corrects for the extra material.

[3]Delta electrons are produced in interactions between the primary particle and the detector material.

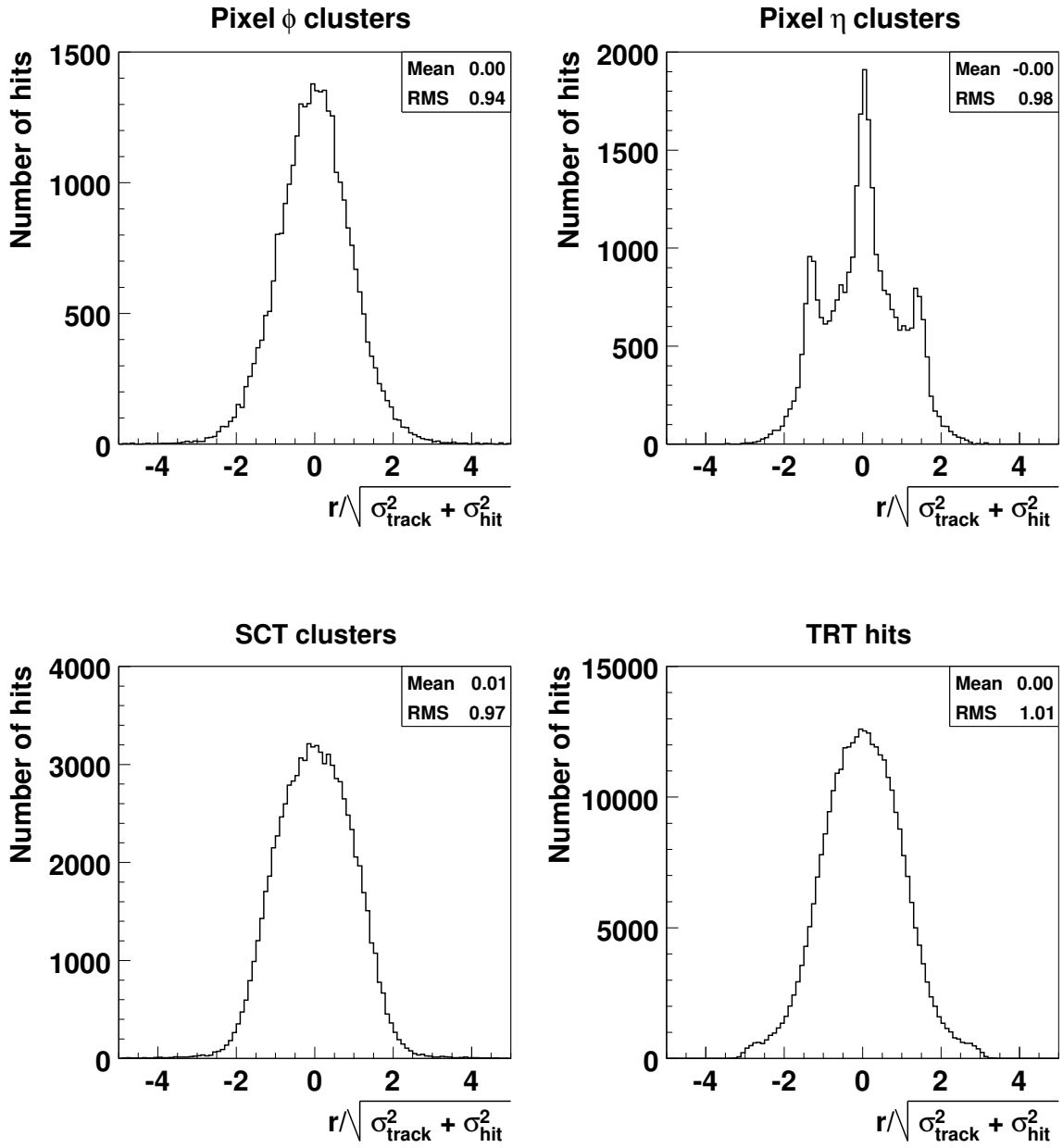

Figure 4.11: *Pull distributions of the measurements in the track fit, using simulated 5 GeV muons. ϕ and η correspond with the precision coordinate and the second coordinate in the pixel sensors, respectively. A simple $\frac{pitch}{\sqrt{12}}$ is used for the pixel and SCT errors, for the TRT an error of 170 microns is used.*

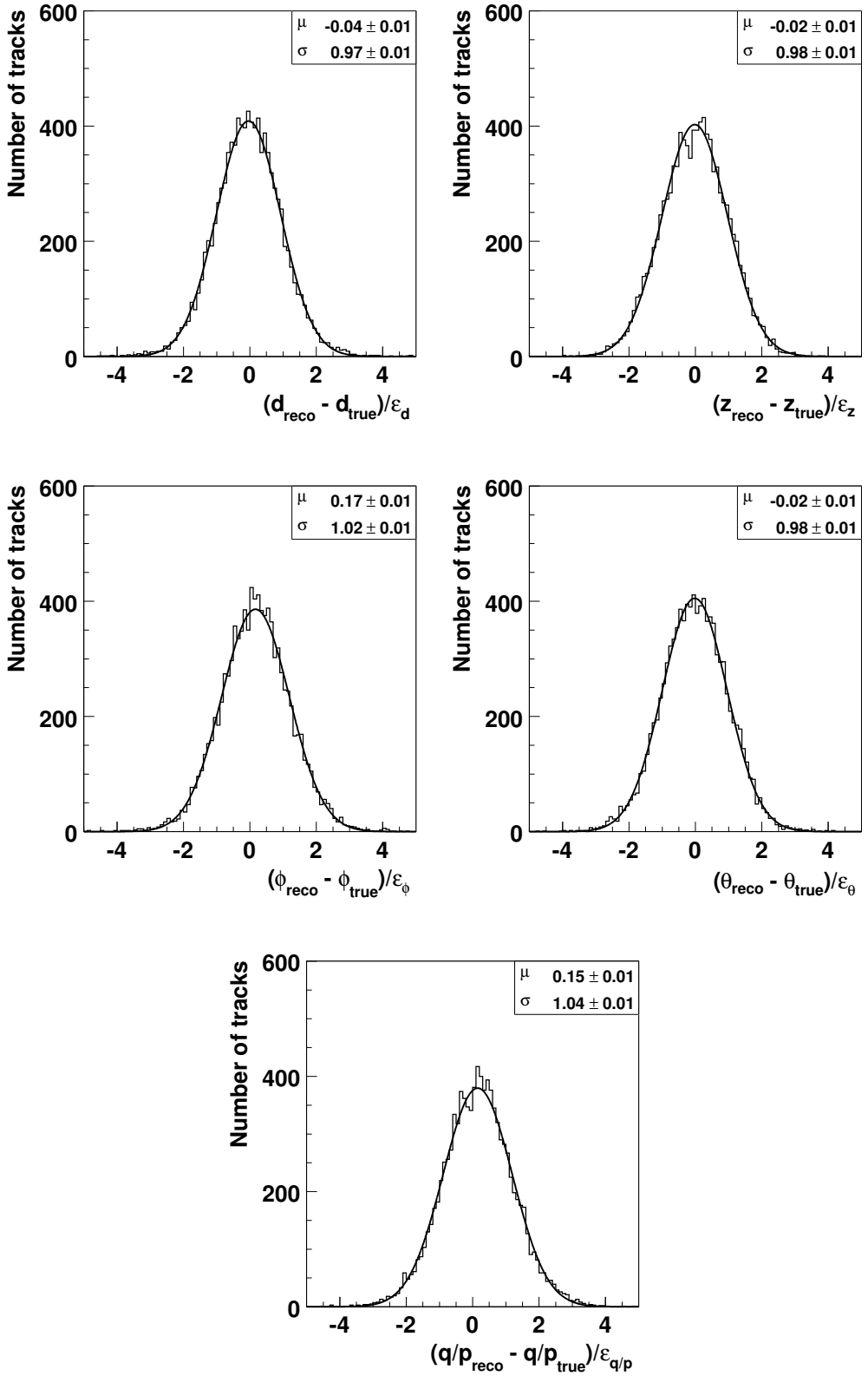

Figure 4.12: *Pull distributions of the track parameters at the vertex, for simulated 5 GeV muons. All the distributions are fitted with a single Gaussian.*

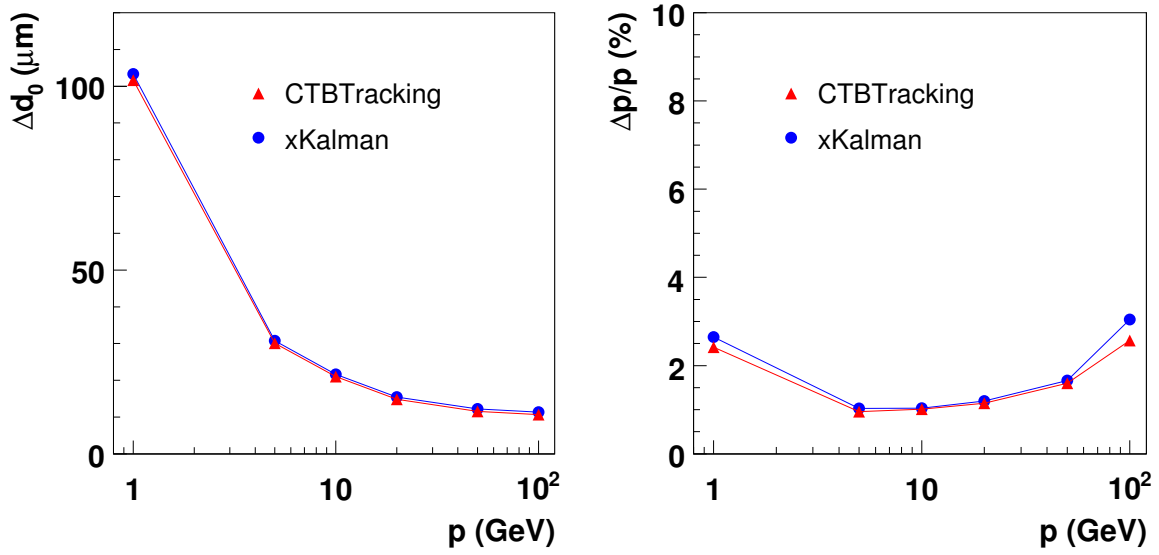

Figure 4.13: *Resolutions of the impact parameter (left) and momentum (right) using simulated single muons, for CTBTracking and xKalman.*

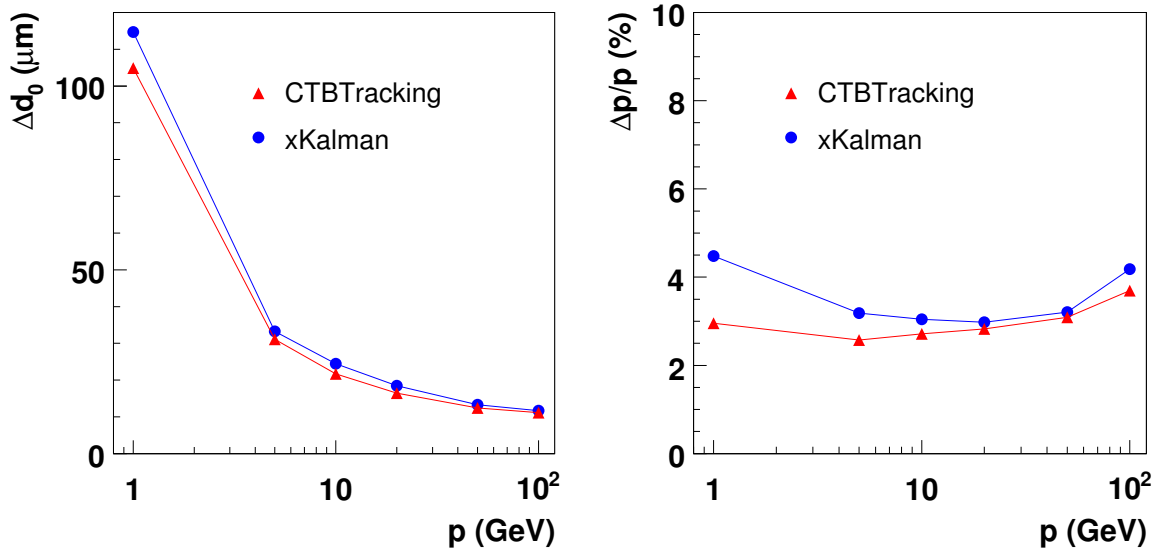

Figure 4.14: *Resolutions of the impact parameter (left) and momentum (right) using simulated single muons, for CTBTracking and xKalman, with extra material in the setup.*

xKalman uses a hardwired material description for ATLAS, hence it does not 'know' about the extra material in the testbeam. xKalman and CTBTracking agree more closely at higher momentum, because multiple scattering plays a less important role there. However, at 100 GeV there is again a difference in the momentum resolution.

Execution speed

The pattern recognition and track fit in CTBTracking have been speed optimized such that they don't form a bottleneck in the reconstruction of testbeam and cosmic ray data. In the testbeam the whole tracking requires about 30 ms per event. Most of the time is spent in the propagation of track parameters through the magnetic field. Events with cosmics take around 10 ms if the tracking starts from the SCT, and 30 ms if it starts from the TRT. All these times are less than the time spent in the data preparation algorithms. Hence, speed optimization efforts should focus on these algorithms rather than on the tracking.

The execution speed of the CTB track fit was compared to the Kalman fitter in the testbeam, by refitting xKalman tracks with both fitters. The Kalman fitter (run without material corrections) needed 5 milliseconds per track, while the CTB track fit needed 9 (17) milliseconds per track when run without (with) material corrections. It is often said that the Kalman fit is a fast algorithm because it does not need to invert large matrices. The comparison shows that the CTB fitter is indeed slower, especially when the material corrections are enabled. The size of the matrix in the CTB fitter is 5×5 without material corrections, and (in this particular run) 29×29 when material corrections are enabled (12 scattering planes times two, plus five track parameters at the origin). At this point it is not clear if the slower performance is due to the matrix, or due to other factors. For example, the fit needs to compute additional derivatives if material corrections are enabled.

The speed of the fit will have to be revisited when it is run on ATLAS events, where there are many tracks per event. For the testbeam and the cosmics we conclude that the fit is fast enough.

4.2.4 The electron fit

For an electron with an energy above a few tens of MeV, the main source of energy loss is Bremsstrahlung. This energy loss is described by the Bethe-Heitler distribution (Fig. 4.15) [58]. Both the average energy loss and the fluctuations are much larger than the ionization energy losses that e.g. muons or pions experience. Therefore electrons need a different treatment in the fit.

The large fluctuations in the energy loss make it impossible to achieve a similar momentum resolution as with muons and pions. In addition, the Bethe-Heitler distribution is highly non-Gaussian, which means that the least squares fit is not the optimal fit algorithm. In the track fit the distribution is approximated with a Gaussian that has the same mean and R.M.S. as the actual distribution. The mean and R.M.S. of the

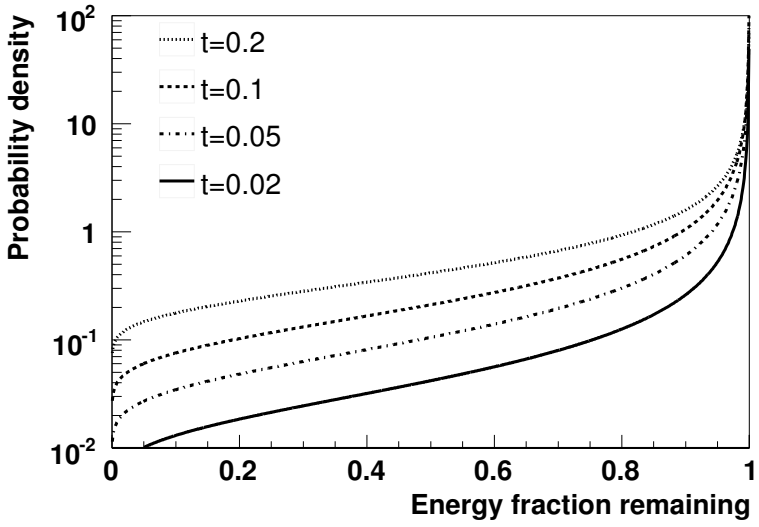

Figure 4.15: *The Bethe-Heitler distribution, which describes the energy loss of an electron when it traverses a material layer. t is the thickness of the layer in radiation lengths, i.e. $t = \frac{x}{X_0}$, with x the thickness in mm, and X_0 the radiation length in mm.*

Bethe-Heitler distribution are given by:

$$\mu = e^{-t}; \tag{4.18}$$

$$\sigma^2 = e^{-t\frac{\ln 3}{\ln 2}} - e^{-2t}. \tag{4.19}$$

Where $t = x/X_0$. The electron fit in CTBTracking works as follows:

- At material layers that represent pixel, SCT or TRT material the energy is lowered according to the average value (Eq. (4.18));
- At material layers that represent extra material, the energy loss becomes a free parameter in the fit.

The energy loss is allowed to change in the extra material because the fluctuations are the largest there. In principle one could allow the energy to change at all the material layers in the fit, but this would make the fit too slow because the momentum derivatives have to be computed numerically. The χ^2 function in the electron fit is:

$$\chi^2 = \sum_{meas} \frac{r^2_{meas}}{\sigma^2_{meas}} + \sum_{scat} \left(\frac{\theta^2_{scat}}{\sigma^2_{scat}} + \frac{(\sin\theta_{loc})^2 \phi^2_{scat}}{\sigma^2_{scat}} \right) + \sum_{Eloss} \frac{(\Delta E - \overline{\Delta E})^2}{\sigma^2_{Eloss}}. \tag{4.20}$$

The second sum runs over the material planes where the energy loss is allowed to change, we will call these planes 'brem points'. Thus the energy losses that are allowed to vary also contribute to the χ^2, just like the scattering angles. What happens effectively is

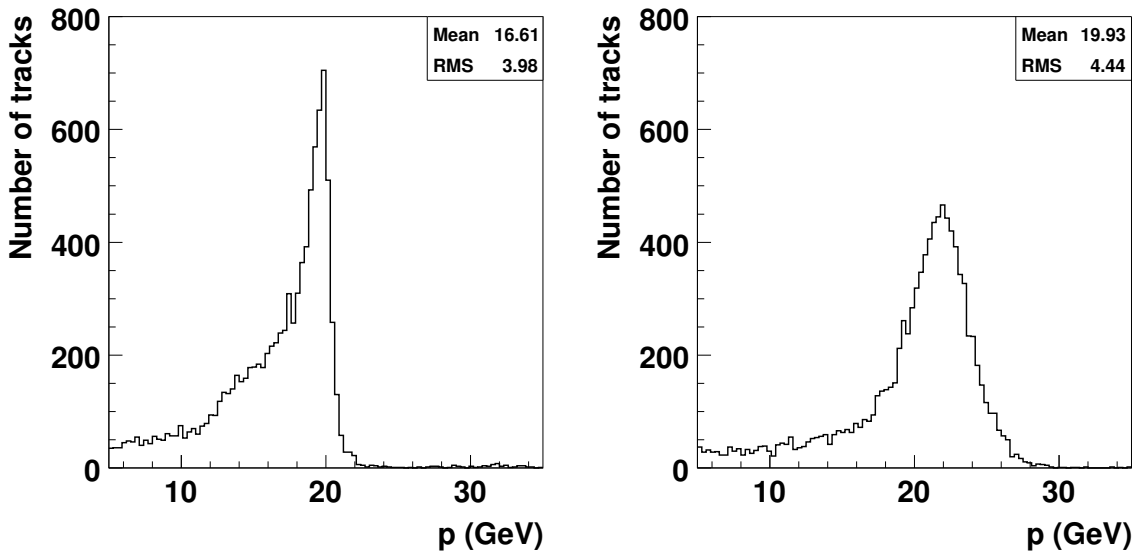

Figure 4.16: *Reconstructed momentum of 20 GeV simulated electrons, using the standard fit (left) and the electron fit (right).*

that the weights of the hits after the brem point are greatly reduced in the fit. This reduces the sensitivity of the fit to Bremsstrahlung, although at the cost of momentum resolution.

Fig. 4.16 shows the reconstructed momentum of simulated electrons with an energy of 20 GeV. The testbeam setup was simulated with the extra material included, giving a total thickness of 60% X_0. It is seen that the resolution of the core has become worse because the electron correction is applied to all electrons, also to those that hardly lost any energy. However, the tail is somewhat improved. For example, the fraction of electrons that have a momentum within 20% of the generated value increases from 61% to 71%. The remaining tail is mainly caused by early and catastrophic energy losses. These are difficult to recover because the first few hits always have full weight in the fit.

Fig. 4.17 shows the momentum pulls with the standard fit and with the electron fit. The pulls are clearly improved with the electron fit: the R.M.S. is about 1.5. Thus, the estimated error on the momentum has become much more realistic, although it is still somewhat underestimated. The underestimation probably comes from the fact that the fit only takes the energy loss fluctuations in the extra material into account, not in the other material (silicon, TRT).

It is clear that the reconstruction of electrons is difficult, and improvements here are desirable. A possible solution would be to apply the electron fit only to those electrons that lose large amounts of energy, and keep the standard fit for the electrons that lose little or no energy. Another solution is to use the calorimeter information in the track fit. It has been shown that the tails can be significantly reduced if the calorimeter cluster is included as a position measurement in the fit [26].

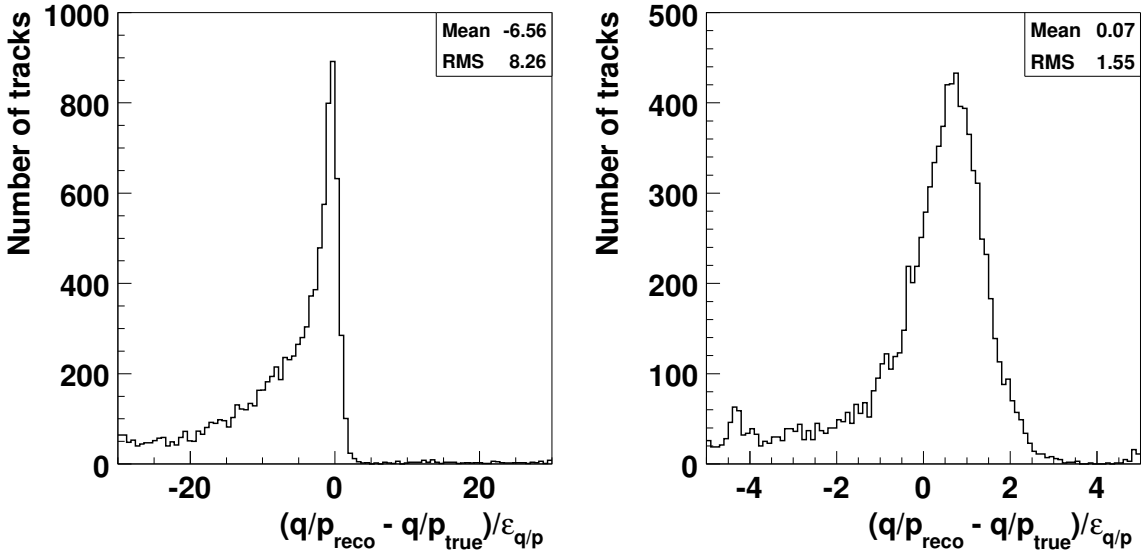

Figure 4.17: *Momentum pull of 20 GeV simulated electrons, using the standard fit (left) and the electron fit (right).*

4.3 Reconstruction of cosmics

The ATLAS inner detector is currently under construction at CERN and at several other institutes across the world. During and after the construction the detector needs to be commissioned, i.e. brought from an assembled state into a fully operational state. An important part of the commissioning is formed by the reconstruction of cosmic muon tracks. The first cosmic tracks in the inner detector were recorded in 2005 and 2006, in the SR1 assembly building at CERN. In this section we will briefly discuss the current status of the reconstruction, which has just become operational with these data.

The data that is currently available was recorded in the TRT barrel, where two phi sectors near the top were read out. Two scintillator plates were put at the top and bottom to form the trigger. The trigger rate is around 1 Hz. In the TRT a gas mixture is used with argon instead of xenon, for cost reasons. The argon mixture gives shorter drift times than xenon, resulting in a worse resolution on the drift radius. The argon also removes the ability to detect transition radiation, but this is of little importance for the cosmics.

CTBTracking remains the baseline reconstruction package for the cosmics. The 'RTF Tracking' package (see section 4.4) is currently being made operational with the cosmics as well, but results are not yet available. A complication for the reconstruction is that the momentum of the cosmic muon tracks cannot be measured, since there is no magnetic field. This prevents the track fit from estimating multiple scattering effects in the detector, because these effects are momentum dependent (Eq. (4.13)). The track fit is therefore a simple straight line fit without any material corrections. Loose cuts are used in order to keep a high efficiency for low momentum tracks: the cut on the drift

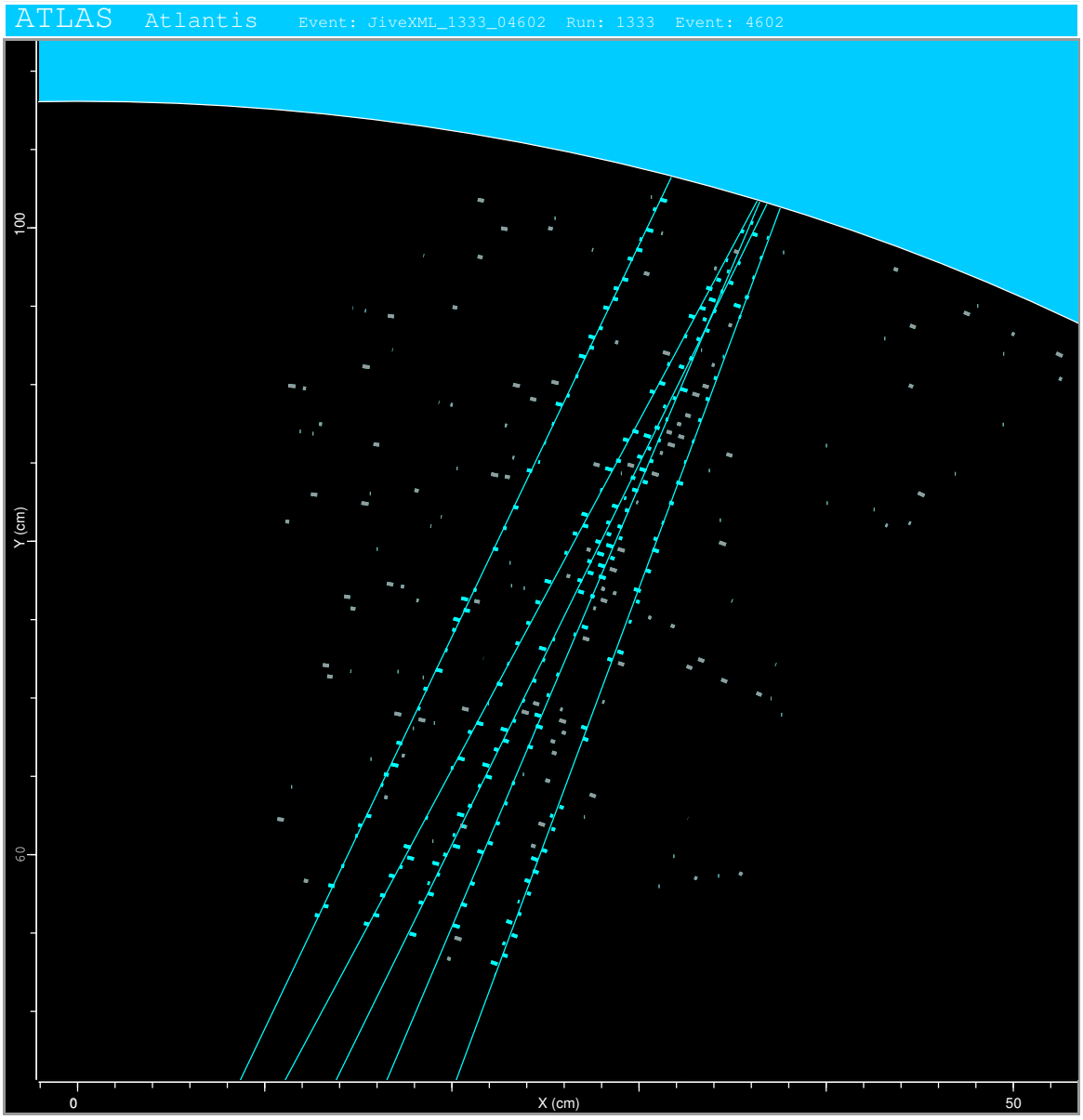

Figure 4.18: *A cosmic shower with several tracks, reconstructed by the CTBTracking reconstruction program.*

circles in the seed finding is set to 2 mm, and the outlier cut in the track fit is set to 10σ (1.7 mm).

Most of the cosmic events have one track. However, Fig. 4.18 shows that showers are also reconstructed correctly. Fig. 4.19 shows that about one third of the events have no reconstructed track. Inspection of the event display shows that these events are empty, because the particle passed outside the acceptance of the TRT. A first calibration is already available and used, which results in track residuals of around 280 microns (Fig. 4.19). The best attainable resolution using the argon mixture is expected to be around

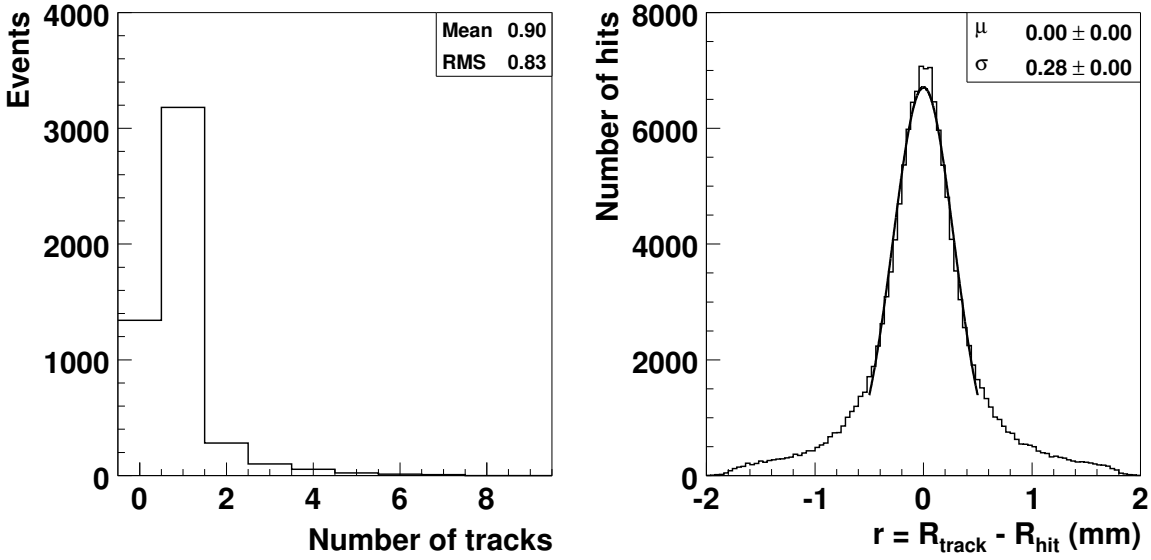

Figure 4.19: *Number of reconstructed cosmic tracks (left) and TRT residuals of the tracks (right).*

200 microns. With further improvements in the calibration and reconstruction it should be possible to reach this figure.

4.4 Track fitting in ATLAS

The track *finding* algorithms in CTBTracking were written specifically for cosmic and testbeam events, and cannot cope with the large hit rates in physics events in ATLAS. On the other hand, the track *fit* is geometry independent and is therefore functional in ATLAS events as well. In this section we will show the current status and performance of the fit in ATLAS, both in the inner detector and in the muon spectrometer.

The track fit collects the material layers on each track using an external tool. The tool that is available for this task in the inner detector is called 'DynamicLayerCreator'. In the muon spectrometer, the 'MboyCollectMatter' tool is used.

4.4.1 Track fitting in the inner detector

In the inner detector, the CTB fitter can refit the tracks from the xKalman [46] and iPatRec [59] packages. Furthermore, it is fully integrated in the 'RTF tracking' package. A detailed description of this tracking package is not yet available. Briefly, the package follows the guidelines of the 'Reconstruction Task Force', who recommended to make the reconstruction software more modular [60]. This implies, for example, that it is possible to choose among several track fitters, one of them being the CTB fitter. The track reconstruction in the RTF tracking package consists of four steps:

- First, track candidates are found in the Pixel and SCT detectors, using combinations of spacepoints. The algorithm starts with performing a fast z-vertex scan using all the spacepoints. Track seeds are then made that point back to this vertex. A narrow road is set up along each seed, and the silicon clusters that fall within this road are collected.

- Next, a full track fit is performed (which is where the CTB fitter comes in). The track candidates that have been found are resolved by an ambiguity processor. This processor assigns a score to each track based on the number of hits on the track, the number of holes (i.e. sensors crossed without a hit), and the χ^2. The tracks with the best scores are selected.

- Then, the fully fitted tracks are extrapolated into the TRT. A road is formed along the extrapolated track, the TRT drift circles that fall within this road are collected and the left/right ambiguities for the TRT drift circles are solved. The output consists of the original tracks together with a list of TRT drift circles that have been associated to them.

- Finally, the extended tracks are processed by the extension processor, which works similar to the ambiguity processor. The extended tracks are fitted by the track fitter, and a score is computed for the new track. The new track replaces the old one if its score is better, otherwise the old track is kept.

The RTF tracking package is still being tested and optimized at the time of writing, but it will soon become the default tracking package for the inner detector. Fig. 4.20 shows a simulated $t\bar{t}H$ event (with the Higgs boson decaying into $b\bar{b}$). The tracks are reconstructed by the RTF tracking software, with the CTB track fit being used as the track fitter.

Fig. 4.21 shows the momentum and impact parameter resolutions as a function of p_T, using simulated single muons. The resolutions obtained with iPatRec are also shown, to obtain a reference point. The momentum resolutions of the two packages are identical, but the CTB track fit achieves a slightly better impact parameter resolution. The most probable cause of this is the weighting of the pixel measurements in the fit, but this requires further investigation. In any case, we conclude that the resolutions obtained with the CTB track fit are satisfactory.

As stated in chapter 2, the resolutions can be parametrized as a function of the momentum (see Eqs. (2.2) and (2.3)). It is useful to revisit the parametrizations that were given in section 2.2.1, because the detector layout has been changed several times over the years, with corresponding increases in the material budget. The studies with the CTB track fit were performed using the 'DC3-02' layout, which is also known to lack some material, but it is certainly much closer to the 'true' layout than the TDR layout. The fitted parametrizations are shown in Fig. 4.21. Note that the resolutions in the plots are averaged over all polar angles θ. The dependency on θ can be factored out by averaging $1/\sin\theta$ over all the tracks in the sample. Thus, we find that the resolutions obtained with the CTB track fit can be approximated as follows:

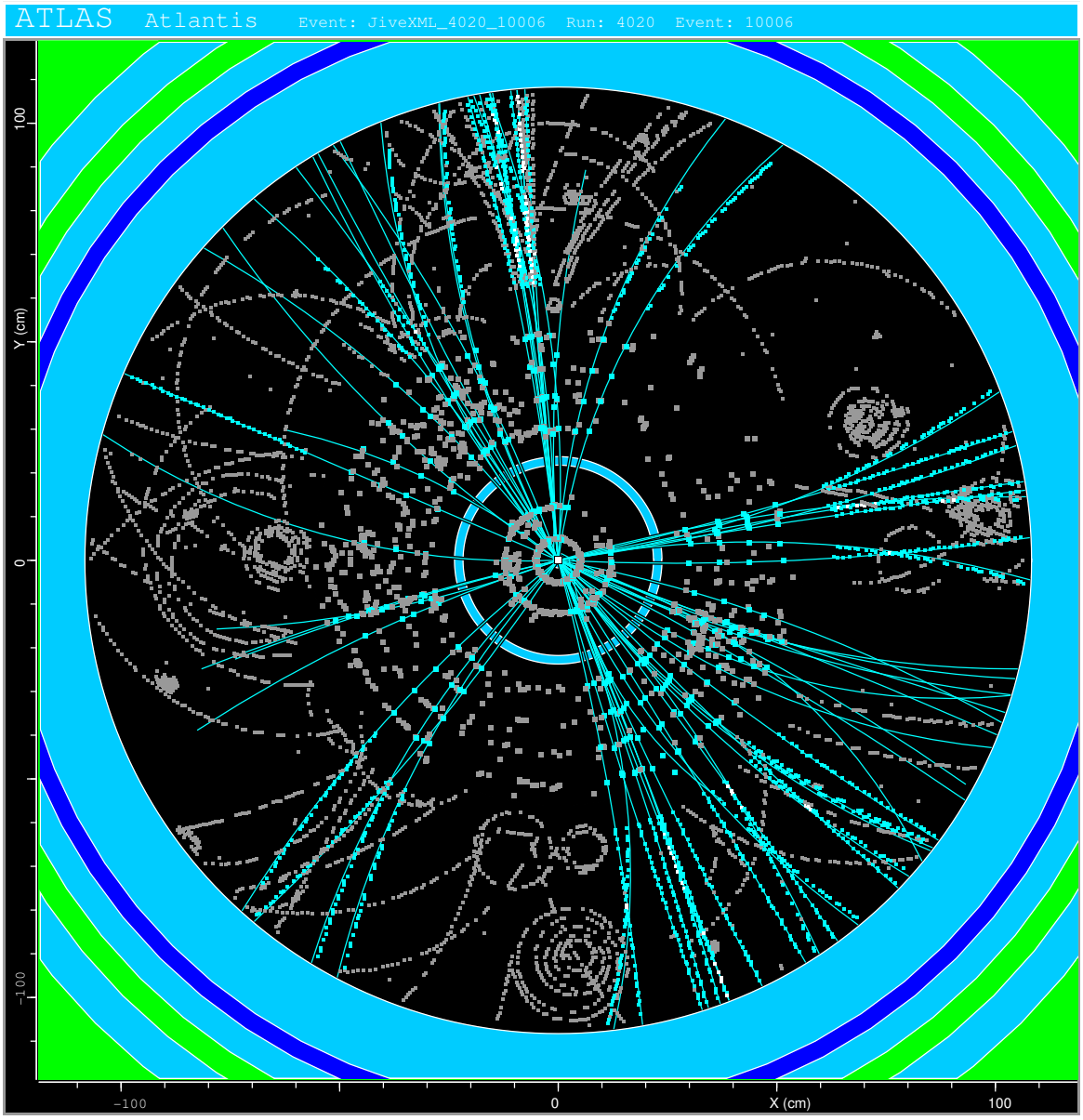

Figure 4.20: *A simulated $t\bar{t}H$ event, with the Higgs boson decaying into $b\bar{b}$. The tracks are fitted using the CTB fitter.*

$$\frac{\sigma_{p_T}}{p_T} = 0.049\% \cdot p_T \oplus \frac{1.4\%}{\sqrt{\sin\theta}} \qquad (p_T \text{ in GeV}), \tag{4.21}$$

$$\sigma_{d_0} = 9\ \mu\text{m} \oplus \frac{122\ \mu\text{m}}{p_T\sqrt{\sin\theta}} \qquad (p_T \text{ in GeV}). \tag{4.22}$$

The refit efficiency of the CTB track fit in the inner detector is 100%. No problems are noted with the stability of the fit.

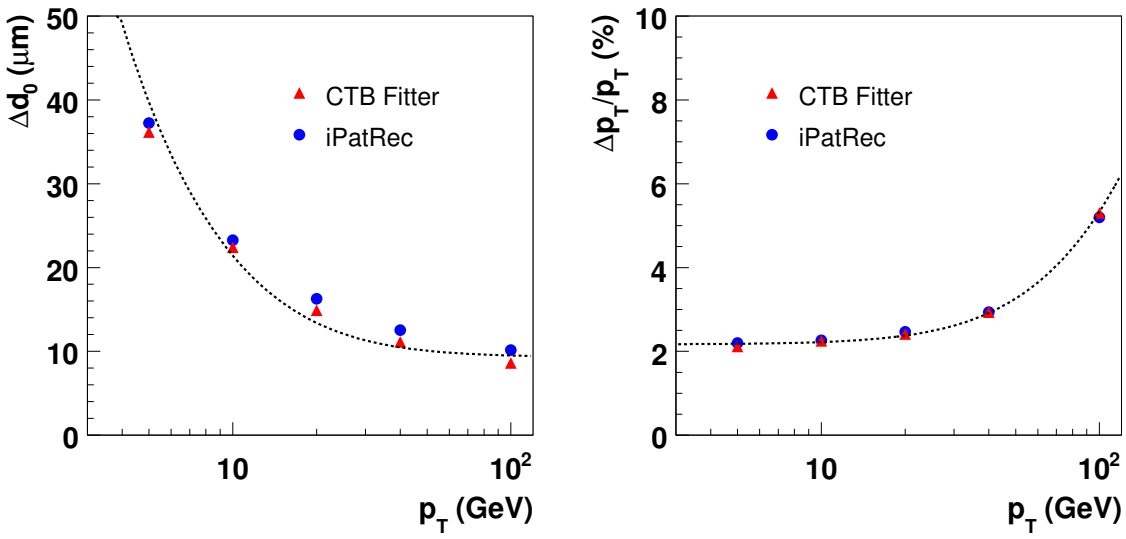

Figure 4.21: *Resolutions of the impact parameter (left) and momentum (right) using simulated single muons, for iPatRec and the CTB fitter. The fitted parametrizations are described in the text.*

4.4.2 Track fitting in the muon spectrometer

Compared to the inner detector, the muon spectrometer is a challenging environment for track fitting. There is far more material that needs to be taken into account in the track fit, even at high energy. The distances between the hits are often several meters, which means that extrapolating from one hit to another is more prone to numerical inaccuracies. Last but not least, the track fit has to deal with a magnetic field that varies strongly, e.g. near the magnet coils.

The Runge-Kutta propagator that is used by the CTB track fit has been extensively tested in the inner detector, but so far it has not been used in the muon system. Since it is likely that a higher precision is required than in the inner detector, the accuracy of the propagator is set to be 100 times better than the default value. This makes the propagator slower, because the propagation has to be done in smaller steps. The execution speed of the refit is around 150 milliseconds per track.

The CTB track fit can refit the tracks from the Muonboy [32] and MOORE [61] muon reconstruction algorithms. Both algorithms store all the hits in the track that they used in the fit, except that Muonboy does not store the CSC[4] precision hits. This is because Muonboy uses its own format for these hits that cannot be read by other track fitters. MOORE does not use the RPC and TGC hits that measure η, but this is not a real problem since this coordinate is already measured by the MDT hits.

The track fit in the muon system starts at the entrance of the muon spectrometer. In principle the choice of reference point is arbitrary, but starting the fit at the beamline would introduce the inner detector magnetic field as an additional complication. In

[4]See chapter 2 for a description of the detector technologies in the muon system.

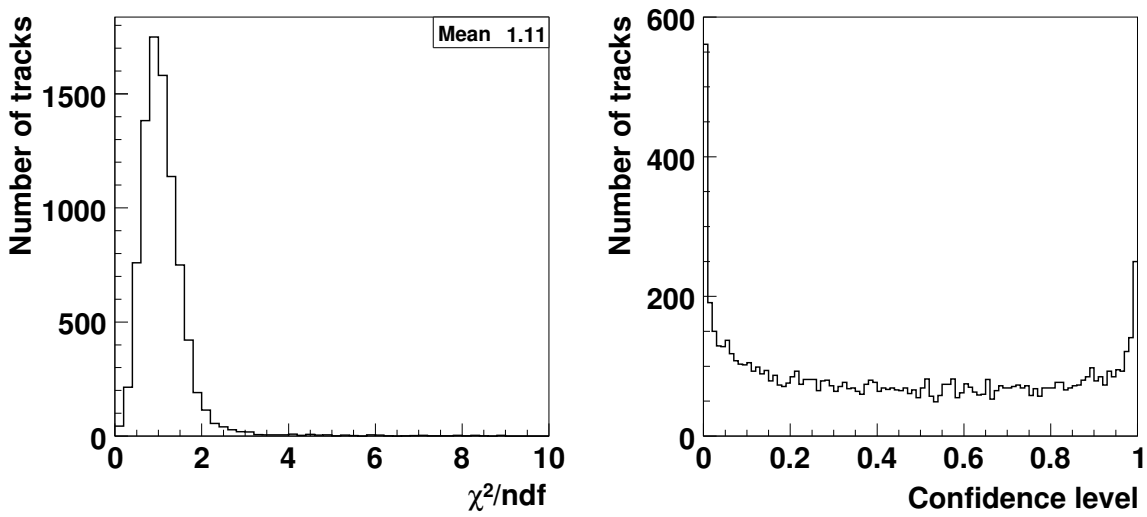

Figure 4.22: *Left: the reduced χ^2 distribution of the refitted tracks in the muon spectrometer. Right: the χ^2 probability distribution of the refitted tracks.*

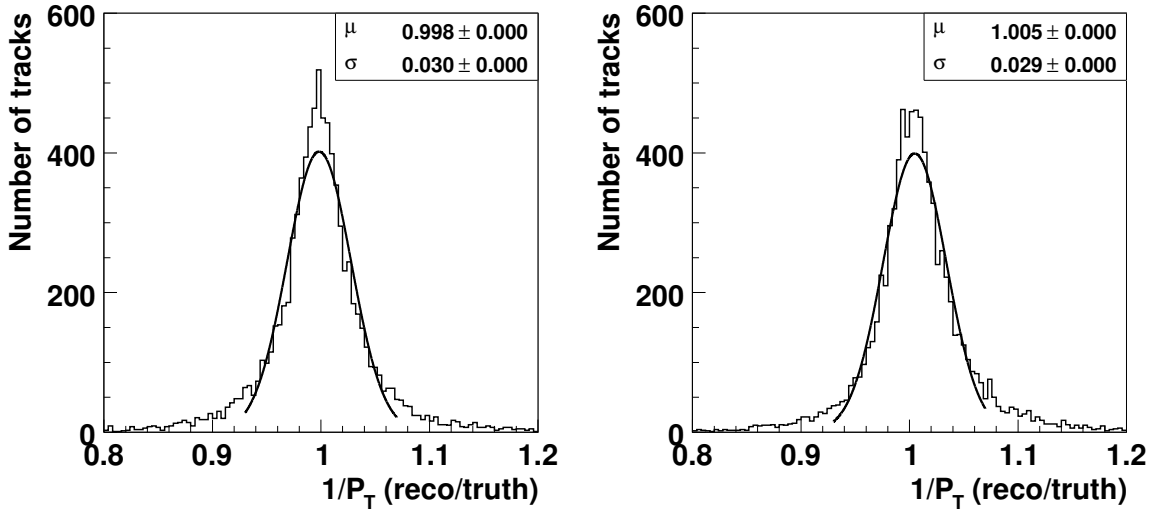

Figure 4.23: *Ratio of reconstructed inverse transverse momentum to true inverse transverse momentum, for MOORE (left) and the CTB fitter (right).*

practice this causes the fit to become unstable when the analytical derivatives are used, although the stability is recovered when numerical derivatives are used instead. Starting the fit at the beamline is equivalent to starting the fit at the muon spectrometer entrance, and then extrapolating the track to the beamline.

The CTB track fit is tested in the muon system by refitting simulated muons with

$p_T = 10$ GeV. Note that the p_T in the muon system is a few GeV lower, due to the energy loss in the calorimeter. The muons were simulated up to a pseudorapidity of ± 3.0. Fig. 4.22 shows the reduced χ^2 and the χ^2 probability distributions of the refit. The peaks at 0 and 1 in the probability distribution indicate that the treatment of material effects could perhaps receive more tuning. Apart from that, the distributions look fine. Fig. 4.23 shows the momentum resolution of the original MOORE tracks and the refitted tracks. Here, the reconstructed momentum is compared to the momentum of the Monte Carlo particle at the muon spectrometer entrance. The momentum resolutions of MOORE and the CTB track fit are practically identical.

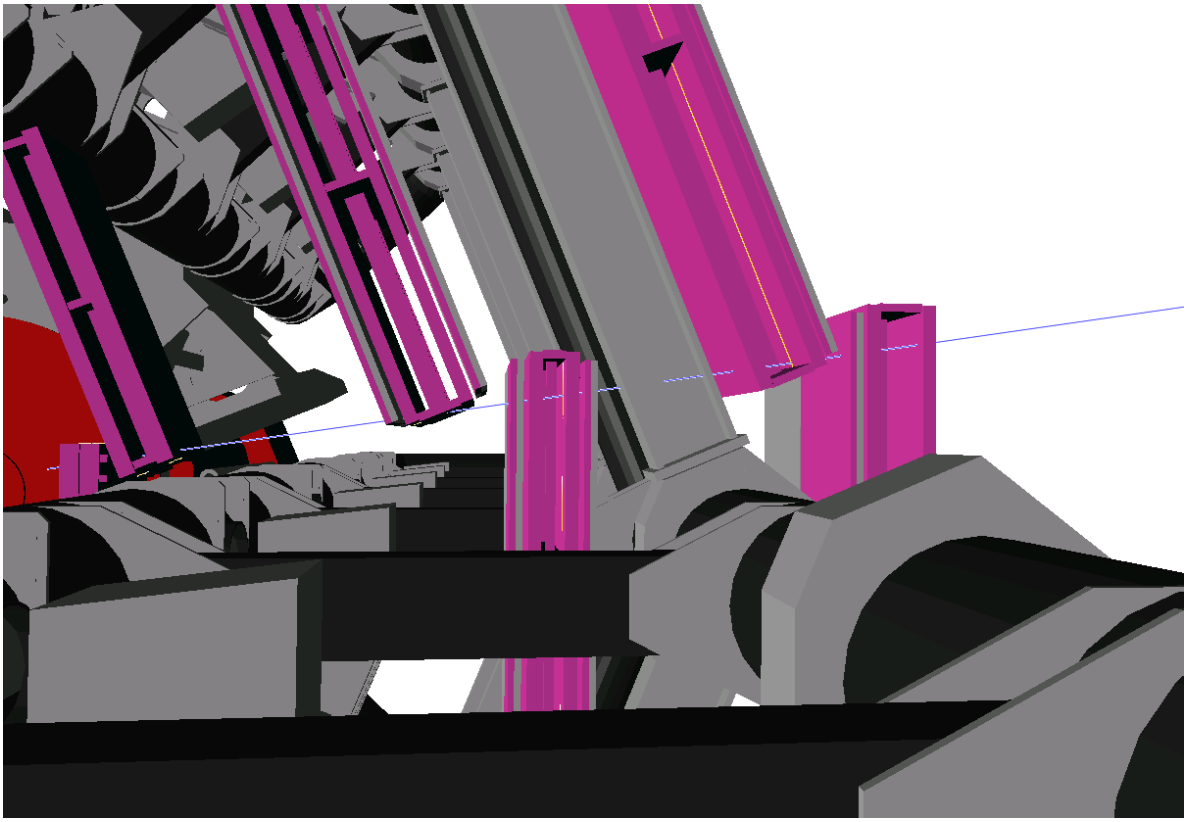

Figure 4.24: *View of a refitted muon track. The muon chambers that were hit by the track are also shown, along with the various support structures and magnet coils. Some parts have been removed to give a better view of the track.*

The refit efficiency of the CTB track fit in the muon spectrometer, using the 10 GeV sample, is 98.5%. In nearly 97% of the cases, the refit succeeds using the analytical residual derivatives. About 2% of the refits fail with the analytical derivatives, but are successfully recovered by attempting the fit again with the numerical derivatives. The remaining 1.5% fail with both the analytical and the numerical derivatives. Some of these tracks have very few hits (less than ten), causing the refit to become underconstrained. For example, the track parameters d_0 and ϕ_0 are not constrained if the track only has

MDT hits. The CTB track fit solves the majority of these cases by adding 'invented' measurements if required.

4.5 Conclusions

In this chapter, the performance of the CTBTracking algorithm has been presented. The algorithm has been precisely tuned for the testbeam and cosmic setups in order to obtain the best possible performance, with only modest CPU requirements. In the tests with simulated testbeam data an efficiency of nearly 100% is achieved with muons, while the efficiency with pions is between 95 and 100%. The track parameter resolutions are at least as good as those obtained with the xKalman program, and the pulls of the hit residuals and the track parameters are close to 1. Thus, the various contributions to the errors in the testbeam setup, such as the detector material, are understood to within a few percent.

The results obtained with real cosmic data show that the algorithm is sufficiently robust for reconstructing real data, even in the presence of problems like misalignments and miscalibrations. The current performance is sufficient for testing and studying various topics, such as the data itself, the calibration, and the online monitoring. While some of these aspects can also be studied with simulated data, the tests with real data are indispensable for getting the detector operational, and for understanding its performance.

The pattern recognition algorithm was designed specifically for the testbeam and cosmic setups. On the other hand, the track fitting algorithm is completely independent of geometry. By dividing the tracker hits into two categories (strip clusters and drift circles), it is possible to incorporate all the different tracker technologies into the fit that are currently in use in ATLAS. The performance of the fit in ATLAS already appears to be sufficient for performing physics studies. Some tuning may still be required, but this will only have a limited effect on the overall performance. Thus, we conclude that the track fit is a full alternative to the other track fitters in ATLAS.

Chapter 5

The ATLAS combined testbeam

As mentioned in chapter 3, the performance of the ATLAS detector can be studied using simulated data. However, there are many aspects that cannot be tested with simulation, e.g. the data acquisition, efficiencies as function of thresholds, deterioration of performance after radiation, etc. Therefore, prototypes of detector elements that will be used in ATLAS are placed in a particle beam, and their response is analyzed. Until 2004 these beam tests were mostly standalone, i.e. each subdetector had its own data acquisition and analysis chain.

In 2004 a fully *combined* testbeam took place. A setup was built where every subdetector is represented, working with a common data acquisition, trigger and clock. The setup represents roughly a wedge of the ATLAS barrel, the total size in terms of channels is about 1% of the full experiment. Fig. 5.1 gives an overview of the setup geometry.

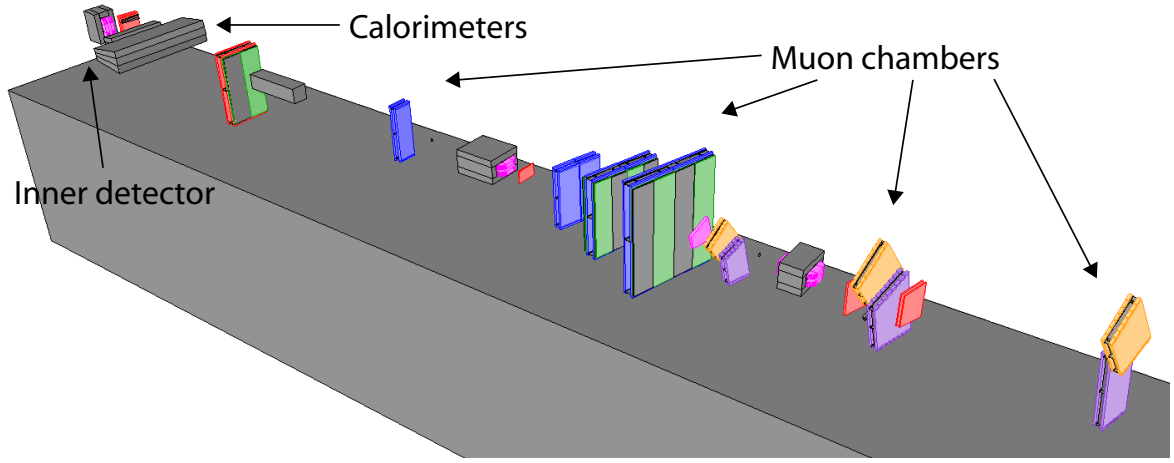

Figure 5.1: *Overview of the combined testbeam setup. The beam traverses the setup from the top left to the lower right.*

For the inner detector, the main goals of the combined testbeam are:

- Test and develop reconstruction, calibration and alignment algorithms, using real detector data;

- Study of the performance of the individual detectors (efficiencies, resolutions, noise etc.);
- Test the tracking performance of the inner detector as a function of material and particle type;
- Combined reconstruction with the other subdetectors: electron identification and recognition of photon conversions with the calorimeter, and combined tracking with the muon spectrometer.

We will discuss the testbeam setup in detail in section 5.1, focusing on the inner detector part of the setup. Section 5.2 deals with the quality of the inner detector data. The calibration and alignment of the inner detector is discussed in section 5.3. Sections 5.4 and 5.5 present the results from track reconstruction in the inner detector, as well as the results on combined muon reconstruction. In section 5.6 the results are summarized.

5.1 Testbeam setup

5.1.1 The particle beam

The combined testbeam was situated at the H8 beamline near the SPS accelerator at CERN. The particles in this beamline could be electrons, pions and muons, and the energy could be adjusted from 1 GeV up to 350 GeV. The spill length was 4.8 s, and there was a spill every 16.8 s. In practice the beam was often a mixture of different particle types, therefore a number of Cherenkov detectors were installed in the beam that can detect the particle type. The detector that was available to the offline analysis is called 'Cherenkov2'. Fig. 5.2 shows a plot with counts from this detector, a clear separation between electrons and pions can be observed. More information about the beamline instrumentation can be found in Ref. [62].

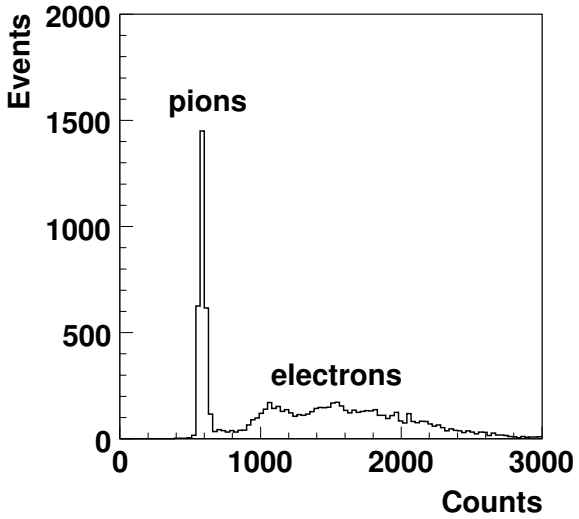

Figure 5.2: *Signal in the Cherenkov detector.*

The trigger consisted of three scintillator triggers that were required to fire in coincidence. In addition, a muon veto was used in the low energy runs, to prevent contamination from high energy muons.

The arrival times of the particles were usually random[1]. The time difference between the trigger and the readout clock was recorded by a time to digital converter (TDC). This time is e.g. needed to correct the drift times in the TRT, because the readout electronics in the TRT measure the drift time relative to the readout clock.

5.1.2 The inner detector

The inner detector consisted of the pixel, SCT and TRT subdetectors. The pixel detector was made of six modules, grouped in three layers of two modules each. Each module was positioned at an angle of about 20 °, and with an overlap of about 1 mm with the other module in the layer. The acceptance of the pixel setup was 6×3 cm^2. This was sufficient in most cases, although there are some runs where the beam profile was larger than this acceptance.

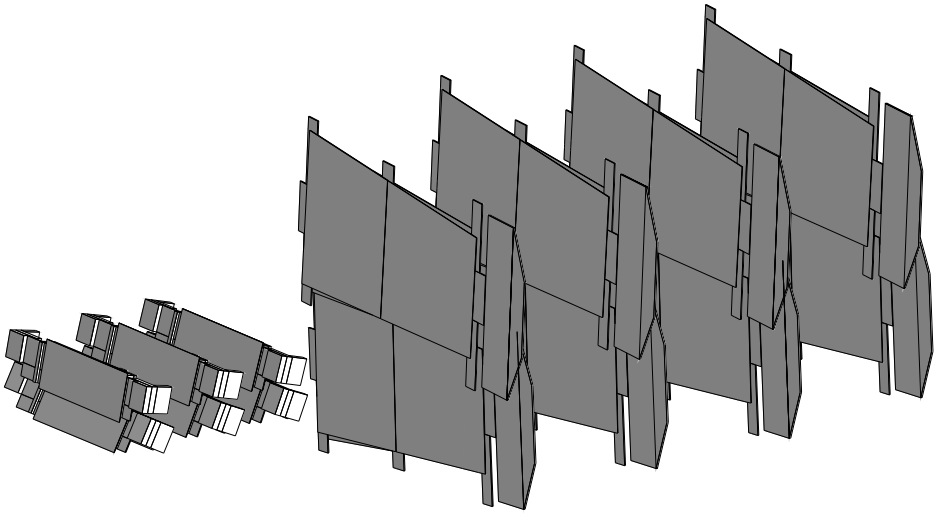

Figure 5.3: *Schematic view of the pixel and SCT modules in the testbeam. The beam enters the setup from the left side.*

The SCT consisted of eight endcap modules, installed in four layers with two modules each. Endcap modules were used because it was not possible at the time to construct a testbeam setup with barrel modules. The two modules in a layer had an overlap of 3 mm. The two middle layers were centered vertically with respect to the beam axis, while the first and last layers were offset by -5 mm and $+5$ mm respectively. The front sensor in the lower module of the third layer was not operational in any of the runs.

The TRT contained two barrel phi sectors, of which only the half that was hit by the beam was read out. Each phi sector contained three modules that represent 1/32 of the TRT barrel in ATLAS. There were thus six modules in the testbeam, with 3284

[1]In some runs the readout clock was synchronized to the beam. However, the inner detector was not yet ready when these runs were taken.

straws in total. The TRT was displaced in z (along the straw direction) such that the active part of the first nine straw layers was hit. The number of straw hits per track is therefore somewhat larger than in ATLAS.

The pixel and SCT modules were installed in cooling boxes, which were situated in the MBPSID magnet. The TRT was situated outside of this magnet, because it was too big to be installed inside. The magnet was 1 meter long, had an aperture of 230 mm, and generated a field of up to 1.4 Tesla. Fig. 5.5 shows the field strength along z as a function of x and y, according to the field map that is used in the reconstruction. The field map was calculated from measurements that were performed with the magnet running at a current of 800A. However, during data taking the magnet was mostly operated at 850A. A simple scaling is applied to the field in the reconstruction, in order to correct for this.

In some runs extra material was installed in the form of two aluminium slabs, in

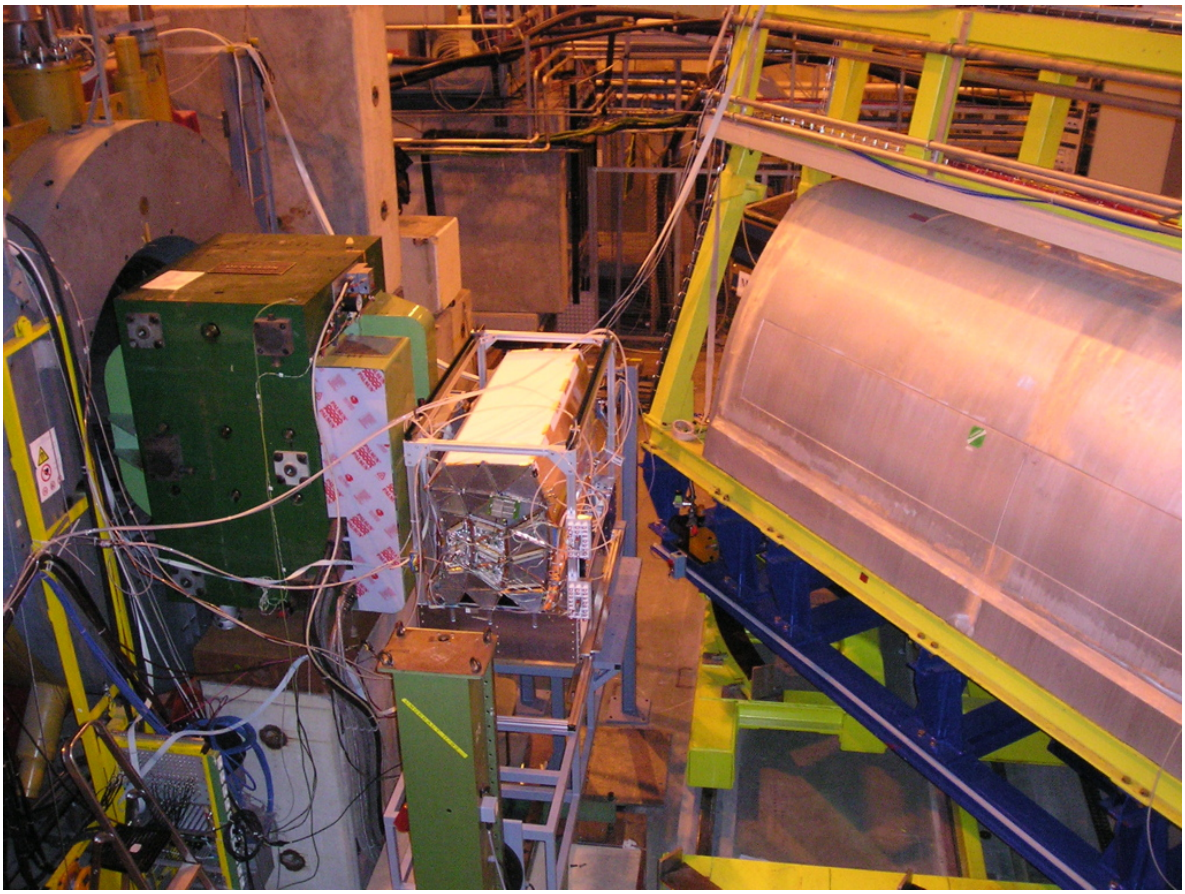

Figure 5.4: *Photograph of the inner detector in the combined testbeam. The square box on the left is the magnet, holding the pixel and SCT setups. The TRT, visible near the middle of the picture, is positioned just outside the magnet. To the right, the cryostat of the liquid argon calorimeter is visible.*

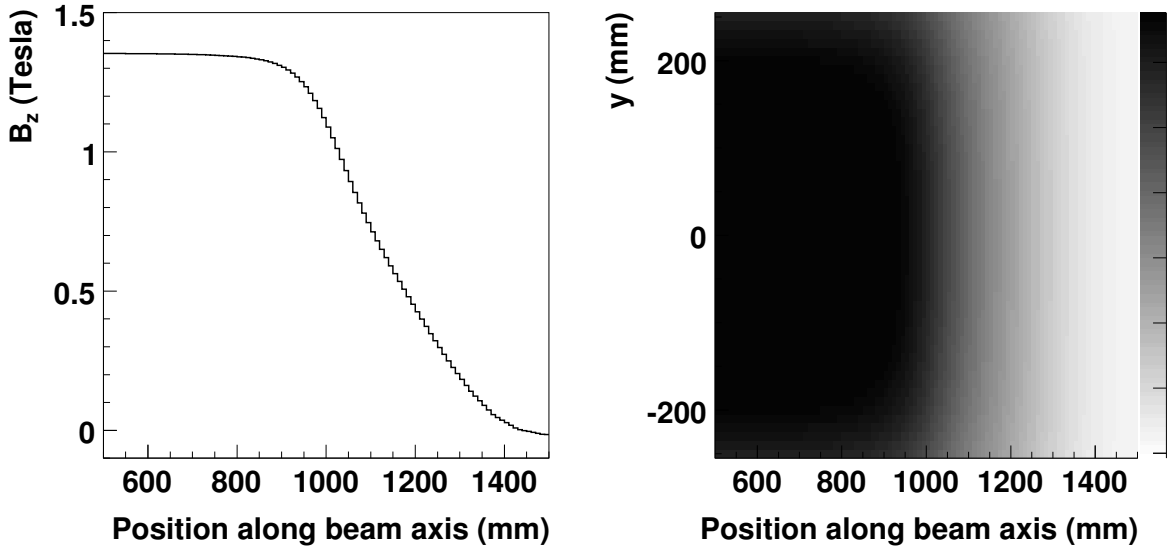

Figure 5.5: *Field strength along z in the inner detector magnet, as a function of x (beam direction) and y (vertical direction). $x = 0$ at the beginning of the magnet.*

order to simulate the ATLAS inner detector at $|\eta| = 1.6$ where there is more material than in the barrel. One slab had a thickness of 10 mm (11% of a radiation length) and was placed between the pixel and SCT detectors. The other slab had a thickness of 20 mm, and was placed just after the SCT.

5.1.3 The calorimeters

The calorimeter system in the testbeam consisted of an electromagnetic and a hadronic part. The electromagnetic calorimeter consisted of a barrel module that was housed in a cryostat. The cryostat was filled with liquid argon. The module was placed as close to the hadronic calorimeter as possible (i.e. near the back of the cryostat), to optimize the containment of hadronic showers. The hadronic calorimeter consisted of three barrel modules stacked on top of each other, next to three extended barrel modules. The two calorimeters were installed on the same table. The table could move and rotate, such as to simulate particles coming from the interaction point at different values of η.

5.1.4 The muon system

The muon detector spanned more than 40 meters in the testbeam. After the hadronic calorimeter, a barrel muon chamber (BOS) was the first that was encountered by the beam. The beam then traversed a block of iron of 3.2 meters long, called the 'dump'. The dump could be either open or closed, depending on the run conditions. Next is the rotating BIL chamber, which was used to obtain the $r(t)$ relation that is used for the

other chambers in the reconstruction. Finally, the beam traversed the chambers that are used for muon tracking studies: six barrel muon chambers divided in three layers of two chambers each, and six endcap muon chambers, also in three layers of two chambers each. The BIL, EIS and EIL chambers have two multilayers with four tube layers each, the other chambers have two multilayers with three tube layers. In the barrel setup, the BML and BOL stations were equipped with RPC trigger chambers that provide a measurement of the second coordinate. In the endcap setup there were three TGC chambers and one CSC chamber.

The barrel and endcap stands were equipped with optical sensors that measured the alignment of the chambers. The data from these sensors was processed by the ASAP [63] and ARAMYS [64] software packages, which results in a set of alignment corrections. These corrections are read from the conditions database in the reconstruction. Note that the alignment of the barrel and endcap chambers was done separately, i.e. there is no alignment between the barrel and endcap part of the setup.

5.2 Data quality

In total more than 80 million events were recorded in the testbeam, which yielded more than 4 TB of data. The performance of the online monitoring was limited and it was only run infrequently, therefore the data had to be validated offline. Typical problems that were encountered are: tripped modules producing hundreds of hits per event or no

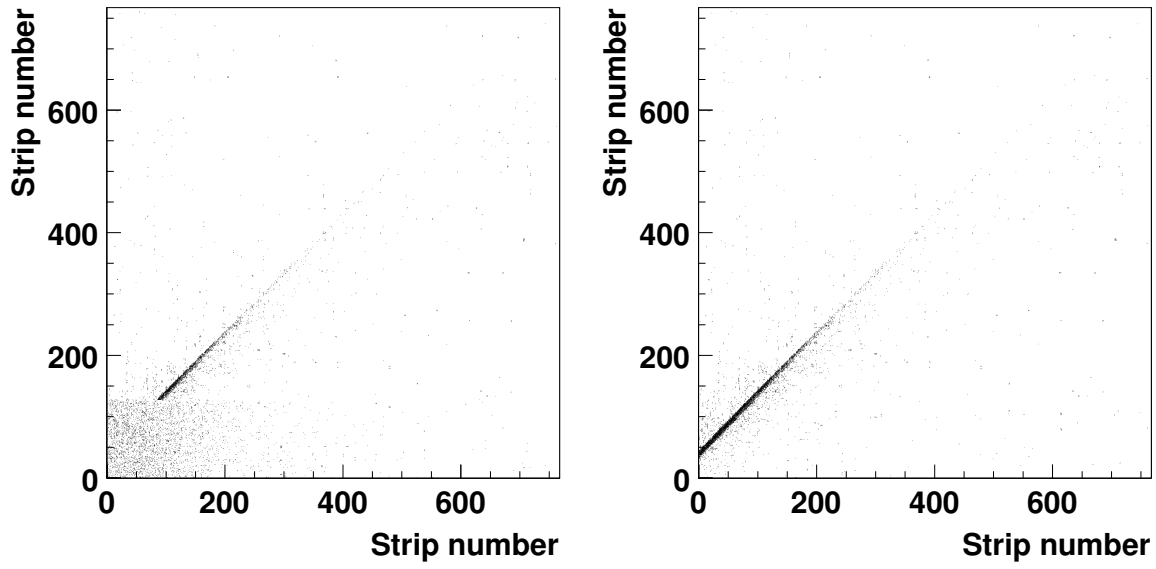

Figure 5.6: *Correlations between the strip numbers in two SCT sensors. Left: the data of the two sensors is taken from the same event. Right: One chip (i.e. 128 strips) in one sensor is offset by one event relative to the other chips.*

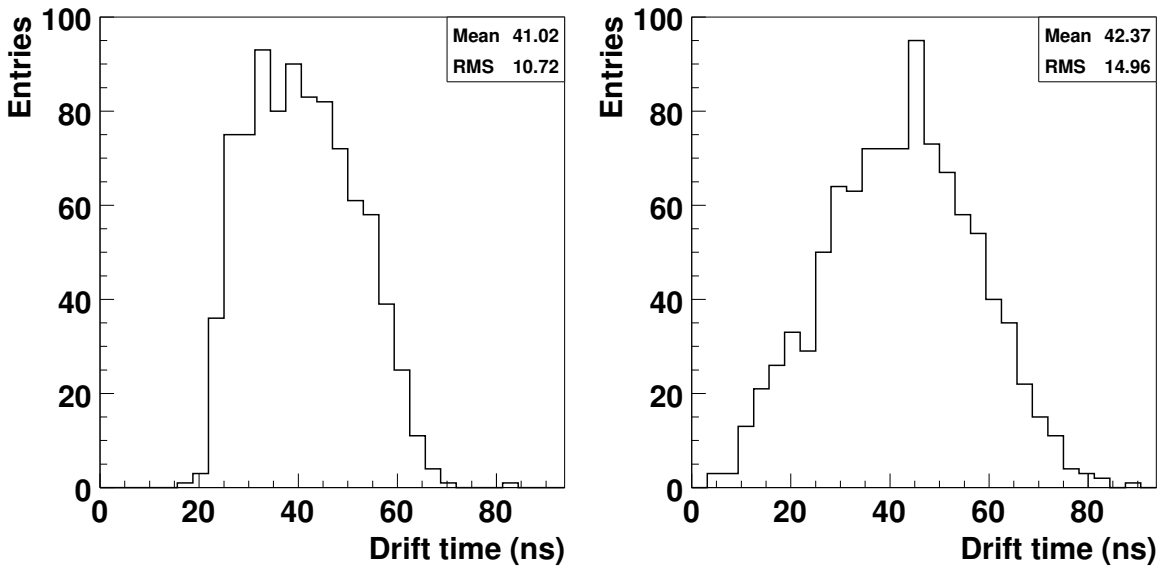

Figure 5.7: *Drift time spectrum of two straws in the testbeam: a straw in the first module layer (left) and a straw in the third module layer (right).*

hits at all, and loss of correlations in and between subdetectors. After validation and offline checks, a total of 22 million events are selected. Unfortunately it turns out that some runs have problems that were only found after the validation period.

An example of a problem in the 'good' runs is shown in Fig. 5.6. The plots show the correlation between the strip number in two SCT sensors. The plot on the left shows that the correlation is lost in the first 128 strips of one of the sensors, the correlation is recovered if the data of these strips are offset by one event. Thus, the readout chip that is connected to these strips was desynchronized by one event when this run was recorded. In principle it is possible to rebuild the events with this problem corrected, but this was not attempted. The effect on track reconstruction is limited, as long as the problem is limited to one or two readout chips. However, there are also runs where the SCT as a whole is desynchronized with respect to the other detectors. Such runs are not usable for track reconstruction.

In the TRT, a serious problem was found in the outer modules (i.e. the modules furthest away from the interaction point). For reasons that are still under investigation, the spatial resolution of the straws in these modules was much worse than in the other modules. Fig. 5.7 shows a symptom of this problem: the time spectrum of the straw on the right does not have a clear leading edge. The leading edge corresponds to hits where the particle crossed the straw very close to the wire, but the problem causes this edge to be smeared out. There is also hardly any correlation between the drift time and the track-wire distance in the affected straws (Fig. 5.8). Further understanding of this problem would require a detailed knowledge of the TRT electronics and straws, and is hence beyond the scope of this thesis. We will not use the outer modules in any of the results in this chapter, unless stated otherwise.

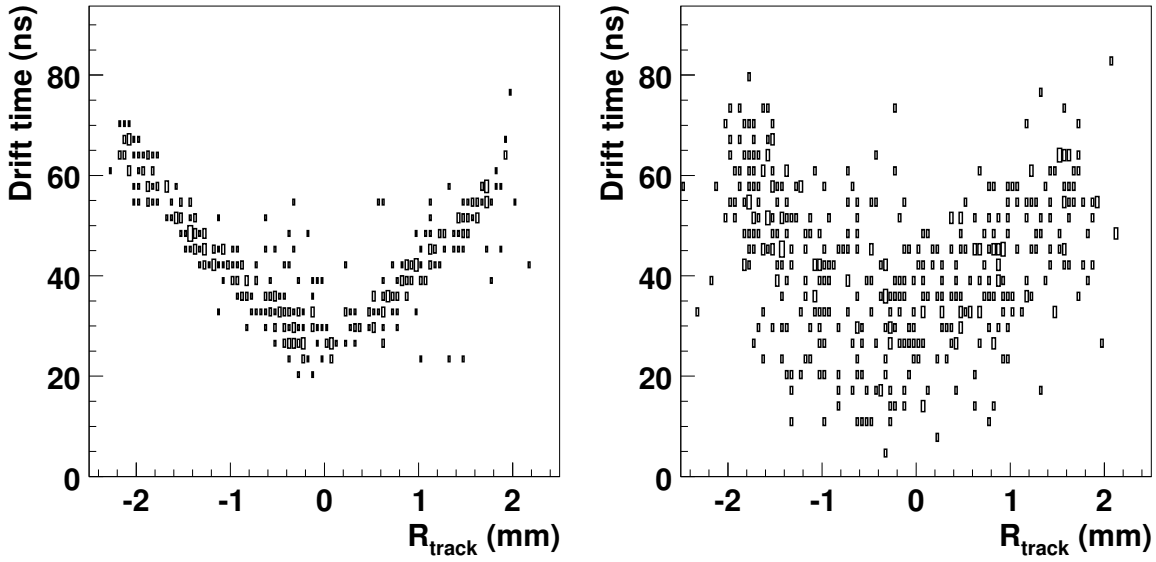

Figure 5.8: *Drift time versus the distance between the track and the wire, for a straw in the first module layer (left), and a straw in the third module layer (right).*

5.3 Calibration and alignment

5.3.1 Calibration

The calibration of the detector consists of two tasks: removal of bad channels, and the conversion of drift times into drift radii in the TRT. In the SCT and TRT, channels that are found to be either dead or noisy are marked as 'bad' in the conditions database. In the reconstruction these channels are removed in the data preparation stage, such that the track reconstruction is not affected. Note that no masking of dead channels is performed for the pixel detector. This is hardly a problem since the pixel detector performed quite well in the testbeam, with very low noise levels.

In the TRT, the distance-drift time relation for each straw has to be determined by a calibration procedure. This relation converts the measured drift time into the best estimate of the distance between the particle and the wire. It is obtained as follows:

- First, a 'V-plot' is made for each straw, i.e. the plot showing the measured drift time versus the signed track-wire distance. A 'V' is fitted to this plot. The vertical offset of this fit corresponds to the t_0, i.e. the drift time corresponding to a particle that passes right through the wire.

- Next, the t_0 is subtracted from all the drift times, and both sides of the V-plot are averaged. The result is a plot of the *absolute* track-wire distance versus the corrected drift time (i.e. $t - t_0$). A third degree polynomial is fitted to the points, which yields the $r(t)$ relation.

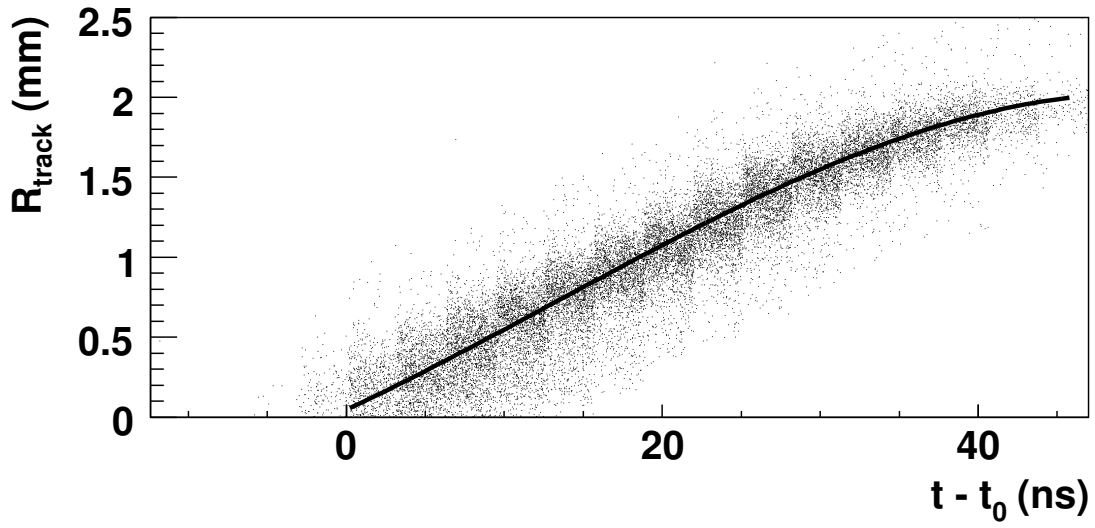

Figure 5.9: *Scatter plot showing the drift times (after t_0 subtraction) versus the predicted track-wire distance R_{track}, obtained from the TRT track fit. The $r(t)$ relation that is used in the reconstruction is also shown. The binning effects in the plot are due to the binning in the TRT electronics (3.125 ns).*

The track-wire distance can be obtained in two ways: by performing a track fit to the TRT hits, or by extrapolating tracks from the pixel and SCT detectors to the TRT. The first method is called 'auto-calibration', since only information in the TRT itself is used. The calibration procedure is found to be slightly better and more stable when external tracks are used [65]. Fig. 5.9 shows a scatter plot of the $r - t$ points, together with the fitted $r(t)$ relation.

5.3.2 Alignment

The task of the alignment procedure is to find the actual positions of the detector elements, starting from the nominal values of these positions. In the testbeam the pixel, SCT and TRT detectors are first aligned internally, before being aligned relative to each other. The pixel and SCT detectors are aligned using the following recipe [66]:

- First the pixel detector is aligned internally, using pixel-only tracks. The residuals are used to build a χ^2 function, which is minimized with respect to two parameters (y_0, ϕ).
- Next, the pixel-only tracks are extrapolated into the SCT, and are used to get a broad SCT alignment.
- Finally, both the pixel and the SCT modules are aligned at the same time, using pixel+SCT tracks. Again a χ^2 function is built which is used to obtain five alignment parameters per module $(y_0, z_0, \phi, \theta, \psi)$.

Note that the coordinate x_0, i.e. the position along the beam axis, is not determined. This parameter cannot be constrained, because of the lack of angle spread in the beam. Therefore the modules are kept at their nominal x-coordinates.

The relative alignment between subdetectors can be checked by producing track segments in each subdetector. The track parameters of these segments will not be the same due to multiple scattering and the detector resolution, but on average the segments should line up. Fig. 5.10 shows the results of comparing segments in the pixel and SCT detectors, using a run with 100 GeV pions and no magnetic field. The misalignment is of the order of 1 micron, which is negligible compared to the detector resolution.

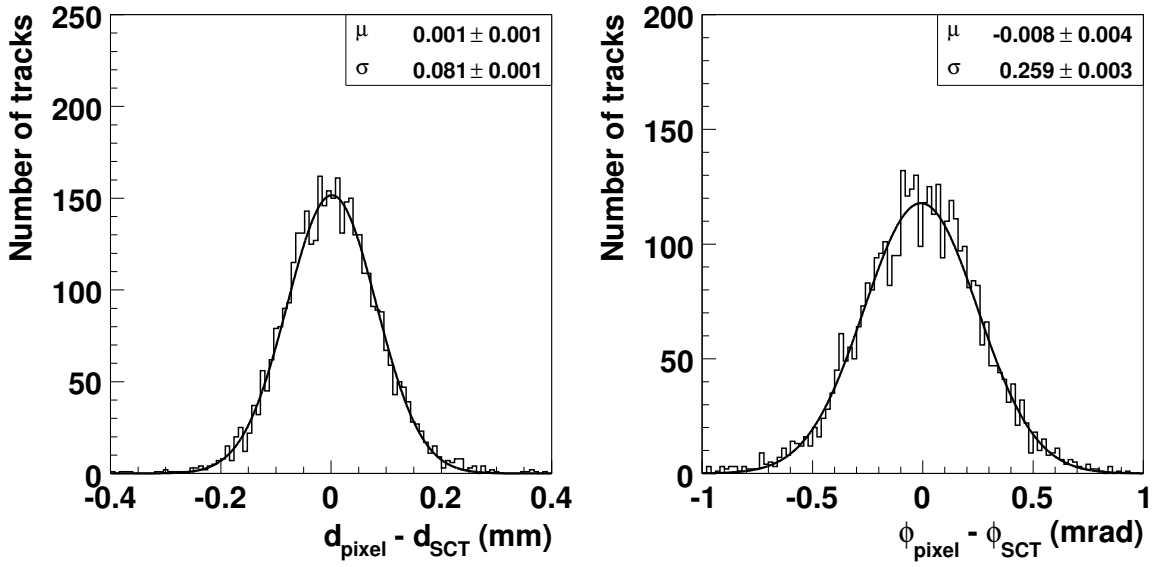

Figure 5.10: *Difference between the impact parameter (left) and azimuthal angle (right) of track segments reconstructed in the pixel and SCT detectors.*

In the TRT, the alignment is first performed internally by moving and rotating the six TRT modules. Then, the TRT as a whole is moved and rotated in order to match the extrapolated tracks from the silicon detectors. The positions of the straws within a module are also determined, their deviation with respect to the nominal position is found to be of the order of 20 microns. These individual straw positions are not used in the reconstruction, i.e. the straws are assumed to be perfectly aligned within a module. Results with a custom track reconstruction show a small improvement in the residuals (about 5 microns) when the individual straw corrections are used [67].

The fit qualities and χ^2 probabilities of the full inner detector tracks are shown in Fig. 5.11. The peak at 0 in the probability distribution is caused by the various non-Gaussian effects in the track fit, e.g. hard scatters which distort the fitted track. Also, in some events the pion initiates a shower in the detector material, which can confuse the pattern recognition. Apart from that the probability distribution is mostly flat, indicating that the errors in the track fit are well understood. In particular, the error on

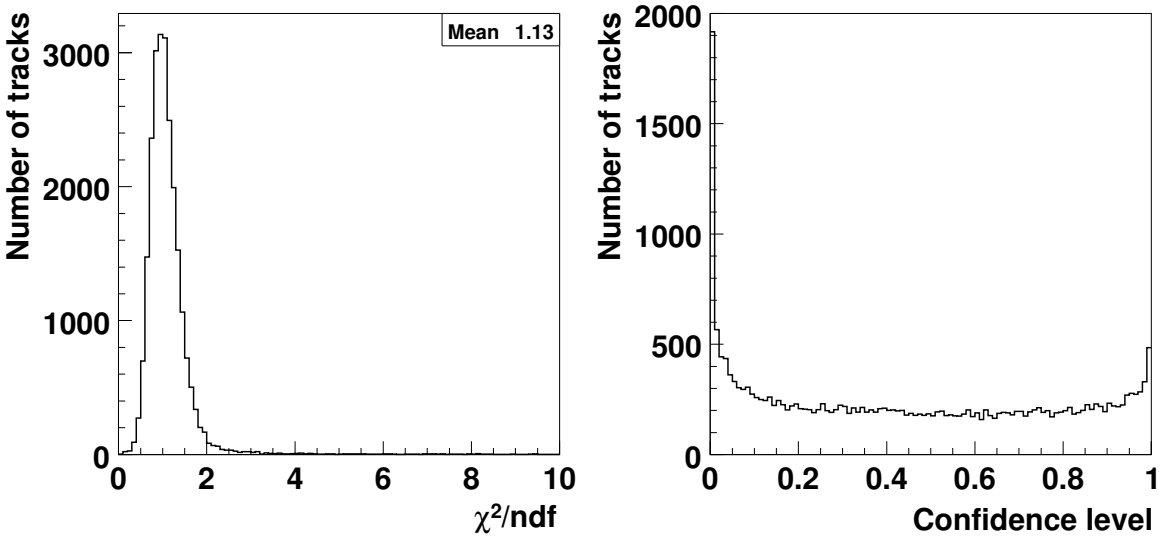

Figure 5.11: *Fit quality and χ^2 probability of the global inner detector track (i.e. pixel, SCT and TRT), in a run with 100 GeV pions and no magnetic field.*

the alignment is assumed to be zero in the fit, therefore we conclude that the alignment is of excellent quality in this run. It should be noted though that the quality of the alignment varies somewhat from run to run. The inner detector was altered several times during the testbeam, e.g. in order to install extra material. There are thus several different run periods, each of which needs its own set of alignment constants. Currently, work is still ongoing to provide a consistent alignment for all of these periods.

5.3.3 Detector resolution

The resolution of each subdetector can be estimated from the distribution of the track fit residuals, i.e. the distance between the hit and the track. The residuals of the pixel, SCT and TRT detectors are shown in Fig. 5.12, for a run with 100 GeV pions and no magnetic field. The residuals in the plots are *unbiased*, i.e. it is evaluated using a track where the hit does not participate in the fit. Note that the distributions are broadened by the error on the track prediction, therefore the detector resolution is somewhat smaller than the width of the distribution. This affects in particular the pixel residuals. Note that the pixel η residuals are highly non-Gaussian. This is because the total number of hits that measure this coordinate is small (about three), and because of the discrete readout of the pixels. The residuals would be smeared out more if there were more hits that measure the η coordinate.

The measurement precision can be obtained from the residuals by quadratically subtracting the tracking error:

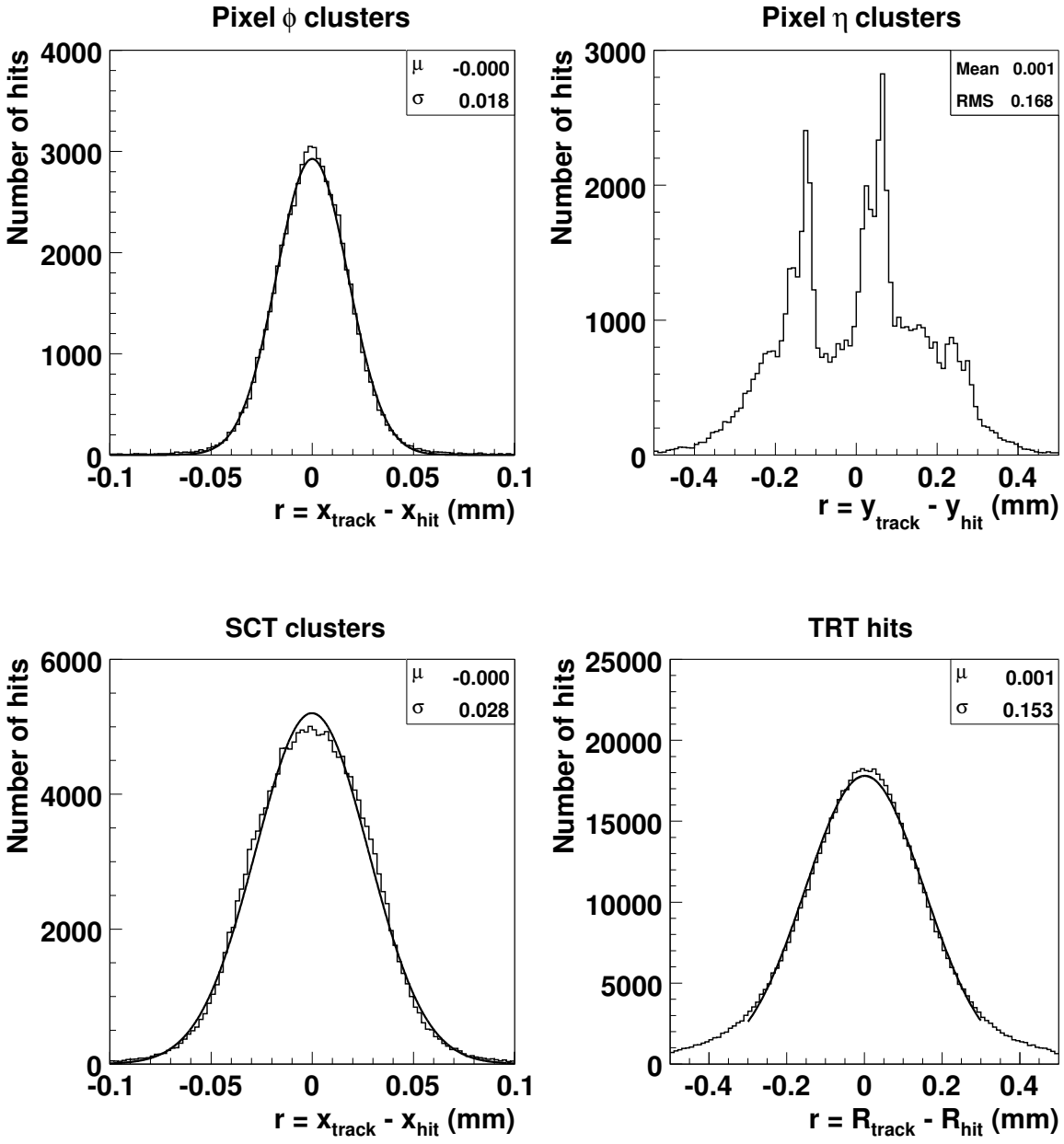

Figure 5.12: *Track fit residuals in the pixel, SCT and TRT detectors, in a run with 100 GeV pions and no magnetic field.*

$$\sigma^2_{meas} = \sigma^2_{resid} - \sigma^2_{track} \tag{5.1}$$

where σ_{track} is given by Eq. (4.8).

The measured resolutions are presented in Table 5.1. The agreement between data and simulation is good.

	Pixel	SCT	TRT
Data (μm)	14 ± 1	26 ± 1	149 ± 2
Simulation (μm)	14 ± 1	24 ± 1	156 ± 2

Table 5.1: *Measured resolutions of the pixel, SCT and TRT detectors, in a run with 100 GeV pions and no magnetic field.*

5.4 Inner detector tracking

5.4.1 Pattern recognition

The reconstruction in the inner detector begins with finding the tracks. The performance of the pattern recognition depends crucially on the quality of the calibration and alignment. On the other hand, the alignment procedures cannot work without tracks. It is therefore important that nearly all the tracks are found, even if a complete set of alignment corrections is not yet available.

The performance of the pattern recognition in CTBTracking with real data is summarized in Tables 5.2 and 5.3. The magnet was running at the full 850A, except for the muon run and the 50 GeV pion run without extra material. We require at least one pixel spacepoint in the event, as a minimal safeguard against 'bad' events (e.g. empty events due to a false trigger). The efficiency with muons is practically 100%. In the case of pions, a few percent of the events have no reconstructed track, due to interactions of the pion in the detector material. The number of secondary particles produced in these interactions increases with energy, thus bringing the average track multiplicity slightly above 1 at higher energies.

Concerning the number of hits on track, it is seen that nearly all the tracks have three pixel hits in them. This shows that the pixel detector was very reliable in the testbeam. The number of SCT hits in pion tracks is mostly between seven and eight, except when one or more SCT readout chips produce faulty data (see section 5.2). Electron tracks clearly have fewer SCT hits than pion tracks, especially when extra material is present between the pixel and SCT setups. This is caused by electrons that suffer catastrophic energy losses, causing them to leave the search window in the pattern recognition (0.7 mm on either side of a circle).

The number of TRT hits is close to 20 per track. However, in some runs the beam is deflected towards a TRT module that was not equipped with readout boards, thus leading to a loss of statistics. This affects for example the 20 GeV pion run without

Particle type	B (Tesla)	Number of tracks per event	Number of hits on track		
			Pixel	SCT	TRT
5 GeV π	1.4	0.97	3.0	6.4	20.3
9 GeV π	1.4	0.99	3.0	5.8	17.7
20 GeV π	1.4	1.02	3.1	7.7	15.4
50 GeV π	0	1.04	3.0	7.8	20.0
100 GeV π	1.4	1.05	3.0	7.8	19.4
20 GeV e	1.4	1.04	3.0	6.0	12.5
180 GeV μ	0	1.00	3.0	7.6	21.2

Table 5.2: *Number of tracks per event and number of hits per track, as a function of particle type and energy.*

Particle type	B (Tesla)	Number of tracks per event	Number of hits on track		
			Pixel	SCT	TRT
5 GeV π	1.4	0.95	3.0	6.2	17.2
9 GeV π	1.4	0.98	3.0	7.5	18.1
20 GeV π	1.4	0.98	3.0	7.1	17.7
50 GeV π	1.4	1.04	3.1	6.8	18.2
100 GeV π	1.4	1.05	3.0	7.8	18.9
20 GeV e	1.4	1.02	3.0	4.9	12.6

Table 5.3: *Number of tracks per event and number of hits per track, as a function of particle type and energy, with extra material in the inner detector setup.*

extra material in the setup. As in the SCT, electron tracks clearly have fewer TRT hits than pion tracks. The average number of TRT hits is actually slightly higher in the run where extra material is present, this is because all the TRT modules were still being read out when that run was taken.

To summarize, we conclude that the performance of the pattern recognition is robust in the testbeam.

5.4.2 Momentum reconstruction

For pions, we expect the following contributions to the momentum resolution:

- The contribution from multiple scattering is given by $\delta p/p \sim 1/\beta$, which is almost constant for relativistic particles;
- The contribution from the precision of the position measurements is proportional to p, i.e. $\delta p/p \sim p$;
- Misalignment of the detector introduces a systematic error on the position measurements, and leads to correlated errors between measurements in different sen-

sors;

- Imperfect knowledge of the magnetic field map introduces a systematic error that scales as $\delta p/p = \delta B/B$;
- For a number of N equidistant measurements, the momentum resolution improves with the square root of N, i.e. $\delta p/p \sim 1/\sqrt{N}$.

The systematic effects only affect the real data, in the simulation the alignment and the magnetic field are assumed to be perfectly known. Note that the observed resolution in the data also depends on the momentum spread in the beam (momentum bite). This spread is quoted to be at most 1%, depending on the beam energy. In the simulation, the uncertainty on the momentum is assumed to be zero.

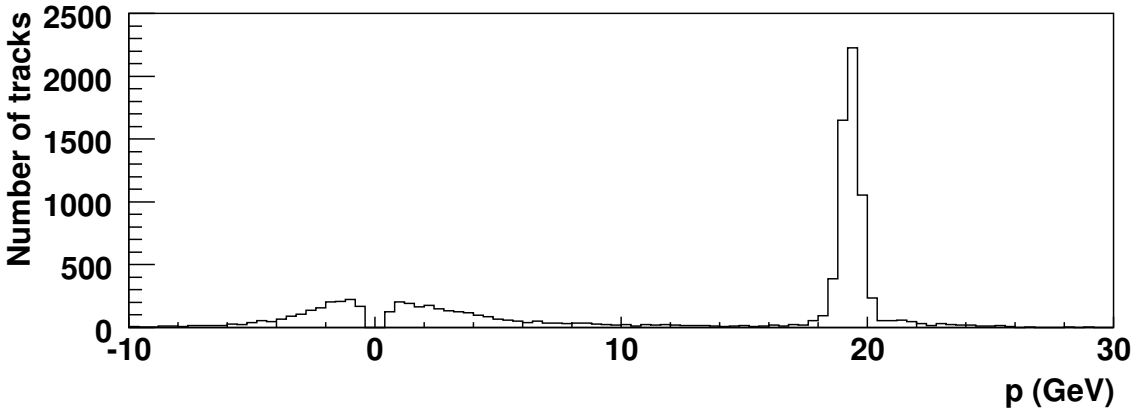

Figure 5.13: *Distribution of reconstructed momenta in a run with 20 GeV pions.*

Fig. 5.13 shows an example of the reconstructed momentum, for pions with a nominal energy of 20 GeV. The peak at 20 GeV is clearly visible, but there is also a bump near $p = 0$. These are low energy electrons that 'contaminate' the beam in this run. They can easily be removed with the Cherenkov detector (requiring $cher2 < 650$). CTBTracking puts a limit of 500 MeV on the particle momentum, this explains the gap at $p = 0$.

We will first investigate the momentum resolution using only the pixel and SCT detectors. These detectors are close to the center of the magnet, where the magnetic field is nearly constant. We expect therefore that the field can only cause a systematic shift in the reconstructed momentum.

The measured resolutions in the runs without (with) extra material are presented in Table 5.4 (5.5). We only use tracks with at least one pixel cluster. The resolution is obtained by performing a Gaussian fit to the observed $1/p$ distribution. Note that $\frac{\delta(1/p)}{1/p} = \frac{\delta p}{p}$, i.e. by measuring the relative resolution on $1/p$ one also obtains the resolution on p.

The resolutions at low momentum are somewhat worse than in the simulation, possibly due to the loss of some SCT hits in these runs (section 5.4.1). In the runs without extra material, the fit qualities of the tracks look quite good, indicating that there are

no major problems with the alignment. The tracks in the runs with extra material are clearly somewhat worse in this respect, and the momentum is systematically shifted by up to 18%. Inspection of the hit residuals in these runs show systematic shifts of up to 25 microns in some modules. Hence, it is likely that misalignment affects the runs with extra material. On the other hand, the momentum resolutions in data and simulation agree fairly well, better than in the runs without extra material. It is clear that the extra material reduces the relative importance of other error sources (e.g. misalignment, loss of hits) for what concerns the momentum resolution. The momentum resolution as a function of energy is summarized in Fig. 5.14.

p (GeV)	Data			Simulation		
	$< \chi^2/ndf >$	shift (%)	σ (%)	$< \chi^2/ndf >$	shift (%)	σ (%)
5	1.03	4.2	4.1	0.91	0.1	2.5
9	0.98	4.1	4.2	0.91	0.2	2.9
20	1.14	3.9	5.1	0.93	0.6	4.3
100	1.08	2.9	17.9	0.88	2.6	18.0

Table 5.4: *Fit quality, momentum resolution and shift in the reconstructed momentum, relative to the nominal momentum, for different data sets. Only the pixel and SCT detectors are used. There is no extra material present.*

p (GeV)	Data			Simulation		
	$< \chi^2/ndf >$	shift (%)	σ (%)	$< \chi^2/ndf >$	shift (%)	σ (%)
5	1.38	8.4	5.1	0.93	0.0	3.7
9	1.20	5.6	4.6	0.93	0.2	4.3
20	1.58	9.4	6.5	0.95	0.6	5.7
50	1.27	12.0	10.8	0.90	1.5	10.0
100	1.14	18.0	18.6	0.87	3.1	18.4

Table 5.5: *Fit qualities, momentum resolutions and shifts in the reconstructed momentum, relative to the nominal momentum, for different data sets. Only the pixel and SCT detectors are used, and there is extra material (11% X_0) between the pixel box and the SCT box.*

The momentum resolutions with the TRT included are summarized in Tables 5.6 and 5.7, and Fig. 5.15. The resolution is up to six times better than what is obtained with only the pixel and SCT hits. This is mostly because one measures the total deflection of the track with the TRT, rather than the sagitta. One can easily show that the deflection (i.e. the distance between the deflected track and the actual track at the first pixel layer) is four times as large as the sagitta, therefore the momentum resolution improves by a factor four. The actual improvement is even bigger because the field integral along the measured part of the track increases when the TRT is included.

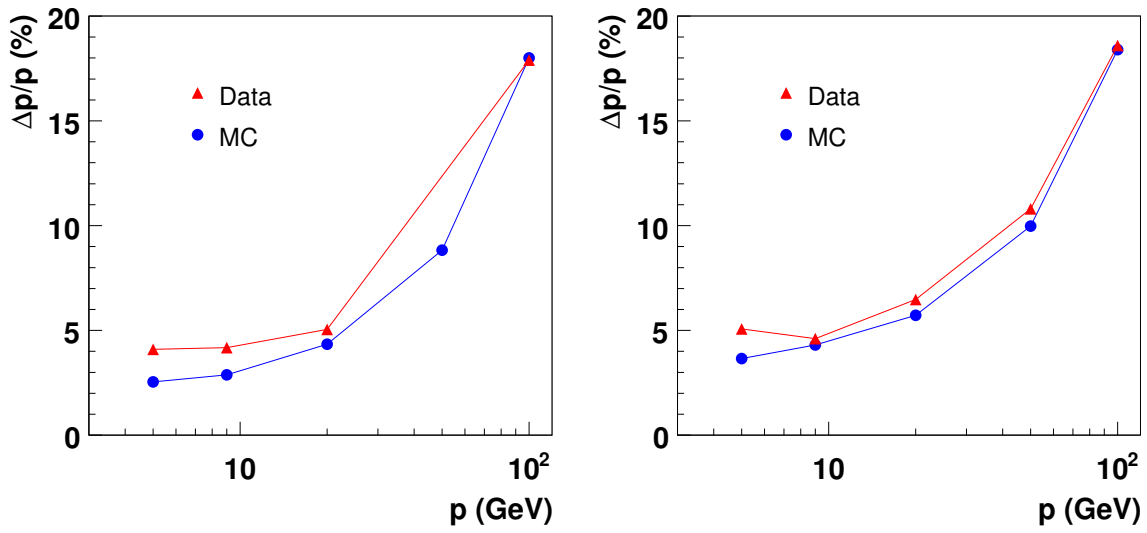

Figure 5.14: *Momentum resolution as a function of energy, using only the pixel and SCT detectors. Left: there was no extra material in the setup. Right: extra material (11% X_0) was installed between the pixel and SCT detectors.*

The results with simulated data show that the intrinsic precision of the detector is very good, giving resolutions at the percent level. This makes the detector quite sensitive to problems with the alignment and the magnetic field, which explains why the resolution in data is two to three times worse than in simulation. There is also a large systematic shift in the momentum at 100 GeV. The alignment of the TRT in this run is still under revision at the time of writing. As before, adding extra material results in a better agreement between data and simulation.

p (GeV)	Data			Simulation		
	$< \chi^2/ndf >$	shift (%)	σ (%)	$< \chi^2/ndf >$	shift (%)	σ (%)
5	1.76	5.6	3.0	1.28	0.0	1.0
9	1.30	6.2	2.8	1.24	0.2	1.0
20	1.56	3.4	2.0	1.21	0.4	1.2
100	1.44	27.5	6.5	1.18	1.6	3.1

Table 5.6: *Fit qualities, momentum resolutions and shifts in the reconstructed momentum, relative to the nominal momentum. The full inner detector is used. There is no extra material present.*

p (GeV)	Data			Simulation		
	$< \chi^2/ndf >$	shift (%)	σ (%)	$< \chi^2/ndf >$	shift (%)	σ (%)
5	1.78	7.1	4.0	1.28	0.1	2.8
9	1.42	6.3	3.0	1.25	0.1	3.0
20	1.92	4.6	3.0	1.23	0.5	3.1
50	1.60	5.7	4.4	1.20	1.0	3.5
100	1.46	15.3	6.9	1.19	1.8	4.2

Table 5.7: *Fit qualities, momentum resolutions and shifts in the reconstructed momentum, relative to the nominal momentum. The full inner detector is used, and there is extra material (11% X_0) between the pixel box and the SCT box, and between the SCT and the TRT (22% X_0).*

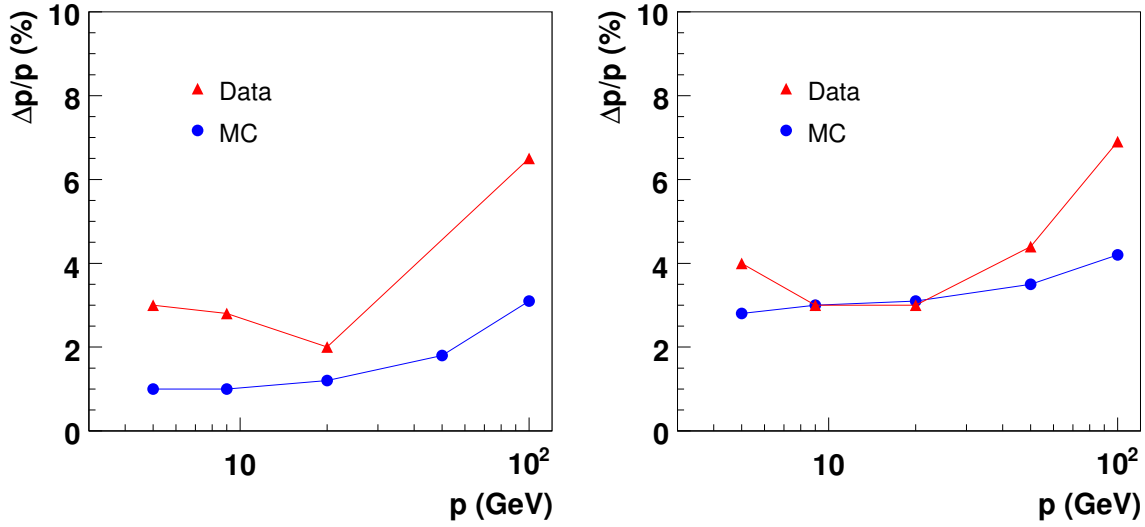

Figure 5.15: *Momentum resolution as a function of energy, using the full inner detector (pixel, SCT, TRT). Left: there was no extra material in the setup. Right: extra material (11% X_0 and 22% X_0) was installed between the pixel and SCT, and between the SCT and TRT detectors.*

5.4.3 Electron reconstruction

Electrons tend to lose large amounts of energy when they traverse material, leading to a long tail towards lower reconstructed momenta. The testbeam is an ideal place to test this effect for different materials. Fig. 5.16 shows the reconstructed momenta in two different runs with 20 GeV electrons, one run with and one run without extra material in the inner detector setup. Note that the shape of the distribution depends crucially on the amount of material in the setup. The amount of material in the inner detector is 0.25 or 0.6 radiation lengths, for runs without and with extra material respectively.

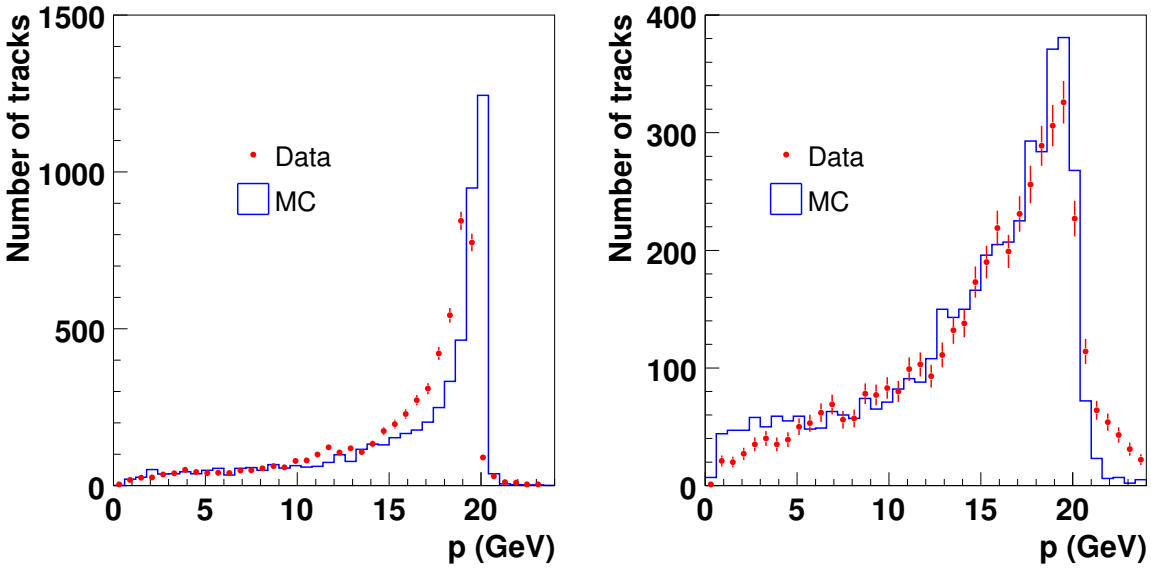

Figure 5.16: *Reconstructed momentum of 20 GeV electrons, in a run without extra material (left) and a run with extra material (right).*

The amount of material in the beam line (upstream of the inner detector) is estimated to be 0.13 radiation lengths, this is also the default value in the simulation.

The agreement between data and simulation in Fig. 5.16 is seen to be reasonable. In the run without extra material, the simulation has a core that is more narrow, and more sharply peaked. This is most likely the result of the momentum resolution that is better in simulation than in real data, as discussed in the previous section. In the run with extra material, the simulation appears to slightly overestimate the fraction of the tail below $p = 5$ GeV. In the data there is a tail towards higher momentum that does not appear in the simulation.

5.5 Combined muon reconstruction

Until now, most studies in the testbeam have focused on understanding the performance of the individual subdetectors. Also correlations between subdetectors have been studied, e.g. the correlation between the impact point of a track in the calorimeter and the position of the calorimeter cluster. However, the ultimate goal of the testbeam is to perform truly *combined* reconstruction, using the information from several detectors at the same time. In this section we will present the results from one such study: the combined inner detector and muon track fit.

The combined fit first attempts to match inner detector tracks with tracks in the muon system. Then, a track fit is performed using all the hits in the inner detector track and the muon track. In ATLAS there are several reasons why such a combined track fit is interesting [68]. The most important ones are:

- The combined fit provides the best possible estimate of the track parameters. For example, the momentum resolution at high momentum improves significantly if the hits in the muon system are included in the fit;

- Requiring a track match in the inner detector and the muon spectrometer reduces the number of fake muons in the reconstruction (i.e. muons that are not produced in the pp-collision). For example, a muon that is produced by a decaying pion will have a bad match with the pion track, due to the kink between the two tracks;

- The momentum resolution in the muon spectrometer suffers from tails, due to energy loss fluctuations in the calorimeter. Including the inner detector in the fit helps to reduce these tails.

The quality of the combined fit clearly depends on the performance of the individual subdetectors. It also introduces additional complications, such as the alignment between the inner detector and the muon detector, and the material that is present in the calorimeter. The material in the calorimeter is equivalent to around 100 radiation lengths, thus it can in no way be ignored in the track fit. In the CTB track fitter, this material is represented by two scattering planes with 50 radiation lengths each. This description is correct up to first order, and is thus sufficient for testing the combined fit procedure.

5.5.1 The muon refit

The combined fit starts by performing a refit on the track in the muon system, which is obtained from the Muonboy package [32]. The muon testbeam software was affected by severe problems with the data decoding and the calibration for an extended period of time, therefore Muonboy could not be completely tuned for the testbeam data. In particular, it has the tendency to drop hits that clearly belong to the track. In our analysis we recover these lost hits by using the track *segments* produced by Muonboy. In the muon system, a segment is a straight line fit to a small number (typically up to eight) of MDT drift circles within a chamber. These segments are an important tool for the pattern recognition. Fig. 5.17 shows an event where Muonboy reconstructs three segments in the EIS muon chamber in the testbeam. Note that only one segment actually belongs to a track, the others can be labeled as background.

With the tracks and segments produced by Muonboy, we use the following procedure to obtain the final list of hits on the track:

- First, the number of segments in the event is checked. If this number is above 50, the event is skipped;

- Only segments are considered that are nearly parallel to the track: the angle between the segment and the track in the local drift plane (i.e. the plane perpendicular to the wires) is not allowed to be larger than 1 degree;

- The distance between the segment and the track in the local drift plane is required to be less than 70 mm. Two such segments are allowed if they lie in different multilayers. No segments are allowed to share one or more hits among them;
- The track is fitted. Then, segments that lie within 5 mm of the refitted track are added to the track, and the track is fitted again. This is repeated until no more segments are added to the track.

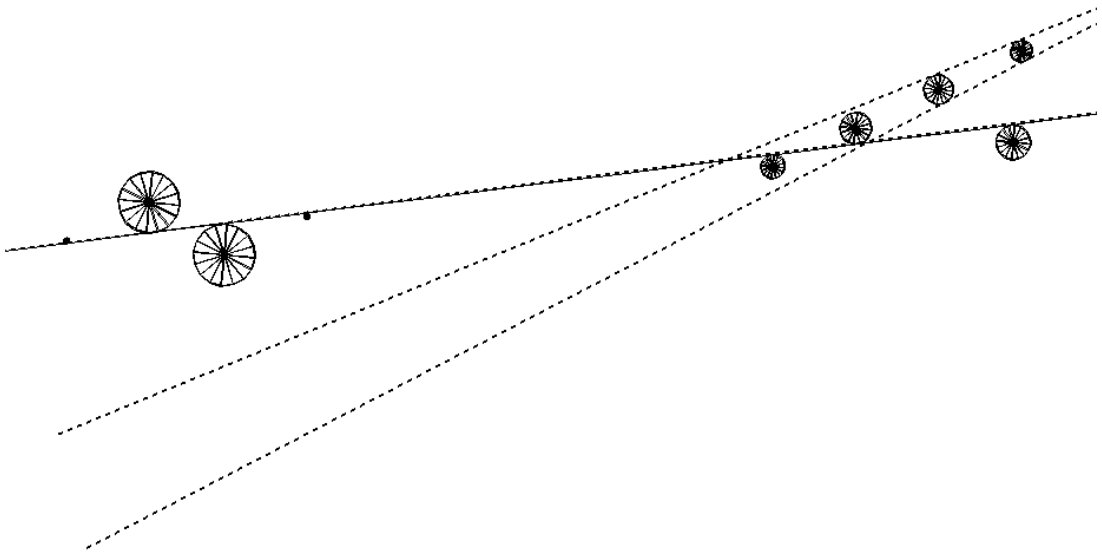

Figure 5.17: *Display of the MDT drift circles in the EIS chamber, in an actual testbeam event. The circles on the left are the hits in the first multilayer, the ones on the right belong to the second multilayer. The Muonboy segments are shown as dotted lines, the Muonboy track is drawn as a straight line.*

Fig. 5.18 shows the number of MDT and RPC hits per track after the refit, in a run with 180 GeV muons. Most tracks have around 50 hits.

The CTB track fit does not correct for multiple scattering in the muon system. Thus, it will only give reasonable results if the effect of multiple scattering is small compared to the detector resolution. In order to test the effect of multiple scattering, the muon refit was tested with simulated testbeam data, where the muon system is perfectly aligned and calibrated. Fig. 5.19 shows that multiple scattering does appear to have some effect on the track fit: the residuals in the MDT chambers are around 120 micron, where 80 micron is expected. We will show in a moment that the resolution per hit is much worse in real data, due to miscalibration and misalignment. We conclude therefore that multiple scattering can be ignored in the muon testbeam.

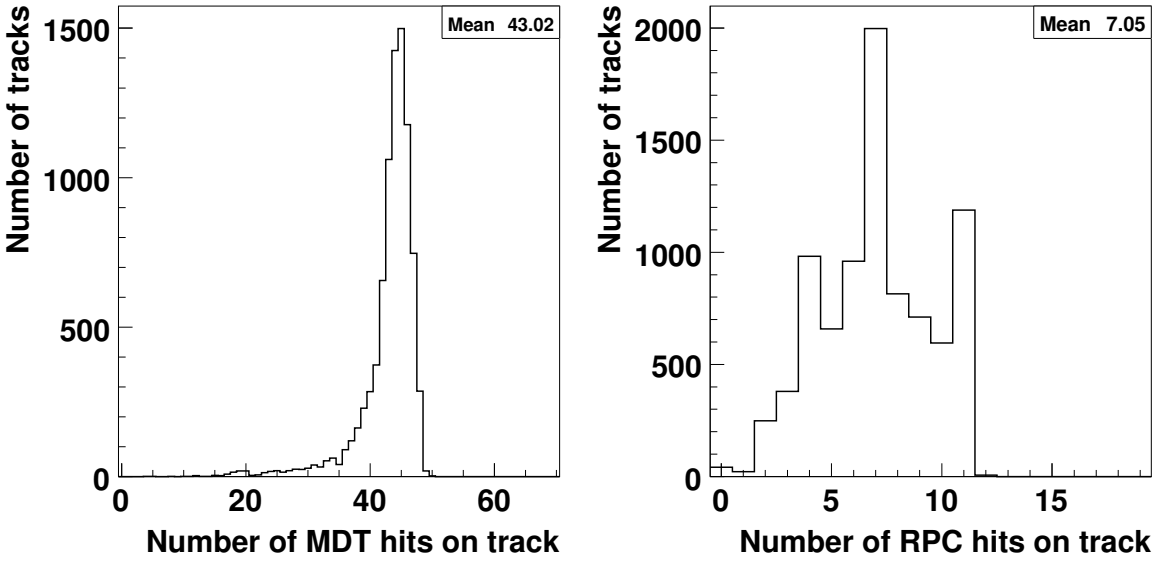

Figure 5.18: *Number of MDT and RPC hits per track, in run 2102550 of the testbeam (180 GeV muons, no magnetic field).*

We now return to the real data. The hit residuals in the track fit are shown for four individual chambers in Fig. 5.20. Two of the plots show clear displacements, indicating that these chambers are misaligned in the reconstruction. The alignment procedures in the barrel and endcap muon setups are completely independent, i.e. no attempt is done to align the barrel setup relative to the endcap. Thus, a track fit that uses the hits in both the barrel and endcap can be expected to reveal such misalignments.

Some of the plots have much longer tails than others, indicating a possible problem with the calibration. As mentioned in section 5.1.4, the $r(t)$ relation that is used in reconstruction is obtained from the rotating BIL chamber. It is possible that temperature variations reduce the validity of this $r(t)$ relation for chambers that are further away from the rotating BIL chamber, in particular for the endcap chambers. The endcap chambers are the ones closest to the big garage door in the H8 building, which was frequently kept open during the testbeam. The longest tails are observed in the EML and EOL chambers, which does not contradict

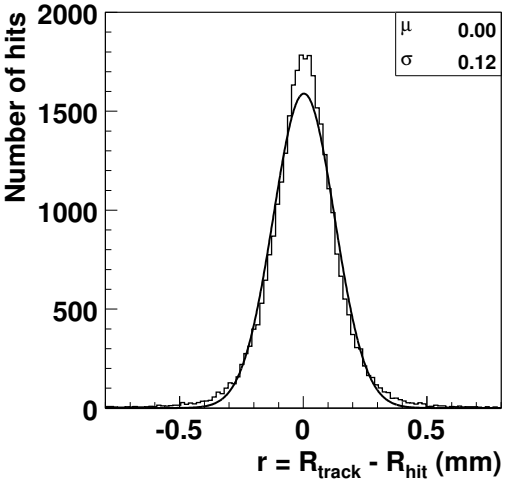

Figure 5.19: *Tracking residuals in the MDTs, for simulated muons of 180 GeV.*

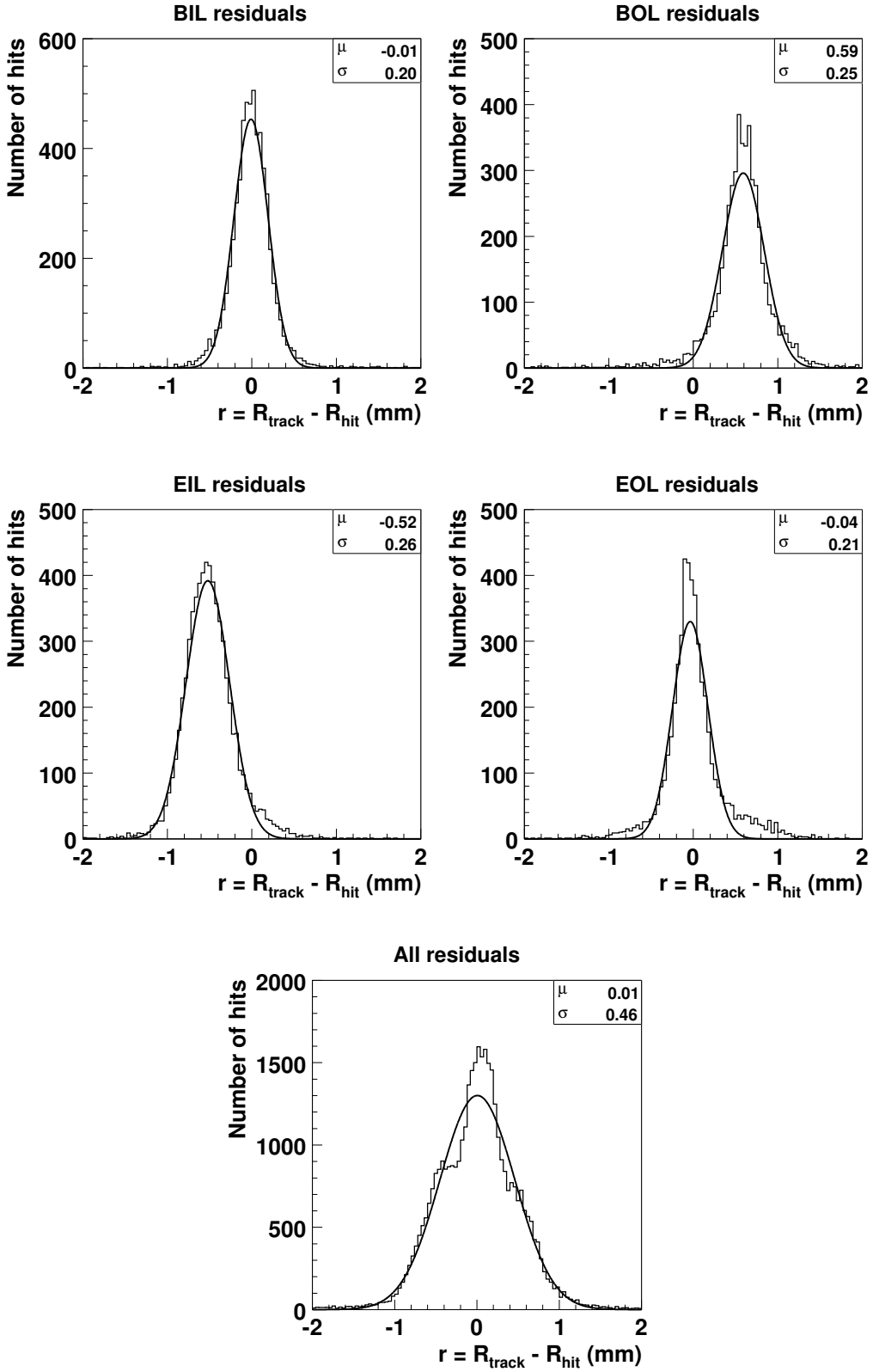

Figure 5.20: *MDT residuals in four different chambers (BIL,BOL,EIL,EOL) in the testbeam, and in all the chambers at once.*

the 'garage door' hypothesis. A separate study also found that the endcap chambers perform somewhat worse than the barrel chambers due to temperature fluctuations [69].

The average residual for all the chambers is found to be around 500 micron. Muonboy has the possibility to set the MDT resolution by hand, this value is then used to calculate the weights of the hits in the fit. The refit with the CTB fitter uses the same value as Muonboy. In our analysis we set the resolution to 0.5 mm.

5.5.2 The combined fit

After producing the tracks in the inner detector and the muon detector, the combined fit can be performed. First, inner detector tracks need to be matched to muon tracks. This step is kept very simple: the combined fit is attempted if both the inner detector and the muon detector have exactly one reconstructed track, which happens in 94% and 89% of the events respectively[2]. The fraction of events with exactly one track in both subsystems is 85%.

As before, we use a run with 180 GeV muons and no magnetic field. The absence of a magnetic field means that the CTB fitter cannot determine the momentum by itself, which it needs to estimate the multiple scattering. In this study we therefore set the momentum in the fit to a fixed value of 180 GeV.

The combined fit is started using the track parameters of the inner detector track, and with the scattering angles initialized to zero. Fig. 5.21 shows that the fit converges rapidly: after a few iterations the χ^2 values have been reduced by five orders of magnitude.

The fit quality and the total number of hits in the combined fit is shown in Fig. 5.22[3]. The fit quality is worse than in the inner detector and muon standalone fits, but it is still reasonable. The TRT hits in the problematic third TRT layer were included in the fit, the fit quality would be even better if these were omitted.

As might be expected, the track fit is dominated by multiple scattering in the calorimeter. Running the fit without material corrections results in χ^2 values that are several orders of magnitude larger. Thus, the results show that the combined fit and the corrections for multiple scattering work quite well.

Fig. 5.23 shows an example of a combined muon track, using the V-ATLAS event display [40]. The liquid argon calorimeter is not visible, because the testbeam setup of this detector has not yet been implemented in the detector description package GeoModel. For the purpose of this analysis, the display was modified to show the scattering centers on the track, and to follow the fitted scattering angles at these centers. These changes are completely generic and will also work in ATLAS, with any fitter that provides the scattering angles on the track.

[2]Note that we consider *all* the events here, not just the ones with at least one pixel space-point.

[3]The SCT became desynchronized with respect to the other detectors after 4000 events, therefore we only use the first 4000 events in the run.

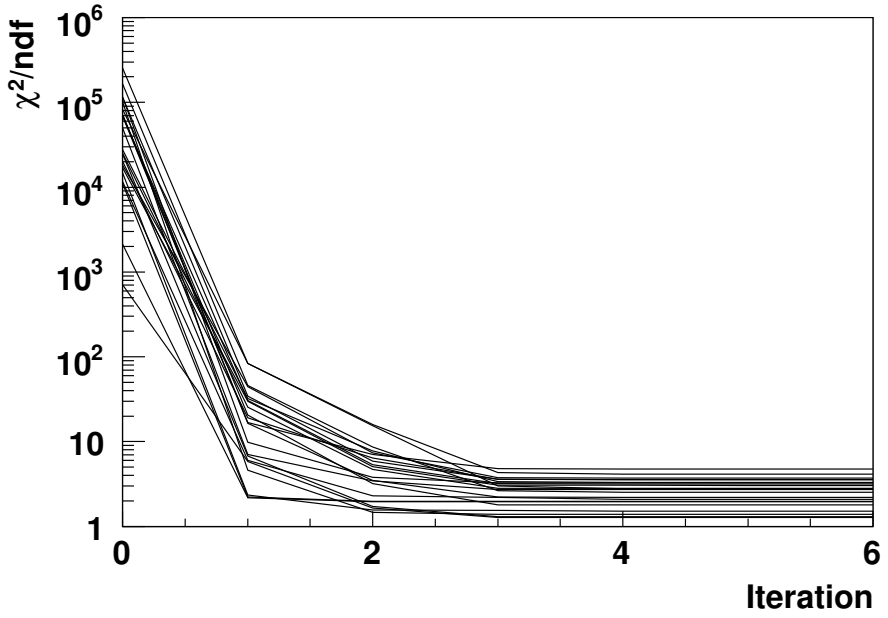

Figure 5.21: *Fit quality of the combined fit, as a function of iteration number.*

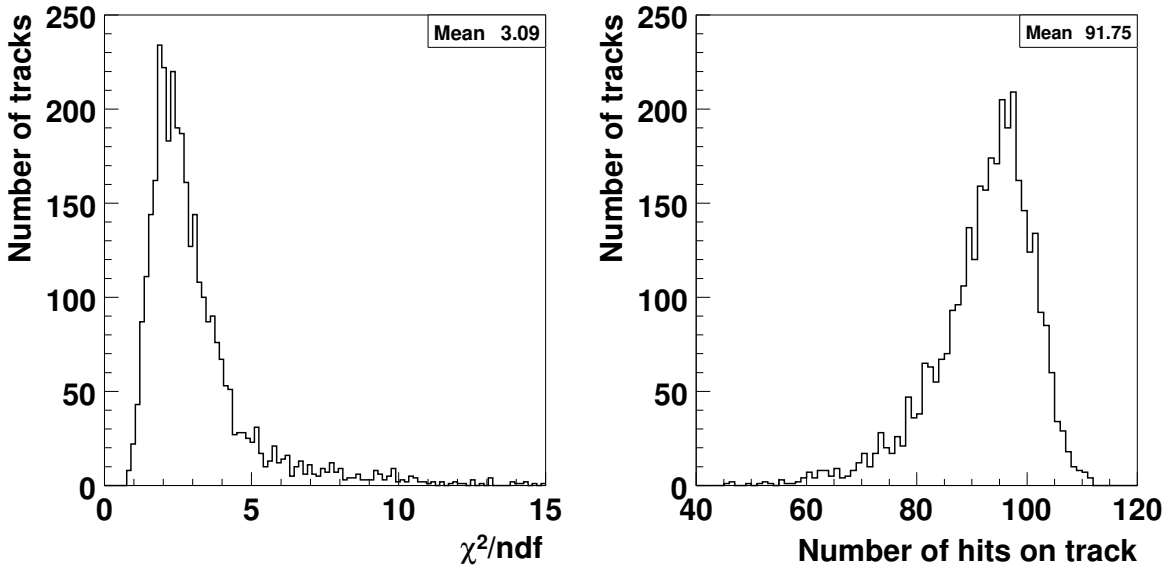

Figure 5.22: *Fit quality and number of hits in the combined muon fit. For the MDT hits a measurement error of 0.5 mm is assumed, for the other hits the nominal error is used (i.e. the expected error in absence of misalignment and miscalibration).*

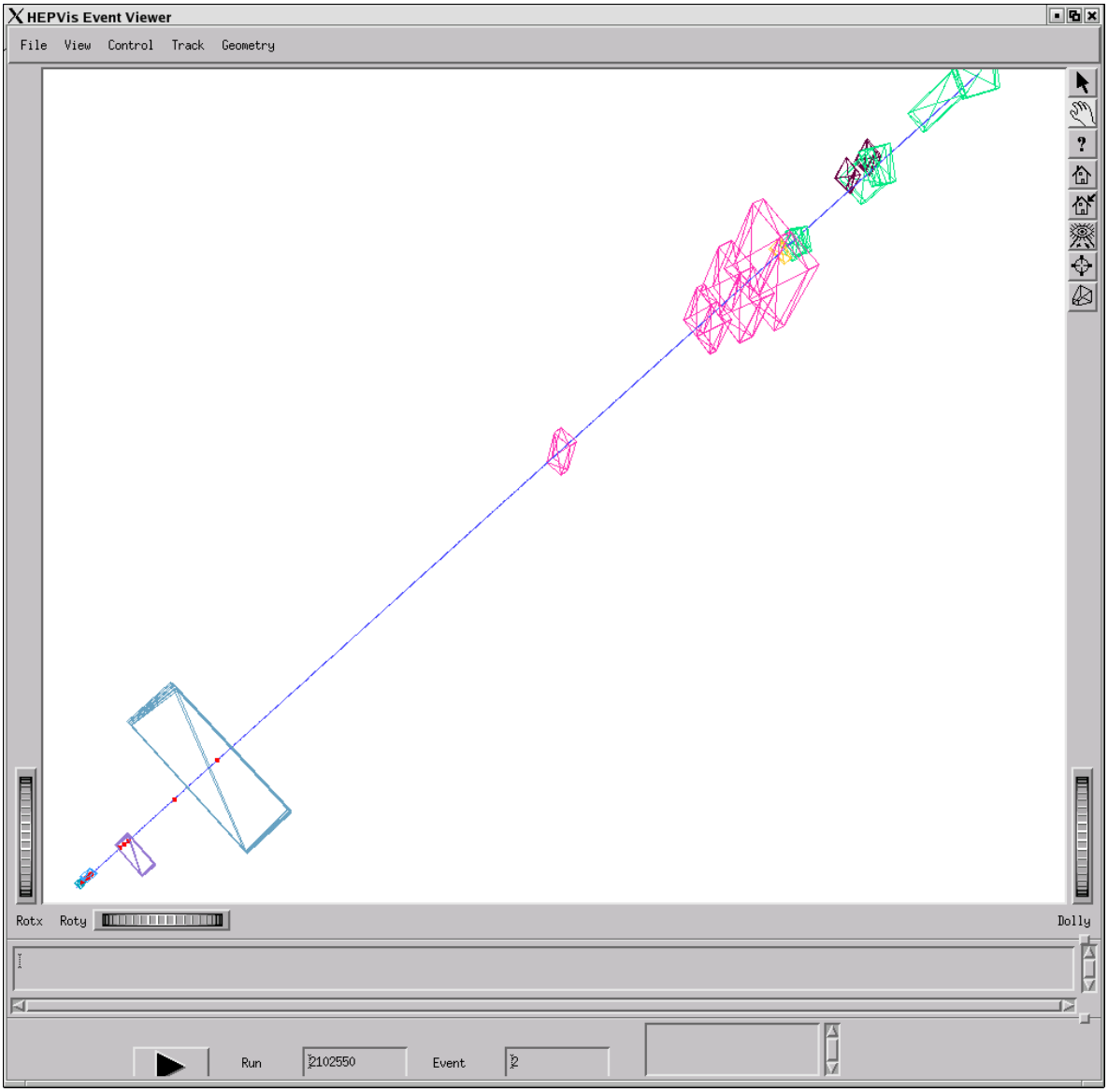

Figure 5.23: *Display of a combined muon fit in the testbeam. From the bottom left to the top right, the track crosses the pixel and SCT boxes, the TRT, the tile calorimeter, and the muon chambers. The track is 60 meter long. The red dots on the track are the scattering centers, i.e. the points where the track is allowed to change its direction in the fit.*

5.6 Conclusions

The combined testbeam was the largest test for ATLAS before actual data taking starts in 2007. Many goals were achieved: for example, it was shown that all the various subdetectors can take data together, using the final (or nearly final) versions of the readout electronics. Some parts of the data acquisition chain were not ready at the time of the testbeam, which resulted in some problems with the data quality. Nevertheless, the results from combined muon reconstruction show that combined reconstruction with all the detectors was indeed possible.

The track reconstruction was able to support the testbeam from the very beginning. There is still room for improvement in the alignment, which explains why the reconstruction performs somewhat worse with the real data than in the simulation. An important aspect of the testbeam was that the reconstruction made use of the conditions database, to obtain the calibration and alignment corrections. The conditions database had not been tested at all before the testbeam took place, because ATLAS simulations were always performed assuming a perfect detector. Some deficiencies were found during the testbeam, e.g. in the offline detector description which sometimes 'forgot' to apply the alignment corrections to the detector elements. Most of these problems have been fixed, such that they won't affect ATLAS when it starts its search for new physics.

Chapter 6

The detection of gravitons in models with extra dimensions

In this chapter the detection of graviton resonances with ATLAS is studied. Since ATLAS is still under construction, the results are based on simulated data. We will study the Randall-Sundrum model, which predicts narrow spin-2 resonances at the TeV scale (see chapter 1).

Section 6.1 gives an overview of the signal and background processes in our model. The generation, simulation and reconstruction of the events is described in section 6.2. The results of detecting the graviton resonance (through the invariant mass of lepton pairs) are presented in section 6.3. In section 6.4 a likelihood fit to the angles of the decay products is performed, to study the properties of the spin-2 state versus the background.

6.1 Signal and backgrounds

Because the graviton (G) couples universally to all the Standard Model particles, there are many different decay channels that can be studied. However, not all of them are potential discovery channels. For example, the $G \to q\bar{q}$ signal would be overwhelmed by QCD di-jet production. The channels that we will study in this chapter are:

$$G \to e^+e^-, \qquad G \to \mu^+\mu^-. \tag{6.1}$$

The presence of two energetic leptons makes it easy to trigger on the events. Furthermore, the mass of the graviton resonance can be reconstructed very precisely in the $G \to e^+e^-$ channel, thanks to the excellent energy resolution of the electromagnetic calorimeter in ATLAS. At very high energies, the electron energy resolution of the calorimeter scales as follows:

$$\frac{\Delta E}{E} \propto \frac{a}{\sqrt{E}} \oplus b. \tag{6.2}$$

Due to the degradation of the muon momentum resolution at higher muon momenta, the mass resolution in the $G \to \mu^+\mu^-$ channel is much poorer. The momentum resolution

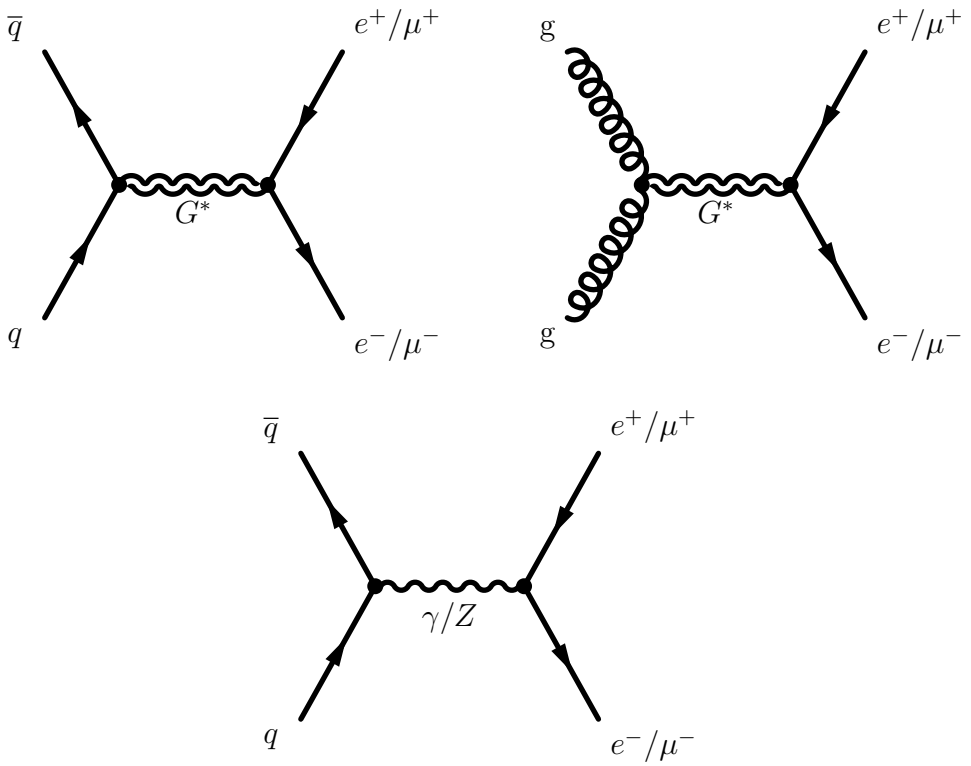

Figure 6.1: Feynman diagrams showing the signal (top) and background (bottom) processes in the analysis.

for muons (measured by the muon spectrometer) scales as:

$$\frac{\Delta p}{p} \propto p. \tag{6.3}$$

Thus, the performance of the trackers (i.e. the inner detector and the muon spectrometer) becomes worse at higher energies, while the calorimeter becomes better.

The decay to muons is not very attractive as a discovery channel, due to the poor mass resolution. However, measuring the branching ratio would still be useful to confirm the universality of the graviton coupling. Note that in the Standard Model, the couplings of the leptons to the gauge fields are also universal. Therefore, a study of the decay into vector bosons (e.g. $G \to ZZ$ or $G \to \gamma\gamma$) would be more interesting in this respect. We did not study the $G \to \gamma\gamma$ channel here, because the background in this channel is not well understood [70].

Several background processes affect the detection of the signal. The Standard Model background is formed by the Drell-Yan process, i.e. $\gamma/Z \to e^+e^-$ and $\gamma/Z \to \mu^+\mu^-$. This background is well understood, and is quite small at the energies that are relevant here. It is an irreducible background, i.e. the signature in the detector is identical to that of the graviton process: two leptons with opposite charge and (approximately) opposite direction at the vertex[1].

[1]The angular distributions of the decay products are different, because the graviton has a

Another possible background would be the hypothetical Z' particle. The Z' behaves like the Z-boson in the Standard Model, except that its mass is much larger. If a signal is found in the ATLAS data, then the question comes up to which particle this signal belongs. The Z' is different from the graviton in the following ways:

- The graviton couples universally to all other particles, unlike the Z'. In particular, the Z' does not decay into two photons. Hence, a study of the decay into a photon pair would make the exclusion of either the graviton or the Z' hypothesis possible.
- In the model that we consider here, the width of the graviton resonance is much smaller than the detector resolution. On the other hand, the width of the Z' is more than 50 GeV for a Z' mass of 2 TeV.
- The Z' is a spin-1 resonance, while the graviton has spin 2. Therefore the angular distributions of the decay products are quite different. A confirmation of the spin-2 nature of the resonance will be the ultimate signal. The determination of the spin of the resonance is discussed in section 6.4.

6.2 Event generation & simulation

The production of gravitons in the proton-proton collisions is simulated using PYTHIA 6.323 [37], with the CTEQ6L1 parton distribution functions (PDFs) [71]. PYTHIA has the option to set the mass of the graviton, as well as a dimensionless coupling $k/\overline{M}_{Pl}$. In our study we leave the coupling at its default value of 0.01. The angular distributions of the decay products are given in Table 6.1. Here θ^* is the angle between the decay electron and the beam direction in the di-lepton center-of-mass frame. Table 6.2 lists the widths of the graviton resonance, and the cross section times branching ratio $\sigma \cdot B$, for the $G \to e^+e^-$ and $G \to \mu^+\mu^-$ channels. Finally, Fig. 6.2 shows the p_T distribution of the electrons generated by PYTHIA, as well as their difference in angle.

Process	Distribution
$gg \to G \to e^+e^-$	$1 - \cos^4\theta^*$
$q\overline{q} \to G \to e^+e^-$	$1 - 3\cos^2\theta^* + 4\cos^4\theta^*$
$q\overline{q} \to V \to e^+e^-$	$1 + \cos^2\theta^*$

Table 6.1: *Angular distributions of leptons in di-lepton production through a graviton intermediate state (G), and through a vector boson intermediate state (V).*

The choice of PDF set requires more discussion. In a number of other analyses that involve gravitons, large discrepancies in the production cross sections have been noted, depending on the particular PDF set that is used [72, 73]. It is likely that differences in

different spin than the photon and the Z-boson. However, this difference has little discriminating power for what concerns event selection.

Mass (GeV)	Γ_G (GeV)	$\sigma \cdot B$ (fb)	Gluon fraction (%)
1000	0.142	6.5	81
1500	0.213	0.72	69
1600	0.227	0.49	68
1700	0.241	0.34	65
1800	0.255	0.24	63
1900	0.270	0.18	60

Table 6.2: *The most relevant parameters in the graviton production as simulated by PYTHIA: the width of the resonance, the cross section times branching ratio for the $G \to e^+e^-$ channel, and the fraction of the $gg \to G$ channel in the total production cross section.*

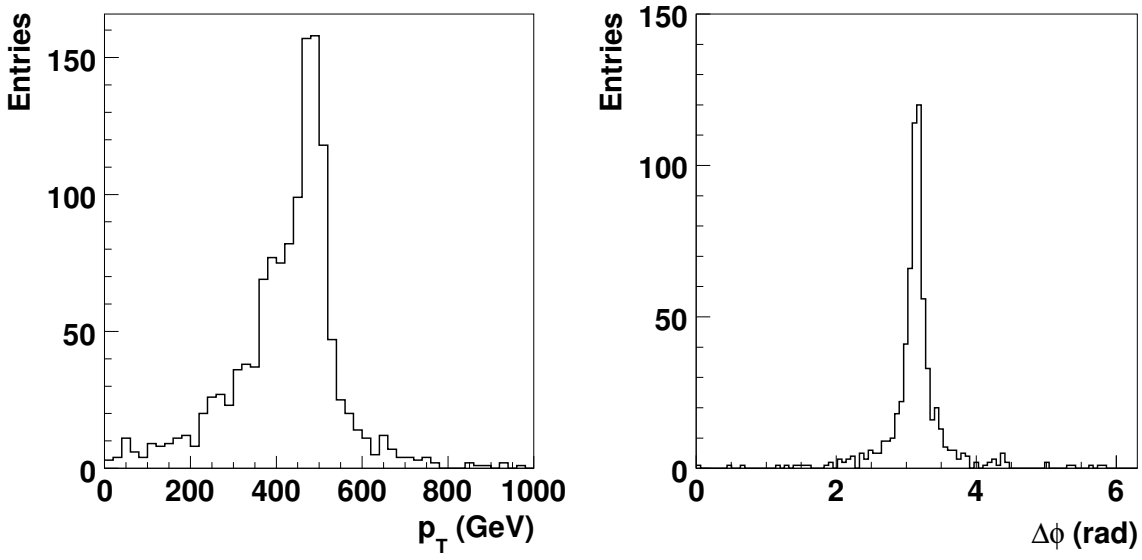

Figure 6.2: *Left: p_T of the electrons at generator level. Right: difference in azimuthal angle between the generated electrons. The graviton mass was 1 TeV.*

the high-x behavior of the PDFs can explain this. We remark here that the cross sections that we observe are almost a factor two lower than the ones reported in Ref. [74].

The final state radiation (FSR) of the particles is simulated using the PHOTOS generator [75]. This has a sizeable effect on the decay leptons: often they radiate one or more photons of hundreds of GeV. The implications of this for the reconstruction will be discussed later in this chapter.

After generating the events, the next step is to simulate the detector response. This is done by the G4ATLAS program, which uses GEANT4 to perform the actual simulation. The simulation was performed on the GRID, in jobs of 50 events each. Each event takes around 20 minutes to complete. Approximately 4000 events were simulated and

reconstructed. No pile-up was included in the simulations, so the study effectively applies to a low luminosity scenario.

To gain more insight into the model, the simulation was also performed using the Atlfast package [76]. Atlfast simulates the detector response by placing cuts on the pseudorapidity of the particles, and by smearing their four-momentum vectors. For muons, the smearing is performed using Gaussians. For electrons, first the momentum is smeared using a function that describes the energy loss of the electron in the detector material. Then, a Gaussian smearing is applied as for muons. Track reconstruction inefficiencies within the detector acceptance are not simulated by Atlfast. In many analyses, an efficiency of 90% is applied for electrons. This point is of no concern to us, since we base our analysis on fully simulated data.

6.3 Detection of the graviton resonance

6.3.1 $G \to e^+e^-$

Electrons are reconstructed by the eGamma package. In this package, electron candidates are built by matching tracks to calorimeter clusters. For candidates that pass an initial set of matching cuts, a flag called 'isEM' is computed. This flag consists of a number of bits (i.e. a '0' or a '1') that represent the outcome of a particular cut. The set of cuts includes cuts on the shower shape in the calorimeter, the quality of the track, and the quality of the track-cluster match (E/p, angle matching)[2]. The electron four-vector is calculated using the energy in the calorimeter cluster, and the direction as measured by the track. The charge is also taken from the track. The momentum of the track is not used because at these high energies, the momentum resolution of the tracker is orders of magnitude worse than the energy resolution of the calorimeter.

The graviton signal can be detected using the invariant mass of electron-positron pairs. We use pairs that satisfy the following criteria:

- The two leptons have opposite charge;
- $p_T > 30$ GeV for both leptons;
- In the isEM flag, only the calorimeter cuts are used.

We will first study the quality of the reconstruction, using the event sample where the graviton mass was 1 TeV. The number of reconstructed electrons that satisfy the p_T and isEM cuts is shown in Fig. 6.3. The plot includes only those events where both leptons were generated inside the acceptance of the tracker (i.e. $|\eta| < 2.5$). The energy resolution of the reconstructed electrons is also shown in Fig. 6.3. Note that the calorimeter actually reconstructs the electron together with its FSR photons: since the FSR photons are collinear with the electron, they end up in the same cluster and the energies just add. Thus, final state radiation does not affect the reconstruction too much in our case[3].

[2] A more complete description of the cuts in the eGamma package can be found in Ref. [77].

[3] In Atlfast, electrons and photons are always treated separately, so the final state radiation

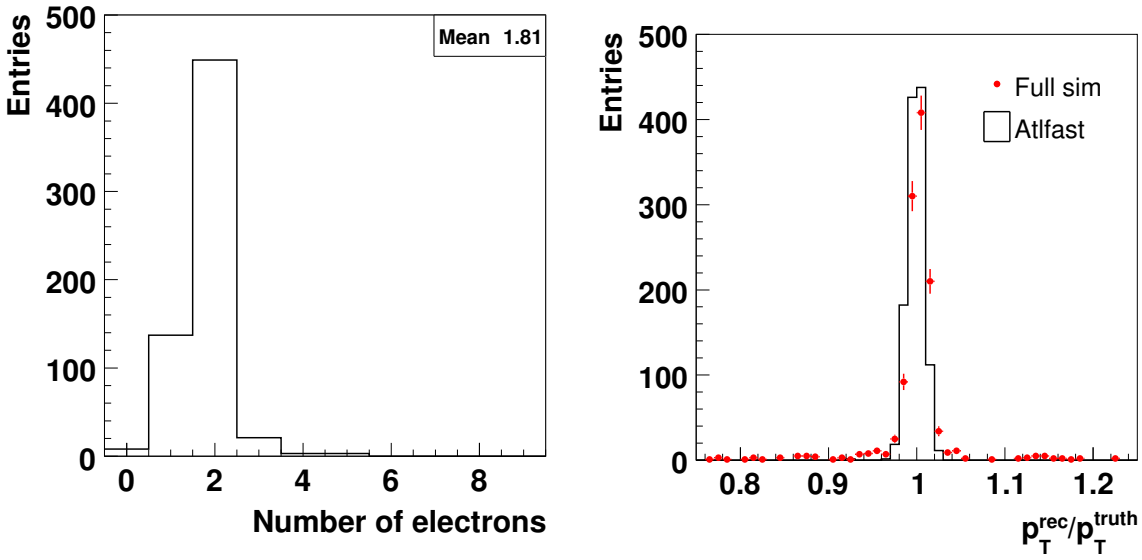

Figure 6.3: *Left: number of reconstructed electrons that pass the quality cuts. Right: energy resolution of the reconstructed electrons.*

To determine the number of signal events, a procedure is required to subtract the number of background events. We fit the background with a function of the form αm^{β}, where m is the invariant mass, and α and β are free parameters. The background is shown together with the fitted function in Fig. 6.5. The signal is prominent above the small Standard Model background. We assume an integrated luminosity of 100 fb^{-1}, which corresponds to one year of LHC running at its design luminosity.

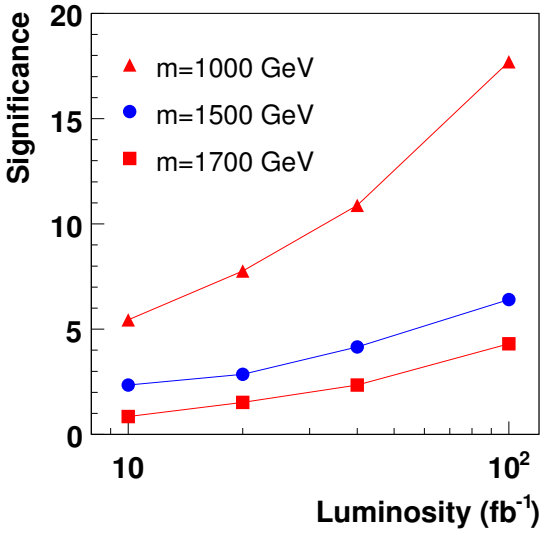

Figure 6.4: *Significance of the signal as a function of integrated luminosity, for the $G \to e^+e^-$ channel.*

Fig. 6.6 gives a closer view of the observed graviton peak, for the sample where the graviton mass was 1 TeV. A mass window around the graviton peak (in this case ± 21 GeV) is selected, and the total number of events within the mass window is counted. The fitted background is integrated over this mass window, to obtain the number of background events. This is subtracted from the total number of events, to get the number

is not recovered. In that case, one would probably have to disable the simulation of FSR.

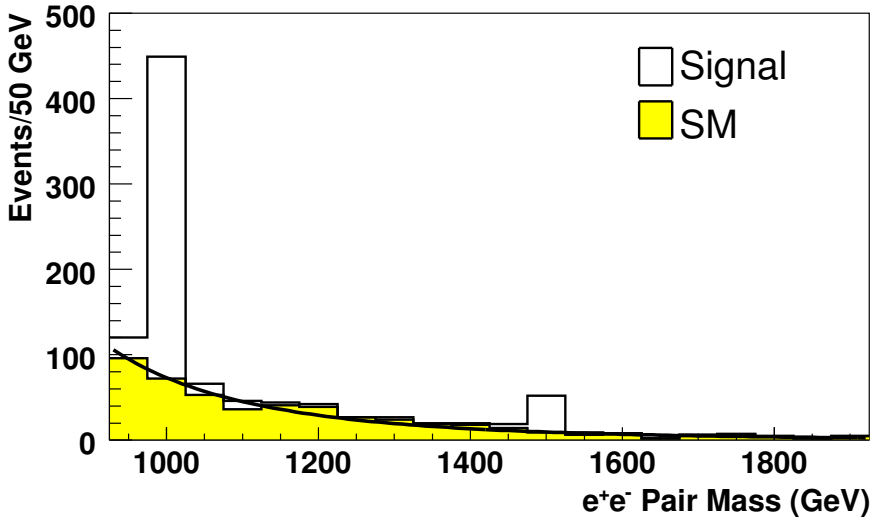

Figure 6.5: *Invariant masses of electron-positron pairs from graviton production with $m_G = 1$ TeV and with $m_G = 1.5$ TeV (signal), superimposed on the expected Standard Model background. The fit to the background is also shown. The number of simulated events corresponds to 100 fb^{-1} of integrated luminosity.*

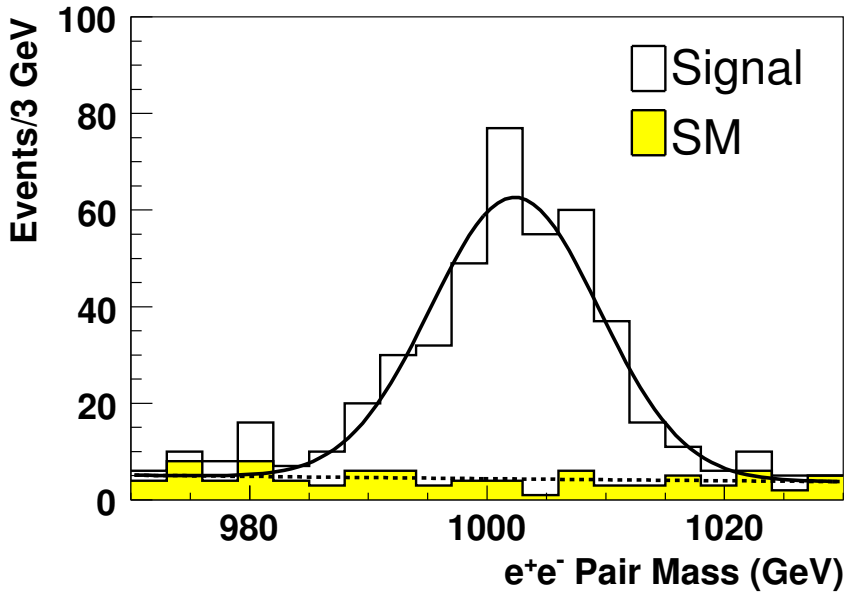

Figure 6.6: *Invariant masses of electron-positron pairs from graviton production with $m_G = 1$ TeV (signal), superimposed on the expected Standard Model background.*

of signal events. Table 6.3 shows the number of signal and background events obtained in this way, as well as the statistical significance of the signal. Also shown is the efficiency, i.e. the ratio of the number of reconstructed gravitons to the number of generated gravitons. Finally, Fig. 6.4 shows, for three different values of the graviton mass, how the statistical significance of the signal improves as the integrated luminosity increases.

Mass (GeV)	Mass window (GeV)	N_{sig}	N_{bg}	$N_{sig}/\sqrt{N_{sig}+N_{bg}}$	Efficiency (%)
1000	±21	364	61.5	17.7	56
1500	±36	51.4	13.6	6.4	72
1600	±36	28.2	9.8	4.6	58
1700	±40	25.0	8.0	4.3	74
1800	±40	16.0	6.0	3.4	67
1900	±40	9.4	4.6	2.5	55

Table 6.3: *The selected mass window, and the number of signal and background events within the mass window. The mass window corresponds to roughly three times the observed width of the resonance.*

6.3.2 $G \to \mu^+\mu^-$

As mentioned in the introduction, the $G \to \mu^+\mu^-$ channel is not very interesting as a discovery channel, because the momentum resolution of muons at the TeV scale is much worse than that of electrons. Still, a measurement of the cross section times branching ratio of this channel would allow a measurement of the coupling. We will therefore briefly discuss this channel.

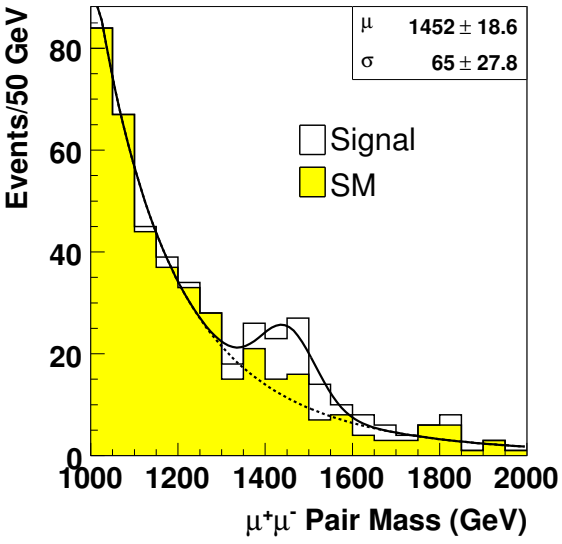

Figure 6.7: *Observed mass peak in the $G \to \mu^+\mu^-$ channel.*

The muons are reconstructed by the MUID package [78]. This algorithm performs a matching between tracks in the inner detector and the muon spectrometer, and then performs a combined fit using all the hits on the track. Energy loss in the calorimeter is taken into account by using the actual energy loss as measured by the calorimeter, or by using a parametrized energy loss. In our analysis we use muon pairs with opposite charge, and we require $p_T > 30$ GeV for both muons. The resulting invariant mass plot, using both signal and background events, is shown in Fig. 6.7. The graviton mass was 1.5 TeV. The data is fitted with a background term of the

Mass (GeV)	NLL (sig+bg)	NLL (bg)	Δ NLL
1000	256.4	292.8	36.4
1500	41.1	47.6	6.5
1600	24.2	27.9	3.7
1700	21.9	23.6	1.7

Table 6.4: *Negative log likelihoods using the fitted p.d.f. (Eq. (6.4)), and using the spin-1 p.d.f. (i.e. $x = 0$).*

form αm^{β}, plus a Gaussian term. The mass resolution is about ten times worse than in the $G \to e^+e^-$ channel. Note that FSR photons are in principle not recovered by the muon reconstruction. It might be useful to try to recover these in our analysis, but we did not investigate this.

6.4 Angular distributions

Once the graviton has been detected, it is necessary to determine its spin by measuring the angles of the decay products. The angular distributions for the graviton and Standard Model production processes were given in Table 6.1. These distributions cannot be directly fitted to the data, because of the detector acceptance. This acceptance is dominated by the coverage of the inner tracker ($|\eta| < 2.5$), which removes events at large $|\cos\theta^*|$. The cutoff is quite sharp for heavy gravitons, which are produced with little longitudinal momentum, while it is more smeared out for lighter gravitons.

The expected angular distributions (i.e. corrected for the detector acceptance) can be obtained from Atlfast, which we will call 'Monte Carlo'. These distributions can then be fitted to the fully simulated 'data'. Fig. 6.8 shows the distributions as obtained from Atlfast, for a graviton mass of 1 TeV. Only the events that fall within the mass window of 1000 ± 21 GeV are used. The distributions are fitted with a fifth order Chebychev polynomial times the theoretical function (i.e. the function in Table 6.1).

We now try to fit the following probability density function (p.d.f.) to the 'data':

$$p.d.f. = x f_{sig}(\cos\theta^*, M) + (1-x) f_{bg}(\cos\theta^*, M) \tag{6.4}$$

The function f_{sig} is a mixture of the $q\bar{q} \to G$ and $gg \to G$ distributions. The gluon-gluon fraction (see Table 6.2) is kept fixed during the fit, only the fraction x is allowed to change. The fitted function is shown together with the data points in Fig. 6.9. The distribution expected for a spin-1 particle (i.e. $x = 0$) is also shown.

Whether the spin-1 hypothesis can be excluded in favor of the spin-2 hypothesis can be checked using the likelihoods of the fits. The likelihood is obtained by evaluating the p.d.f. at each event, and multiplying the results. Table 6.4 lists the negative log likelihood (NLL) using the fitted x, and using $x = 0$. The larger the difference between these two, the more likely the spin-2 hypothesis becomes. In our case, the spin-1 hypothesis can be excluded with more than 90% confidence level up to a graviton mass of 1.7 TeV.

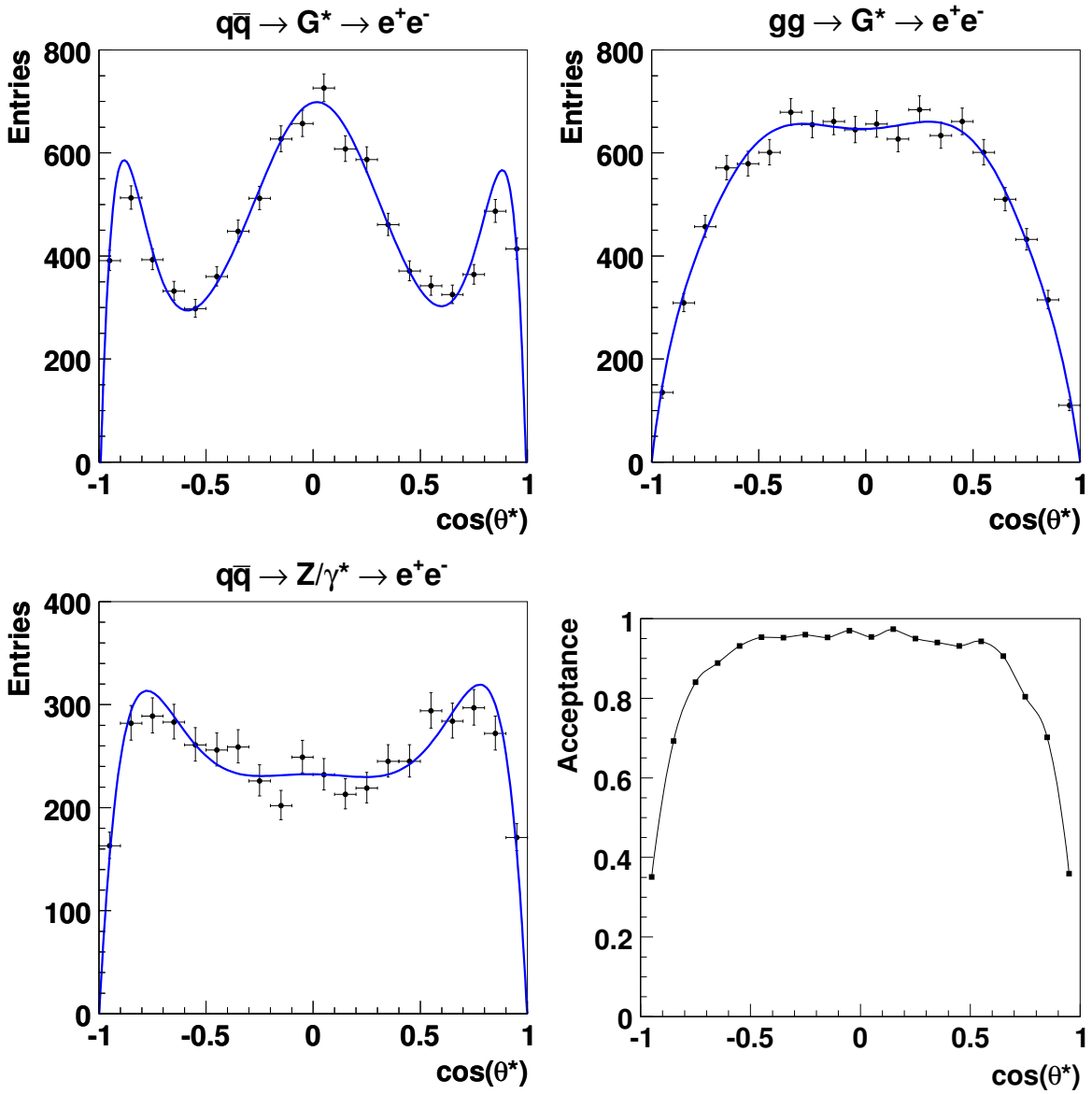

Figure 6.8: *Angular distributions of the decay leptons for the three production processes, obtained using Atlfast. The fitted functions are described in the text.*

6.5 Conclusions

In this chapter the detection of graviton resonances with ATLAS was studied. In the $G \rightarrow e^+e^-$ channel, a signal at the 5σ level could be obtained up to a graviton mass of 1.5 TeV. This is clearly lower than the discovery limit that was reported in earlier work, due to changes in the underlying PDF set. Apart from that the discovery potential with ATLAS is robust, with a mass resolution of the order of 1%.

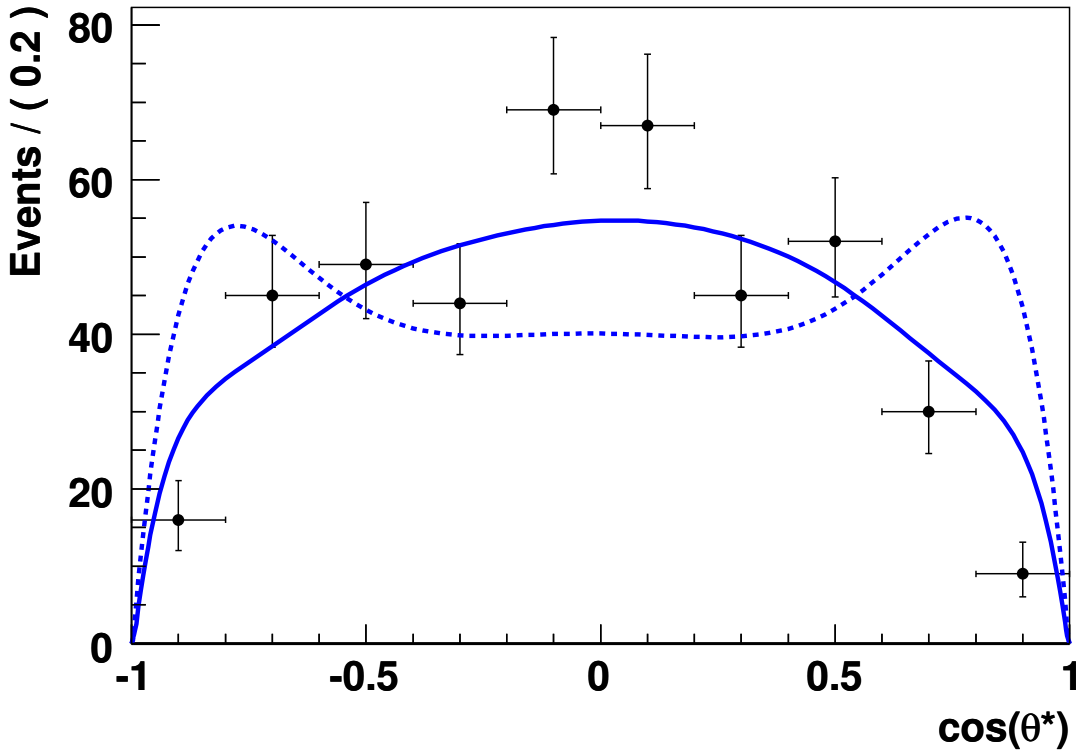

Figure 6.9: *Angular distribution of the decay leptons, after detector effects, shown together with the fitted p.d.f. (solid). The spin-1 p.d.f. (dotted) is also shown. The graviton mass was 1 TeV.*

Appendix A

Residual derivatives

In this appendix we present the derivation of the analytical residual derivatives that are used in the track fit. The expressions were checked and simplified using the Mathematica program. Let $\vec{x}_{track}$ be the position of the track near a hit, i.e. the point of closest approach to a wire, or the intersection with a sensor. This position will move by an amount $\vec{\epsilon}$ if one of the track parameters is changed by an amount ϵ. For the track parameters d_0, z_0, ϕ and θ, the vectors $\vec{\epsilon}$ are given by:

$$\vec{\epsilon}_{d_0} = \epsilon \begin{pmatrix} -\sin\phi_0 \\ \cos\phi_0 \\ 0 \end{pmatrix} \tag{A.1}$$

$$\vec{\epsilon}_{z_0} = \epsilon \begin{pmatrix} 0 \\ 0 \\ 1 \end{pmatrix} \tag{A.2}$$

$$\vec{\epsilon}_{\phi} = \epsilon \begin{pmatrix} -\Delta y \\ \Delta x \\ 0 \end{pmatrix} \tag{A.3}$$

$$\vec{\epsilon}_{\theta} = \epsilon \begin{pmatrix} \frac{\Delta x \Delta z}{\sqrt{(\Delta x)^2+(\Delta y)^2}} \\ \frac{\Delta y \Delta z}{\sqrt{(\Delta x)^2+(\Delta y)^2}} \\ -\sqrt{(\Delta x)^2+(\Delta y)^2} \end{pmatrix} \tag{A.4}$$

where $(\Delta x, \Delta y, \Delta z)$ is the vector from the rotation center to $\vec{x}_{track}$. For the azimuthal angle ϕ_0 at the perigee one rotates around the z-axis, so Δx and Δy are just the x- and y-components of $\vec{x}_{track}$, respectively. The rotation center of the polar angle θ_0 is $(-d_0 \sin\phi_0, d_0 \cos\phi_0, z_0)$, the perigee coordinates. For the scattering angles one rotates around the intersection of the track with the scattering plane.

The derivative now follows by projecting the displaced track from $\vec{x}_{track} + \vec{\epsilon}$ back into the measurement plane of the hit, calculating the change in the residual, and keeping the terms proportional to ϵ.

Strip cluster derivatives

We will first discuss the case of a strip sensor. For the derivative with respect to z_0, the equation to be solved is

$$\begin{pmatrix} x \\ y \\ z+\epsilon \end{pmatrix} + \lambda \begin{pmatrix} \cos\phi \sin\theta \\ \sin\phi \sin\theta \\ \cos\theta \end{pmatrix} = \begin{pmatrix} x \\ y \\ z \end{pmatrix} + a\hat{\phi} + b\hat{\eta} \tag{A.5}$$

where (x, y, z) is the position of the track at the sensor, ϕ and θ are the azimuthal and polar angles of the track at the sensor, and $\hat{\phi}$ and $\hat{\eta}$ are two unit vectors in the sensor plane, perpendicular and parallel to the strips respectively. The left side of Eq. (A.5) gives the intercept of the displaced track with the plane (approximating the track with a straight line). The equation can be solved for λ, eliminating a and b, giving

$$\lambda = \epsilon \frac{-\hat{\eta}_y\hat{\phi}_x + \hat{\eta}_x\hat{\phi}_y}{(\hat{\eta}_y\hat{\phi}_x - \hat{\eta}_x\hat{\phi}_y)\cos\theta + \Big((\hat{\eta}_z\hat{\phi}_y - \hat{\eta}_y\hat{\phi}_z)\cos\phi + (\hat{\eta}_z\hat{\phi}_x - \hat{\eta}_x\hat{\phi}_z)\sin\phi\Big)\sin\theta} \tag{A.6}$$

To make the expressions that will follow a bit more simple, we define the variable μ:

$$\begin{aligned}\mu \equiv\ & (\hat{\eta}_x\hat{\phi}_y - \hat{\eta}_y\hat{\phi}_x)\cos\theta + \Big((\hat{\eta}_y\hat{\phi}_z - \hat{\eta}_z\hat{\phi}_y)\cos\phi \\ & + (\hat{\eta}_z\hat{\phi}_x - \hat{\eta}_x\hat{\phi}_z)\sin\phi\Big)\sin\theta\end{aligned} \tag{A.7}$$

By entering Eq. (A.6) into the left side of Eq. (A.5), taking the difference with (x, y, z), dividing by ϵ, and taking the dot product with $\hat{\phi}$, we get the derivative:

$$\begin{aligned}\frac{\partial r}{\partial z_0} = \Bigg[\Bigg(& \Big(-\hat{\phi}_y(\hat{\eta}_x\hat{\phi}_x + \hat{\eta}_z\hat{\phi}_z) + \hat{\eta}_y(\hat{\phi}_x^2 + \hat{\phi}_z^2)\Big)\cos\phi \\ & + \Big(\hat{\eta}_y\hat{\phi}_x\hat{\phi}_y + \hat{\eta}_z\hat{\phi}_x\hat{\phi}_z - \hat{\eta}_x(\hat{\phi}_y^2 + \hat{\phi}_z^2)\Big)\sin\phi\Bigg)\sin\theta\Bigg]/\mu\end{aligned} \tag{A.8}$$

The other three derivatives are calculated in the same way. For the angle derivatives one should in principle take the change of the direction of the track into account. However, from Eq. (A.5) it is seen that this gives a term proportional to ϵ^2, since both λ and the change in the direction are proportional to ϵ. This change can therefore be ignored. The results for the other derivatives are

$$\begin{aligned}\frac{\partial r}{\partial d_0} = \Big[& \hat{\eta}_x(\hat{\phi}_y^2 + \hat{\phi}_z^2) - \hat{\eta}_y\hat{\phi}_x\hat{\phi}_y - \hat{\eta}_z\hat{\phi}_x\hat{\phi}_z - \cos\phi_0\cos\theta \\ & - \Big(\hat{\phi}_y(\hat{\eta}_x\hat{\phi}_x + \hat{\eta}_z\hat{\phi}_z) - \hat{\eta}_y(\hat{\phi}_x^2 + \hat{\phi}_z^2)\Big)\cos\theta\sin\phi_0 \\ & - \Big(\hat{\eta}_z(\hat{\phi}_x^2 + \hat{\phi}_y^2) - (\hat{\eta}_x\hat{\phi}_x + \hat{\eta}_y\hat{\phi}_y)\hat{\phi}_z\Big)\cos(\phi_0 - \phi)\sin\theta\Big]/\mu\end{aligned} \tag{A.9}$$

$$\frac{\partial r}{\partial \phi} = \Big[\Big(- \hat{\eta}_y\hat{\phi}_x\hat{\phi}_y\Delta_x + \hat{\eta}_x(\hat{\phi}_y^2 + \hat{\phi}_z^2)\Delta_x - \hat{\eta}_x\hat{\phi}_x\hat{\phi}_y\Delta_y + \hat{\eta}_y(\hat{\phi}_x^2 + \hat{\phi}_z^2)\Delta_y - \hat{\eta}_z\hat{\phi}_z(\hat{\phi}_x\Delta_x + \hat{\phi}_y\Delta_y)\Big)\cos\theta - \Big(\hat{\eta}_z(\hat{\phi}_x^2 + \hat{\phi}_y^2) - (\hat{\eta}_x\hat{\phi}_x + \hat{\eta}_y\hat{\phi}_y)\hat{\phi}_z\Big)\Big(\Delta_x\cos\phi + \Delta_y\sin\phi\Big)\sin\theta\Big]/\mu \quad \text{(A.10)}$$

$$\begin{aligned}\frac{\partial r}{\partial \theta} = \Big[\Big(&\Big(\hat{\phi}_y(\hat{\eta}_x\hat{\phi}_x + \hat{\eta}_z\hat{\phi}_z) - \hat{\eta}_y(\hat{\phi}_x^2 + \hat{\phi}_z^2)\Big)\Delta_x \\ &- \Big(\hat{\eta}_y\hat{\phi}_x\hat{\phi}_y + \hat{\eta}_z\hat{\phi}_x\hat{\phi}_z - \hat{\eta}_x(\hat{\phi}_y^2 + \hat{\phi}_z^2)\Big)\Delta_y\Big)\Delta_z\cos\theta \\ -\Big\{&\Big(\Big(\hat{\eta}_y(\hat{\phi}_x^2 + \hat{\phi}_z^2) - \hat{\phi}_y(\hat{\eta}_x\hat{\phi}_x + \hat{\eta}_z\hat{\phi}_z)\Big)\Big(\Delta_x^2 + \Delta_y^2\Big) \\ &+ \Big(\hat{\eta}_z(\hat{\phi}_x^2 + \hat{\phi}_y^2) - (\hat{\eta}_x\hat{\phi}_x + \hat{\eta}_y\hat{\phi}_y)\hat{\phi}_z\Big)\Delta_y\Delta_z\Big)\cos\phi \\ +\Big(&\Big(\hat{\eta}_y\hat{\phi}_x\hat{\phi}_y + \hat{\eta}_z\hat{\phi}_x\hat{\phi}_z - \hat{\eta}_x(\hat{\phi}_y^2 + \hat{\phi}_z^2)\Big)\Big(\Delta_x^2 + \Delta_y^2\Big) \\ &- \Big(\hat{\eta}_z(\hat{\phi}_x^2 + \hat{\phi}_y^2) - (\hat{\eta}_x\hat{\phi}_x + \hat{\eta}_y\hat{\phi}_y)\hat{\phi}_z\Big)\Delta_x\Delta_z\Big)\sin\phi\Big\}\sin\theta\Big]/ \\ &\Big(\mu\sqrt{\Delta_x^2 + \Delta_y^2}\Big)\end{aligned} \quad \text{(A.11)}$$

Drift circle derivatives

We now turn our attention to the derivatives of the drift circle residuals. It is useful to calculate them in local hit coordinates, i.e. in the plane perpendicular to the wire. The transformation from global to local hit coordinates is given by

$$S = \begin{pmatrix} \cos\theta\cos\phi & \cos\theta\sin\phi & -\sin\theta \\ -\sin\phi & \cos\phi & 0 \end{pmatrix} \quad \text{(A.12)}$$

where θ and ϕ are the polar and azimuthal angle of the wire. The transformation is unity if the wire points along the z-axis. The local change in the track can be found by applying S to the vectors $\vec{\epsilon}$ (Eqs. (A.1)-(A.4)), we will call these local shifts $\vec{\epsilon}$ from now on.

Fig. A.1 shows how the position and the direction of the track changes. We denote the track direction in local coordinates with ϕ_{tr}. If r is the original radius of the drift circle, $\hat{r}$ is a unit vector along the original radius, and $\hat{r'}$ is a unit vector along the new radius, then the change in the radius is given by

$$\delta r = \vec{\epsilon}\cdot\hat{r'} - r(1 - \cos\delta\phi_{tr}) \quad \text{(A.13)}$$

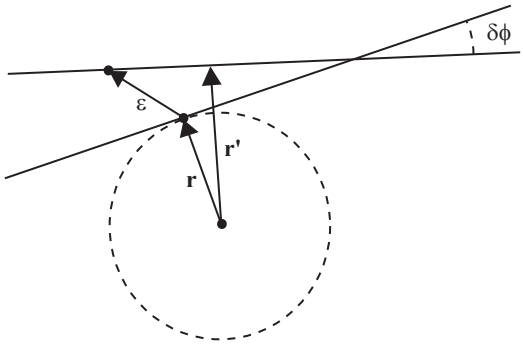

Figure A.1: *The distance between the original track and the wire is r. If one of the track parameters is changed by an amount ϵ, the point of closest approach $\vec{r}$ moves to $\vec{r}+\vec{\epsilon}$. The new distance between the track and the wire is r'.*

Up to first order in ϵ, this amounts to

$$\delta r = \vec{\epsilon}\cdot\hat{r}, \tag{A.14}$$

$$\hat{r} = \begin{pmatrix} -\sin\phi_{tr} \\ \cos\phi_{tr} \end{pmatrix} \tag{A.15}$$

Thus, again it is true that the change in the direction of the track can be ignored. Using Eqs. (A.1)-(A.4), (A.12) and (A.15), the derivatives can now be computed to be

$$\frac{\partial r}{\partial d_0} = -\cos\theta\sin(\phi-\phi_0)\sin\phi_{tr} + \cos(\phi-\phi_0)\cos\phi_{tr} \tag{A.16}$$

$$\frac{\partial r}{\partial z_0} = \sin\theta\sin\phi_{tr} \tag{A.17}$$

$$\begin{aligned}\frac{\partial r}{\partial \phi} = {} & \Delta_y\cos\theta\cos\phi\sin\phi_{tr} - \Delta_x\cos\theta\sin\phi\sin\phi_{tr} \\ & + \Delta_y\sin\phi\cos\phi_{tr} + \Delta_x\cos\phi\cos\phi_{tr}\end{aligned} \tag{A.18}$$

$$\begin{aligned}\frac{\partial r}{\partial \theta} = {} & -\sin\phi_{tr}\left(\frac{\Delta_x\Delta_z}{\sqrt{\Delta_x^2+\Delta_y^2}}\cos\theta\cos\phi + \frac{\Delta_y\Delta_z}{\sqrt{\Delta_x^2+\Delta_y^2}}\cos\theta\sin\phi + \sqrt{\Delta_x^2+\Delta_y^2}\sin\theta\right) \\ & + \cos\phi_{tr}\left(-\frac{\Delta_x\Delta_z}{\sqrt{\Delta_x^2+\Delta_y^2}}\sin\phi + \frac{\Delta_y\Delta_z}{\sqrt{\Delta_x^2+\Delta_y^2}}\cos\phi\right)\end{aligned} \tag{A.19}$$

Scattering angle derivatives

The derivatives of the residuals with respect to the scattering angles are given by Eqs. (A.18) and (A.19) if the hit lies behind the scattering plane (i.e. the particle first traverses the scattering plane before reaching the hit). If the hit is in front of the scattering plane then the derivatives are zero, because multiple scattering can only affect the downstream part of the track.

The scattering angles contribute to the χ^2, so the derivatives of these contributions should also be taken into account. The residuals are just the scattering angles themselves:

$$r_{\phi,i} = \sin\theta_{loc}\phi_{scat,i} \tag{A.20}$$

$$r_{\theta,i} = \theta_{scat,i} \tag{A.21}$$

where the index i denotes the scattering plane, and θ_{loc} is the angle between the track and the z-axis at the scattering plane. The derivatives are thus:

$$\frac{\partial r_{\phi,i}}{\partial \phi_{scat,j}} = \begin{cases} \sin\theta_{loc} & \text{if } i = j \\ 0 & \text{if } i \neq j \end{cases} \tag{A.22}$$

$$\frac{\partial r_{\theta,i}}{\partial \theta_{scat,j}} = \begin{cases} 1 & \text{if } i = j \\ 0 & \text{if } i \neq j \end{cases} \tag{A.23}$$

Energy loss derivatives

The energy loss at a brem point is fitted by making the momentum after the brem point an additional fit parameter. Let p_0 be the momentum just after the previous brem point, or at the vertex if the current brem point is the first brem point on the track. Then the momentum just before the current brem point is given by $p_0 + a$, where a is the (constant) energy loss in the material between the previous brem point (or the vertex) and the current one. If p_1 is the momentum just after the brem point, then the energy loss is given by:

$$\Delta E = -sign(q/p_0)\left(\frac{1}{q/(p_0+a)} - \frac{1}{q/p_1}\right) \tag{A.24}$$

The derivatives are then given by:

$$\frac{\partial(\Delta E)}{\partial(q/p_0)} = sign(q/p_0)\frac{1}{(q/p_0)^2} \tag{A.25}$$

$$\frac{\partial(\Delta E)}{\partial(q/p_1)} = -sign(q/p_0)\frac{1}{(q/p_1)^2} \tag{A.26}$$

The fit also needs to evaluate the derivatives of the other residuals with respect to q/p_1. This is done numerically (just like q/p_0), i.e. the fit makes a small change in the fit parameter, and calculates the resulting change in the residual.

Appendix B

Athena technicalities

In this appendix we will discuss some details concerning the implementation of the tracking code in the Athena framework. The various joboption switches are shown, and a list of the quantities that are computed and stored in the tracks is given.

B.1 SiCTBTracking

The algorithm can be run by including:

```
include ("SiCTBTracking/SiCTBTracking_options.py")
```

Then, the following options can be set:

- `SiCTBTracking.tracksname` Name of the track collection that is written out. Default is "SiTB_Tracks".
- `SiCTBTracking.tracksupname` Name of the tracks that are fitted in the upper half of the cosmics setup. Default is "SCT_Cosmic_TracksUp".
- `SiCTBTracking.trackslowname` Name of the tracks that are fitted in the lower half of the cosmics setup. Default is "SCT_Cosmic_TracksLow".
- `SiCTBTracking.processPixels` When false, no pixel points are used. Default is true.
- `SiCTBTracking.processSCT` When false, no SCT points are used. Default is true.
- `SiCTBTracking.MinNumberOfPointsOnTrack` Minimum number of spacepoints on a track. Default is 4.
- `SiCTBTracking.MaxNumberOfPoints` If the total number of spacepoints exceeds this value, the event is skipped. Default is 120.
- `SiCTBTracking.OnePointPerModule` Consider a module only if it has one spacepoint in it, otherwise it is ignored. Note that this automatically excludes ganged pixels. Default is false.

- `SiCTBTracking.GangedPixels` If set to false, ganged pixels are ignored in the tracking. Default is true.
- `SiCTBTracking.TrackFitter` Type and name of the track fitter to be used. Default is "Trk::GlobalChi2Fitter/GlobalChi2Fitter".
- `SiCTBTracking.ExtrapolatorName` Name of the extrapolator tool, e.g. "CTB_FullExtrapolator".
- `SiCTBTracking.Cosmics` Enables tracking for the cosmics. Default is disabled.
- `SiCTBTracking.matEffects` Sets the particle hypothesis for the track fit. Possible values are: 0 (electron),1 (muon), 2 (pion), 3 (proton), and 4 (noninteracting).
- `SiCTBTracking.runOutlier` Enables the outlier logic in the track fit. Default is disabled.
- `SiCTBTracking.MaskedWafers` Disables one or more silicon sensors in the tracking. This option takes a list of integers, where each integer should correspond with the IdentifierHash of the sensor in the detector description. For an SCT sensor the integer should be offset by 5000 relative to this IdentifierHash.

B.2 InDetCTBTracking

The algorithm can be run by including:

```
include ("InDetCTBTracking/InDetCTBTracking_options.py")
```

Then the following options can be set:

- `InDetCTBTracking.DriftCircleCut` Maximum distance between a TRT drift circle and a seed in the TRT track search, in millimeters. Default is 1.5.
- `InDetCTBTracking.InputTracksName` Name of the track collection with tracks from the silicon detectors. Default is "SiTB_Tracks".
- `InDetCTBTracking.OutputTracks` Name of the track collection that is written out. Default is "InDetTB_Tracks".
- `InDetCTBTracking.OutputTracksUp` Name of the tracks that are fitted in the upper half of the cosmics setup. Default is "InDetCosmic_TracksUp".
- `InDetCTBTracking.OutputTracksLow` Name of the tracks that are fitted in the lower half of the cosmics setup. Default is "InDetCosmic_TracksLow".
- `InDetCTBTracking.TRTHitsOnTrack` Minimum number of TRT hits on a track. Default is 25.

- `InDetCTBTracking.TrackFitter` Type and name of the track fitter to be used. Default is "Trk::GlobalChi2Fitter/GlobalChi2Fitter".
- `InDetCTBTracking.ExtrapolatorName` Name of the extrapolator tool, e.g. "CTB_FullExtrapolator".
- `InDetCTBTracking.Cosmics` Enables tracking for the cosmics. Default is disabled.
- `InDetCTBTracking.Chi2cut` The maximum reduced χ^2 value of a fitted track.
- `InDetCTBTracking.WeightFactor` Sets the weight factor w in the TRT track search (see Eq. (4.1))
- `InDetCTBTracking.matEffects` Sets the particle hypothesis for the track fit. Possible values are: 0 (electron),1 (muon), 2 (pion), 3 (proton), and 4 (noninteracting).
- `InDetCTBTracking.runOutlier` Enables the outlier logic in the track fit. Default is disabled.
- `InDetCTBTracking.ExtendToSCT` When enabled, tracks that are found in the TRT are extrapolated to the SCT to associate SCT points to the track. Default is disabled, for the cosmics it is automatically enabled.

B.3 Track fit (TrkGlobalChi2Fitter)

The track fit stores its output in the new common track class (`Trk::Track`). The quantities that it stores are:

- The track parameters at the perigee (d_0, z_0, ϕ_0, θ_0, q/p) and their errors, accessible through `track->perigeeParameters()`
- The overall χ^2 and the number of degrees of freedom of the track, accessible through `track->fitQuality()`
- A list of measurements on the track, accessible through `track->measurementsOnTrack()`
- A list of track parameters at each measurement, including their errors.
- A list of scattering angles at each scattering center, including their variances. Stored in the `Trk::ScatteringAngleOnSurface` class.

The configuring of options is done using a Python setup class, called 'ConfiguredGlobalChi2Fitter'. This is setup as follows:

```
include ("TrkGlobalChi2Fitter/ConfiguredGlobalChi2Fitter.py")
myfitter=ConfiguredGlobalChi2Fitter(trackmodel='helix', instname = None,
                 extrapolator = None, rotcreator   = None,
                 updator = None)
```

As shown, the setup class takes a number of arguments: the track model (either 'line' or 'helix'), the name of the fitter instance (e.g. 'myfitter'), and instances of the `Extrapolator`, `RIO_OnTrackCreator` and `Updator` tools. If one or more of these tools are not given, the fitter will construct these tools by itself.

Once the fitter has been constructed using the setup class, the following options can be set:

- `myfitter.setChi2Cut([...])` Sets the χ^2 cut for the fast, spacepoint based fits.
- `myfitter.setOutlierCut(...)` Sets the outlier cut for drift circle hits (e.g. TRT), in units of σ. Default is 5.
- `myfitter.useSignedDriftRadius(False/True)` When enabled, the fit sticks to the sign of the radius that it is given by the drift circle hits. Default is disabled.
- `myfitter.allowEmptyMeastOnTrack(False/True)` Allow null pointers in the list of hits on the track. Default is false.
- `myfitter.ExtraMaterial1(False/True)` When enabled, a scattering plane with 11% X_0 is placed between the pixel and SCT detectors. This is needed when a testbeam run with extra material is chosen. Default is disabled, in InDetTBRecExample it is automatically enabled when needed.
- `myfitter.ExtraMaterial2(False/True)` When enabled, a scattering plane with 22% X_0 is placed between the SCT and TRT detectors. This is needed when a testbeam run with extra material is chosen. Default is disabled, in InDetTBRecExample it is automatically enabled when needed.
- `myfitter.Momentum(...)` Fixes the momentum to the specified value (in MeV). This allows one e.g. to perform a straight line fit with material effects enabled, since these effects are momentum dependent.
- `myfitter.SortPoint([...])` Sets the reference point for the hit sorting, i.e. the hits are sorted according to the distance to this point. Default is [0,0,0].
- `myfitter.Shift(...)` Shifts all the material layers of the hardwired testbeam material description by the specified value. Default is 146 (correct when $x = 0$ at the beginning of the magnet)
- `myfitter.VertexShift(...)` Shifts the vertex in x by the specified amount (experimental). Default is 0.
- `myfitter.NumericalDerivs(False/True)` Use numerical residual derivatives. Default is False, i.e. analytical derivatives are used (faster).

References

[1] The CDF Collaboration, *Observation of Top Quark Production in $\overline{p}p$ Collisions with the CDF Detector at Fermilab*, Phys. Rev. Lett. **74** (1995) 2626.

[2] M.E. Peskin and D.V. Schroeder, *An Introduction to Quantum Field Theory*, Perseus Books, 1995.

[3] D. Griffiths, *Introduction to Elementary Particles*, Wiley, 1987.

[4] K. Hagiwara et al. (the particle data group), *Review of particle physics*, Phys. Rev. **D66** (2002) .

[5] P. Higgs, *Broken Symmetries, Massless Particles and Gauge Fields*, Phys. Lett. **12** (1964) 132.

[6] B.W. Lee, C. Quigg, and H.B. Thacker, *Weak interactions at very high energies: The role of the Higgs-boson mass*, Phys. Rev. **D 16** (1977) 1519.

[7] H. Davoudiasl, J.L. Hewett, and T.G. Rizzo, *Warped Phenomenology*, Phys. Rev. Lett. **84** (2000) 2080, hep-ph/9909255.

[8] Y. Kubyshin, *Models with Extra Dimensions and Their Phenomenology*, hep-ph/0111027, 2001.

[9] N. Arkani-Hamed, S. Dimopoulos, and G. Dvali, *The Hierarchy Problem and New Dimensions at a Millimeter*, Phys. Lett. **B249** (1998) 263, hep-ph/9803315.

[10] N. Arkani-Hamed, S. Dimopoulos, and G. Dvali, *Phenomenology, Astrophysics and Cosmology of Theories with Sub-Millimeter Dimensions and TeV Scale Quantum Gravity*, hep-ph/9807344, 1998.

[11] E.G. Adelberger, B.R. Heckel, and A.E. Nelson, *Tests of the Gravitational Inverse-square Law*, Ann. Rev. Nucl. Part. Sci. **53** (2003) 77, hep-ph/0307284.

[12] C.D. Hoyle et al., *Sub-millimeter Tests of the Gravitational Inverse-square Law*, hep-ph/0405262, 2004.

[13] G.F. Giudice, R. Rattazzi, and J.D. Wells, *Quantum Gravity and Extra Dimensions at High-Energy Colliders*, Nucl. Phys. **B544** (1999) 3, hep-ph/9811291.

[14] L. Randall and R. Sundrum, *Large Mass Hierarchy from a Small Extra Dimension*, Phys. Rev. Lett. **83** (1999) 3370, hep-ph/9905221.

[15] H. Davoudiasl, J.L. Hewett, and T.G. Rizzo, *Experimental Probes of Localized Gravity: On and Off the Wall*, Phys. Rev. **D63** (2001) 075004, hep-ph/0006041.

[16] J.L. Hewett and M. Spiropulu, *Particle Physics Probes Of Extra Spacetime Dimensions*, Ann. Rev. Nucl. Part. Sci. **52** (2002) 397.

[17] L. Vacavant and I. Hinchliffe, *Model Independent Extra-dimension signatures with ATLAS*, hep-ex/0005033, 2000.

[18] L. Vacavant and I. Hinchliffe, *Signals of models with large extra dimensions in ATLAS*, J. Phys. **G27** (2001) 1839.

[19] V. Kabachenko, A. Miagkov, and A. Zenin, *Sensitivity of the ATLAS detector to extra dimensions in di-photon and di-lepton production processes*, ATL-PHYS-2001-012, 2001.

[20] P. Lefèvre and T. Pettersson, *The Large Hadron Collider: conceptual design*, CERN-AC-95-05-LHC, 1995.

[21] CERN, *LEP shuts down after eleven years of forefront research*, `http://press.web.cern.ch/Press/PressReleases/Releases2000/PR14.00ELEPstop.html`, 2000.

[22] ATLAS Collaboration, W. Armstrong et al., *ATLAS : Technical Proposal for a General-Purpose pp Experiment at the Large Hadron Collider at CERN*, CERN/LHCC/94-43, 1994.

[23] CMS Collaboration, *Technical Proposal*, CERN/LHCC/94-38, 1994.

[24] LHCb Collaboration, S. Amato et al., *LHCb Technical Proposal*, CERN/LHCC/98-4, 1998.

[25] ALICE Collaboration, N. Ahmad et al., *A Large Ion Collider Experiment - Technical Proposal*, CERN/LHCC/95-71, 1995.

[26] ATLAS Collaboration, *ATLAS Detector and Physics Technical Design Report*, CERN/LHCC/99-14&15, 1999.

[27] ATLAS Inner Detector Collaboration, *ATLAS Inner Detector Technical Design Report*, CERN/LHCC/97-16&17, 1997.

[28] S. Peeters, *The ATLAS Semiconductor Tracking Endcap*, Ph.D. thesis, NIKHEF, 2003.

[29] M. Vos, *The ATLAS inner tracker and the detection of light Super-Symmetric Higgs bosons*, Ph.D. thesis, Universiteit Twente, 2003.

[30] ATLAS LARG Unit, *Liquid Argon Calorimeter Technical Design Report*, CERN/LHCC/96-41, 1996.

[31] ATLAS Tile Calorimeter Collaboration, *Tile Calorimeter Technical Design Report*, CERN/LHCC/96-42, 1996.

[32] ATLAS Muon Collaboration, *ATLAS Muon Spectrometer Technical Design Report*, CERN/LHCC/97-22, 1997.

[33] ATLAS Level-1 Trigger Group, *Level-1 Trigger Technical Design Report*, CERN/LHCC/98-14, 1998.

[34] ATLAS HLT/DAQ/DCS Group, *ATLAS High Level Trigger, Data Acquisition and Controls Technical Design Report*, CERN/LHCC/2003-022, 2003.

[35] *The ATHENA Homepage*, `http://atlas.web.cern.ch/Atlas/GROUPS/SOFTWARE/OO/architecture/`.

[36] G. Barrand et al., *GAUDI - A software architecture and framework for building HEP data processing applications*, Comp. Phys. Comm. **140** (2001) 45.

[37] T. Sjöstrand et al., *High-Energy-Physics Event Generation with Pythia 6.1*, Computer Physics Comm. **238** (2001) , hep-ph/0010017.

[38] G. Corcella et al., *HERWIG 6: An event generator for hadron emission reactions with interfering gluons (including supersymmetric processes)*, JHEP **0101** (2001) 010, hep-ph/0011363.

[39] GEANT4 Collaboration, S. Agostinelli et al., *Geant4: A simulation toolkit*, Nucl. Instrum. Meth. **A506** (2003) 250.

[40] J. Boudreau and V. Tsulaia, *The HEPVis/v-atlas FAQ*, `http://boudreau.home.cern.ch/boudreau/v-atlas-hepvis.htm`.

[41] *The Atlantis Homepage*, `http://atlantis.web.cern.ch/atlantis/`.

[42] S. Gadomski, *Model of the SCT detectors and electronics for the ATLAS simulation using Geant4*, ATL-SOFT-2001-005, 2001.

[43] H. Spieler, *Semiconductor Detectors I: Principles*, `http://www-physics.lbl.gov/~spieler/physics_198_notes_1999/PDF/V-1-Principles.pdf`.

[44] P. Kluit, *private communication.*

[45] *STEP - Simultaneous Track and Error Propagation*, `https://uimon.cern.ch/twiki/bin/view/CMS/STEP`.

[46] I. Gavrilenko, *Description of Global Pattern Recognition Program (xKalman)*, ATL-INDET-97-165, 1997.

[47] M. Abramowitz and I.A. Stegun (Eds.), *Handbook of Mathematical Functions with Formulas, Graphs, and Mathematical Tables*, Dover, New York, 1964.

[48] R. Bock et al., *Data analysis techniques for high-energy physics experiments*, Cambridge University Press, 1990.

[49] A. Salzburger, *The Track Extrapolation package in the new ATLAS Tracking Realm*, Proceedings CHEP 04 , `http://indico.cern.ch/getFile.py/access?contribId=109&sessionId=24&resId=1&materialId=paper&confId=0`.

[50] M.J. Costa Mezquita, *Commissioning status report from inner detector*, `http://indico.cern.ch/getFile.py/access?contribId=21&sessionId=s14&resId=0&materialId=slides&confId=a06105`, 2006.

[51] P. Avery, *Fitting Theory I: General Least Squares Fitting Theory*, CBX 91-72, 1991.

[52] F. Akesson et al., *ATLAS Tracking Event Data Model*, ATL-SOFT-PUB-2006-004, 2006.

[53] M. Woudstra, *Precision of the ATLAS Muon Spectrometer*, Ph.D. thesis, NIKHEF, 2002.

[54] V. L. Highland, *Some Practical Remarks On Multiple Scattering*, Nucl. Instrum. Meth. **129** (1975) 497.

[55] A. Poppleton, *private communication.*

[56] R. van der Eijk, *Track reconstruction in the LHCb experiment*, Ph.D. thesis, NIKHEF, 2002.

[57] R. Frühwirth, *Application of Kalman filtering to track and vertex fitting*, Nucl. Instrum. Meth. **A262** (1987) 444.

[58] H. Bethe and W. Heitler, *On the stopping of fast particles and the creation of positive electrons*, Proc. Roy. Soc. A **146** (1934) 83.

[59] R. Clifft and A. Poppleton, *IPATREC: inner detector pattern-recognition and track-fitting*, ATL-SOFT-94-009, 1994.

[60] V. Boisvert et al., *Final Report of the ATLAS Reconstruction Task Force*, ATL-SOFT-2003-010, 2003.

[61] D. Adams et al., *Track reconstruction in the ATLAS Muon Spectrometer with MOORE*, ATL-SOFT-2003-007, 2003.

[62] ATLAS Collaboration, *Beamline instrumentation in the 2004 combined ATLAS testbeam*, ATL-TECH-PUB-2005-001, 2005.

[63] *ASAP home page*, http://florian.home.cern.ch/florian/Asap.html.

[64] *ARAMYS home page*, http://amelung.home.cern.ch/amelung/aramys.html.

[65] P. Hansen, *TRT Calibration and Alignment, CTB status*, http://agenda.cern.ch/askArchive.php?base=agenda&categ=a052086&id=a052086s22t7/transparencies, 2005.

[66] S. Gonzalez and S. Marti, *CTB04 Silicon alignment: Valencia recipe*, http://agenda.cern.ch/askArchive.php?base=agenda&categ=a061308&id=a061308s0t0/transparencies.

[67] P. Hansen, *TRT Calibration and Alignment, test beam results and future*, http://agenda.cern.ch/askArchive.php?base=agenda&categ=a042357&id=a042357s24t4%2Ftransparencies%2FCalibration.pdf, 2005.

[68] W. Lavrijsen, *Combined Muon Reconstruction For ATLAS*, Ph.D. thesis, University of Nijmegen, 2002.

[69] F. Bauer et al., *ATLAS 2004 Combined Test Beam results: Muon Chamber Alignment and Muon Reconstruction*, ATL-COM-MUON-2006-012.

[70] B.C. Allanach et al., *Exploring Small Extra Dimensions at the Large Hadron Collider*, hep-ph/0211205, 2002.

[71] J. Pumplin et al., *New Generation of Parton Distributions with Uncertainties from Global QCD Analysis*, hep-ph/0201195, 2002.

[72] O.K. Øye, *A full simulation analysis of the graviscalar discovery potential in ATLAS*, ATL-PHYS-PUB-2005-008, 2005.

[73] D. Dannheim, *First look at Randall-Sundrum Graviton with Pythia*, http://agenda.cern.ch/askArchive.php?base=agenda&categ=a044505&id=a044505s1t5/transparencies, 2004.

[74] B.C. Allanach et al., *Searching for Narrow Graviton Resonances with the ATLAS Detector at the Large Hadron Collider*, hep-ph/0006114, 2000.

[75] E. Barberio and Z. Was, *PHOTOS - A universal Monte Carlo for QED radiative corrections: version 2.0*, Comp. Phys. Comm. **79** (1994) 291.

[76] E. Richter-Was et al., *ATLFAST 2.0: a fast simulation package for ATLAS*, ATL-PHYS-98-131, 1998.

[77] F. Derue and C. Serfon, *Electron/jet separation with DC1 data*, ATL-PHYS-PUB-2005-016, 2005.

[78] T. Lagouri, *A Muon Identification and Combined Reconstruction Procedure for the ATLAS Detector at the LHC at CERN*, ATL-CONF-2003-011, 2003.

Summary

In the past century a theory has been developed that describes elementary particles and their interactions, the so-called 'Standard Model'. The Standard Model unifies two theories: the electroweak theory by Glashow, Weinberg and Salam, and the theory of the strong interaction, also called 'quantum chromodynamics'. It turns out that the Standard Model describes the world around us extremely well, giving theoretical predictions that are in superb agreement with the experimentally measured values. So far, there is not a single experimental observation that contradicts the theory. However, an essential part of the theory has not been established experimentally so far: the Higgs mechanism, which gives masses to the elementary particles.

Although the Standard Model has proven to be extremely successful, it is also clear that the theory is not complete, because it does not describe gravity. This interaction is many orders of magnitude weaker than the other three interactions (strong, weak and electromagnetic), in physics this is called the 'hierarchy problem'. Recently a number of theories have been developed that explain this hierarchy by assuming that there exist extra space dimensions. The observed weakness of the gravitational interaction is then not fundamental, it is a consequence of the extra dimensions. No evidence exists so far that suggests the existence of these extra dimensions, thus it is far from certain that these theories are correct. However, the theories make a number of clear predictions, that can be checked with the next generation of particle accelerators.

The new accelerator at CERN near Geneva will be the Large Hadron Collider (LHC). Starting from 2008, this accelerator will collide protons with a center-of-mass energy of 14 TeV. This energy, which is much higher than at previous accelerators, will allow physicists to perform new discoveries. For example, it is expected that the Higgs particle will be discovered, if it exists. Four experiments are under construction that will analyze the collisions: ALICE, LHCb, CMS, and the experiment that is the subject of this thesis: ATLAS.

ATLAS consists of a number of detector layers around the interaction point, where the protons collide. In the innermost layer, the 'inner tracker', the trajectories of the charged particles are detected. The energies of the particles are measured by the calorimeters, which are built around the inner tracker. The only charged particles that can penetrate the calorimeters are muons, which are detected in the outermost layer, the muon spectrometer.

In this thesis, emphasis is placed on the analysis of the data from the inner tracker and the muon spectrometer. For each particle, the detector performs a number of position measurements. From this set of three-dimensional points, the trajectory of the

particle can be reconstructed using computer calculations. In this thesis an algorithm is described that is based on the minimization of a global χ^2 function. The algorithm corrects for energy loss and scattering in the detector material, by introducing extra fit parameters for these material effects. The propagation of the tracks through the magnetic field in the detector is performed using a fourth order Runge-Kutta procedure. This procedure is numerical, therefore it requires a significant amount of computation time. It turns out that the derivatives of the measurements with respect to the track parameters can be evaluated analytically, which reduces the amount of computation time required.

The algorithm has been developed for analyzing the data from the 'combined testbeam' setup in ATLAS. This setup consisted of prototypes of the detectors that will be used in ATLAS, and was placed in the particle beam of the SPS accelerator at CERN. Despite a number of problems with the readout electronics, it turned out that the algorithm was capable of reconstructing the tracks quickly and efficiently. The measured resolutions of the individual subdetectors are in good agreement with the expected values. The measured resolutions of the track parameters are somewhat worse than expected, mainly because the alignment of the detector has not yet been completed. Finally, it has been attempted to perform combined muon reconstruction, using all the position measurements in the inner tracker and the muon detector in the testbeam setup. The results show that the combined muon reconstruction works as expected.

An important test for ATLAS is the detection of cosmic rays. With some modifications, the track reconstruction algorithm was suited for analyzing the cosmic ray data. The first results show that the inner tracker can detect the cosmic rays quite well. This is encouraging given the fast approaching starting date of the LHC experiments, which is planned for the end of 2007.

The quality of the reconstruction program can be checked using simulated data, by measuring the difference between the simulated track and the reconstructed track. It turns out that the testbeam reconstruction algorithm performs clearly better in the testbeam setup than the standard ATLAS reconstruction algorithms. Furthermore, the uncertainties on the track parameters are estimated correctly. Apart from the testbeam setup, the testbeam algorithm can also be used for analyzing simulated collisions in ATLAS. The algorithm can fit tracks in the inner tracker and the muon spectrometer. Again the resolutions turn out to be just as good as those obtained with the standard ATLAS reconstruction algorithms, in some cases even better.

In the last part of this thesis, the potential of ATLAS to detect gravitons has been investigated, using simulated data. Gravitons are extremely heavy particles, that are predicted by theories with extra dimensions. In this case the Randall-Sundrum model has been studied, which predicts narrow graviton resonances with a mass in the order of 1 TeV. The most promising discovery channel is the channel where the graviton decays into an electron-positron pair. It is found that up to a mass of 1.5 TeV, enough gravitons are produced for detecting a statistically significant signal. The mass resolution is about 1%. The spin of the resonance is determined by performing a likelihood fit to the decay angles of the electron-positron pairs. It turns out that it is possible to determine the spin of the graviton in this way.

Samenvatting

In de afgelopen eeuw is een theorie ontwikkeld die de elementaire deeltjes en hun interacties beschrijft, het zogenaamde 'Standaard Model'. Het Standaard Model verenigt twee theorieën: de elektro-zwakke theorie van Glashow, Weinberg en Salam, en de theorie van de sterke wisselwerking, ook wel quantumchromodynamica genoemd. Het blijkt dat het Standaard Model de werkelijkheid bijzonder goed beschrijft, de theoretische voorspellingen kloppen met de experimenteel gemeten waarden tot op vele cijfers achter de komma. Tot nu toe is geen enkele experimentele observatie strijdig met de theorie. Er is echter een essentieel onderdeel in de theorie dat nog niet experimenteel is bevestigd: het Higgs- mechanisme, dat verantwoordelijk is voor de massa's van de elementaire deeltjes.

Hoewel het Standaard Model bijzonder succesvol is gebleken, is ook duidelijk dat de theorie niet compleet is, aangezien de zwaartekrachtsinteractie niet wordt beschreven. Deze interactie is vele ordes van grootte zwakker dan de andere drie interacties (sterk, zwak en elektromagnetisch), dit wordt in de natuurkunde het 'hiërarchie-probleem' genoemd. Recent is een aantal theorieën ontwikkeld, die dit verklaren door aan te nemen dat er extra ruimte-tijd dimensies bestaan. De waargenomen zwakte van de zwaartekracht is dan niet fundamenteel, het is een consequentie van de extra dimensies. Tot nu toe bestaat er geen enkel experimenteel bewijs dat deze extra dimensies bestaan, het is dus allerminst zeker dat deze theorieën juist zijn. De theorieën doen echter een aantal duidelijke voorspellingen, die met de volgende generatie deeltjesversnellers getoetst kunnen worden.

De nieuwe versneller van CERN bij Genève wordt de Large Hadron Collider (LHC). Deze machine zal vanaf 2008 protonen op elkaar laten botsen met een zwaartepuntsenergie van 14 TeV. Deze energie, die veel hoger is dan bij de vorige versnellers, zal natuurkundigen in staat stellen om nieuwe ontdekkingen te doen. Zo is de verwachting dat het Higgs-deeltje ontdekt zal worden, als het bestaat. Er zijn vier experimenten in aanbouw die de botsingen zullen analyseren: ALICE, LHCb, CMS, en het experiment dat het onderwerp is van dit proefschrift: ATLAS.

ATLAS is opgebouwd uit een aantal lagen van detectoren rond het interactiepunt, waar de protonen op elkaar botsen. In de binnenste laag, de 'inner tracker', worden de sporen van de geladen deeltjes gedetecteerd. Vervolgens komen de deeltjes in de calorimeters terecht, die de energieën van de deeltjes meten. De enige geladen deeltjes die door de calorimeters heen komen zijn muonen (een soort zware elektronen), deze worden in de buitenste laag gemeten, de muon spectrometer.

In dit proefschrift ligt de nadruk op de analyse van de data van de inner tracker en de muon spectrometer. De detector meet op een aantal plaatsen waar het deeltje

precies doorheen is gevlogen. Uit deze verzameling punten kan met behulp van computerberekeningen het spoor van het deeltje gereconstrueerd worden. In dit proefschrift wordt een algoritme beschreven dat is gebaseerd op de minimalisatie van een globale χ^2 functie. Het algoritme houdt rekening met energieverlies en verstrooiing in het materiaal van de detector, door extra fit parameters te introduceren voor deze materiaaleffecten. De propagatie van de sporen door het magneetveld in de detector gebeurt met behulp van een vierde orde Runge-Kutta procedure. Deze procedure is numeriek en vereist dus veel rekentijd. Het blijkt dat de afgeleiden van de metingen naar de spoorparameters analytisch bepaald kunnen worden, waardoor de rekentijd verkleind wordt.

Het algoritme is ontwikkeld om de data te analyseren van de 'gecombineerde testbundel' opstelling in ATLAS. Deze opstelling bestond uit prototypes van de detectoronderdelen die in ATLAS gebruikt zullen worden, en was geplaatst in de deeltjesbundel van de SPS versneller op CERN. Ondanks enkele problemen met de uitleeselektronica, bleek dat het algoritme in staat was om snel en efficiënt de sporen te reconstrueren. De gemeten resoluties in de individuele subdetectoren komen goed overeen met de verwachte waarden. De resoluties van de spoorparameters zijn enigszins slechter dan verwacht, met name doordat de uitlijning van de detector nog niet is voltooid. Tenslotte is geprobeerd om een gecombineerde reconstructie van muonen uit te voeren, gebruik makend van alle positiemetingen in de inner tracker en de muon-detector in de testbundel-opstelling. De resultaten laten zien dat de gecombineerde reconstructie naar behoren werkt.

Een belangrijke test voor ATLAS is de detectie van kosmische muonen. Met enkele wijzigingen bleek het spoorreconstructie-algoritme ook geschikt te zijn om deze data te analyseren. De eerste resultaten geven aan dat de inner tracker de kosmische sporen goed kan detecteren, wat bemoedigend is met het oog op de naderende start van de LHC experimenten, die voorlopig staat gepland voor eind 2007.

De kwaliteit van het reconstructie-programma kan worden bestudeerd met gesimuleerde data, door het verschil tussen het gesimuleerde spoor en het gereconstrueerde spoor te meten. Het blijkt dat het testbundel-algoritme duidelijk beter presteert dan de standaard ATLAS reconstructie-algoritmen in de testbundel-opstelling. Verder blijkt dat de onzekerheden op de spoorparameters goed geschat worden. Naast de testbundel-opstelling, kan het testbundel-algoritme ook toegepast worden om gesimuleerde botsingen in ATLAS te analyseren. Ook hier blijken de resoluties even goed of zelfs beter te zijn dan de standaard ATLAS reconstructie-algoritmen, zowel in de inner tracker als in de muon spectrometer.

In het laatste deel van het proefschrift is het potentieel van ATLAS onderzocht om gravitonen te detecteren, met behulp van gesimuleerde data. Gravitonen zijn extreem zware deeltjes, die worden voorspeld door theorieën met extra dimensies. In dit geval is het Randall-Sundrum model bestudeerd, dat nauwe gravitonresonanties met een massa in de orde van 1 TeV voorspelt. Het meest veelbelovende ontdekkingskanaal is het kanaal waarbij het graviton vervalt in een elektron-positron paar. Het blijkt dat er tot een massa van 1.5 TeV genoeg gravitonen worden geproduceerd om een statistisch significant signaal te detecteren. De massa-resolutie is ongeveer 1%. De spin van de resonantie wordt bepaald door middel van een likelihood fit aan de vervalshoeken van de elektron-positron paren. Het blijkt dat het mogelijk is om de spin van het graviton te bepalen.

Acknowledgements

In de afgelopen vier jaar hebben vele mensen bijgedragen om dit proefschrift tot stand te brengen.

Allereerst wil ik graag mijn promotor Frank Linde bedanken, omdat hij vertrouwen in mij had en mij heeft aangenomen als promotiestudent. Dankzij jouw aanwijzingen kon ik de tekst en met name de plaatjes beter maken. Stan en Peter waren mijn begeleiders, Stan met name in het begin, Peter vooral in het laatste jaar. Stans kennis over software was voor mij onmisbaar om zelf ingevoerd te raken in de ATLAS software. Peters expertise in spoorreconstructie was bijzonder nuttig om het track fit algoritme te voltooien en alle aspecten te begrijpen. De mede-promovendi op NIKHEF hebben mij in het begin veel uitgelegd over hoe een hoge-energie experiment nou eigenlijk werkt, iets waar ik als theoreet maar weinig van wist. Met name wil ik mijn kamergenoot Niels bedanken. Ik hoop dat je spoedig klaar bent met je eigen proefschrift. Thanks to Grant Gorfine, getting involved in the inner detector software couldn't have been easier (although software is never easy to work with!).

At CERN I enjoyed working in the inner detector software group. With the risk of forgetting somebody, I would like to thank Markus Elsing, Daniel Froidevaux, Wolfgang Liebig, María José Costa, Andreas Salzburger, Thomas Koffas, Tuan Vu Anh, Alan Poppleton, Tom Atkinson, Sergio Gonzalez Sevilla and Ed Moyse for the useful discussions we had. I would especially like to thank Wolfgang for proofreading the manuscript. Isabel Trigger's help was crucial for getting the muon track fit in the testbeam to work. The tours in the weekends with the CERN velo club were magnificent. I would especially like to thank Peter, Sylvia, Henrik and Kenneth. I hope I can soon meet all of you again at CERN.

Tenslotte wil ik de mensen bedanken die voor mij het belangrijkst zijn. Mijn oom Ton en broer Bas, bedankt dat jullie mijn paranimfen willen zijn. Bas, ik hoop dat ik spoedig je eigen promotie mag bijwonen. Maar de grootste steun in de afgelopen vier jaar waren mijn ouders. Lieve ouders, dank je wel dat jullie altijd voor mij klaar stonden als ik jullie nodig had. Jullie hebben de plaatjes voor de kaft gemaakt, dus jullie bijdrage is het meest zichtbare deel van het proefschrift. Hopelijk doet dat een beetje recht aan alle tijd en moeite die jullie in mij hebben geïnvesteerd.

Thijs

Amsterdam, oktober 2006.